REDUCED-ORDER MODELING OF NON-BOLTZMANN THERMOCHEMISTRY AND RADIATION FOR HYPERSONIC FLOWS

BY

AMAL SAHAI

DISSERTATION

Submitted in partial fulfillment of the requirements
for the degree of Doctor of Philosophy in Aerospace Engineering
in the Graduate College of the
University of Illinois at Urbana-Champaign, 2019

Urbana, Illinois

Doctoral Committee:

Associate Professor Marco Panesi, Chair and Director of Research
Professor J. Craig Dutton
Professor Carlos Pantano-Rubino
Dr. Christopher O. Johnston, NASA Langley Research Center

Abstract

The non-equilibrium aerothermal environment during hypersonic flows is determined by the interaction between a multitude of disparate physical phenomena with varying characteristic time scales. The multi-physics nature of this flight regime renders the task of accurately estimating vehicular characteristics both theoretically and computationally challenging. The rapid dissipation of flow velocity into thermal energy in the post-shock region drives collisional-radiative processes that alter the chemical and energy composition of the flowfield. Traditional thermochemical and radiative models often introduce ad-hoc simplifications and rely on model parameters calibrated for a limited range of experimental conditions. Recent advances in computing power have allowed non-equilibrium internal state population distributions of gaseous species to be precisely determined using *ab-initio* quantum-chemistry calculations, referred to as the state-to-state (StS) approach. Similarly, first-principles based databases for different chemical species are now available that can characterize radiative behavior by accounting for millions of individual radiative transitions, referred to as line-by-line (LBL) modeling. Although exceedingly accurate, both StS and LBL approaches are computationally expensive and cannot be viably applied for solving practical physical problems. This thesis is aimed at developing a unified reduced-order framework for describing non-equilibrium thermochemistry and radiative heating which retains the physical fidelity of the aforementioned approaches but at dramatically lowered computational costs.

A computationally tractable description of non-Boltzmann thermochemistry is obtained using the multi-group maximum-entropy (MGME) framework. This involves dividing individual internal states into bins and then reconstructing the state population distribution using the maximum entropy principle. The current work introduces an adaptive grouping methodology that incorporates state-specific kinetics for further improving the MGME method. Two strategies are considered – *Modified Island Algorithm* and *Spectral Clustering Method* – for identifying clusters of states that are likely to equilibrate faster with respect to each other and then lumping them together into bins. The efficacy of MGME-based model reduction is assessed by studying non-equilibrium characteristics of two chemical systems, molecular nitrogen and carbon-dioxide, in a homogeneous chemical reactor. The introduction of adaptive binning which correctly accounts for localized thermalization due to preferential transition pathways allows the complex dynamics of about $9,000$ internal states to be modeled using only 10-30 bins.

The multi-variate nature of radiative transfer is tackled by breaking it down into two components: geometric transfer and spectral modeling. A combination of discrete-ordinate method and finite-volume discretization with mesh sweeping is used to resolve generalized three-dimensional radiation fields in the angular and spatial domains. A reduced-order representation of the spectral variation in absorption/emission behavior is obtained through multi-group Planck-averaging. A formal interpretation for Planck-averaging is obtained based on maximum entropy closure in frequency space which allows a direct equivalence to be drawn with the MGME framework. Furthermore, a new generalized grouping strategy for non-equilibrium radiation is proposed that considers both absorption and emission coefficients while defining reduced-order groups. A detailed line-of-sight analysis for various Earth and Jovian entry problems indicates that Planck-averaging combined with the new grouping procedure allows reliable predictions while achieving a two orders-of-magnitude speed-up with respect to narrow-band methods (and three to four orders with respect to full LBL modeling).

The new simulation framework, with its focus on minimizing computational outlays, is ideally suited for realizing flow-radiation coupled simulations on large computational meshes. This is demonstrated by investigating, in conjunction with the US3D flow solver, the impact of vibrational non-equilibrium on CO_2 wake flows and resultant infrared radiation around NASA's Mars 2020 vehicle. Predictions for flowfield properties and radiative transfer are obtained using the conventional two-temperature model, bin-based StS model, and for decoupled/coupled flow-radiation calculations. Conventional two-temperature models overestimate the rate of thermal equilibration in the near-wake region resulting in the population of mid-lying and upper CO_2 vibrational levels being underpredicted by multiple orders of magnitude. Additionally, the two-temperature approach (in comparison to bin-based StS) overpredicts the rate of CO_2 dissociation thereby leading to erroneous estimates for flow properties in the post-shock region (primary source of afterbody radiative emission). This results in inflated values for surface radiative heat flux with conventional two-temperature modeling, although overall differences in radiative behavior are moderated by factors such as fast characteristic relaxation times for ground vibrational levels.

Acknowledgments

At the outset, I would like to express gratitude to my advisor, Professor Marco Panesi, for his support and guidance over the years. His forthrightness and emphasis on imbibing the foundational principles while tackling complex problems has helped immensely in my development as a researcher. I would like to thank my committee members, Professor Panesi, Professor Dutton, Professor Pantano, and Dr. Johnston, for their appraisal of this research and valuable feedback.

I am indebted to Dr. Christopher Johnston and Dr. Bruno Lopez for all their assistance and continued patience while addressing my countless queries. I could investigate the many facets of hypersonic planetary entry problem because they made different property databases and computational tools readily available to me. I am also grateful to Prof. Elena Kustova and Dr. Iole Armenise for their assistance with the CO_2 state-to-state model.

I would like to acknowledge the role of my colleagues at the University of Illinois, Andrea Albterti, Vegnesh Jayaraman, Dr. Robyn Macdonald, Dr. Alessandro Munafò, Przemyslaw Rostkowski, Maitreyee Sharma, and Simone Venturi in keeping me motivated and being able to surmount a seemingly endless list of challenges. I am also fortunate for the support of my friends, Kshitij Bhuyar, Fabian Dettenrieder, Dhruv Gelda, Kaustav Mohanty, Rambod Mojgani, Anirudh Yadav, and others I met during my time in Champaign.

I would like to thank my parents, Alka and Amit, and sister, Ambika, for their unflagging love and encouragement. I am grateful that I had Priti in my corner throughout the last four years, ensuring that I remained persistent in my efforts.

Table of Contents

List of Tables

List of Figures

List of Abbreviations

BDF	Backward Differentiation Formula
Bol	Boltzmann
CE	Chapman-Enskog
CFD	Computational Fluid Dynamics
CL	Centerline
CR	Collisional-Radiative
DOM	Discrete Ordinate Method
el	Electronic
FHO	Forced Harmonic Oscillator
FE	Finite Element
FV	Finite Volume
HARA	High-temperature Aerothermodynamic Radiation
inel	Non-reactive inelastic
int	Internal
IR	InfraRed
LAURA	Langley Aerothermodynamic Upwind Relaxation Algorithm
lavg	Logarithmic-average
LBL	Line-by-Line
LOS	Line-of-Sight
LTE	Local Thermodynamic Equilibrium
LU	LowerUpper
MBOB	Multi-Band Opacity-Binning

MGME	Multi-group Maximum-Entropy
MT	Multi-Temperature
NC	Normalized Cut
NERO	Non-Equilibrium RadiatiOn
neq	Non-equilibrium
NLTE	Non Local Thermodynamic Equilibrium
ODE	Ordinary Differential Equation
OpenBLAS	Open Basic Linear Algebra Subprograms
OpenMP	Open Multi-Processing
PAM	Partitioning Around Medoids
PES	Potential Energy Surface
QCT	Quasi-Classical Trajectory
rad	Radiative
react	Reactive
rot	Rotational
RTE	Radiative Transfer Equation
SRB	Smeared Rotational Band
SSH	Schwartz-Slawsky-Herzfeld
SLEPc	Scalable Library for Eigenvalue Problem Computations
StS	State-to-State
SUNDIALS	SUite of Nonlinear and DIfferential/ALgebraic Equation Solvers
sy	Symmetric
tot	Total
tr	Translation
VE	Vibration-Electronic
vib	Vibration
VT	Vibration-Translation
VV	Vibration-Vibration

List of Symbols

A	Chemical species
B	Chemical species
$\mathcal{B}$	Set of chemical species
b	Number of macroscopic bins
C	Species
C_p	Specific heat capacity at constant pressure
C	Bin-averaged rate coefficient
$\mathbf{C}$	Peculiar velocity vector
$\mathbf{c}$	Molecular velocity vector
c	Speed of light
$\boldsymbol{\mathcal{D}}$	Degree matrix
D	Species
E	Bin energy density
e	Internal energy (including translational energy) per unit mass
F	Flow factor
f	Velocity distribution function
g	Degeneracy
H	Mixture enthalpy per unit mass
h	Species/bin enthalpy
$\mathrm{h_P}$	Planck constant
$\boldsymbol{\mathcal{I}}$	Identity matrix
I	Radiative intensity
$\mathcal{I}$	Set of internal energy levels
i	Energy level index or species index
J	Rotational quantum number or emission coefficient
j	Energy level index or species index
K	Bin-averaged rate coefficient
$\mathrm{k_B}$	Boltzmann constant
$\mathbf{L}$	Graph Laplacian
$\mathcal{M}$	Molar mass
m	Particle mass, order of moment, or energy level index
N	Bin number density
$\mathrm{N_{Av}}$	Avogadro number
NB	Non-Boltzmann factor
n	Number density
P	Pressure
Q	Collision operator or partition function
$\mathbf{q}$	Heat flux
R	Gas constant
$\mathcal{R}$	Set of chemical species
$\boldsymbol{S}$	Aread vector
$\boldsymbol{\mathcal{S}}$	Dissimilarity matrix
$\mathcal{S}$	Set of chemical species

s	Entropy density or distance along line-of-sight
T	Temperature
t	Time
$\mathbf{u}$	Bulk flow velocity or eigen-vectors
$\boldsymbol{\mathcal{V}}$	Diffusion velocity
V	Volume
v	Vibrational quantum number
$\boldsymbol{\mathcal{W}}$	Graph adjacency matrix
w	Quadrature weight
$\mathbf{X}$	Cluster affinity matrix
$\mathbf{x}$	Position vector
α	Bin-wise distribution coefficient
β	Bin-wise distribution coefficient
β_{E}	Spectral clustering parameter
β_{I}	Modified island algorithm parameter
β_{K}	Spectral clustering parameter
$\mathcal{E}$	Total energy (including bulk flow kinetic energy) per unit mass
ϵ	Internal energy of level
κ	State-to-state reaction rate coefficient or opacity coefficient
ν	Frequency
ρ	Mass density
σ	Absorption cross-section
τ	Characteristic time-scale, optical thickness, or viscous stress tensor
$\boldsymbol{\Omega}$	Direction vector
Ω	Solid angle or energy source term
ω	Mass source term

Chapter 1

Introduction

1.1 Motivation

The pursuit of space exploration and national security objectives has fostered extensive research in the field of hypersonic aerothermodynamics over the preceding decades. An oft-studied problem in the hypersonic flow regime is the entry of space vehicles into a planetary atmosphere from outer space [1]. The vehicle encounters denser atmospheric layers as it descends towards the surface, resulting in dissipation of kinetic energy through drag. A strong bow shock develops upstream and envelops the entire vehicle. The sheer magnitude of the incoming flow velocity causes the post-shock temperature to rise up by several thousands of Kelvin [2]. This sudden transfer of flow kinetic energy to thermal energy of the constituent gas particles triggers strong collisions among them, inducing changes in chemical composition of the gas and exciting the internal energy modes of its atoms and molecules [3]. Similarly, photochemical processes involving interactions with photons are initiated, which redistribute energy around the vehicle and effect further chemical transformation and energy relaxation [4]. Thus, the characteristics of hypersonic flight are shaped by a combination of disparate physical phenomena such as chemistry, radiation, fluid dynamics, and ablation. The various physical facets associated with atmospheric entry are outlined in Fig. 1.1. Owing to logistical and cost constraints, experimental testing cannot replicate exact flight conditions in their entirety. Instead, a bulk of the vehicular design process is driven by computational fluid dynamics (CFD) simulations. The accuracy of these calculations, in turn, is reliant upon incorporating numerical models originating from a wide cross-section of fields such as fluid mechanics, chemistry, material science, high-performance computing, and applied mathematics that can resolve both spatial and temporal scales of the physics-rich hypersonic flowfield.

The bow shock constitutes a sharp discontinuity in space across which certain flow properties undergo an instantaneous change. The translational mode of atoms and molecules, owing to the small difference in energies between successive levels, equilibrates immediately to post-shock conditions. Contrastingly, the internal energy modes (rotational, vibrational, electronic) require a finite amount of time to respond to the rapid dissipation of flow kinetic energy downstream of the shock. The properties of these modes are assumed to be invariant or "frozen" across the shock [4]. Similarly, the chemical composition of the gaseous mixture cannot be altered abruptly. This engenders a state of strong thermochemical non-equilibrium in the post-shock region. Finite-rate changes as the flow proceeds further occur through distinct collisional-radiative (CR) processes involving atoms and molecules. This includes both energy transfer between different internal modes and chemical changes in the form of exchange, dissociation, and ionization reactions. Non-equilibrium ensues wherever the characteristic times of CR processes are of the same order as the flow transit time. Thus, in addition to the forebody, non-equilibrium effects can also become prevalent in regions with expanding flows [5] such as the shoulder and afterbody region of the spacecraft (Fig. 1.1). Rapid expansion results in a sharp decline in number density and the resultant collision frequency. Under such conditions, the time for equilibration can become sufficiently large for the chemical/internal

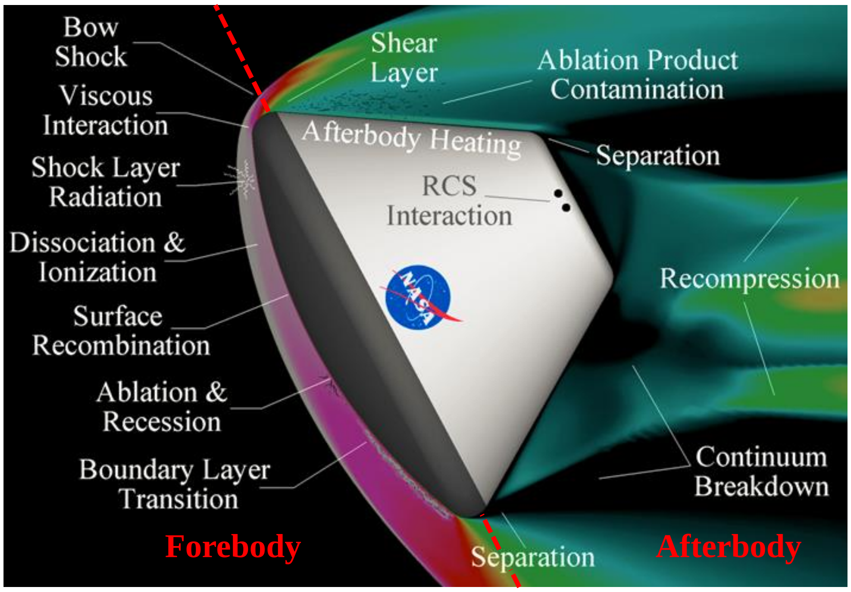

Figure 1.1: Flowfield during hypersonic vehicular planetary entry.
(Source: NASA)

energy make-up of the gaseous mixture to remain unvarying or “freeze” in the flowfield.

The occurence of radiative transfer adds another layer of complexity to non-equilibrium dynamics during planetary entry [6]. An obvious modification to the flowfield is through the additional mechanism of energy exchange between discontiguous regions in the form of radiative heat flux [7]. In a similar vein, radiative transitions – local emission and absorption of the globally determined radiative intensity – can spur chemical changes/internal excitation [8, 9], especially in expansion regions where collisional processes are retarded due to lowered number densities [10]. At the same time, radiative properties are strongly dependent on the chemical constitution of the gaseous mixture [11] and the exact internal state population distribution [12]. This particular two-way coupling and the larger inter-dependency between various physical phenomena typical of hypersonic problems makes it imperative that finite-rate thermochemistry, radiation, fluid mechanics and other phenomena be dealt with in a unified manner. An accurate assessment of non-equilibrium deviations occurring in the flow is critical for determining thermal and aerodynamic loads experienced by spacecraft [13]. A simulation methodology that can deliver such detailed predictions is expected to continue gaining relevance with both increasingly complex extraterrestrial landings and Earth-return missions on the anvil. Another motivator is the focus on devising efficient designs that employ more aggressive safety margins (in lieu of the traditional “over-engineering” [14]) to improve the overall economic viability and scientific potential of planned missions.

1.2 Literature Review

A simulation framework for resolving non-equilibrium thermochemistry and coupled radiation hydrodynamics for complex three-dimensional domains can be structured in the manner outlined in Fig. 1.2. The three interconnected components are: a) an improved non-equilibrium thermochemical model that sheds ad-hoc empiricism to provide a more complete description of chemical kinetics and internal energy relaxation, b) detailed radiation calculations which account for non-equilibrium in the internal energy modes of the gas and spatial variation in flowfield properties, c) and a computational fluid dynamics (CFD) solver that can resolve the multitude of flow structures characterizing the forebody and wake regions. This section reviews some of the existing numerical approaches for developing thermochemical and radiative response models (which represent the major thrust areas of this work) that are suitable for non-equilibrium hypersonic flows.

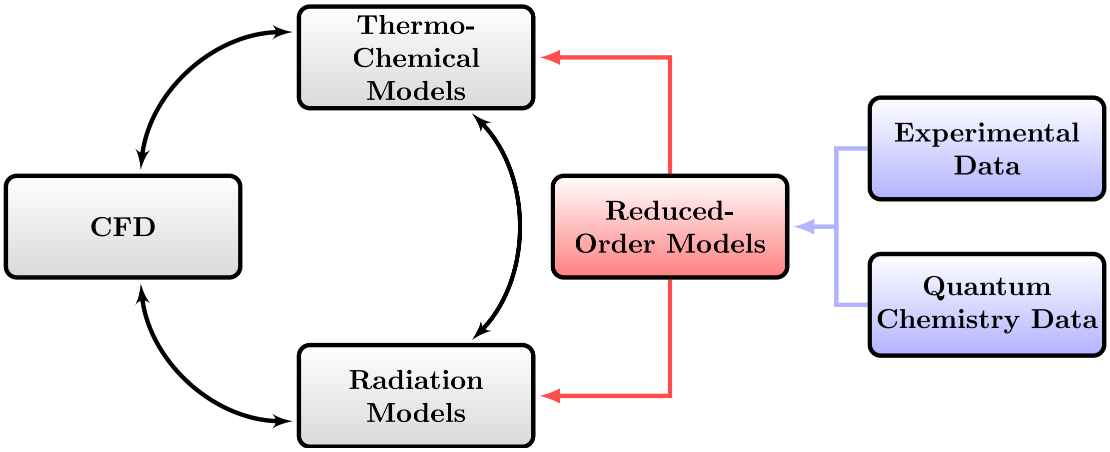

Figure 1.2: Numerical framework for performing radiation hydrodynamics simulations under non-equilibrium conditions.

1.2.1 Non-equilibrium Thermochemistry

A wide gamut of techniques exist for describing non-equilibrium chemical reactions and energy exchange, ranging from computationally tractable semi-empirical models that are calibrated using experimental data to highly accurate first-principles quantum chemistry methods which are prohibitively expensive for use in complex CFD problems.

1.2.1.1 Multi-Temperature Models

The different multi-temperature (MT) models proposed in the literature share a foundational paradigm. The total internal energy corresponding to individual quantum states of reacting species is divided into contributions from translational, rotational, vibrational, and electronic modes. These internal modes are assumed to be in equilibrium, with their populations defined using Maxwell-Boltzmann distributions at a common temperature or multiple independent temperatures. An MT approach was first used by Appleton and Bray [15] to describe non-equilibrium in ionized gases using separate heavy particle and free-electron temperatures. An extension of this methodology was later used by Lee [16] for detailing vibrational non-equilibrium during drag-induced braking of spacecraft. An important step in the widespread proliferation of the MT framework was its generalization by Park [4, 17, 18, 19] to include all internal energy modes of atoms and molecules (rotational, vibrational, and electronic). The system of hydrodynamic equations incorporating MT modeling includes additional independent conservation equations for energy corresponding to different internal modes in addition to those for mass, momentum, and total energy. This translates to distinct equations for translational-rotational and vibrational-electronic energies when using the most common Park two-temperature (2-T) model. A detailed description of governing equations and different constitutive properties when applying the two/three temperature models to compressible flows can be found in [2, 20].

The additional conservation equations introduced through MT models require closure relationships for source terms defining the rate of energy exchange between different energy modes. A vast body of work has been dedicated to characterizing vibrational-translational (V-T) energy exchanges [21, 22], vibrational-vibrational (V-V) energy exchanges [23, 24], and the coupling between vibrational mode and chemistry [25, 26]. The focus on these specific interactions stems from a) energy differences between individual vibrational levels being relatively large which results in longer inter/intra modal equilibration times compared to rotational/translational modes, and b) chemical processes such as dissociation being biased by vibrational excitation. The sluggish rate of vibrational relaxation generates more complex non-equilibrium scenarios for polyatomic molecules with multiple vibrational modes, *e.g.*, the CO_2 molecule which has three distinct vibrational modes: symmetric stretching, asymmetric stretching, and bending [27, 28]. The characteristic times for relaxation can vary between vibrational modes [29, 30]. A similar non-equilibrium can exist between the vibrational modes of different molecules (with distinctly different arrangements of vibrational levels). Thus, an accurate MT-based non-equilibrium description of such gaseous mixtures could involve defining distinct temperatures corresponding to vibrational modes of different molecules or even different types of vibrational modes for the same molecule [31, 32].

A popular choice for modeling vibrational-translational energy transfer is the Landau-Teller model [33] which is based on characteristic relaxation times obtained either through theory or experiments [34, 35, 36]. Additionally, this form for the V-T energy term is derived assuming only mono-quantum transitions. Thus, its validity in high-enthalpy hypersonic flowfields which produce significant multi-quantum jumps can become suspect [37, 38]. The two-way coupling between vibrational energy and chemistry – vibrational energy lost due to dissociation and in return effective reaction rates being informed by vibrational excitation – needs to be resolved. The first instance of such a coupled vibrational-dissociation (CVD) model, based on the idea of dissociation probabilities being higher for upper vibrational levels, was formulated by Hammerling et al. [39]. The large number of chemistry coupling models that have been developed over the succeeding decades are reviewed in [40]. These range from experimentally calibrated empirical approaches such as the Park model involving geometric averages of translational and vibrational temperatures [4, 18] to more theoretical models that are rooted in fundamental theory [24, 41, 42]. Despite significant advances, these efforts are impeded by a common constraint – internal levels being forced into Boltzmann distributions – and the semi-empiricism that stems from it. Thus, MT models are fundamentally incapable of representing strong non-equilibrium effects which stem from complicated non-Boltzmann dynamics of internal state population distributions.

1.2.1.2 State-to-State Models

The need to supplant the empirical MT approach has inspired the development of state-to-state (StS) thermochemical models which treat individual internal energy levels as distinct species with independent conservation equations. This allows the internal level population distribution in all manner of flow conditions to be accurately computed by accounting for all relevant state-specific collisional and radiative (CR) processes for a given gaseous mixture. StS models, based on the number of underlying assumptions and the resultant level of accuracy, can be broadly classified as *electronic*, *vibrational*, or *rovibrational* StS models. Electronic StS modeling [43, 44, 45, 46] only considers transitions between different electronic states, while prescribing MT-based Boltzmann population distributions for the rotational and vibrational modes. Vibrational StS models [47, 48, 49, 50] provide a detailed characterization of processes between molecular vibrational states while assuming the rotational energy mode is equilibrated. The most complete description for non-equilibrium is obtained through rovibrational StS modeling [51, 52, 53, 54], which allows the population of each rovibrational state to be directly computed without making any *ad-hoc* assumptions. Although this approach is exceedingly accurate in resolving the dynamics of internal excitation, it introduces a large number of additional conservation equations corresponding to rovibrational states ($\sim 10^4 - 10^5$) even for simple diatomic molecules. Thus, the practical utility of such models with regards to simulating large multi-dimensional flow problems using CFD solvers is extremely limited.

The development of accurate StS models strongly hinges on ascertaining kinetics data for the underlying processes between states. A large amount of research effort in this regard has focused on evolving computationally efficient techniques that are based on empirical approaches such as the ladder climbing model or variations of semi-classical theoretical frameworks like the Forced Harmonic Oscillator (FHO) [26, 55] or the Schwartz-Slawsky-Herzfeld (SSH) [22, 56] models. Recent advances in computational chemistry have allowed transition probabilities governing the collisions between different internal states of atoms, molecules, electrons and photons to be computed accurately using first principles quantum chemistry methods. These calculations are performed in two steps: a) the potential energy surface (PES) [57], which characterizes the forces between nuclei for different geometric configurations, is obtained by solving the Schrödinger's equation or through experimental data, b) reaction rates coefficients are then computed by simulating a large number of collisions between particles, governed by Hamilton's equations of motion and the previously determined PES trajectory, using methods that vary from the quasi-classical trajectory (QCT) model [58] to those that fully account for quantum mechanics [54]. This *ab-initio* approach combining PES and trajectory calculations has been used to study state-specific kinetics of different chemical species such as N_2 and O_2 that are relevant to planetary entry problems [48, 50, 59, 60].

1.2.1.3 Reduced-order Models

State-to-state modeling in the context of general CFD applications is usually computationally prohibitive. Instead, a more prudent alternative is using the large amount of information encapsulated in state-specific models to inform the development of more physics-based thermochemical models. The most straightforward approach that ensures immediate compatibility with conventional hypersonic flow codes is based around updating reaction parameters and coupling coefficients for MT models using detailed quantum chemistry data. An illustration of this methodology can be found in the work of Bender et al. [61] and Chaudhry et al. [62] who studied non-equilibrium dynamics for nitrogen and oxygen within the two-temperature paradigm. However, the fundamental constraints inherent in MT models, due to the assumption of Boltzmann state population distributions, persist despite these improvements. Singh and Schwartzentruber [63] have attempted to overcome this limitation by deriving a functional form for rovibrational non-equilibrium population distribution using surprisal analysis. Another viable alternative to MT modeling has been proposed by Bellemans et al. [64] based on the application of principal component analysis for reducing the complexity of StS reaction mechanisms.

Coarse grain methods alleviate the high computational costs of StS modeling by grouping individual levels together into a reduced number of macroscopic bins (the term bins and groups are used interchangeably while describing reduced-order thermochemical models in the current work). Furthermore, states within bins are assumed to equilibrate locally whereas the overall non-Boltzmann effects are captured since bins can remain in non-equilibrium with respect to one another. This approach has been used to study non-equilibrium pertaining to both electronic and rovibrational states during hypersonic flows [65, 66, 67]. The work by Liu et al. [68, 69, 70] – referred to as the multi-group maximum entropy method (MGME) – establishes a mathematically rigorous formulation for the time evolution of macroscopic bin properties (population, energy, and higher-order moments) while retaining all microscopic processes from the StS model. Unlike StS models, the populations of individual states no longer serve as system unknowns. Instead, they are reconstructed using bin-specific distribution functions (polynomials of a given order) that maximize entropy and are constrained by bin properties. The reduced system of governing equations for bin properties is derived by summing up moments of the StS master equations. The MGME framework allows for a generalized representation of non-equilibrium, yielding other coarse grain and MT models with requisite simplifications.

Previous research incorporating coarse grain or MGME methods has largely overlooked the importance of selecting a physically consistent grouping strategy to improve the quality of predictions. The most common approach consists of defining bins as non-overlapping continuous intervals of equal width in internal energy space. Individual energy levels are subsequently divided into these bins irrespective of their rotational and vibrational states and without any regard for the details of the kinetics of excitation. As a result, the conventional energy approach is inherently unable to capture the composite structure of the time-varying internal energy distribution characterized by: a multi-mode relaxation for the low-lying energy levels, where the rotational and vibrational states follow a very different path to relaxation; the middle of the distribution, where the internal energy states relax independently of their rotational and vibrational state; and the tail of the distribution, where the probability of tunneling controls the population of the predissociated states [51]. More recently, Munafò et al. [71] have published a new grouping strategy based on kinetic considerations for the $\mathrm{N_2(^1\Sigma_g^+) - N(^4S_u)}$ system. Although this approach improves predictions for non-equilibrium relaxation, it requires manually selecting energy levels that would be placed in the same bin based on an intrinsic knowledge of the $\mathrm{N_2(^1\Sigma_g^+) - N(^4S_u)}$ system. Thus, the underlying grouping procedure is not general and cannot be easily extended to other chemical systems.

1.2.2 Radiation Modeling

The most complete description of radiative transfer can be obtained through quantum electrodynamics (QED). However, this is a formidable proposition when dealing with the propagation of electromagnetic waves through generalized participating media both in terms of developing the underpinning theoretical framework and realizing cost-effective numerical predictions. The characteristic length-scales associated with typical hypersonic applications are large enough for ignoring wave effects. Therefore, techniques derived from QED or even the classical analogue based on Maxwell's equations are superfluous in terms of significantly improving estimates for the radiative environment during atmoshperic entry. Instead, a more straightforward analysis can be obtained using corpuscular theory (which is also equivalent to period-averaging for waves [72]), *i.e.*, radiative energy transfer occurs through a stream of photons with directional, spatial, and frequency dependence [11]. This description allows radiative transitions to be viewed in the same manner as collisional processes – only instead of collisions strictly being between atoms/molecules, interactions with photons occur [9, 73]. The frequency variation in radiative properties also becomes obvious when they are decomposed into a set of constitutive transition reactions between discrete internal levels obtained through quantum mechanics calculations. Since each of these mechanisms (classified as spontaneous emission, absorption, and stimulated emission) involves photons with specific energies, the absorption and emission behavior of chemical species can vary rapidly with respect to frequency. In general, multi-dimensional asymmetric high-enthalpy flows engender radiative fields that vary in the solid angle (direction), spatial, and frequency spaces [74]. The fundamental governing equation – referred to as the radiative transfer equation (RTE) – describes the evolution of monochromatic spectral intensity (radiant energy flux per unit area per unit per unit frequency) in a given direction. Thus, a complete resolution of radiative transfer can be bifurcated into the geometric aspect involving spatial-angular integration of RTEs, and spectral modeling which defines the manner in which emission/absorption coefficients are ascribed.

1.2.2.1 Geometric Component of Radiative Transfer

The angularly integrated RTE is an integro-differential equation in five independent variables (three spatial and two directional coordinates). Thus, semi-analytical solutions for non-homogeneous media can only be obtained for either physically limiting regimes (diffusion approximation in optically thick conditions) or for simplified domains with property variations limited to one-dimension such as parallel-plane slab, infinitely-long cylinders, and spheres [11, 75]. A general numerical scheme for tackling radiative transfer needs to address both spatial and angular dependencies. The central theme amongst popular approaches is to effect a transformation from the original integro-differential equation into a series of simultaneous partial differential equations (PDEs). The discrete ordinate method (DOM), first introduced by Chandrasekhar [76] for stellar problems, approximates the integral over the complete solid angle as a summation of calculations in discrete directions. The resultant systems of PDEs, corresponding to fixed directions from a numerical quadrature scheme, can then be solved using a broad range of techniques based on finite-difference schemes [77, 78], finite-volume method [79, 80], finite-element discretization [81, 82], and ray-tracing [83]. Research has also been directed towards minimizing this explicit separation between the directional and spatial terms. This can involve using finite-volume or finite-element methods not only for spatial discretization but for the angular domain as well [84, 85].

A holistic framework is provided by the method of spherical harmonics which expresses intensity as a generalized Fourier series where each term consists of the product between position-dependent coefficients and directional spherical harmonics [86, 87]. The governing equations for the unknown position-dependent coefficients are obtained by taking angularly integrated moments of the RTE with respect to spherical harmonics and then exploiting their orthogonality properties. A similar approach based on taking moments of the RTE with increasing exponents of the directional unit vector was used by Eddington [88] to study radiative transfer in a one-dimensional parallel slab. These angular moment equations have spawned an entire family of methods which prescribe an optimal closed-form expression for describing the distribution of intensity over the solid angle. The functional form for this reconstruction is based on maximizing a certain quantity (entropy [89, 90], rate of entropy generation [91, 92]) in addition to satisfying constraints based on the moments of intensity. Despite certain advantages, moment methods (especially with lower order reconstruction) can introduce significant errors while characterizing strongly anisotropic intensities. Incorporating higher order moments results in a rapid increase in mathematical/computational complexity with often limited gains in accuracy [11].

Besides the aforementioned deterministic techniques, radiative transfer problems can also be solved heuristically using Monte Carlo methods [93]. This involves tracking statistically meaningful random bundles of photons or rays as they propagate through the medium while being attenuated (absorption) or amplified (emission) at certain probabilities determined by the local gaseous mixture. A major drawback for Monte Carlo-based approaches is the substantial sampling requirement when analyzing large domains with complicated spatial distributions of flowfield properties. A comprehensive outline of different numerical methods for modeling radiative dynamics in participating media can be found in [11, 94].

1.2.2.2 Frequency Variations

The interaction between photons and gas particles can trigger a multitude of fundamental processes that can result in absorption (increasing the energy of gas), scattering, or emission (lowering the energy of gas). These radiative transitions are differentiated into: a) *bound-bound* processes that occur between bound or undissociated atomic or molecular states, b) *bound-free* (absorption) or *free-bound* (emission) processes that occur between bound and unbound (such as a free electron) states, c) and *free-free* processes between unbound particles. The *bound-bound* transitions in particular result in photons of certain energy being released or captured. This introduces strong spectral variation in transition probabilities and the corresponding radiative behavior. The frequency distribution of radiative properties can be modeled with differing degrees of fidelity. The current work uses the classification set forth in [11, 72] to summarize the different spectral modeling approaches in decreasing order of accuracy – line-by-line, narrow-band, wide-band, global models. The highest spectral resolution is obtained using "line-by-line" (LBL) calculations. These are based on large spectroscopic databases such as HITRAN [95], HITEMP [96], CDSD-4000 [97], NEQAIR96 [98], and the National Standards and Technology online database [99], that give detailed descriptions of emission and absorption due to every single spectral line. A complete resolution of radiative transfer can involve evaluations at millions of individual frequencies ($\mathcal{O}(10^6 - 10^8)$). Thus, the LBL approach (analogous to StS thermochemical modeling) is cost prohibitive when applied to radiation calculations for large-scale CFD problems.

The other family of methods, lower in the hierarchy of spectral modeling, attempt to limit the number of frequency-wise calculations that are required to predict total radiative quantities. This involves approximating the actual values of absorption coefficients (stemming from individual lines) with smoothed, appropriately-averaged constant values or functions over larger spectral ranges. Subsequently, instead of repeating the RTE solution procedure for each line, this calculation is performed only once (or relatively fewer times) for the encompassing interval. Narrow-band methods perform this averaging over relatively narrow spectral ranges. Nevertheless, the resultant coarsening of the spectral grid still translates into $\mathcal{O}(10^5 - 10^6)$ distinct frequency points. A number of models have been proposed to compute the effective narrow-band averages accurately. The most straightforward of these is the Elasser model which assumes equally spaced lines with matching shapes and strengths over the narrow-band interval [100]. A more nuanced description is obtained through statistical models which abolish the equality assumption in favor of randomly distributed lines (with dissimilar strength and overlap) in the narrow-band. The earliest such methods are those proposed by Goody [101] and Malkmus [102] and prescribe an exponential form to the probability distribution function describing line strength. More recent examples include the statistical narrow model [103, 104], narrow-band correlated-k method [11]), smeared-rotational band (SRB) method [8, 105], and narrow-band weighted-sum-of-grey-gases (NBWSCG) method [106]. These different approaches have been extensively applied to various radiative systems and often offer levels of accuracy comparable to LBL calculations.

Realizing the fundamental two-way radiation-hydrodynamics coupling requires multiple complete evaluations of radiative transport as the surrounding flowfield continues evolving. Thus, while LBL remains entirely out of the question, the cost of narrow-band models is also further multiplied to the extent that detailed calculations for practical problems are rendered unfeasible. This motivates the development of wide-band models which integrate LBL or narrow-band results so that the entire frequency space is reduced to $\mathcal{O}(10^2 - 10^3)$ groups. These methods differ in how the net contribution of these wide-band spectral ranges (or reduced-order groups) to the overall radiative field is accurately approximated. Two computationally inexpensive approaches – Planck and Rosseland means – set the representative value of group absorption coefficients based on simple weighted-averaging [76, 100]. The resultant averaged values are exact only in certain limiting physical regimes such as optically thin (Planck) and optically thick (Rosseland) media. However, numerical methods based on the previously mentioned maximum entropy closure (*e.g.*, M-1 model [89, 90]) present a more generalized interpretation of Planck-averaging. According to Bose-Einstein statistics, Planck blackbody spectral intensity represents the distribution function that maximizes entropy subject to certain constraints. Thus, Planck-averaging should be viewed as a piece-wise maximum entropy reconstruction in the absence of complete information [107], *i.e.*, the exact distribution is unknown and only the summation of moments (total group intensity) is available. This could serve to explain the high level of fidelity obtained using Planck-averaged reduced-order models for a wide range of complex, non-equilibrium, and optically intermediate to thick radiative problems [108, 109].

Paralleling the basic methodologies developed for narrow-band models, statistics-based techniques can also inform the formulation of wide-band models. Two such approaches are the k-distribution [11, 110] models and theory of homogenization [111, 112]. A switch to statistics-based methods can often improve robustness, but results in more complex procedures for pre-computing/tabulating reduced-order properties and modeling overlapping radiative systems [110]. The global model, at the extreme end of the spectral-fidelity ladder, specifies a single universal (spectrally invariant) value for radiative coefficients. These can be determined in a variety of ways, which include Planck/Rosseland averaging or k-distribution but applied to the entire spectral range rather than smaller intervals. Despite the obvious reduction in computational overhead, global models introduce far too many simplifications to be sufficiently representative of the radiative environment during hypersonic planetary entry.

1.3 Scope of this Thesis

This thesis presents self-consistent reduced-order models for thermochemistry and radiative transfer under strong non-equilibrium conditions. These models are then assimilated into a computationally tractable simulation methodology for coupled radiation-hydrodynamics calculations that allows a unified description of different physical aspects – chemistry, energy relaxation, radiation, and fluid dynamics – constituting hypersonic entry problems. Non-Boltzmann thermochemical response is predicted using the MGME framework which allows optimal representation of internal state population dynamics using constrained maximum entropy closure. The applicability of MGME-based model reduction is further improved through the use of novel adaptive binning strategies that leverage both state-specific kinetics and energies. Clusters of internal states that are more likely to equilibrate locally due to preferential transition pathways are identified *a priori*. Consequently, the two-layered resolution scheme inherently imposed by the multi-bin paradigm – locally thermalized states within bins are estimated using bin-wise maximum entropy reconstruction while overall non-equilibrium is still accurately captured through bin properties – becomes more reflective of the actual population dynamics.

The multi-variate dependence of radiative transfer is resolved through a two-pronged approach. The geometric aspect, *i.e.*, solution of the system of RTEs in the angular and spatial domain, is tackled through a combined discrete-ordinate and finite-volume method solver. This ensures a high degree of commonality with conventional CFD codes (key to expeditious flow-radiation coupling) while providing a desirable balance between speed and accuracy. Similarly, frequency distributions of radiative properties are characterized through numerically efficient wide-band models. Planck-averaging supplemented by a new generalized grouping strategy for non-equilibrium radiation allows both total quantities-of-interest and detailed spectral features to be reproduced at a fraction of the resources required for LBL or narrow-band methods. The thesis is organized as follows:

- Chapter 2 details the development of non-Boltzmann thermochemical models used in the current work. The chapter begins with a brief insight into non-equilibrium gaseous mixtures from a kinetic theory point of view. This is followed by a summary of the MGME method including derivations for bin-wise kinetics and thermodynamics. Adaptive grouping based on two strategies – island algorithm and spectral clustering – are discussed next.

- The efficacy of MGME reduced-order models is analyzed using an ideal homogeneous chemical reactor in Chapter 3. Two chemical systems relevant for Earth and Mars planetary entry problems are studied: $\mathrm{N_2(^1\Sigma_g^+) - N(^4S_u)}$ rovibrational StS system and $\mathrm{CO_2(X^1\sum_g^+) - M}$ vibrational system. The introduction of kinetics-infused adaptive grouping has a conspicuous impact on accuracy, allowing even complex state population distributions borne out of high probability parity-preserving, intra-vibrational (N_2) transitions or faster V-V relaxation (CO_2) to be accurately reproduced using $\mathcal{O}(10)$ bins.

- Numerical techniques for resolving radiative transfer in the spatial, angular, and spectral domains are presented in Chapter 4. Angular and spatial discretization of the RTE is performed using discrete-ordinate and finite-volume methods respectively. Three commonly used wide-band reduced-order spectral models are discussed – Planck-averaging, k-distribution, and theory of homogenization. These conventional techniques are shown to be equivalent and strictly derived only for LTE radiation. Thus, a new generalized non-equilibrium radiation grouping strategy is proposed for augmented predictive capabilities for a wider range of radiative environments.

- A comparative study into the accuracy accorded by different wide-band models during hypersonic Jovian and Earth entry is presented in Chapter 5. Reference solutions based on detailed spectral models are computed for a reference line-of-sight. These are then used to benchmark the aforementioned wide-band models and also delineate the impact of improved radiation grouping.

- This unified reduced-order simulation framework is used in conjunction with the US3D flow solver [113, 114, 115] to investigate non-equilibrium radiation-hydrodynamics in the afterbody region of the Mars 2020 vehicle [116, 117] in Chapter 6. This choice of application further highlights the collective qualities of the current methodology with regards to cost-effective high-fidelity non-equilibrium predictions for large-scale three-dimensional CFD problems with complex underlying flowfield dynamics.

- Finally, key conclusions and future work are summarized in Chapter 7.

1.4 Outcomes of this work

The current research yielded the following publications:

1. **A. Sahai**, B. Lopez, C.O. Johnston, M. Panesi. Adaptive coarse graining method for energy transfer and dissociation kinetics of polyatomic species. *The Journal of Chemical Physics*, 147(5):054107, 2017.
2. **A. Sahai**, C.O. Johnston, B. Lopez, M. Panesi. Flow-radiation coupling in CO_2 hypersonic wakes using reduced-order non-Boltzmann models. *Physical Review Fluids*, 2019. Accepted.
3. **A. Sahai**, B. Lopez, C.O. Johnston, M. Panesi. Comparative analysis of reduced-order spectral models and grouping strategies for non-equilibrium radiation. *Journal of Quantitative Spectroscopy and Radiative Transfer*, Manuscript in preparation.

The current research yielded the following peer reviewed conference publications:

1. **A. Sahai**, B. Lopez, C.O. Johnston, M. Panesi. Reduced-order modeling of non-equilibrium kinetics and radiation for CO_2 axisymmetric wake flows. *Proceedings of the 31st International Symposium on Rarefied Gas Dynamics*, 2132(1):130002, 2019.

The current research yielded the following conference publications:

1. **A. Sahai**, B. Lopez, M. Panesi. A reduced-order maximum entropy model for chemical and thermal non-equilibrium in high temperature CO_2 gas. *46th AIAA Thermophysics Conference*, AIAA Paper 2016-3695, 2016.
2. **A. Sahai**, B. Lopez, C.O. Johnston, M. Panesi. Novel Approach for CO_2 state-to-state modeling and application to multidimensional entry flows. *55th AIAA Aerospace Sciences Meeting*, AIAA Paper 2017-0213, 2017.
3. **A. Sahai**, B. Lopez, C.O. Johnston, M. Panesi. Novel approach for modeling CO_2 non-equilibrium radiation: Application to wake flows. *57th AIAA Aerospace Sciences Meeting*, AIAA Paper 2019-1051, 2019.

The current research was presented at the following workshops:

1. **A. Sahai**, B. Lopez, C.O. Johnston, M. Panesi. A reduced-order maximum entropy model for chemical and thermal non-equilibrium in high temperature CO_2 gas. *7th International Workshop on Radiation of High Temperature Gases*, Stuttgart, Germany, 2016.
2. **A. Sahai**, C.O. Johnston, B. Lopez, M. Panesi. Reduced-order non-equilibrium radiative transfer for 3D problems. *8th International Workshop on Radiation of High Temperature Gases*, Madrid, Spain, 2019.

Chapter 2

Non-Boltzmann Thermochemical Models

This chapter presents a detailed outline of the various thermochemical models for chemical kinetics, energy exchange, and thermodynamics used in the present work. The high computational costs associated with CFD simulations dictate that property models are designed for efficiency and often incorporate crude approximations for bulk properties without necessarily replicating gas behavior at the molecular level. Consequently, traditional non-equilibrium thermochemistry relies on sweeping simplifications and is no longer representative of the detailed internal statistics of evolving gaseous species. The MGME method in conjunction with adaptive grouping provides a framework for computational tractability while retaining key features of elementary kinetic processes. This chapter is organized as follows: a) Section 2.1 presents an overview of the kinetic theory approach to thermochemical non-equilibrium modeling using Boltzmann and Maxwell transfer equations. b) The state-to-state master equations which provide an exact description of the evolution of internal energy states due to particle collisions are described in Section 2.2. c) The different facets of the MGME method, which applies the variational principle to entropy maximization for reduced-order reconstruction of StS dynamics, are detailed in Section 2.3. d) Section 2.4 describes the adaptive grouping strategy for improving the applicability of the MGME framework by accurate identification of rapidly thermalizing clusters of states using StS data. e) A short summary for the chapter is provided in Secion 2.5.

2.1 Boltzmann and Maxwell Transfer Equations

A gaseous mixture comprises of atomic and molecular species. This mixture is represented by set $\mathcal{S}$ and contains individual species $\{A, B, C, D, \ldots\}$. Individual particles can only possess internal energy from a discrete set of values for a given chemical species. Contrastingly, the separation between translational energy levels is multiple orders of magnitude smaller and is assumed to vary continuously. The discrete internal energy structure for atoms stems from all possible electronic states. The internal energy for molecules introduces additional permutations based on rotational and vibrational configurations. The set of internal energy levels of species A is denoted by $\mathcal{I}_\mathrm{A}$ whereas individual levels are represented by $\{i, j, k, l, \ldots\}$. The exact number of particles per unit volume for species A in internal state i with velocity $[\mathbf{c}_{\mathrm{A}_i}, \mathbf{c}_{\mathrm{A}_i} + d\mathbf{c}_{\mathrm{A}_i}]$ at time t and located within $\mathbf{x} + d\mathbf{x}]$ can be defined through a velocity distribution function f_{A_i}:

$$dn^i_\mathrm{A} = f_{\mathrm{A}_i}\, d\mathbf{c}_{\mathrm{A}_i}\, d\mathbf{x} \tag{2.1}$$

The spatio-temporal evolution of f_{A_i} is modeled using the Boltzmann equation:

$$\partial_t f_{\mathrm{A}_i} + \mathbf{c}_{\mathrm{A}_i} \cdot \boldsymbol{\nabla}_{\boldsymbol{x}} f_{\mathrm{A}_i} = Q_{\mathrm{A}_i} \tag{2.2}$$

where ∂_t is the partial time derivative $\partial/\partial t$, $\boldsymbol{\nabla}_{\boldsymbol{x}}$ is the spatial gradient, and Q_{A_i} is the collision operator resulting from elastic, non-reactive inelastic (change of internal energy mode), and chemically reactive collisions. The current work focuses only on a continuum description of gaseous flows and therefore, the particle description afforded by the Boltzmann equations is unnecessarily comprehensive. Thus, moments of Eq. 2.2 are integrated in the velocity space $\Re^3$ to yield the Maxwell transfer equations which govern changes in species (or mixture) averaged properties such as density, momentum, and energy due to bulk motion and collisions of particles [118, 119]. This entails defining particle-averaged $\bar{\phi}_{\mathrm{A}_i}(\mathbf{x}, t)$ and mixture particle-averaged properties $\bar{\phi}(\mathbf{x}, t)$ from a particle property $\phi_{\mathrm{A}_i}(\mathbf{c}_{\mathrm{A}_i})$:

$$\bar{\phi}_{\mathrm{A}_i} = \int_{\Re^3} \phi_{\mathrm{A}_i} f_{\mathrm{A}_i} d\mathbf{c}_{\mathrm{A}_i}\ \forall\ i \in \mathcal{I}_\mathrm{A}\,,\ A \in \mathcal{S}\ ; \qquad \bar{\phi} = \sum_{\substack{i \in \mathcal{I}_\mathrm{A} \\ A \in \mathcal{S}}} \bar{\phi}_{\mathrm{A}_i} \tag{2.3}$$

Following Eq. 2.3, state number and mass densities, and mixture mass density can be defined:

$$n_{\mathrm{A}_i} = \int_{\Re^3} f_{\mathrm{A}_i} d\mathbf{c}_{\mathrm{A}_i}\ \forall\ i \in \mathcal{I}_\mathrm{A}\,,\ A \in \mathcal{S}\ ; \qquad \rho_{\mathrm{A}_i} = m_\mathrm{A} n^i_\mathrm{A}\ ; \qquad \rho = \sum_{\substack{i \in \mathcal{I}_\mathrm{A} \\ A \in \mathcal{S}}} \rho_{\mathrm{A}_i} \tag{2.4}$$

The bulk hydrodynamic flow velocity is denoted by $\mathbf{u}$. A peculiar velocity $\mathbf{C}_{\mathrm{A}_i} = \mathbf{c}_{\mathrm{A}_i} - \mathbf{u}$ is defined for describing particle thermal motion in the absence of mean flow. These two quantities are then used for computing the particle-averaged diffusion velocity $\boldsymbol{\mathcal{V}}_{\mathrm{A}_i}$.

$$\mathbf{u} = \sum_{\substack{i\in\mathcal{I}_{\mathrm{A}}\\ A\in\mathcal{S}}} \frac{m_{\mathrm{A}}}{\rho} \int_{\Re^3} \mathbf{c}_{\mathrm{A}_i} f_{\mathrm{A}_i} d\mathbf{c}_{\mathrm{A}_i} \; ; \qquad \boldsymbol{\mathcal{V}}_{\mathrm{A}_i} = \frac{m_{\mathrm{A}}}{\rho_{\mathrm{A}_i}} \int_{\Re^3} \mathbf{C}_{\mathrm{A}_i} f_{\mathrm{A}_i} d\mathbf{C}_{\mathrm{A}_i} \; \forall \; i \in \mathcal{I}_{\mathrm{A}} \, , \; A \in \mathcal{S} \tag{2.5}$$

The Maxwell transfer equations for the particle-averaged quantity $\bar{\phi}_{\mathrm{A}_i}$ and its summation for a mixture $\bar{\phi}$ can be recast as follows:

$$\partial_t \bar{\phi}_{\mathrm{A}_i} + \boldsymbol{\nabla}_{\boldsymbol{x}} \cdot \left(\bar{\phi}_{\mathrm{A}_i} \mathbf{u}\right) + \boldsymbol{\nabla}_{\boldsymbol{x}} \cdot \int_{\Re^3} \bar{\phi}_{\mathrm{A}_i} \mathbf{C}_{\mathrm{A}_i} f_{\mathrm{A}_i} d\mathbf{C}_{\mathrm{A}_i} = \int_{\Re^3} \bar{\phi}_{\mathrm{A}_i} Q_{\mathrm{A}_i} d\mathbf{C}_{\mathrm{A}_i} \tag{2.6}$$

$$\partial_t \bar{\phi} + \boldsymbol{\nabla}_{\boldsymbol{x}} \cdot \left(\bar{\phi}\, \mathbf{u}\right) + \boldsymbol{\nabla}_{\boldsymbol{x}} \cdot \sum_{\substack{i\in\mathcal{I}_{\mathrm{A}}\\ A\in\mathcal{S}}} \int_{\Re^3} \bar{\phi}_{\mathrm{A}_i} \mathbf{C}_{\mathrm{A}_i} f_{\mathrm{A}_i} d\mathbf{C}_{\mathrm{A}_i} = \sum_{\substack{i\in\mathcal{I}_{\mathrm{A}}\\ A\in\mathcal{S}}} \int_{\Re^3} \bar{\phi}_{\mathrm{A}_i} Q_{\mathrm{A}_i} d\mathbf{C}_{\mathrm{A}_i} \tag{2.7}$$

The second term on the left hand side of equations 2.6 and 2.7 captures the effect of convective flux due to the hydrodynamic velocity. The third term represents changes induced by the diffusive or transport fluxes. The volumetric change through particle collisions constitutes the right hand side. The system of hydrodynamic equations is developed from the Maxwell transfer equations by choosing different collisional invariants, *i.e.* properties such as mass, momentum, and energy that are conserved during particle collision, as $\bar{\phi}$ [120]. Additional constitutive relations for defining transport fluxes and the collisional production term solely as functions of flow properties result in a closed system of equations [118, 119, 121]. The different mathematically rigorous approaches for obtaining these relations usually center around the Chapman-Enskog (CE) perturbation method based on asymptotic solutions of the Boltzmann equations [121, 122, 123]. The convection-diffusion hydrodynamic equations for describing multi-dimensional non-equilibrium flows will be revisited in Chapter 6.

2.2 State-to-State Master Equations

The number density of particles in different internal states, the total momentum, and the total energy is conserved during elastic collisions. Starting from these collisional invariants, while deriving the Maxwell transfer equations, results in the contribution of elastic collisions to the velocity integral of the Q_{A_i} operator becoming zero [119]. The resultant convection-diffusion system consists of conservation equations for partial densities of individual internal energy levels for different chemical species, mixture momentum, and mixture energy. Thus, the StS approach with independent state-specific mass continuity equations serves as the most comprehensive characterization of a non-equilibrium gaseous mixture transforming due to elementary collisional processes. Without any loss in generality, the kinetic processes (induced by particle collisions) considered in this analysis can be broadly classified in the following manner:

$$\text{Excitation and de-excitation: } \mathrm{A}^i + \mathrm{B} \quad \longleftrightarrow \quad \mathrm{A}^j + \mathrm{B} \tag{2.8}$$

$$\text{Ionization, dissociation, and recombination: } \mathrm{A}^i + \mathrm{B} \quad \longleftrightarrow \quad \mathrm{C} + \mathrm{D} + \mathrm{B} \tag{2.9}$$

If $i < j$, then the forward reaction in Eq. 2.8 represents collisional excitation, whereas the backward process results in de-excitation. Species without an index, such as the collision partner B, do not undergo changes in their internal energies, or equivalently their internal structure, is not resolved using a state-specific description. Thermochemistry models and the subsequent reduced-order analysis presented here are centered on determining volumetric effects due to collisional processes and do not depend on the presence of convective and/or diffusive fluxes. Thus, the microscopic state equations governing the population of individual internal levels are presented for a zero-dimensional homogeneous chemical reactor with no mean flow or spatial variance in properties:

$$\begin{aligned}\frac{\partial n_{\mathrm{A}_i}}{\partial t} &= \sum_{\substack{j \in \mathcal{I}_\mathrm{A} \\ j \neq i}} \left(-\kappa^{\mathrm{e}}_{i,j}\, n_{\mathrm{A}_i}\, n_\mathrm{B} + \kappa^{\mathrm{e}}_{j,i}\, n_{\mathrm{A}_j}\, n_\mathrm{B}\right) \\ &\quad + \left(-\kappa^{\mathrm{d}}_i\, n_{\mathrm{A}_i}\, n_\mathrm{B} + \kappa^{r}_i\, n_\mathrm{C}\, n_\mathrm{D}\, n_\mathrm{B}\right) \qquad \forall i \in \mathcal{I}_\mathrm{A}\end{aligned} \tag{2.10}$$

The frequency of elastic collisions in aerothermodynamic flows is much higher than those for inelastic and reactive collisions. Thus, the translational mode is assumed to instantly equilibrate in a Maxwell-Boltzmann distribution at temperature T [124], whereas the internal state population and mixture chemical composition require finite time to reach local equilibrium. The mass production terms on the right hand side of Eq. 2.10 arise due to these finite-rate energy transfer and chemical change processes. The quantities $\kappa^{\mathrm{e}}_{i,j}$ and $\kappa^{\mathrm{e}}_{j,i}$ represent the forward and backward rate coefficients for energy exchange between states i and j. The rate coefficients for the dissociation and recombination reactions for i are denoted by κ^{d}_i and κ^{r}_i, respectively. The total number density of species A is computed by summing the population of all its internal states. Consequently, the time rate of change of total number density can be obtained by summing Eq. 2.10 for individual levels of A. Similarly, the total internal energy of A and its time rate of change can be obtained by performing a summation across all internal states weighted by the energy $\epsilon^{i}_{\mathrm{A}}$ of each individual level. Mixture density and energy can then be computed by adding the contributions of all chemical species included in S.

2.3 Reduced-order Modeling

State-to-state modeling requires the solution to a large system of equations, since different internal energy levels of reacting particles are treated as distinct chemical species. This description although exceedingly accurate, has limited applicability to multi-dimensional CFD problems due to its prohibitive cost. The present work overcomes this limitation through the use of the multi-group maximum entropy method [68]. The process of model reduction can be broken down into two steps:

- **Local Representation and Reconstruction:** Individual internal energy states are combined into larger macroscopic energy bins. A bin-wise distribution function based on macroscopic quantities (bin population, energy, *etc.*) and the maximum entropy principle is used to reconstruct the population of grouped levels.

- **Macroscopic Moment Equations and Rate Coefficients:** Governing equations for macroscopic quantities are derived by taking moments of the microscopic master equations and performing a summation over all internal states belonging to a common bin.

The use of bin-wise distribution functions allows the temporal evolution of state population to be modeled accurately without solving the master equations for individual levels. The current study employs a linear form for the distribution function, which results in a thermalized local Boltzmann distribution within individual bins. This function is defined as follows:

$$\mathcal{F}^{b}_{\mathrm{A}}\left(\epsilon_{\mathrm{A}_i}\right): \quad \log\left(\frac{g_{\mathrm{A}_i}}{n^{i}_{\mathrm{A}}}\right) \;=\; \alpha^{b}_{\mathrm{A}} + \beta^{b}_{\mathrm{A}}\epsilon_{\mathrm{A}_i} \tag{2.11}$$

where g_{A_i} and ϵ_{A_i} represent the degeneracy and energy, respectively, of internal state i of species A that has been assigned to the b^{th} bin. Recent work on the MGME method has explored the impact of introducing a quadratic term [125] in Eq. 2.11 which is akin to performing p-refinement in computational fluid dynamics. However, the quadratic approach results in a significant increase in overall complexity due to a) the introduction of an additional bin-specific governing equation (corresponding to the second-order energy moment), b) development of fits/look-up tables and then their evaluation for a larger number of bin-specific properties, and c) the inversion problem for obtaining the reconstruction coefficients being numerically stiff. In light of these challenges, quadratic and other higher-order reconstructions have not been incorporated into the present study. The bin-specific coefficients α^{b}_{A} and β^{b}_{A} in Eq. 2.11 are formulated in terms of the macroscopic constraints – total bin population N^{b}_{A} and energy E^{b}_{A} per unit volume – using the maximum entropy principle and the variational method outlined in [69]:

$$N^{b}_{\mathrm{A}} = \sum_{i\in\hat{\mathcal{I}}^{b}_{\mathrm{A}}} n_{\mathrm{A}_i}, \qquad E^{b}_{\mathrm{A}} = \sum_{i\in\hat{\mathcal{I}}^{b}_{\mathrm{A}}} n_{\mathrm{A}_i}\,\epsilon_{\mathrm{A}_i} \tag{2.12}$$

The set of energy states belonging to the b^{th} bin is denoted by $\hat{\mathcal{I}}^{b}_{\mathrm{A}}$. This procedure matches the one employed in classical thermodynamics for computing the equilibrium Boltzmann distribution using the method of Lagrange multipliers [126]. The only difference is that instead of maximizing the entropy of the total internal distribution for a chemical species (and subject to constraints on total species population and energy), bin-wise entropy (representing only a subset of internal states $\hat{\mathcal{I}}^{b}_{\mathrm{A}} \subset \mathcal{I}_{\mathrm{A}}$) is now maximized while satisfying constraints on bin properties. Paralleling relations derived for equilibrium Boltzmann distributions, β^{b}_{A} for the linear bin-wise state distribution function can be recast in the following manner:

$$\left(\frac{\partial s^{b}_{\mathrm{A}}}{\partial E^{b}_{\mathrm{A}}}\right)_{V,N^{b}_{\mathrm{A}}} = \frac{1}{T^{b}_{\mathrm{A}}} = \mathrm{k_B}\,\beta^{b}_{\mathrm{A}}\;; \qquad \beta^{b}_{\mathrm{A}} = \beta^{b}_{\mathrm{A}}\left(\frac{E^{b}_{\mathrm{A}}}{N^{b}_{\mathrm{A}}}\right) \tag{2.13}$$

It can be deduced that β^b_{A} is only a function of the bin specific internal energy. Therefore, the corresponding bin temperature T^b_{A} can be obtained from a non-linear inversion of $E^b_{\mathrm{A}}/N^b_{\mathrm{A}}$. The coefficient α^b_{A} can be generalized to complete the bin-wise state distribution function $\mathcal{F}^b_{\mathrm{A}}$:

$$\alpha^b_{\mathrm{A}} = \log\left(\frac{{}^0Q^b_{\mathrm{A}}}{N^b_{\mathrm{A}}}\right) = \log\left(\frac{{}^1Q^b_{\mathrm{A}}}{E^b_{\mathrm{A}}}\right) = \ldots = \log\left({}^mQ^b_{\mathrm{A}} \Big/ \sum_{i\in\hat{\mathcal{I}}^b_{\mathrm{A}}} n_{\mathrm{A}_i} \, (\epsilon_{\mathrm{A}_i})^m \right) \tag{2.14}$$

where ${}^mQ^b_{\mathrm{A}} = \sum_{i\in\hat{\mathcal{I}}^b_{\mathrm{A}}} g_{\mathrm{A}_i} \exp(-\beta^b_{\mathrm{A}}\epsilon_{\mathrm{A}_i}) \, (\epsilon_{\mathrm{A}_i})^m$ is the m^{th} order bin partition function. The method of moments [127] is then applied to derive governing equations for the bin-specific macroscopic constraints. This involves first taking successive moments of the master equations (Eq. 2.10) with internal energy levels $(\epsilon_{\mathrm{A}_i})^m \mid m \in \{0, 1, 2, \ldots\}$. Then, summing up the resultant equations for all energy states included in a particular bin to obtain the corresponding equation for a bin property. The reduced system of governing equations can be expressed as:

$$\begin{aligned}
\sum_{i\in\hat{\mathcal{I}}^b_{\mathrm{A}}} \frac{\partial n_{\mathrm{A}_i}}{\partial t} \, (\epsilon_{\mathrm{A}_i})^m \;&=\; \sum_{i\in\hat{\mathcal{I}}^b_{\mathrm{A}}} \sum_{j\in\hat{\mathcal{I}}^c_{\mathrm{A}}} \Big[-\,\kappa^{\mathrm{e}}_{i,j} \, n_{\mathrm{A}_i} n_{\mathrm{B}} \, (\epsilon_{\mathrm{A}_i})^m \,+\, \kappa^{\mathrm{e}}_{j,i} \, n_{\mathrm{A}_j} n_{\mathrm{B}} \, (\epsilon_{\mathrm{A}_i})^m \Big] \\
&\quad + \sum_{i\in\hat{\mathcal{I}}^b_{\mathrm{A}}} \Big[-\,\kappa^{\mathrm{d}}_{i} \, n_{\mathrm{A}_i} n_{\mathrm{B}} \, (\epsilon_{\mathrm{A}_i})^m \,+\, \kappa^{r}_{i} \, n_{\mathrm{C}} n_{\mathrm{D}} n_{\mathrm{B}} \, (\epsilon_{\mathrm{A}_i})^m \Big]
\end{aligned} \tag{2.15}$$

where m indicates the order of the moment. The total population and energies of the bins (Eq. 2.12) serve as the set of unknowns for a reduced-order system based on linear reconstruction. The macroscopic equations for these quantities corresponding to the b^{th} bin can be recovered by setting m equal to zero and one, respectively:

$$\begin{aligned}
\dot{\omega}^b_{\mathrm{col,A}} \times \mathrm{N}_{\mathrm{Av}} \;:\; \qquad \frac{\partial}{\partial t} N^b_{\mathrm{A}} \;&=\; \sum_c \Big(-\,{}^0K_{b,c} \, N^b_{\mathrm{A}} \, n_{\mathrm{B}} \,+\, {}^0\bar{K}_{c,b} \, N^c_{\mathrm{A}} \, n_{\mathrm{B}} \Big) \\
&\quad + \Big(-\,{}^0C_b \, N^b_{\mathrm{A}} \, n_{\mathrm{B}} \,+\, {}^0\bar{C}_b \, n_{\mathrm{C}} \, n_{\mathrm{D}} \, n_{\mathrm{B}} \Big)
\end{aligned} \tag{2.16}$$

$$\begin{aligned}
\Omega^b_{\mathrm{col,A}} \times \frac{\mathrm{N}_{\mathrm{Av}}}{\mathcal{M}^b_{\mathrm{A}}} \;:\; \qquad \frac{\partial}{\partial t} E^b_{\mathrm{A}} \;&=\; \sum_c \Big(-\,{}^1K_{b,c} \, E^b_{\mathrm{A}} \, n_{\mathrm{B}} \,+\, {}^1\bar{K}_{c,b} \, E^c_{\mathrm{A}} \, n_{\mathrm{B}} \Big) \\
&\quad + \Big(-\,{}^1C_b \, E^b_{\mathrm{A}} \, n_{\mathrm{B}} \,+\, {}^1\bar{C}_b \, n_{\mathrm{C}} \, n_{\mathrm{D}} \, n_{\mathrm{B}} \Big)
\end{aligned} \tag{2.17}$$

2.3.1 Bin-averaged Kinetics

The forward and backward bin-averaged rate coefficients for the m^{th} moment, encapsulating all internal excitation processes between the b^{th} and the c^{th} bins are denoted by ${}^{m}K_{b,c}$ and ${}^{m}\bar{K}_{c,b}$. Similarly, the bin-wise dissociation and recombination coefficients for the b^{th} bin are ${}^{m}C_{b}$ and ${}^{m}\bar{C}_{b}$. The bin-averaged rate coefficients are obtained directly from elementary StS processes after defining internal state population distributions through equations 2.11, 2.14, and 2.13. Internal energy exchange between the b^{th} and the c^{th} bins can be described as follows:

$$\begin{aligned}
&\sum_{i\in\hat{\mathcal{I}}^{b}_{\mathrm{A}}}\sum_{j\in\hat{\mathcal{I}}^{c}_{\mathrm{A}}}\Big[-\kappa^{\mathrm{e}}_{i,j}\,n_{\mathrm{A}_i}n_{\mathrm{B}}\,(\epsilon_{\mathrm{A}_i})^{m} \;+\; \kappa^{\mathrm{e}}_{j,i}\,n_{\mathrm{A}_j}n_{\mathrm{B}}\,(\epsilon_{\mathrm{A}_i})^{m}\Big] \\
&\qquad = \sum_{i\in\hat{\mathcal{I}}^{b}_{\mathrm{A}}}\sum_{j\in\hat{\mathcal{I}}^{c}_{\mathrm{A}}}\Bigg[\;-\;\kappa^{\mathrm{e}}_{i,j}\,\frac{g_{\mathrm{A}_i}\exp\{-\epsilon_{\mathrm{A}_i}/(\mathrm{k_B}\,T^{b}_{\mathrm{A}})\}}{{}^{m}Q^{b}_{\mathrm{A}}}\,(\epsilon_{\mathrm{A}_i})^{m}\;N^{b}_{\mathrm{A}}n_{\mathrm{B}} \\
&\qquad\qquad\qquad +\;\kappa^{\mathrm{e}}_{j,i}\,\frac{g_{\mathrm{A}_j}\exp\{-\epsilon_{\mathrm{A}_j}/(\mathrm{k_B}\,T^{c}_{\mathrm{A}})\}}{{}^{m}Q^{c}_{\mathrm{A}}}\,(\epsilon_{\mathrm{A}_i})^{m}\;N^{c}_{\mathrm{A}}n_{\mathrm{B}}\Bigg] \qquad (2.18)
\end{aligned}$$

The corresponding bin-averaged rate coefficients ${}^{m}K^{i}_{b,c}$ and ${}^{m}\bar{K}_{c,b}$ are:

$$ {}^{m}K_{b,c} \;=\; \frac{1}{{}^{m}Q^{b}_{\mathrm{A}}}\sum_{i\in\hat{\mathcal{I}}^{b}_{\mathrm{A}}}\sum_{j\in\hat{\mathcal{I}}^{c}_{\mathrm{A}}}\kappa^{\mathrm{e}}_{i,j}\,g_{\mathrm{A}_i}\exp\{-\epsilon_{\mathrm{A}_i}/(\mathrm{k_B}\,T^{b}_{\mathrm{A}})\}\,(\epsilon_{\mathrm{A}_i})^{m} \qquad (2.19)$$

$$ {}^{m}\bar{K}_{c,b} \;=\; \frac{1}{{}^{m}Q^{c}_{\mathrm{A}}}\sum_{i\in\hat{\mathcal{I}}^{b}_{\mathrm{A}}}\sum_{j\in\hat{\mathcal{I}}^{c}_{\mathrm{A}}}\kappa^{\mathrm{e}}_{j,i}\,g_{\mathrm{A}_j}\exp\{-\epsilon_{\mathrm{A}_j}/(\mathrm{k_B}\,T^{c}_{\mathrm{A}})\}\,(\epsilon_{\mathrm{A}_i})^{m} \qquad (2.20)$$

A similar procedure for the dissociation and recombination processes yields:

$$ {}^{m}C_{b} \;=\; \frac{1}{{}^{m}Q^{b}_{\mathrm{A}}}\sum_{i\in\hat{\mathcal{I}}^{b}_{\mathrm{A}}}\kappa^{\mathrm{d}}_{i}\,g_{\mathrm{A}_i}\exp\{-\epsilon_{\mathrm{A}_i}/(\mathrm{k_B}\,T^{b}_{\mathrm{A}})\}\,(\epsilon_{\mathrm{A}_i})^{m} \qquad (2.21)$$

$$ {}^{m}\bar{C}_{b} \;=\; \sum_{i\in\hat{\mathcal{I}}^{b}_{\mathrm{A}}}\kappa^{r}_{i}\,(\epsilon_{\mathrm{A}_i})^{m} \qquad (2.22)$$

It should be noted that the bin-averaged rate coefficients only depend on the translational temperature of the gas mixture and the bin internal temperatures T^{b}_{A} (forward excitation and dissociation/recombination) and T^{c}_{A} (backward excitation). Therefore, they can be pre-computed and stored as two-dimensional fits or look-up tables for use during actual simulations.

2.3.2 Bin Thermodynamics

Standard operators from statistical thermodynamics can be applied to bin partition functions in order to obtain bin-wise properties [126]. The total bin partition function can be defined as:

$$Q^b_{(\mathrm{tot,A})} = Q_{(\mathrm{tr,A})}\, Q^b_{(\mathrm{int,A})} = Q_{(\mathrm{tr,A})}\, {}^0Q^b_{\mathrm{A}} \tag{2.23}$$

where $Q_{(\mathrm{tr,A})}$ is the translational partition function for species A and $Q^b_{(\mathrm{int,A})} = {}^0Q^b_{\mathrm{A}}$ is the bin-specific internal partition function. Enthalpy, specific heat capacity, and entropy due to internal energy states included in the b^{th} bin can be defined in a straightforward manner:

$$\frac{h^b_{(\mathrm{int,A})}}{\mathrm{R}T} = T\left(\frac{\partial \ln Q^b_{(\mathrm{int,A})}}{\partial T}\right)_V \tag{2.24}$$

$$\frac{C^b_{\mathrm{p,(int,A)}}}{\mathrm{R}} = \left[\frac{\partial}{\partial T}T^2\left(\frac{\partial \ln Q^b_{(\mathrm{int,A})}}{\partial T}\right)\right]_V \tag{2.25}$$

$$\frac{s^b_{(\mathrm{int,A})}}{\mathrm{R}} = T\left(\frac{\partial \ln Q^b_{(\mathrm{int,A})}}{\partial T}\right)_V + \ln Q^b_{(\mathrm{int,A})} \tag{2.26}$$

The MGME method can be applied to the whole hierarchy – vibronic, vibrational, electronic – of StS models outlined in Chapter 1. A switch in the type of StS modeling would merely change the form for the total bin partition function:

$$Q^b_{(\mathrm{tot,A})} = Q_{(\mathrm{tr,A})}\, Q_{(\mathrm{rot,A})}\, Q^b_{(\mathrm{VE,A})} \quad , \quad \text{(Vibrational StS)} \tag{2.27}$$

$$Q^b_{(\mathrm{tot,A})} = Q_{(\mathrm{tr,A})}\, Q_{(\mathrm{rot,A})}\, Q_{(\mathrm{vib,A})}\, Q^b_{(\mathrm{el,A})} \; , \quad \text{(Electronic StS)} \tag{2.28}$$

The rotational (for Vibrational/Electronic StS) and vibrational (for Electronic StS) partition functions can be computed using standard models (rigid rotor, harmonic oscillator amongst others) [126, 128] and are common across all bins for a given species. The bin-specific partition functions only include the contribution of the explicit internal states (VE: vibrational-electronic, E:electronic) listed for a specific StS model. Furthermore, analogous to multi-temperature modeling, additional assumptions regarding thermal equilibrium between different types of internal modes (bin or species wise) can be introduced, resulting in fewer independent energy conservation equations. These different models ($T^b_\mathrm{A} = T^c_\mathrm{A} = \ldots = \mathrm{Const}$ [129], $T^b_\mathrm{A} = T^c_\mathrm{A} = \ldots = T$ [73], $T^b_\mathrm{E,A} = T^c_\mathrm{E,A} = \ldots \neq T$ [12]) for defining the underlying Boltzmann distributions simply alter the temperatures at which the various partition functions and the resultant thermodynamic operators are evaluated. Thus, the MGME framework can be repurposed for any desired level of fidelity while making non-equilibrium thermochemical predictions.

2.4 Binning Strategy

The MGME method (or coarse-graining in general) with linear bin-wise distribution functions implicitly assumes that energy levels that belong to the same bin are in a state of thermal equilibrium. The present work is aimed at improving the applicability of the MGME methodology by leveraging the details of state-specific chemical kinetics to construct a more physics-based grouping strategy (referred to as *Adaptive Binning* hereafter). This allows the difference in time scales (defined with respect to the characteristic flow time) between fast and slow processes to be identified accurately [121, 130]. The reduced-order model needs to describe only the slow processes, while the fast processes leading to localized equilibrium can be ignored. The impact of fast reactions can be accounted for by grouping together the participating states into a common bin, with their population accurately described using the maximum entropy principle [131]. To this aim, new metrics shaped by both the energy difference and relevant reaction processes are proposed to accurately characterize the strength of connection between different internal energy levels for a given chemical species. Two different techniques are considered for clustering individual energy levels into bins using these affinity metrics: the *Modified Island Algorithm* [132, 133] and the *Spectral Clustering* [134, 135, 136] method.

Clustering of data with "similar behavior" is one of the most actively researched areas and can be broadly categorized into supervised and unsupervised techniques [137]. Supervised clustering relies on an input preliminary data-set that has already been divided (or labeled) appropriately which can then inform how newer problems are tackled. No such initial classification can be made about internal energy states without completely analyzing the myriad of possible interactions included in StS kinetics. Additionally, a clustering solution that might be appropriate for a given chemical system cannot be readily applied to another problem comprising of differing molecules and atoms. Instead, unsupervised strategies that are free of inadequately informed biases and are driven by structures/features enshrined in the StS database can more reliably assess a general system. The modified island algorithm and spectral clustering are two approaches, with different levels of sophistication, for effecting unsupervised segmenting of internal states.

2.4.1 Modified Island Algorithm

This clustering technique borrows from existing algorithms that are designed to find connected components in a system comprising of individual objects or nodes. Connected components are sets of nodes (also described as *islands* of nodes) that are directly or indirectly linked to one another but are disconnected from other islands. In the context of coarse grain modeling, the nodes are analogous to internal energy levels and the islands represent prospective macroscopic bins which group together states that quickly thermalize with each other.

A wide variety of formulations for the island algorithm have been proposed in the literature by Dijkstra [138] and Kosaraju [139]. This work relies on a modified form of the depth-first search technique, developed by Hopcroft and Tarjan [132, 133], to identify connected components in linear time, *i.e.*, the time complexity of the algorithm scales linearly with the number of nodes. In order to be able to cluster the states into islands, this algorithm requires the definition of "fast" and "slow" transitions. The following definition based on log-averaging is proposed in the present work:

$$\begin{aligned} \log_{10}\left(\kappa_{\mathrm{fast}}\right) &= \log_{10}\left(\kappa_{\mathrm{lavg}}\right) + \beta_{\mathrm{I}}\left[\log_{10}\left(\kappa_{\mathrm{min}}\right) - \log_{10}\left(\kappa_{\mathrm{lavg}}\right)\right] \\ \Rightarrow \qquad \kappa_{\mathrm{fast}} &= \kappa_{\mathrm{lavg}}^{(1-\beta_{\mathrm{I}})}\,\kappa_{\mathrm{min}}^{\beta_{\mathrm{I}}} \end{aligned} \tag{2.29}$$

where β_{I} is a tunable parameter whose optimal value varies between different chemical systems. Threshold values κ_{fast} for the forward and backward processes of excitation reactions are calculated separately. Any transition with a reaction rate coefficient greater than the corresponding value of κ_{fast} in either the forward or backward direction is considered a fast reaction. The log averaged value for the rate coefficient is denoted by κ_{lavg} and can be computed as follows:

$$\log_{10}\left(\kappa_{\mathrm{lavg}}\right) = \left(\sum_{i=1}^{\mathcal{N}_r} \log_{10}\kappa_i^{\mathrm{e}}\right) \Big/ \mathcal{N}_r \tag{2.30}$$

where κ_i^{e} is the rate coefficient for the i^{th} internal excitation reaction, and $\mathcal{N}_r$ is the total number of excitation reactions. The lowest value of the reaction rate coefficient for all transitions included in the kinetic scheme is represented by $\kappa_{\min}$ in Eq. 2.29. This process of delineating "fast" and "slow" transitions can also be supplemented by additional qualitative information regarding the nature of different types of collisional processes. Certain StS models, such as the $\mathrm{CO_2}(\mathrm{X}^1\sum_{\mathrm{g}}^{+})$ system [56, 140, 141] discussed in Chapter 3, comprise of various categories of state-specific transitions that are clearly separated in terms of their characteristic time scales. In such cases, these physical distinctions can simply be employed to identify rapidly thermalizing processes instead of characterizing the system through log-averaging and β_{I}.

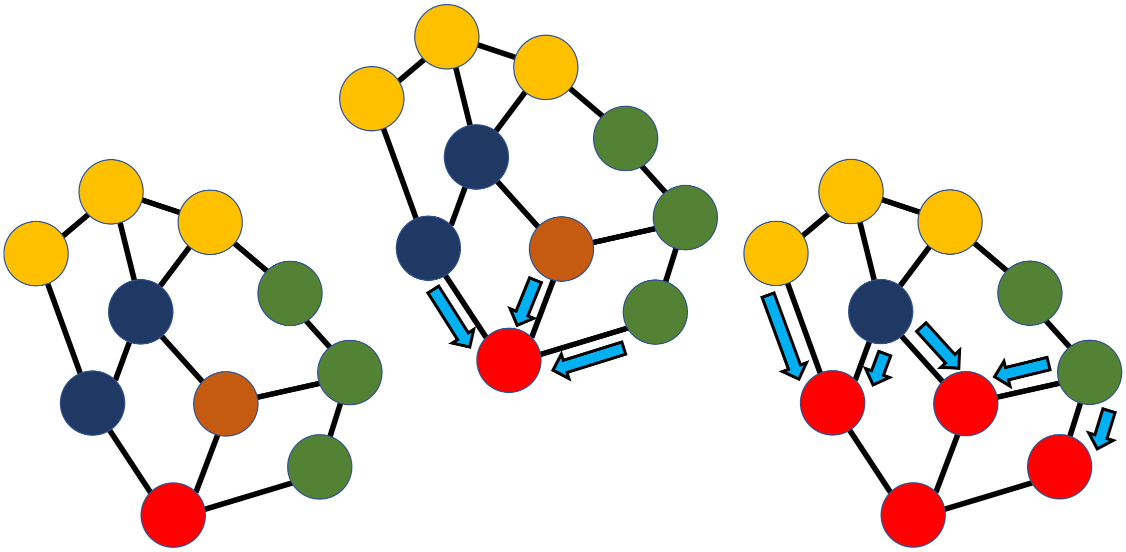

Figure 2.1: Recursive re-binning of internal states connected by "fast" transitions using island algorithm. States with the same color occupy a common macroscopic bin.

Once states connected by "fast" transitions have been mapped out, the island algorithm can proceed further. The subsequent recursive re-binning of internal states on the basis of these high probability energy-exchange mechanisms is presented in Fig. 2.1. A preliminary bin assignment for the internal states is obtained using the conventional energy-based grouping approach [68, 69]. States that are placed in a common energy bin have the same color initially in Fig. 2.1. Subsequently, a loop over all possible energy levels i is initiated; all states connected to level i through fast reactions are pulled from their original bins into the same bin as i. The next subfigure in Fig. 2.1 represents this phase, with the first layer of connected states being re-assigned to the red bin. The algorithm then moves on to the states which were just processed. The same sequence of steps – mapping out connected states and assigning them the same bin as i – is repeated recursively until all connected components of the island have been visited. The possibility of getting caught in an infinite loop is avoided by allowing the bin index of a particular state to be changed only once. Thus, the recursive exploration (based on analyzing successive layers of connected states) is stopped once a previously redistributed internal state is encountered. The algorithm then restarts from the next state i in the main loop.

The island algorithm is a recursive exploratory method which relies on local searches to map out strongly coupled internal states. The focus on evaluating the relationship only between a pair of states at any given time limits the algorithm's ability to analyze the entire system more comprehensively. Additionally, the binary approach of classifying transitions as "fast" or "slow" (Eq. 2.29) provides an incomplete picture of the impact of collisional processes included in the state-specific chemistry model.

2.4.2 Spectral Clustering

Spectral clustering has emerged as the method of choice for identifying natural clusters in large sets of data for a wide range of machine learning applications such as image processing, online traffic analysis, and dimension reduction. This technique has evolved from graph partitioning theory which allows all direct or indirect connections between individual states (and not just a localized analysis) to shape the clustering process. Consequently, a major drawback of the island algorithm – pairs of states being compared independently of all other internal energy levels – is eliminated and the system is analyzed in its entirety. Additionally, by employing a more sophisticated coupling metric instead of an arbitrary threshold value for defining fast transitions, spectral clustering yields more physically representative clusters. The next two subsections provide a detailed roadmap for effecting spectral clustering, starting from detailed StS models to a rigorous formulation for partitioning undirected graphs.

2.4.2.1 StS Model to Graph Partitioning

The first step towards implementing spectral clustering is a quantitative assessment of the degree of connectedness between energy states, which encapsulates both energy and state-to-state kinetics. The following expression for defining the strength of connection between levels i and j is proposed in the current work:

$$\boldsymbol{\mathcal{S}}(i,j) : \qquad \mathcal{S}_{ij} = \frac{|\epsilon_{\mathrm{A}_i} - \epsilon_{\mathrm{A}_j}|^{\beta_{\mathrm{E}}}}{\left(\kappa^{\mathrm{e}}_{i,j}\right)^{\beta_{\mathrm{K}}}} \tag{2.31}$$

It must be emphasized that optimal values for parameters β_{E} and β_{K} can vary between different chemical systems. Pairs of internal states that are less likely to be in equilibrium, due to the combined effect of their energies being different and the transitions linking them being improbable, are characterized by larger-valued elements in the strength of connection matrix $\boldsymbol{\mathcal{S}} \in \mathcal{R}^{n \times n}$. Conversely, lower values in $\boldsymbol{\mathcal{S}}$ represent states that have stronger interactions and therefore, equilibrate faster with respect to one another.

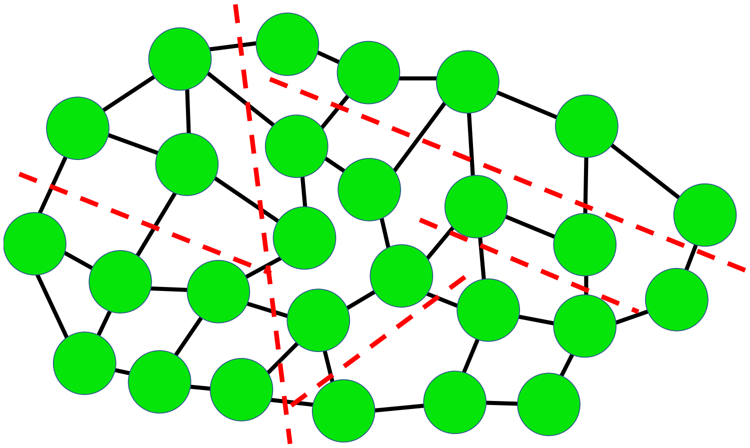

Figure 2.2: Recasting internal state binning as a graph partitioning problem: Green vertices represent individual states and edges are weighted by $\boldsymbol{\mathcal{W}}$ (Eq. 2.32).

The second step in effecting spectral clustering is the re-formulation of the original clustering problem into a graph partitioning problem (Fig. 2.2). The different internal levels along with the strength of connection matrix $\boldsymbol{\mathcal{S}}$ are represented as an undirected similarity graph $\boldsymbol{\mathcal{G}}$. The internal states constitute the set of vertices $\boldsymbol{\mathcal{V}}$ in graph $\boldsymbol{\mathcal{G}}$. The edge between two states (or vertices) i and j is assumed to be weighted by the appropriate non-zero term $\mathcal{W}_{ij}$ from the graph adjacency matrix

$\boldsymbol{\mathcal{W}} \in \mathcal{R}^{n \times n}$. The value of $\mathcal{W}_{ij}$ lies in the interval $[0, 1]$, with a larger value indicative of a stronger connection or higher degree of similarity. The graph adjacency matrix is derived from the strength of connection matrix using a Gaussian similarity function in the following manner:

$$\boldsymbol{\mathcal{W}}(i,j) : \qquad \mathcal{W}_{ij} \, = \, \exp\left(\frac{-\mathcal{S}_{ij}}{\sqrt{\sigma_i \, \sigma_j}}\right) \tag{2.32}$$

where σ_i is the local scaling factor associated with state i. It determines how rapidly similarity with state i falls off as the strength of connection with it decreases. The current study sets σ_i equal to $\mathcal{S}_{iN}$ which is the strength of connection between state i and its N^{th} closest neighbor, *i.e.*, the state corresponding to the N^{th} smallest element in the i^{th} row of $\boldsymbol{\mathcal{S}}$ [142]. This approach, unlike using a single global scaling factor σ, allows vertices that are located at different scales of proximity to be automatically accounted for while identifying optimal clusters. The graph adjacency matrix $\boldsymbol{\mathcal{W}}$ needs to be symmetric, in order to ensure that graph $\boldsymbol{\mathcal{G}}$ is undirected, *i.e.*, the edges have no orientation and their weights are constant irrespective of direction. This requires that the original strength of connection matrix $\boldsymbol{\mathcal{S}}$ be symmetric as well. Therefore, only the rate constant corresponding to the excitation process between i and j is used to define both $\mathcal{S}_{ij}$ and $\mathcal{S}_{ji}$. Since, $\kappa_{i,j}$ and $\kappa_{j,i}$ are assigned the same value (with the de-excitation process ignored), Eqn 2.31 yields a system with $\mathcal{S}_{ij} = \mathcal{S}_{ji}$.

The computational cost of clustering is decreased by reducing the number of non-zero entries in the graph adjacency matrix $\boldsymbol{\mathcal{W}}$. This can be achieved using various criteria [136], namely: a) ϵ-neighborhood, b) k-nearest neighbors, c) and mutual k-nearest neighbors. The third criterion based on mutual k-nearest neighbors is used in the present work. A non-zero value of $\mathcal{W}_{ij}$ (computed in Eq. 2.31) is retained only if both i is among the k-nearest neighbors of j, and j is among the k-nearest neighbors of i. Otherwise, $\mathcal{W}_{ij}$ is assigned a value of zero, thereby increasing the overall sparsity of $\boldsymbol{\mathcal{W}}$. This process ensures that despite the original similarity graph being simplified, the local neighborhood relationships between energy levels with the strongest connections are still modeled accurately.

2.4.2.2 Optimal Graph Cuts

The current clustering problem of dividing closely linked states into groups can finally be recast as follows – graph $\boldsymbol{\mathcal{G}}$ needs to partitioned in a manner that edges defined between different groups carry low weights (states assigned to different clusters are dissimilar) while the edges within a group are characterized by high weights (states within a common cluster are strongly coupled). The sum of similarities [143] (SS) between two potential clusters $\boldsymbol{\mathcal{C}}_i$ and $\boldsymbol{\mathcal{C}}_j$ can be defined as:

$$\mathrm{SS}\left(\boldsymbol{\mathcal{C}}_i, \boldsymbol{\mathcal{C}}_j\right) = \sum_{u \in \boldsymbol{\mathcal{C}}_i, v \in \boldsymbol{\mathcal{C}}_j} \mathcal{W}_{uv} \tag{2.33}$$

An optimal clustering solution can be obtained by minimizing the normalized cut (Ncut) objective function [134]:

$$\mathcal{F}_{\mathrm{NC}} = \sum_{i=1}^{K} \frac{\mathrm{SS}\left(\boldsymbol{\mathcal{C}}_i, \overline{\boldsymbol{\mathcal{C}}}_i\right)}{\mathrm{SS}\left(\boldsymbol{\mathcal{C}}_i, \boldsymbol{\mathcal{V}}\right)} \tag{2.34}$$

where K is the target number of clusters (or macroscopic bins) being sought for a given reduced-order model. The numerator $\mathrm{SS}\left(\boldsymbol{\mathcal{C}}_i, \overline{\boldsymbol{\mathcal{C}}}_i\right)$ ascertains how closely states in $\boldsymbol{\mathcal{C}}_i$ are linked with the rest of the data set $\overline{\boldsymbol{\mathcal{C}}}_i$. The denominator term in Eq. 2.34 drives down disparity in the sizes of different clusters and ensures a more balanced partitioning. The objective function $\mathcal{F}_{\mathrm{NC}}$ can be expounded by defining an $n \times K$ cluster affinity matrix $\mathbf{X}$:

$$X_{ij} = \begin{cases} 1\,, & \text{if } i^{th} \text{ vertex } \in j^{th} \text{ cluster} \\ 0\,, & \text{otherwise} \end{cases} \tag{2.35}$$

The normalized cut (Eq. 2.34) minimization problem can be expressed more succinctly as:

$$\min_{\boldsymbol{X}} \quad \mathcal{F}_{\mathrm{NC}} = \sum_{j=1}^{K} \frac{\boldsymbol{X}_{*j}^{T}\,(\boldsymbol{\mathcal{D}} - \boldsymbol{\mathcal{W}})\boldsymbol{X}_{*j}}{\boldsymbol{X}_{*j}^{T}\,\boldsymbol{\mathcal{D}}\boldsymbol{X}_{*j}} = \mathbf{Tr}\left(\frac{\boldsymbol{X}^{T}\,(\boldsymbol{\mathcal{D}} - \boldsymbol{\mathcal{W}})\boldsymbol{X}}{\boldsymbol{X}^{T}\,\boldsymbol{\mathcal{D}}\boldsymbol{X}}\right) \tag{2.36}$$

where $\boldsymbol{X}_{*j}$ is an n-dimensional vector comprising of the j^{th} column of the affinity matrix. The operator $\mathbf{Tr}\,(\,.\,)$ yields the trace of a matrix. The degree matrix $\boldsymbol{\mathcal{D}}$ is defined as follows:

$$\boldsymbol{\mathcal{D}}(i,j)\ : \qquad \mathcal{D}_{ij} \ = \begin{cases} \sum_{j=i}^{n} \mathcal{W}_{ij}\,, & \text{if } i = j \\ 0\,, & \text{otherwise} \end{cases} \tag{2.37}$$

Equation 2.36 can be further developed by defining a symmetric normalized graph Laplacian [135, 144] $\mathbf{L}_{\text{sy}} = \boldsymbol{\mathcal{I}} - \boldsymbol{\mathcal{D}}^{-1/2}\,\boldsymbol{\mathcal{W}}\,\boldsymbol{\mathcal{D}}^{-1/2}$, with $\boldsymbol{\mathcal{I}}$ being the identity matrix:

$$\begin{aligned} \min_{\boldsymbol{X}} \quad \mathcal{F}_{\text{NC}} \ &= \ \sum_{j=1}^{K} \frac{\boldsymbol{X}_{*j}^{T}\,(\boldsymbol{\mathcal{D}} - \boldsymbol{\mathcal{W}})\,\boldsymbol{X}_{*j}}{\boldsymbol{X}_{*j}^{T}\,\boldsymbol{\mathcal{D}}\,\boldsymbol{X}_{*j}} \\ &= \ \sum_{j=1}^{K} \frac{\boldsymbol{X}_{*j}^{T}\,\boldsymbol{\mathcal{D}}^{1/2}\,(\boldsymbol{\mathcal{I}} - \boldsymbol{\mathcal{D}}^{-1/2}\,\boldsymbol{\mathcal{W}}\,\boldsymbol{\mathcal{D}}^{-1/2})\,\boldsymbol{\mathcal{D}}^{1/2}\,\boldsymbol{X}_{*j}}{\boldsymbol{X}_{*j}^{T}\,\boldsymbol{\mathcal{D}}^{1/2}\,\boldsymbol{\mathcal{D}}^{1/2}\,\boldsymbol{X}_{*j}} \\ &= \ \sum_{j=1}^{K} \boldsymbol{Y}_{*j}^{T}\,\mathbf{L}_{\text{sy}}\,\boldsymbol{Y}_{*j}\ , \qquad \boldsymbol{Y}_{*j} \ = \ \boldsymbol{\mathcal{D}}^{1/2}\,\boldsymbol{X}_{*j}\,/\,||\boldsymbol{\mathcal{D}}^{1/2}\,\boldsymbol{X}_{*j}|| \end{aligned} \tag{2.38}$$

where $||\,.\,||$ is the l_2-norm. Equivalently, Eq. 2.38 can be expressed as a trace minimization problem:

$$\min_{\boldsymbol{Y}} \quad \mathcal{F}_{\text{NC}} \ = \ \mathbf{Tr}\,(\boldsymbol{Y}^{T}\,\mathbf{L}_{\text{sy}}\,\boldsymbol{Y})\ , \qquad \boldsymbol{Y}^{T}\,\boldsymbol{Y} \ = \ \boldsymbol{\mathcal{I}} \tag{2.39}$$

A general optimization problem of the form outlined in Eq. 2.39 has been proven to be NP-hard [145] and therefore, no direct solution for it can be easily obtained. Instead, spectral clustering attempts to solve a relaxed form of the problem [134, 136] by doing away with the discrete nature of the affinity matrix and allowing it to take any real value, *i.e.*, $X_{ij} \notin \{0, 1\}$. A minimum bound for the relaxed form of Eq. 2.39 can be obtained using K. Fan's theorem [146, 147], which generalizes the Rayleigh-Ritz theorem [148]:

$$\min_{\boldsymbol{Y}} \quad \mathbf{Tr}\,(\boldsymbol{Y}^{T}\,\mathbf{L}_{\text{sy}}\,\boldsymbol{Y}) \ \geq \ \lambda_1 + \cdots + \lambda_K\ , \qquad \mathbf{L}_{\text{sy}}\,\boldsymbol{w}_m = \lambda_m \boldsymbol{w}_m$$

where $\lambda_1 \ \leq, \cdots \ \leq \ \lambda_K$ are the K smallest eigenvalues of $\mathbf{L}_{\text{sy}}$. Since the normalized Laplacian is positive semi-definite [149], its eigenvalues and the minimum value of $\mathcal{F}_{\text{NC}}$ cannot be less than zero. The normalized affinity matrix $\boldsymbol{Y}$ that results in this optimal solution comprises of the eigenvectors corresponding to these K eigenvalues. The i^{th} row of $\mathbf{Y}$ represents a point in the $\Re^K$ space, with component Y_{ij} representing the likelihood of the i^{th} vertex being in the j^{th} cluster. Individual vertices are then grouped into clusters based on the cluster-affinity relationship encapsulated in these absolute coordinates in a K-dimensional space instead of the original graph adjacency matrix. Ng et al. [135, 136] employed arguments based on matrix perturbation theory [150] for proving that $\mathbf{Y}$ based on $\mathbf{L}_{\text{sy}}$ requires a further row-normalization step $\mathbf{Y}_{i*} \,/\, ||\mathbf{Y}_{i*}||$ to sufficiently eliminate noise and correctly identify cluster connections. Instead, the use of the asymmetric normalized Laplacian $\mathbf{L}_{\text{rw}} = \boldsymbol{\mathcal{I}} - \boldsymbol{\mathcal{D}}^{-1}\boldsymbol{\mathcal{W}}$ in Eq. 2.40, as done by Shi and Malik [134], involves no such extra step while solving for balanced optimal clusters. A formal equivalence can also be established with the random walk interpretation of spectral clustering [151] which adds further credence to the use of $\mathbf{L}_{\text{rw}}$. A detailed analysis of the spectral clustering method, including different perspectives based on graph cuts, random walk, and perturbation theory, can be found in [134, 135, 136, 152].

2.4.2.3 Solution Procedure

The present study is based on the asymmetric normalized spectral clustering approach proposed by Shi and Malik [134], which can be summarized as follows:

- Construct a sparse $n \times n$ weighted adjacency matrix $\boldsymbol{\mathcal{W}}$ using a Gaussian similarity function and mutual k-nearest neighbors criterion.
- Compute the asymmetric normalized graph Laplacian $\mathbf{L}_{\text{rw}} = \boldsymbol{\mathcal{I}} - \boldsymbol{\mathcal{D}}^{-1}\boldsymbol{\mathcal{W}}$.
- Compute eigenvectors $\mathbf{u}_1, \mathbf{u}_2, \ldots, \mathbf{u}_K$ corresponding to the K smallest eigenvalues of $\mathbf{L}_{\text{rw}}$.
- Form an $n \times K$ matrix $\hat{\boldsymbol{Y}}$ with vectors $\mathbf{u}_1, \mathbf{u}_2, \ldots, \mathbf{u}_K$ as columns.
- Row vectors $\mathbf{Y}_{i*}$ represent points in $\Re^K$ space. Finally, perform clustering on $\mathbf{Y}^T$ to obtain $\boldsymbol{\mathcal{C}}_1, \ldots, \boldsymbol{\mathcal{C}}_K$.

The final clustering of absolute coordinates in $\Re^K$ space has been performed using a popular K-medoids algorithm called partitioning around medoids (PAM) [153]. PAM attempts to identify medoids which are data points that are centrally located in clusters and can serve as their representatives. The remaining points in $\mathbf{Y}$ are then partitioned into clusters based on the closest medoid.

The level of dissimilarity within clusters is iteratively minimized by selecting better medoids (average dissimilarity to all points in a cluster is minimal) and then re-grouping the data-set based on the updated set of medoids. Unlike the more popular K-Means method [154, 155], K-medoids clustering is less sensitive to outliers. Thus, its use in conjunction with spectral clustering allows optimal clusters to be created for a wider variety of problems.

2.5 Summary

This chapter presents a detailed outline of the MGME framwork for obtaining reduced-order representation of internal state population dynamics. This entails combining internal states for a given chemical species into larger macroscopic bins. Thereafter, the bin-wise state population distribution is reconstructed using polynomials based on entropy maximization and constrained by bin-specific properties. This paves the way for modeling non-equilibrium response in a computationally cost-effective manner by treating only bin properties as independent degrees of freedom. The bin governing equations are derived in a consistent manner by applying maximum entropy reconstruction and the method of moments to the StS master equations without further simplifications. Existing reduced-order models based on this multi-group paradigm rely on a simplistic grouping strategy that can lead to erroneous predictions of non-equilibrium chemical kinetics and energy exchange. These approaches group states solely based on energy considerations, completely disregarding the characteristics of the StS kinetics and the presence of preferential transition pathways between certain states. This chapter introduces two new binning strategies that incorporate state-specific chemistry to improve the accuracy of MGME reduced-order models: the *Modified Island Algorithm* and the *Spectral Clustering* method. The modified island algorithm is a recursive method based on mapping out islands (bins) of internal states that are connected directly or indirectly by highly probable transitions. However, this approach is still limited by the binary classification of "fast"/"slow" transitions and analyzing only individual pairs of states at a time. Spectral clustering remedies these shortcomings by evolving more sophisticated metrics for characterizing localized equilibration and evaluating all possible connections in the StS system concurrently. The resultant clustering procedure in conjunction with partitioning around medoids is able to extract optimal macroscopic bins by analyzing the strength of connection between internal states based on kinetic processes and energy difference. The impact of different grouping techniques while evolving physics-based MGME reduced-order models from different StS systems will be studied in the next chapter.

Chapter 3

Chemical Reactor Analysis of Adaptive Multi-group Maximum Entropy Method

The adaptive MGME paradigm outlined in Chapter 2 provides for computationally efficient predictions for complex non-Boltzmann kinetics while retaining key attributes of StS models. A reduced-order description of collisional reaction mechanisms is sought for accurately estimating volumetric source terms emanating from internal energy transfer and chemical change. Thus, an idealized homogeneous chemical reactor with no spatial variation and devoid of convective/diffusive fluxes serves as the ideal test-bed for characterizing MGME-based model reduction. Molecular nitrogen and carbon-dioxide represent two of the most abundant atmospheric species on planetary bodies that are the focus of current and near-future hypersonic entry, descent, and landing (EDL) missions. These include Mars [156]: 95.3 % CO_2 and 1.9 % N_2, Titan [157]: 98.4 % N_2, Venus [158]: 96.5 % CO_2 and 3.5 % N_2, and Earth [159]: 78.1 % N_2, with species concentration listed in percentage volume. The thermochemical response of the gaseous flowfield enveloping the vehicle during such planetary entries would be dominated by N_2 and CO_2. The current chapter presents results obtained using StS modeling of N_2 and CO_2 in an isochoric chemical reactor, which allows an exact representation of thermal and chemical non-equilibrium in these species. Next, the accuracy of different reduced-order MGME models based on binning strategies outlined in Section 2.4 is assessed using the full StS solution. This chapter is organized as follows: a) Section 3.1 outlines the numerical framework and computational tools employed for studying the unsteady chemical reactor problem. b) The impact of binning strategies on the applicability of MGME models for the $N_2(^1\Sigma_g^+) - N(^4S_u)$ rovibrational StS system is studied in Section 3.2.1. c) Section 3.3.1 presents a similar analysis for the $CO_2(X^1\sum_g^+) - M$ vibrational system. d) The key conclusions from the chapter are summarized in Section 3.4.

3.1 Computational Methodology

State-to-state modeling in an isochoric chemical reactor with spatially invariant properties and no bulk flow represents a system of nonlinear ordinary differential equations (ODEs) in time of the form outlined in Eq. 2.10. The following approach is used for studying non-equilibrium dynamics in this chapter: a) The initial conditions inside the reactor are defined by total pressure P_0, temperature $T = T_0$, and total mole-fractions $X_{0,i}$ for different chemical species. Internal energy states are assumed to be in thermal equilibrium with the translational mode at T_0. Thus, the number density of internal state i is obtained through the Maxwell-Boltzmann distribution:

$$\frac{n_{\mathrm{A}_i}}{N_{\mathrm{A}}} = \frac{g_{\mathrm{A}_i} \exp\{-\epsilon_{\mathrm{A}_i}/(\mathrm{k_B}\, T_0\}}{Q_{\mathrm{A}}} \tag{3.1}$$

b) At $t = 0$ s, the translational temperature T of the chemical reactor is increased instantly to T_f which induces strong thermal and chemical non-equilibrium c) A time-accurate solution for the internal population distribution is computed till equilibrium is reached at T_f. The isothermal assumption for translational temperature results in state-specific rate coefficients ($\kappa^e_{i,j}$, $\kappa^e_{j,i}$, κ^d_i, κ^r_i) remaining constant at T_f for the duration of the simulation. Reduced-order modeling of this unsteady zero-dimensional problem involves solving equations 2.16 and 2.17. The change in bin energy E^b_{A} requires the corresponding bin temperature T^b_{A} to be updated through a non-linear inversion as the simulation proceeds. The varying bin internal state distribution (characterized by T^b_{A}) results in the bin-averaged rate coefficients (${}^{m}K_{b,c}$, ${}^{m}\bar{K}_{c,b}$, ${}^{m}C_b$) also evolving in time. The set of internal states belonging to a given bin $\hat{\mathcal{I}}^b_{\mathrm{A}}$ is determined prior to non-equilibrium simulations and does not change in time (or space for multi-dimensional problems discussed later). Three observables are calculated and compared: chemical composition, total internal energy profiles, and the populations of the internal states.

The ideal reactor ODE system with time-dependent parameters is not only large (number of internal states for StS modeling are $\mathcal{O}(10^4)$) but also extremely stiff due to state populations and reaction rates varying by multiple orders of magnitude. Thus, performing time integration on this system is a challenging and computationally expensive process. The present work makes extensive use of the CVODE ODE solver [160] which is a part of the larger SUNDIALS package [161].

Backward Differentiation Formulas (BDFs) of orders ranging from 1 to 5 are used to step forward in time. The non-linear system obtained at each integration step is solved using the modified Newton's method. A dense direct solver from the OpenBLAS library [162, 163] has been employed to tackle linear systems within the Newton sub-iterations. A shared memory parallel framework based on OpenMP [164] is employed by OpenBLAS to speed-up the process of LU factorization and subsequently, back-solving linear problems. The large number of possible state-to-state processes yields a mass matrix with low sparsity. This precludes the use of preconditioned Krylov linear solvers [165] which exhibit poor convergence behavior even while using a relatively high-dimensional Krylov subspace.

The K-smallest eigenvalues and corresponding eigenvectors for asymmetric normalized graph Laplacians $\mathbf{L}_{\mathrm{rw}}$ during spectral clustering have been computed using the SLEPc [166, 167] software library. The SLEPc library provides a range of methods for solving large-scale sparse eigenvalue problems efficiently on parallel computers. The current study uses the Krylov-Schur approach [168] to identify the required eigenvalues for $\mathbf{L}_{\mathrm{rw}}$. Although K-medoid clustering based on Partitioning Around Medoids (PAM) is an expensive procedure ($\mathcal{O}(n^2)$), the second phase of PAM based on improving clustering quality by swapping existing medoids with other data points can easily be parallelized. This has been achieved using OpenMP, resulting in a computational implementation that performs clustering at reduced time outlays.

3.2 $\mathbf{N_2(^1\Sigma_g^+) - N(^4S_u)}$ System

The NASA Ames ab-initio quantum chemistry database [59, 60, 169, 170] comprises a complete and self-consistent set of thermodynamic and kinetic information needed to describe the elementary state-to-state kinetics of $\mathrm{N_2 - N}$ and $\mathrm{N_2 - N_2}$ interactions. While the analysis carried out in this work is restricted to the study of $\mathrm{N_2 - N}$ relaxation, an ongoing effort investigates the dynamics of the $\mathrm{N_2 {-} N_2}$ system [129, 171, 172]. The database includes $9,390$ rovibrational energy levels $\mathrm{N_2}(v, J)$ for the electronic ground-state of nitrogen, where indices v and J represent the vibrational and rotational quantum numbers, respectively. These levels can also be sorted by increasing energy and then described using a single global index i. The relation between i and (v, J) notations is expressed as:

$$i = i(v, J), \quad \text{where} \quad v = 0, \ldots, v_{\max} \quad \text{and} \quad J = 0, \ldots, J_{\max}(v)$$

and conversely by the relations:

$$v = v(i), \quad J = J(i), \quad i \in \mathcal{I}_{\mathrm{N}_2},$$

where $\mathcal{I}_{\mathrm{N}_2}$ is the set of internal energy levels for molecular nitrogen. The database for the $\mathrm{N}_2 - \mathrm{N}$ system comprises more than 2×10^7 individual reactions that can be classified into three types of processes: collisional dissociation of bound and quasi-bound states; predissociation or tunneling of quasi-bound states; and collisional excitation transitions between different states:

$$\mathrm{N}_2^i(^1\Sigma_g^+) + \mathrm{N}(^4\mathrm{S}_u) \longleftrightarrow \mathrm{N}_2^j(^1\Sigma_g^+) + \mathrm{N}(^4\mathrm{S}_u) \qquad i, j \in \mathcal{I}_{\mathrm{N}_2} \tag{3.2}$$

$$\mathrm{N}_2^i(^1\Sigma_g^+) + \mathrm{N}(^4\mathrm{S}_u) \longleftrightarrow 2\,\mathrm{N}(^4\mathrm{S}_u) + \mathrm{N}(^4\mathrm{S}_u) \qquad i \in \mathcal{I}_{\mathrm{N}_2} \tag{3.3}$$

$$\mathrm{N}_2^i(^1\Sigma_g^+) \longleftrightarrow 2\,\mathrm{N}(^4\mathrm{S}_u) \qquad i \in \mathcal{I}_{\mathrm{N}_2} \tag{3.4}$$

The collisional excitation transitions include the contribution of both inelastic (non-reactive) and exchange processes. The cross-sections for these reactions have been computed using the QCT method with an analytical PES that was fit to accurate quantum chemistry calculations for the $\mathrm{N}_2 - \mathrm{N}$ system. The NASA Ames database has been extensively used to study non-equilibrium kinetics of the population distribution in gases undergoing dissociation [51, 52, 53, 68, 71]. These results suggest that higher accuracy is required in the modeling of the distribution function of the low-lying states, while quasi-bound states can be adequately described using the energy-based grouping strategy discussed by Munafo *et al.* [173]. Consequently, only the bound states (the first 7,421 rovibrational levels) are considered in the present work. It is interesting to note that adaptive grouping relies on identifying only the most probable pathways for transitions. Thus, even if the current methodology is applied to low accuracy StS models which may ignore the less likely processes (due to limited number of trajectories during QCT simulations), the overall impact on the binning procedure and subsequently the dynamics of thermalization should be minimal.

3.2.1 State-to-State Solution

The exact population distribution for rovibrational levels of N_2 molecules requires solving $7,421$ coupled state-specific ODEs and an additional equation for the ground electronic state of N atoms. The volumetric composition of the initial mixture is 95% N_2 and 5% N. The internal states of N_2 are assumed to be in a Boltzmann distribution at $T_i = 2,000$ K and $P_i = 10,000$ Pa. Mass fraction and internal energy profiles are presented in Fig. 3.1 for the two values of the final reactor temperatures T_f being considered: $10,000$ K and $30,000$ K. In both cases, the initially cold N_2 molecules rapidly undergo excitation due to the sudden increase in translational temperature. For $T_f = 10,000$ K, the thermal relaxation process takes up to 10 μs and is completed without any significant changes to the composition of the reaction mixture. The onset of dissociation occurs only after $t = 5 \times 10^{-6}$ s, causing a drop in the total internal energy of the molecules. It should be noted that for this low temperature case internal energy relaxation and dissociation are distinct processes, barring a brief period of overlap from $t = 5 \times 10^{-6}$ s to $t = 10^{-5}$ s. On the other hand, internal excitation and dissociation take place simultaneously for $T_f = 30,000$ K, with no clear temporal separation between the two processes.

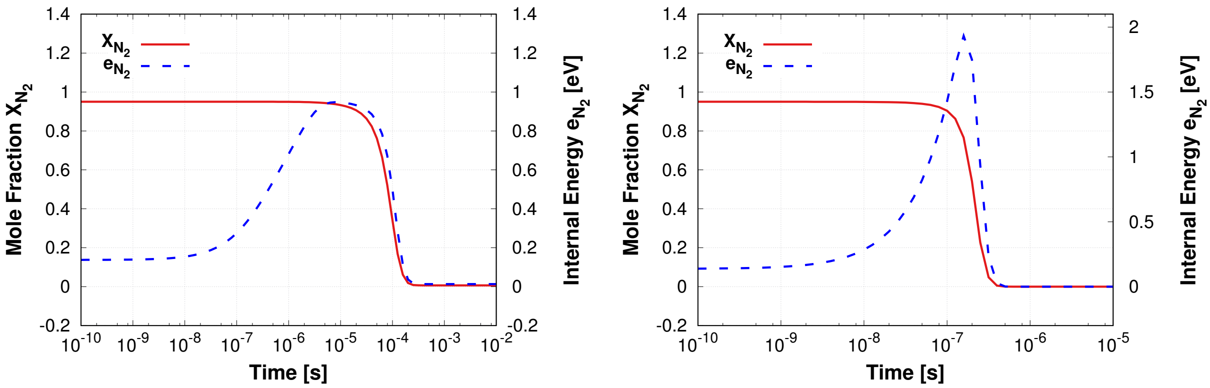

(a) $T_f = 10,000$ K

(b) $T_f = 30,000$ K

Figure 3.1: Evolution of total mole fraction and internal energy of N_2.

Figure 3.2 shows the population of different internal states of N_2 at $t = 3 \times 10^7$ s for $T_f = 10,000$ K. The relaxation process for the low-lying levels ($\epsilon_i < 5$ eV) appears to occur differently compared to the rest of the distribution. In the early stages of thermal relaxation, these levels form a fork-like structure consisting of multiple linear strands in a state of local equilibrium.

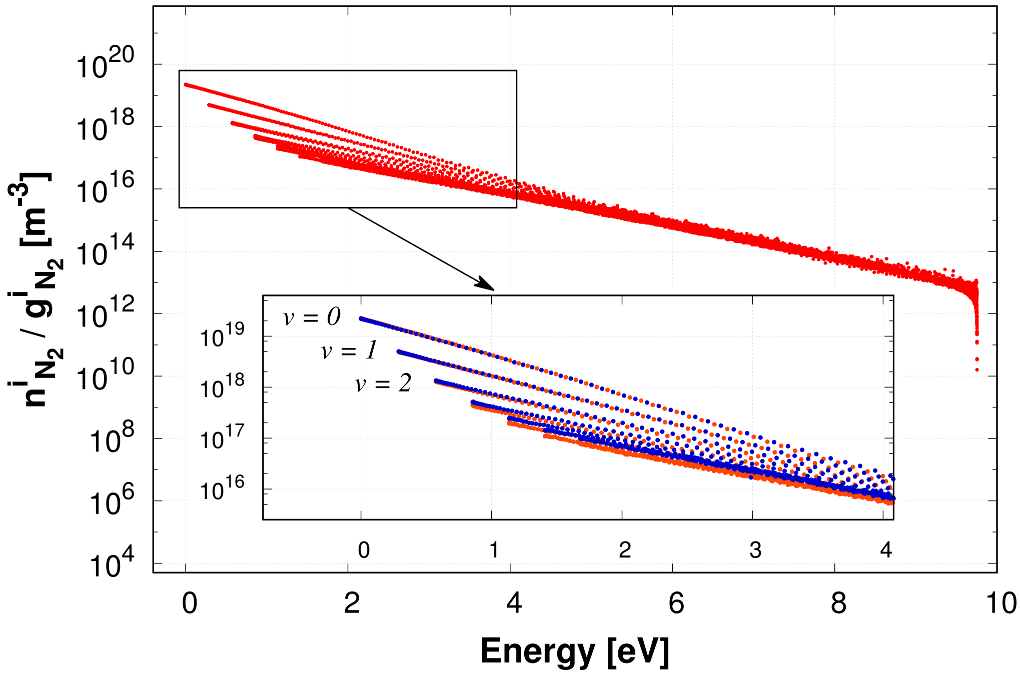

Figure 3.2: Population distribution of N_2 internal states at $t = 3 \times 10^{-7}$ s for $T_f = 10,000$ K. The inset figure magnifies the distinct fork-like structure formed in the region defined by internal energy less than 5 eV. Internal states with even and odd rotational quantum numbers are represented by orange and blue symbols, respectively.

Further analysis indicates that each strand is composed of states that have a common vibrational quantum number v, but different rotational quantum numbers J. Individual vibrational strands are further divided into sub-branches corresponding to states with even and odd rotational quantum numbers [67]. This complex multi-modal structure is magnified in Fig. 3.2, with even rotational quantum states represented by orange symbols and the odd rotational quantum states represented by blue symbols. The pseudo-Boltzmann distributions defining individual strands are characterized by different rotational temperatures, which appear to increase with v. This behavior is not observed in the tail of the population distribution. States in this region are characterized by larger values for rotational and vibrational quantum numbers which results in total rovibrational energy being dominated by higher-order non-linear terms [126]. Additionally, internal energy exchange at higher energies is more likely to occur through N_2 exchanging one of the bound nitrogen atoms with the colliding N rather than through a purely inelastic process [170]. This limits the process of preferential thermalization between the same vibrational levels. Consequently, different linear strands coalesce together into a narrow distribution as the rovibrational energy of the internal levels exceeds 5 eV, with no distinctive sub-branches for different v's and J's.

The biggest challenge in developing a macroscopic multi-bin model for N_2 is the ability to accurately resolve the behavior of this fork like structure at the lower end of the internal energy spectrum. A key feature of the microscopic population distribution in this region is that two states despite having similar energies but different vibrational quantum numbers can be in strong non-equilibrium with respect to each other. The same is true for states with the same vibrational quantum number but characterized by different parity for the rotational quantum numbers. Thus, a simple binning strategy that classifies states only on the basis of internal energy while ignoring state-to-state kinetics can no longer be expected to have sufficient fidelity for this problem.

3.2.2 Maximum Entropy Linear Bins

The accuracy of the multi-bin model for a given grouping strategy is contingent only upon the number of bins being employed and the form assumed for the group state distribution functions. Thus, reduced-order predictions can be improved either by increasing the number of bins or incorporating higher order terms in the piecewise representation of state population within a bin. The present work assumes a linear form for the reconstructed bin-wise state distribution functions. Therefore, the accuracy of MGME reduced-order models is adjusted only by changing the number of macroscopic groups or the grouping strategy. The current section compares results obtained for the $\mathrm{N_2}(^1\Sigma_\mathrm{g}^+) - \mathrm{N}(^4\mathrm{S_u})$ system using three binning methods:

i) The conventional strategy (referred to as *"energy bins"*) of dividing the internal energy space uniformly and assigning bins only on the basis of a given state's energy [68].

ii) Adaptive binning approach (referred to as *"island bins"*) that incorporates state-to-state kinetics of N_2 through the modified island algorithm outlined in Section 2.4.1. The threshold value for defining fast reactions is obtained by setting $\beta_\mathrm{I} = 0.8$ in Eq. (2.29).

iii) The third binning technique (referred to as *"spectral bins"*) which combines internal energy and state-to-state kinetics considerations using the spectral clustering method (Section 2.4.2). The strength of connection (Eq. (2.31)) between states is defined using $\beta_\mathrm{E} = 0.85$ and $\beta_\mathrm{K} = 2.35$. A value of $N = 10$ is used for determining the local scaling factor for state i in

Eq. (2.32). The 10 nearest neighbors of each state are considered while assembling the final sparse graph adjacency matrix $\boldsymbol{\mathcal{W}}$.

The aforementioned values of β_{I}, β_{E}, and β_{K} for the $\mathrm{N}_2\,(^1\Sigma_g^+)\;-\;\mathrm{N}\,(^4S_u)$ system are an outcome of parametric studies based on minimizing discrepancies between multi-bin models and the exact solution provided by StS calculations. More specifically, this choice of model parameters reduces errors associated with the state distribution function (Fig. 3.10), and total mole fraction (Fig. 3.5a) and internal energy (Fig. 3.5b) profiles. The variation in relative errors corresponding to global quantities and the state population distribution with respect to β_{K} and β_{E} for $T_f = T_{bin} = 10,000$ K is presented in Appendix A. Additionally, since the adaptive binning methodology relies on a knowledge of excitation/de-excitation rate coefficients to group internal states, an additional parameter T_{bin} has been introduced. The value of T_{bin} indicates the translational temperature at which state-specific kinetics rates are evaluated while performing binning. The solution of the master equations outlined in the previous section is labeled as the *"Full Set"* solution in all subsequent discussion. Results obtained by means of the reduced-order models are referred to using a combination of the number of bins used; the binning strategy adopted; and the temperature at which kinetics data was evaluated to construct the model. For example, "*20 Spectral Bins* - $T_{bin} = 10,000$ K" represents a reduced system with 20 macroscopic bins developed using the spectral clustering procedure performed at $10,000$ K. Similarly, "*20 Energy Bins*" describes a system with 20 macroscopic bins based on the conventional energy-based binning strategy.

A comparison between the time evolution of total mole fraction and internal energy of N_2, with $T_f = T_{bin} = 10,000$ K, predicted using different numbers of bins and binning strategies is presented in figures 3.3 and 3.4. Figure 3.3 clearly demonstrates that reduced-order models based on uniform energy bins are not able to accurately capture the dynamics of the global mole fraction of N_2 after the onset of dissociation. This discrepancy is not rectified simply by increasing the number of macroscopic bins, and reduced-order solutions appear to converge slowly to the exact solution. The adaptive bins based on the island method, despite incorporating information on preferential transition pathways into the grouping process, are also unable to overcome this problem. The use of the more sophisticated spectral clustering grouping technique alleviates these shortcomings and reduced-order solutions rapidly approach the full StS results as the number of bins is increased.

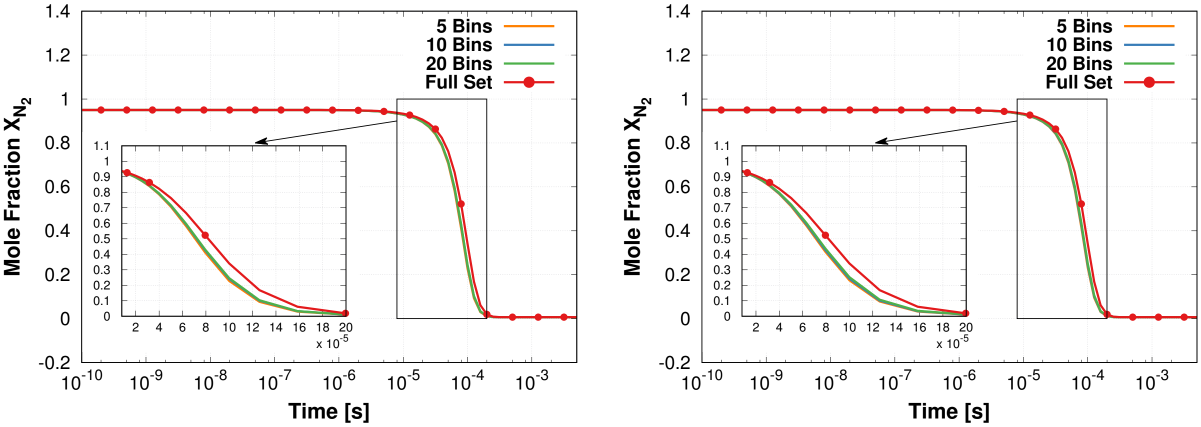

(a) Energy-based binning **(b)** Adaptive binning using island algorithm

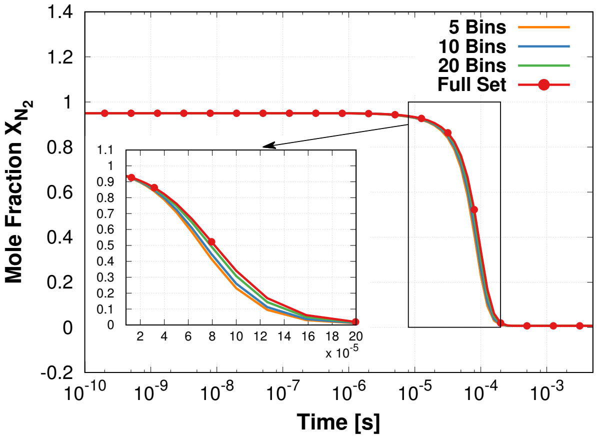

(c) Adaptive binning using spectral clustering

Figure 3.3: Time evolution of the total mole fraction of N_2 molecules for $T_f = 10,000$ K, predicted using different numbers of bins and binning strategies. Adaptive binning is performed at $T_{bin} = 10,000$ K.

This behavior is also observed in Fig. 3.5a which compares the relative error in predicted values of total mole fraction using 20 linear bins based on different grouping strategies and T_{bin} values. The maximum error is decreased by more than a factor of two when using spectral clustering. A similar analysis for the total internal energy of N_2 is presented in Fig. 3.4, with the corresponding error for reduced systems comprising of 20 linear bins shown in Fig. 3.5b. The reduced-order solution when using energy bins and the island algorithm diverges from the exact solution in two distinct time intervals – while the process of internal energy change is still ongoing and after the onset of dissociation. A switch to spectral clustering results in improved predictions with consistently lower errors at all time instances. Additionally, the accuracy of this technique appears to be relatively

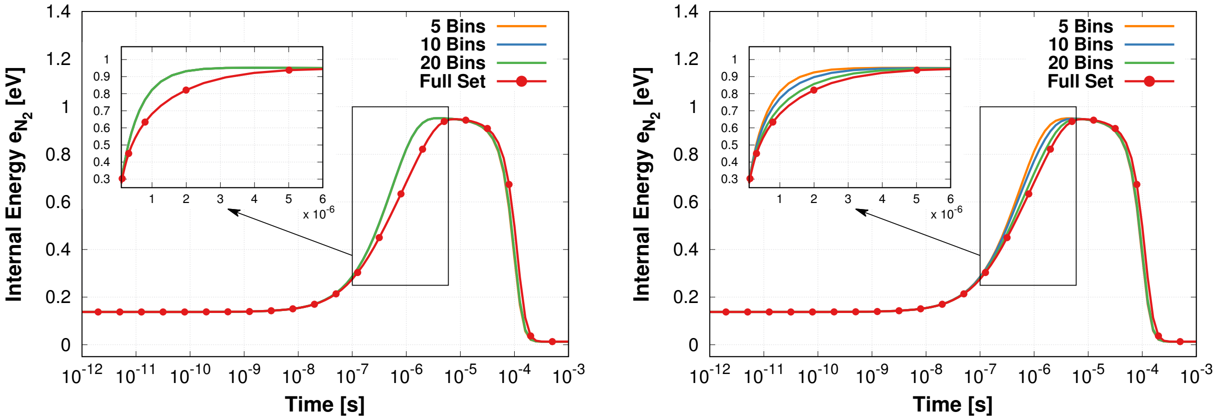

(a) Energy-based binning **(b)** Adaptive binning using island algorithm

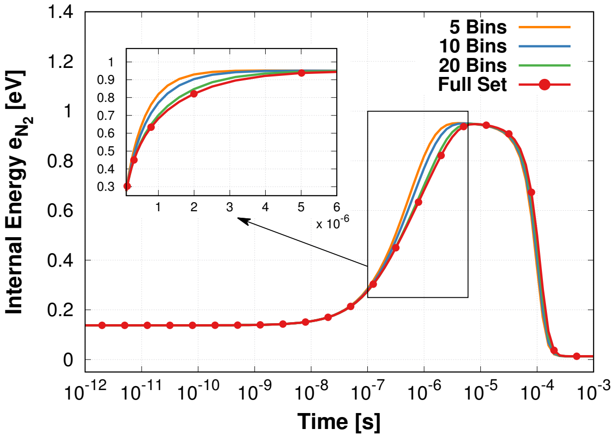

(c) Adaptive binning using spectral clustering

Figure 3.4: Time evolution of the total internal energy of N_2 molecules for $T_f = 10,000$ K, predicted using different numbers of bins and binning strategies. Adaptive binning is performed at $T_{bin} = 10,000$ K.

invariant with respect to changes in T_{bin}.

An important motivation for this study is to enable high fidelity predictions for the population distribution of individual energy levels using reduced-order modeling. The N_2 state population at different time instants obtained using 20 linear bins based on different binning strategies, with $T_f = T_{bin} = 10,000$ K, are compared with the full set solution in figures 3.6 and 3.7. Energy binning is well-suited for providing an averaged approximation for the actual distribution because the locally thermalized macroscopic bins are assumed to have no overlap in the energy space. This is an adequate representation when excitation processes depend only on the internal energy and not the quantum state of the molecule before and after collision. In such a regime, the rate

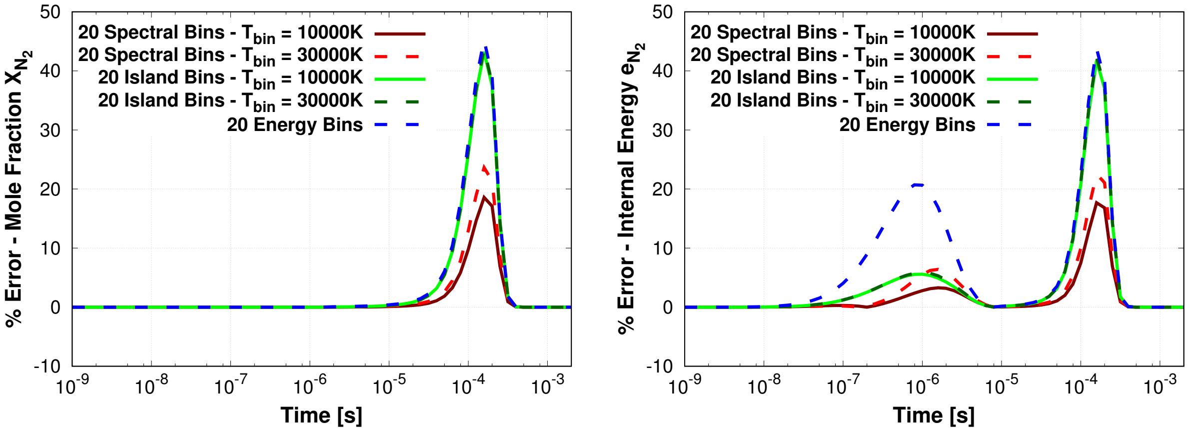

(a) Total Mole Fraction

(b) Total Internal Energy

Figure 3.5: Comparison of relative errors in predictions for global quantities with $T_f = 10,000$ K, obtained using 20 linear bins based on different binning strategies and T_{bin} values.

coefficients for reactions from a given level to other levels with similar energies (independent of their quantum configuration) are comparable. Consequently, the time-varying population of states with approximately the same energy are also similar. This behavior is observed at the upper end of the internal energy spectrum for N_2, resulting in a population distribution that has a smaller spread and no underlying structures. This lack of distinct features in the distribution function can easily be approximated using the averaged reconstruction provided by the energy bins. However, it is evident from figures 3.6 and 3.7 that as energy relaxation proceeds, the lower end of the population distribution eventually splits into a set of distinct overlapping linear strands characterized by a common vibrational quantum number and constant parity associated with the rotational quantum number. The energy bins cannot account for non-equilibrium between states with similar energies, since they are grouped into the same macroscopic bin and are described using a single Boltzmann distribution. Thus, the complex fork-like structure cannot be resolved using the non-overlapping energy binning approach. The inability to correctly model the lower energy part of the distribution results in significant errors while predicting macroscopic properties such as the total N_2 mole fraction and internal energy, as shown in Fig. 3.5.

The use of adaptive binning addresses this drawback by placing internal levels that are connected by fast transitions in the same bin. These preferential pathways for energy transfer ensure that the characteristic time for equilibration between strongly connected states is smaller. Therefore, both

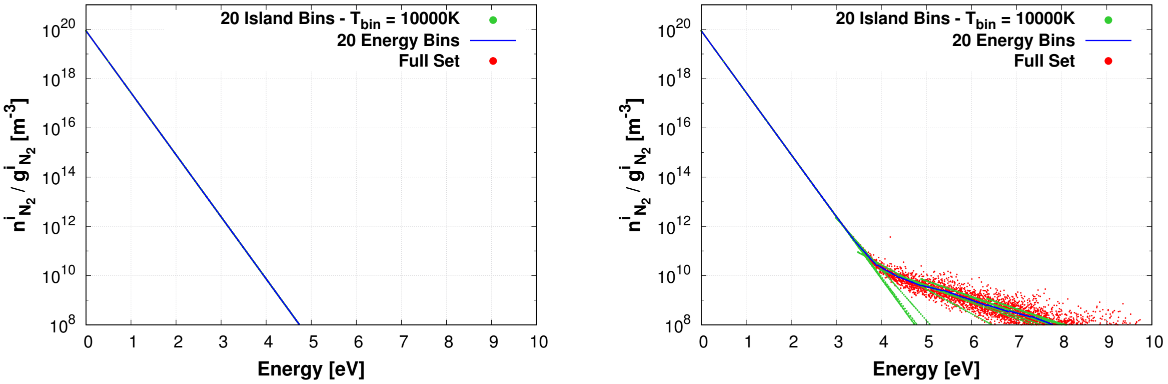

(a) $t = 0$ s **(b)** $t = 10^{-12}$ s

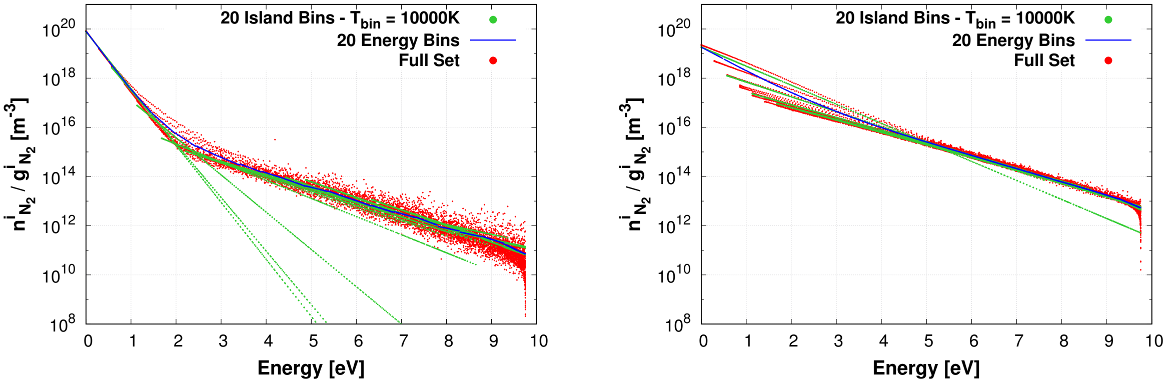

(c) $t = 10^{-8}$ s **(d)** $t = 3 \times 10^{-7}$ s

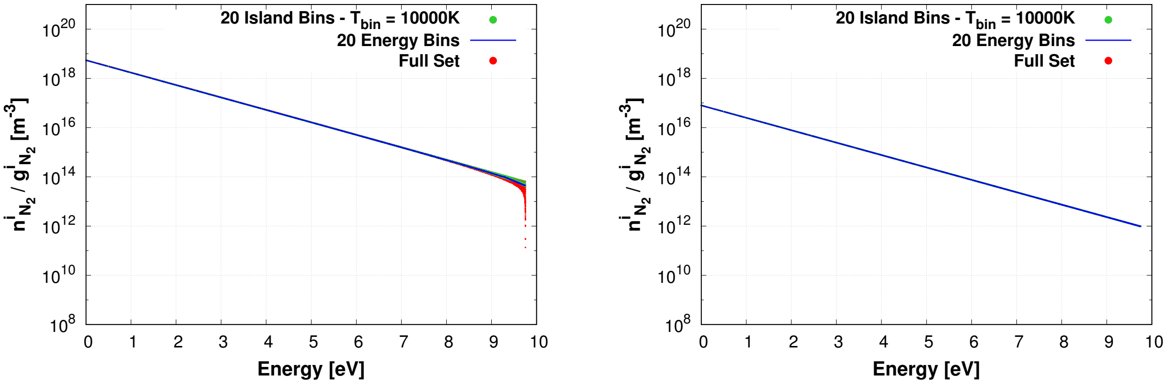

(e) $t = 3 \times 10^{-5}$ s **(f)** $t = 10^{-2}$ s

Figure 3.6: Comparison of time evolution of the N_2 rovibrational state distribution for $T_f = T_{bin} = 10,000$ K, predicted using 20 linear bins based on the modified island algorithm, 20 linear bins based on energy binning, and the full state-to-state model.

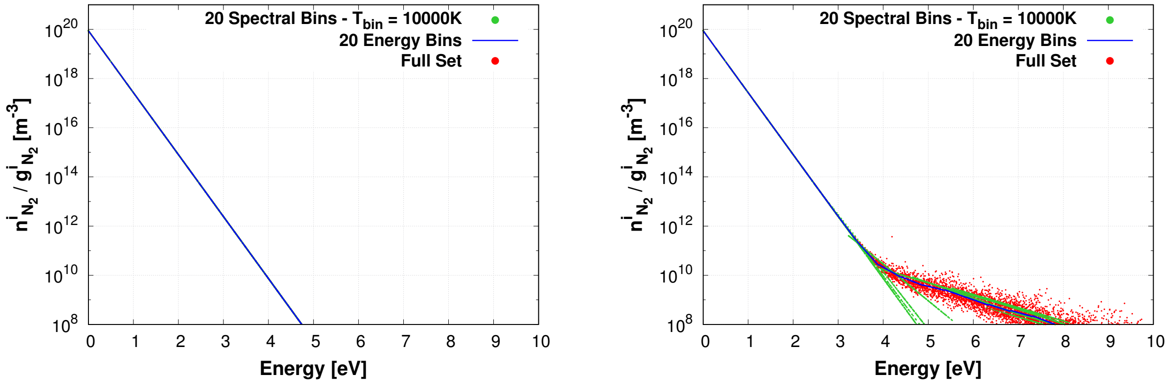

(a) $t = 0$ s **(b)** $t = 10^{-12}$ s

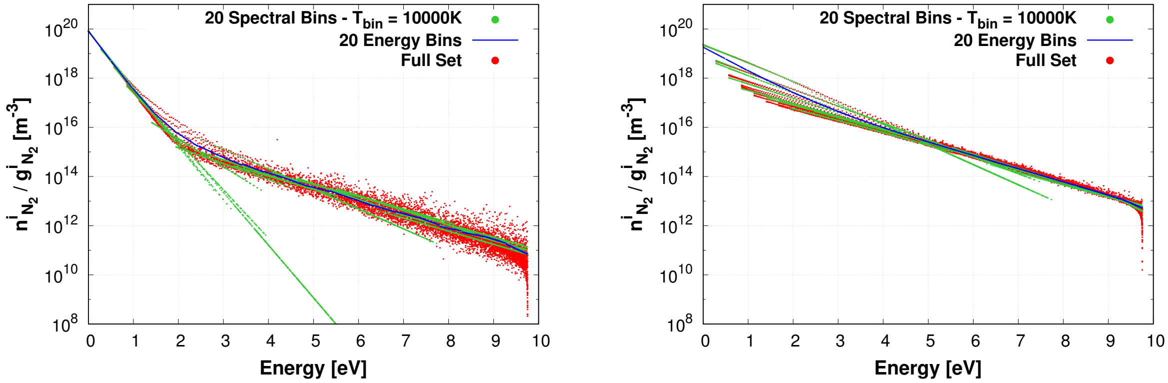

(c) $t = 10^{-8}$ s **(d)** $t = 3 \times 10^{-7}$ s

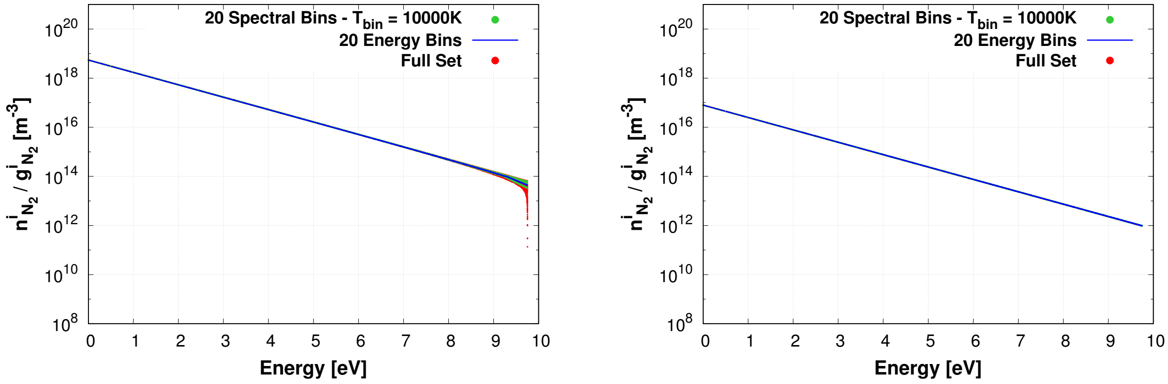

(e) $t = 3 \times 10^{-5}$ s **(f)** $t = 10^{-2}$ s

Figure 3.7: Comparison of time evolution of the N_2 rovibrational state distribution for $T_f = T_{bin} = 10,000$ K, predicted using 20 linear bins based on spectral clustering, 20 linear bins based on energy binning, and the full state-to-state model.

adaptive grouping strategies (island and spectral) yield far better predictions for both microscopic state population and the macroscopic properties. The overlapping fork-structure obtained due to selective local equilibration is correctly resolved through the reconstructed reduced-order solution. Small discrepancies in the population of the middle part of the distribution observed during the early stages of the relaxation process ($t < 10^{-8}$ s) are due to the choice of linear reconstruction within individual bins. Research is currently underway for including higher-order terms in the bin-wise state distribution function defined in Eq. (2.11). This would introduce curvature in the reconstructed microscopic state population distribution and allow a more accurate representation of the full state-to-state solution [125].

Figures 3.8 and 3.9 compare predictions made using the two adaptive binning algorithms – island method and spectral clustering – with those obtained through conventional energy-based binning and the full StS model. Although bins developed using the island algorithm predict the basic structure for the distribution function correctly, they are unable to accurately resolve individual linear strands populated by states with the same values for v and the parity associated with J. This problem is redressed by using spectral clustering which provides a superior description of the population densities for the low-lying levels. The improved accuracy accorded by this method is a direct outcome of the global, system-wide character of the underlying analysis driving the binning procedure. The spectral clustering method allows different networks of states that would equilibrate faster through a direct process, or more importantly through a series of intermediate transitions, to be mapped out for the entire system. In other words, each group is the result of a holistic analysis involving all possible transition mechanisms included in the StS model. The island algorithm on the other hand divides individual states into different bins based on a local, pairwise analysis that involves only states that are directly linked through fast processes. It is a recursive procedure that moves from state to state without analyzing the entire system as a whole. Also, in order to avoid infinite loops, the construction of each group is essentially sequential in nature. Any given state can be moved between bins only once and therefore, the bin index of a previously evaluated state cannot be updated based on the outcome of any subsequent analysis by the algorithm. This introduces a degree of directional biasing and results in sub-optimal reduced-order models. In order to better characterize the discrepancies between model predictions, the cumulative relative error

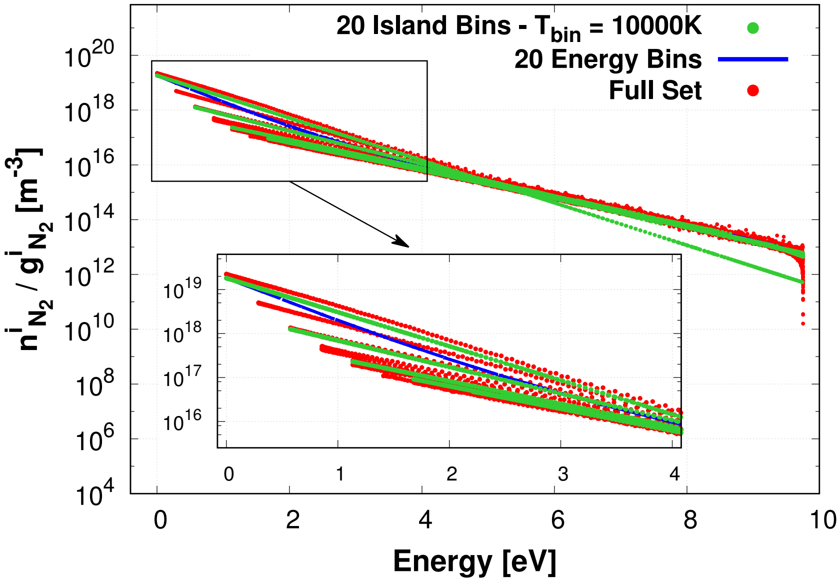

Figure 3.8: N_2 rovibrational state population, with $T_f = T_{bin} = 10,000$ K, for 20 linear bins based on the modified island algorithm, 20 linear bins based on energy binning, and the full state-to-state description at $t = 3 \times 10^{-7}$ s.

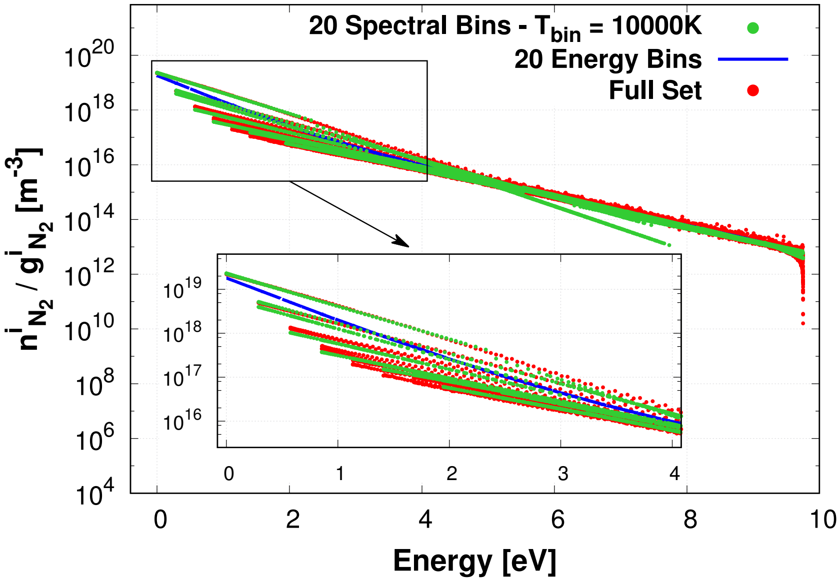

Figure 3.9: N_2 rovibrational state population, with $T_f = T_{bin} = 10,000$ K, for 20 linear bins based on spectral clustering, 20 linear bins based on energy binning, and the full state-to-state description at $t = 3 \times 10^{-7}$ s.

in state population distribution is presented in Fig. 3.10 (at $t = 3 \times 10^{-7}$ s) for different binning strategies. The least accurate prediction is obtained while using uniform energy bins, with the higher errors stemming from an inability to capture the overlapping linear strands in the lower part of the distribution. Results obtained using bins based on spectral clustering are significantly more accurate when compared to the conventional energy-based approach over the entire energy spectrum and independent of the choice of T_{bin}. Higher resolution solutions (albeit less accurate when compared to spectral clustering) are also obtained while employing the island algorithm. Although errors associated with island bins appear to be relatively invariant with respect to T_{bin}, numerical investigations indicate that this appears to be the case only for $T_{bin} \geq 10,000$ K when $T_f = 10,000$ K. The accuracy of reduced-order models developed using the island algorithm is rapidly degraded for $T_{bin} < 10,000$ K. This sudden drop in predictive capabilities is not observed for spectral clustering, leading to the conclusion that it is the most reliable technique for obtaining consistently accurate reduced-order models for varying values of T_f and T_{bin}.

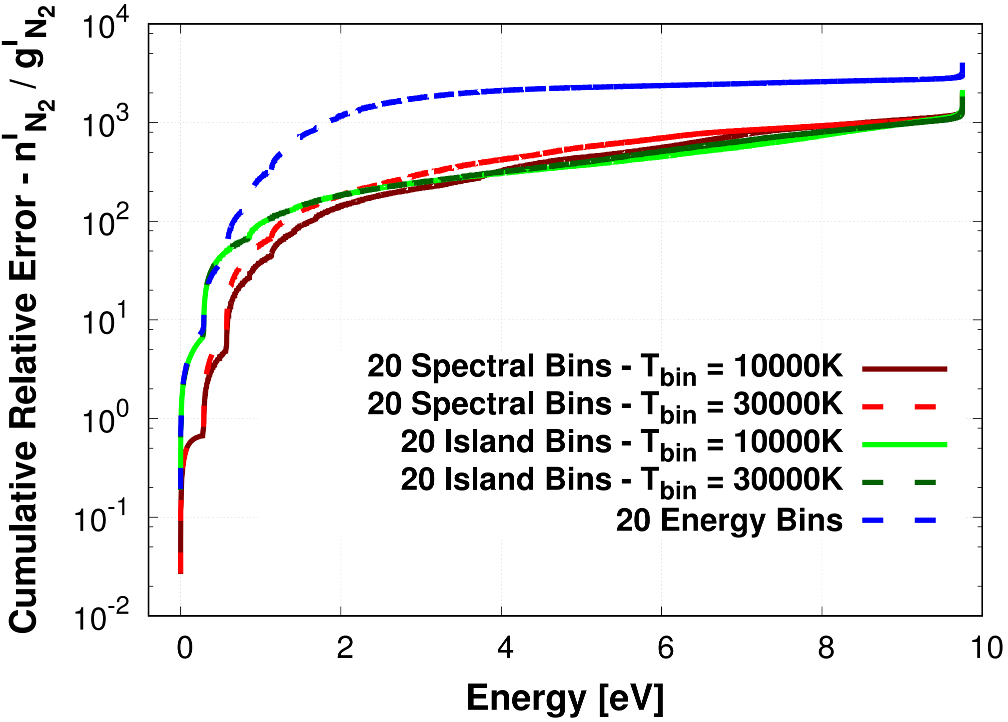

Figure 3.10: Comparison of cumulative relative error in predictions for N_2 rovibrational state population for $T_f = 10,000$ K, obtained using 20 linear bins based on different binning strategies and T_{bin} values at $t = 3 \times 10^{-7}$ s.

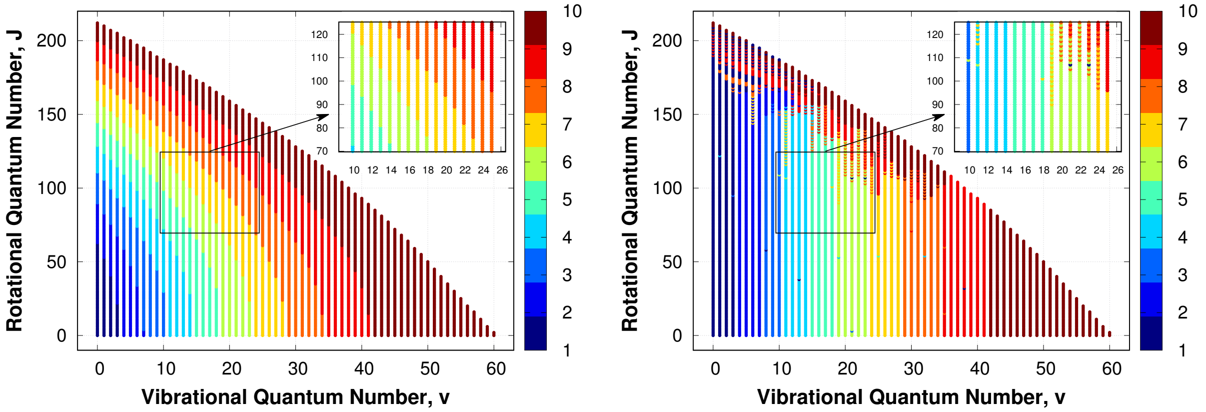

(a) Energy-based binning

(b) Adaptive binning using island algorithm

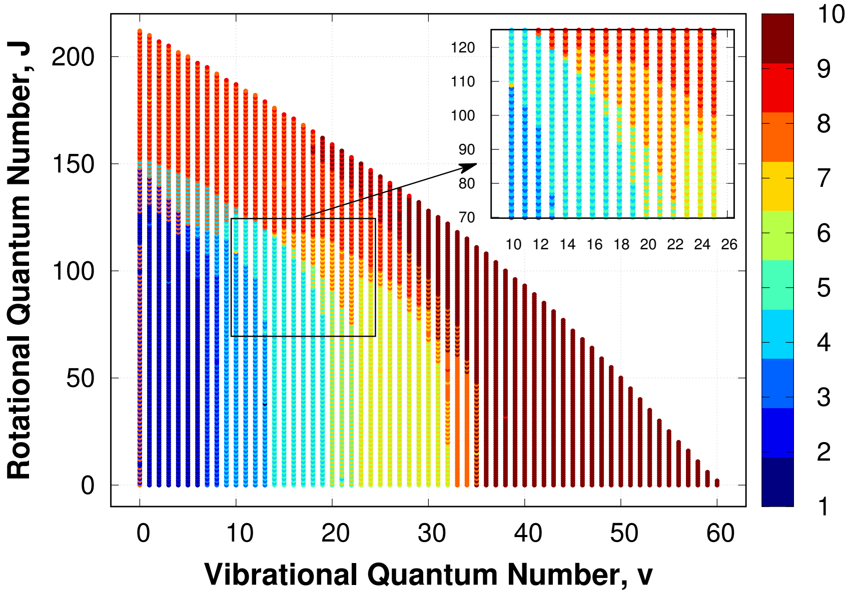

(c) Adaptive binning using spectral clustering

Figure 3.11: Quantum configuration of individual states clustered into different bins. The color map on the right represents the bin index for a reduce-order model comprising of 10 linear bins. Adaptive binning is performed at $T_{bin} = 10,000$ K.

Fig. 3.11 provides insight into the bin-wise distribution of states for various reduced-order models by plotting the vibrational and rotational quantum numbers for individual states in different bins. Energy-based binning, by disregarding kinetics information, is completely insensitive to the quantum configuration of a given state. This results in a monotonic increase in bin-index as energy of internal states (roughly represented by the distance from the origin in any given direction) increases. The modified island algorithm, on the other hand, tends to group together states with similar vibrational quantum numbers. Although this biasing results in a better resolution of the low-energy part of the distribution, it leads to significant errors in predictions for the population of high lying states. Energy-based binning appears to be a better model reduction strategy for this region where internal states appear to undergo relaxation independently of their rotational and vibrational states. The macroscopic bins developed using spectral clustering can be viewed as a convolution between reduced-order models based on energy binning and the island-algorithm. Consequently, lower energy states that are characterized by multi-modal relaxation defined using v and J are clustered in a manner similar to the island algorithm. The grouping for high lying states, where anharmonic effects result in a breakdown of the fork-like structure, appears to be dominated by energy considerations. This results in the quantum configuration of states in the higher bins being comparable to results from energy-based binning. An additional feature that is only resolved by spectral clustering is the stronger coupling between states with the same v and odd/even J. This behavior stems from non-exchange reactions with $\Delta v = 0$ and $\Delta J = 2n \,|\, n \in \{0, 1, 2, \ldots\}$ being favored. Consequently, the bin-index of states for a fixed value of v and increasing J appears to alternate only for spectral clustering in Fig. 3.11.

Numerical investigations assessing the accuracy of the proposed model reduction techniques have also been performed for $T_f = 30,000$ K. The corresponding figures detailing predictions for macroscopic properties and the state population distribution using different binning strategies have been included in Appendix A. Spectral clustering is a computationally intensive method due to the high costs associated with performing eigenvalue decomposition and the subsequent partitioning around medoids (PAM). The island algorithm is relatively cheaper, involving simple iterative reordering of internal states assigned between different bins. Therefore, reduced-order modeling derived using the island algorithm can provide an inexpensive, first-order accurate insight into the dynamics of large state-to-state (STS) systems. This is especially useful for applications that require the reduced-order model (and therefore, bin assignment for internal states) to be repeatedly recomputed on the fly in conjunction with other expensive simulations (*e.g.*, QCT).

3.3 $\mathbf{CO_2(X^1\sum_g^+)}$ – M System

The current non-equilibrium framework incorporates the vibrational state-to-state thermochemistry model developed by Kustova *et al*. [56, 140, 141]. Electronic excitation is neglected and only the ground electronic state $CO_2(X^1\sum_g^+)$ is considered. Carbon dioxide is a linear molecule and possesses four vibrational modes – one symmetric stretching mode, two degenerate bending modes, and one asymmetric stretching mode. The energy of individual CO_2 vibrational levels is described using the anharmonic oscillator expression [27]:

$$\begin{aligned} E_{v_1,v_2^l,v_3}\,/\,\mathrm{h_P}c \;=\;& \sum_{k=1}^{3}\omega_k\left(v_k+\frac{d_k}{2}\right)+\sum_{k=1}^{3}\sum_{j\geq k}^{3}\chi_{kj}\left(v_k+\frac{d_k}{2}\right)\left(v_j+\frac{d_j}{2}\right) \\ &+\sum_{k=1}^{3}\sum_{j\geq k}^{3}\sum_{i\geq j\geq k}^{3}y_{kji}\left(v_k+\frac{d_k}{2}\right)\left(v_j+\frac{d_j}{2}\right)\left(v_i+\frac{d_i}{2}\right)+\ldots \end{aligned} \qquad (3.5)$$

where $\mathrm{h_P}$ is the Planck constant, c is the speed of light, and indices i, j and k define parameters associated with the symmetric, bending, and asymmetric vibrational modes, respectively. Spectroscopic constants such as ω_k, χ_{kj}, and y_{kji} that appear in Eq. 3.5 are obtained from experimental data [174]. The vibrational quantum number and corresponding degeneracy for mode i are denoted by v_i and d_i, respectively. A simplified form of the anharmonic oscillator expression is employed which retains only the first three summation terms in Eq. (3.5) and neglects higher-order contributions. The existence of multiple vibrational modes allows states with otherwise distinctly different vibrational quantum numbers to have comparable energies which has a strong impact on the dynamics of the population distribution function. Furthermore, the carbon dioxide molecule is assumed to have no quasi-bound states, and vibrational energy is capped at the dissociation energy of $CO_2(X^1\sum_g^+)$ (5.52 eV). Thus, the maximum vibrational quantum numbers are 34, 67, and 20 for the symmetric stretching, bending, and asymmetric stretching modes, respectively, resulting in 9,056 vibrational levels.

The complex internal structure of the CO_2 molecule results in a rich set of disparate reaction mechanisms that shape vibrational relaxation. Quantum selection rules make inelastic interactions between the translational and symmetric/asymmetric modes less likely. Thus, vibrational-translational equilibration occurring through transitions involving only the bending mode while leaving the other two modes unchanged are considered:

$$\text{V-T}_2 \quad : \quad \text{CO}_2(v_1, v_2, v_3) \;+\; \text{M} \longleftrightarrow \text{CO}_2(v_1, v_2 \pm 1, v_3) + \text{M} \tag{3.6}$$

where M denotes the collision partner whose internal state remains unaltered during the reaction. The next category of collisional processes considered are inter-modal V-V$_{m-k}$ exchanges resulting in energy transfer between two or more vibrational modes:

$$\begin{aligned}
\text{V-V}_{1-2} \quad &: \quad \text{CO}_2(v_1, v_2, v_3) \;+\; \text{M} \longleftrightarrow \text{CO}_2(v_1 \pm 1, v_2 \mp 2, v_3) + \text{M} && (3.7)\\
\text{V-V}_{2-3} \quad &: \quad \text{CO}_2(v_1, v_2, v_3) \;+\; \text{M} \longleftrightarrow \text{CO}_2(v_1, v_2 \pm 3, v_3 \mp 1) + \text{M} && (3.8)\\
\text{V-V}_{1-2-3} \quad &: \quad \text{CO}_2(v_1, v_2, v_3) \;+\; \text{M} \longleftrightarrow \text{CO}_2(v_1 \pm 1, v_2 \pm 1, v_3 \mp 1) + \text{M} && (3.9)
\end{aligned}$$

Finally, state-specific dissociation/recombination reactions are also added to the kinetic scheme:

$$\text{Dissociation} \quad : \quad \text{CO}_2(v_1, v_2, v_3) \;+\; \text{M} \longleftrightarrow \text{CO} \;+\; \text{O} \;+\; \text{M} \tag{3.10}$$

A common bottleneck while developing CO_2 StS models is the paucity of state-specific rate data available in the open literature. Additionally, experimental data is only available for transitions between the lowest energy states. It is imperative that low energy experimental data be combined with existing theoretical models to yield a self-consistent StS chemistry database. Consequently, the hybrid approach propounded by Kustova and Nagnibeda [28, 140, 141] is used for computing rate coefficients for vibrational states of CO_2: a) rate coefficient data for transitions between the lowest vibrational states are obtained directly from experimental measurements [175], b) rate coefficients for higher states are calculated using SSH theory modified for polyatomic molecules [22]. Lastly, the global dissociation rate constant (legacy values outlined in [36, 176]) is unpacked into state-specific values using a generalized form of the Treanor – Marrone model [26].

3.3.1 State-to-State Solution

As outlined before, the full state-to-state model consists of different collisional transitions between $9,056$ vibrational energy states of the CO_2 molecule. The rotational energy mode of CO_2 is assumed to be in equilibrium with the translational mode, and characterized by the translational temperature T. Similary, the internal energies of the products of dissociation of CO_2: carbon monoxide CO and atomic oxygen O, are also considered to be in equilibrium at the translational temperature T. Thus, an exact description of CO_2 vibrational state-specific population requires solving a system of $9,058$ coupled ODEs.

Numerical simulations have been performed in an isochoric reactor to study CO_2 vibrational non-equilibrium under recombination conditions. The Arrhenius fits reported by Shevelev et al. [176] for CO_2 global dissociation rate-coefficients is used in this analysis. The initial hot mixture, at $T_i = 5,000$ K and $P_i = 5,000$ Pa, consists of equal mole fractions of CO and O (47.5 %) seeded with a small amount of CO_2 molecules (5 %). Then, the translational temperature is instantaneously brought down to $T_f = 1,500$ K. The parameters T_i, P_i, and T_f have been selected to represent flight conditions in the back shell region of a spacecraft during Martian atmospheric entry.

The temporal evolution of CO_2 vibrational state population under cooling is presented in Fig. 3.12. Starting from a Boltzmann distribution at T_i, the vibrational states require approximately 10^2 s to re-equilibrate at T_f. Population inversion is observed for states at the upper end of the energy spectrum due to recombination processes dominating internal energy exchange. This is also evident from the upper states quickly thermalizing at the final translational temperature T_f, while the rest of the population remains almost frozen at T_i. Eventually, starting from the lowest energy levels, the state population distribution starts equilibrating to its final value. The interplay between the recombination process and internal exchange processes produces a transient cloud of states in the middle of the energy spectrum that is in strong non-equilibrium. This region shifts towards higher vibrational energies with time, while correcting overpopulation in the upper levels.

The biggest challenge in developing reduced-order CO_2 models is accurately predicting the dynamics of this non-equilibrium region connecting equilibrated lower states and overpopulated upper levels. The comb-like structure of this section, consisting of multiple linear strands of states in local equilibrium, is highlighted in Figure 3.14. The current state-to-state collisional rate coefficient database limits transitions to mono-quantum jumps between states with specific sets of quantum numbers. This allows only a limited number of states to directly interact with each other. The

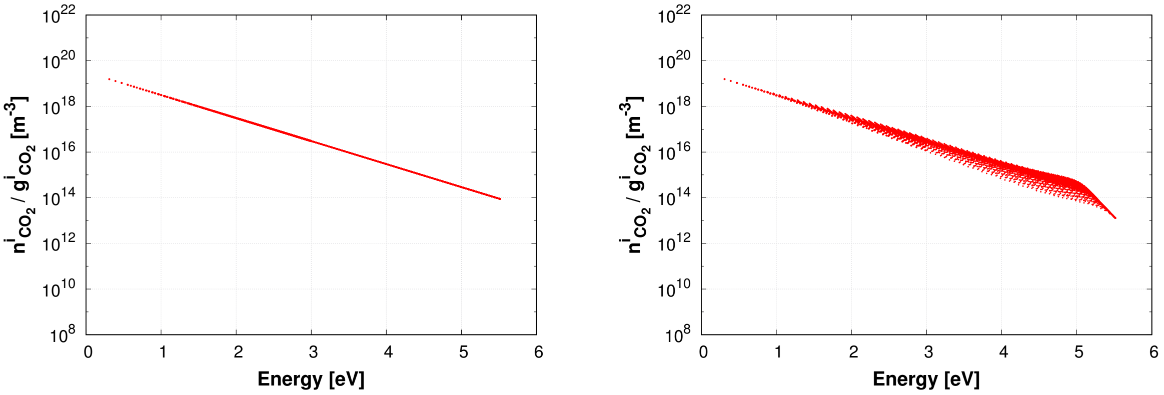

(a) $t = 0$ s

(b) $t = 10^{-8}$ s

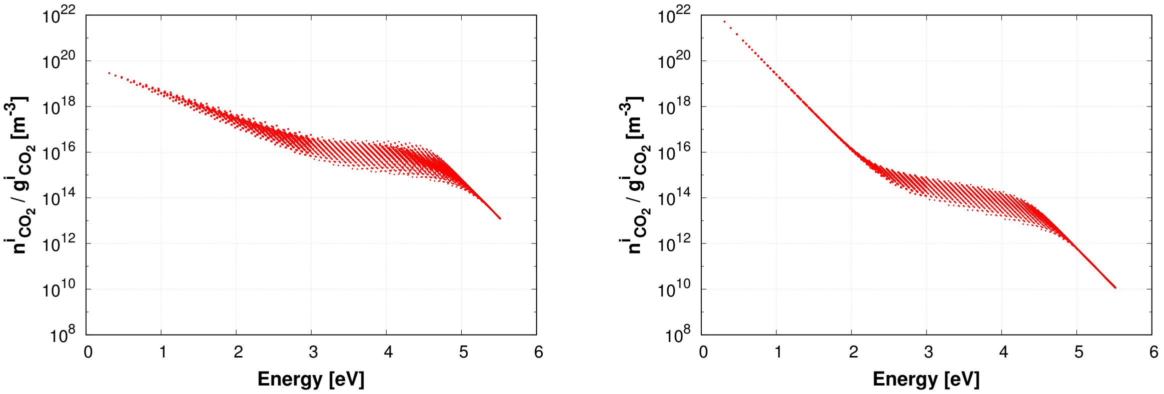

(c) $t = 10^{-6}$ s

(d) $t = 10^{-3}$ s

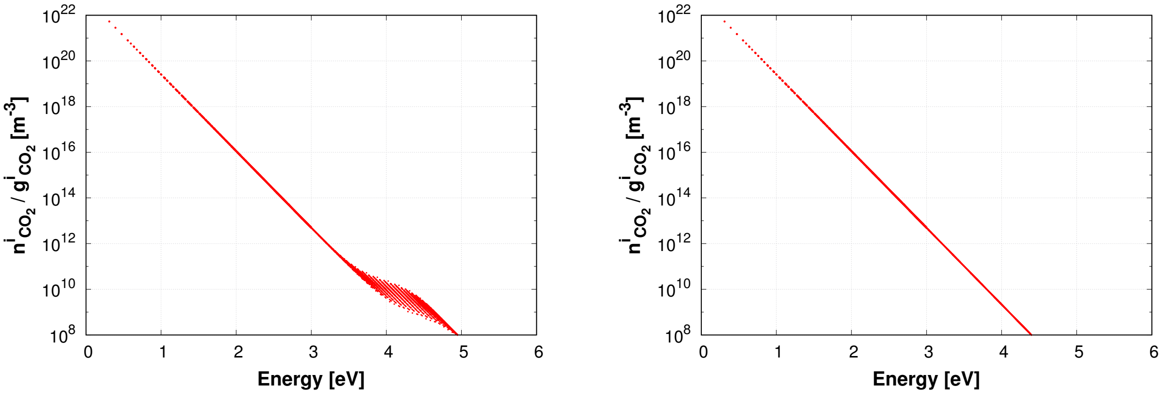

(e) $t = 10^{-1}$ s

(f) $t = 10^{3}$ s

Figure 3.12: Time-varying vibrational state population of CO_2 vibrational states computed using StS master equations.

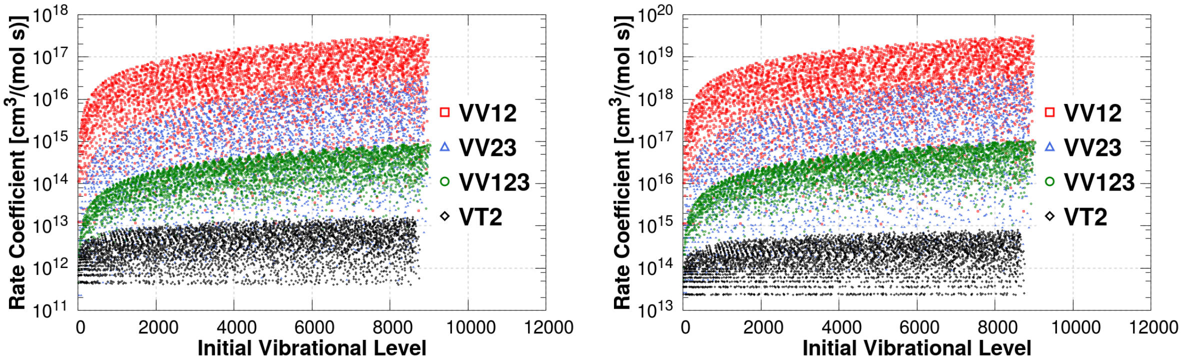

(a) $T = 1,500$ K **(b)** $T = 5,000$ K

Figure 3.13: Comparison of rate coefficients for inter-mode VV_{m-k} and vibrational-translational VT_2 excitation processes with $\mathrm{M} = \mathrm{CO}_2$.

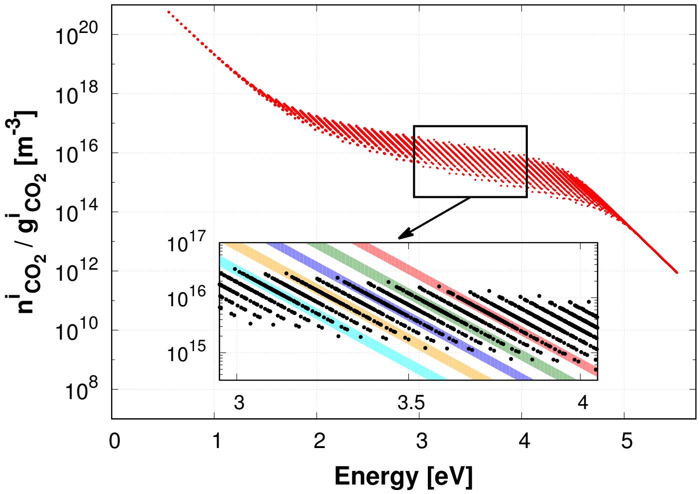

Figure 3.14: Population distribution of CO_2 vibrational states at $t = 10^{-4}$ s. The inset figure magnifies the distinct comb-like structure of the non-equilibrium region.

formation of this distinctive comb-structure and the overall process of reaching the final distribution via a transiting strong non-equilibrium region is an artifact of the limitations imposed by the current SSH-based description for chemical kinetics. Kustova and Nagnibeda [140] have reported that the characteristic times of various vibrational relaxation processes ($\mathrm{V}\text{-}\mathrm{T}_2$, $\mathrm{V}\text{-}\mathrm{V}_{1-2}$, $\mathrm{V}\text{-}\mathrm{V}_{2-3}$, $\mathrm{V}\text{-}\mathrm{V}_{1-2-3}$) can differ by multiple orders of magnitude. The rate coefficients for VV_{m-k} and VT_2 processes are evaluated for two temperatures relevant for Martian wake flows – $T = 1,500$ K and $T = 5,000$ K – in Fig. 3.13. The horizontal axis in Fig. 3.13 corresponds to the initial vibrational level v (global index based on sorting levels by increasing energy) for a given StS excitation process. It is evident that barring limited outliers, a clear separation exists between the bulk of VV_{m-k} and VT_2 processes. Rate coefficient values for both $1,500$ K and $5,000$ K suggest that the most probable excitation pathways in descending order are VV_{1-2}, VV_{2-3}, VV_{1-2-3}, and VT_2. This fact is reflected in the composition of individual linear strands from the non-equilibrium comb structure. A careful analysis of vibrational states occupying the same locally thermalized thread indicates that they are connected through either V-V_{1-2}, V-V_{2-3}, or V-V_{1-2-3} processes. A visual representation is provided in the inset of Fig. 3.14 where states enclosed within the same colored box have one or more VV_{m-k} transitions defined between them. It is also observed that states in two adjacent strands are connected through slower V-T_2 processes. Thus, a key feature of this unsteady population distribution is that two states despite having similar vibrational energies but completely different quantum numbers can be in non-equilibrium with respect to each other. Thus in the same vein as N_2, a simple binning strategy based on dividing the internal energy space uniformly can no longer be expected to accurately describe this system.

3.3.2 Maximum Entropy Linear Bins

Analyzing the full StS solution indicates that characteristic time-scales of inter-modal V-V_{m-k} exchanges and vibrational-translational relaxation V-T_2 follow the general trend:

$$\tau\,(\,\text{V-V}_{1-2}\,) \;<\; \tau\,(\,\text{V-V}_{2-3}\,) \;<\; \tau\,(\,\text{V-V}_{1-2-3}\,) \;\ll\; \tau\,(\,\text{V-T}_2\,) \tag{3.11}$$

This separation within the StS model renders the approximate classification for “fast” and “slow” processes based on log-averaging and β_I redundant. Instead, physically representative island binning can be more easily performed by identifying inter-modal V-V_{m-k} reactions as “fast” and the remaining V-T_2 transitions as “slow”. However, parametric studies indicate that an equivalent reduced-order system can also be obtained by setting $\beta_\text{I} = 0.31$ in Eq. 2.29, and then proceeding with the fast/slow mathematical categorization outlined in Section 2.4.1. The current state-specific chemistry model for $CO_2(X^1\sum_g^+)$ ($\sim 100,000$) consists of significantly fewer reactions compared to the $N_2 - N$ system ($\sim 2 \times 10^7$) due to it being based on mono-quantum SSH scaling relations rather than ab-initio QCT calculations. Furthermore, unlike N_2 only a limited number of CO_2 vibrational states are able to directly interact with each other. Thus, simple pair-wise recursive exploration through the island algorithm is sufficient for identifying clusters of states connected through rapid V-V$_{m-k}$ transitions. Reduced-order models based on the more computationally onerous spectral clustering do not improve accuracy and are not presented here.

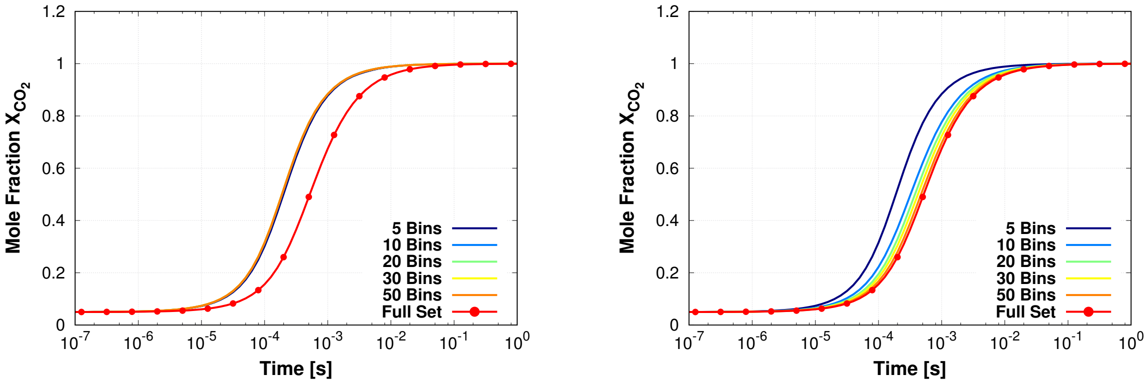

(a) Energy-based binning **(b)** Adaptive binning using island algorithm

Figure 3.15: Time evolution of the total mole fraction of CO_2 molecules for $T_f = 1,500$ K, predicted using different numbers of bins and binning strategies.

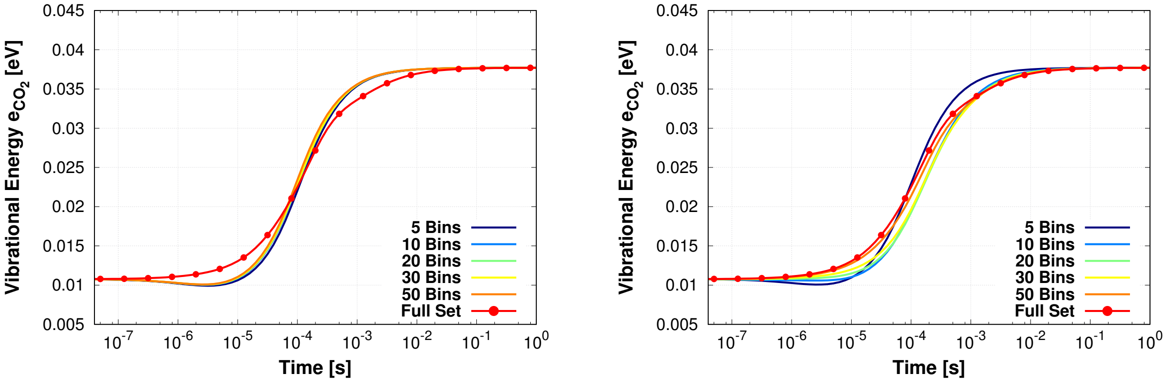

(a) Energy-based binning **(b)** Adaptive binning using island algorithm

Figure 3.16: Time evolution of the total vibrational energy of CO_2 molecules for $T_f = 1,500$ K, predicted using different numbers of bins and binning strategies.

The same nomenclature as Section 3.2.2 is used while comparing reduced-order results for energy-based binning (*"Energy Bins"*) and adaptive binning based on the island algorithm (*"Island*

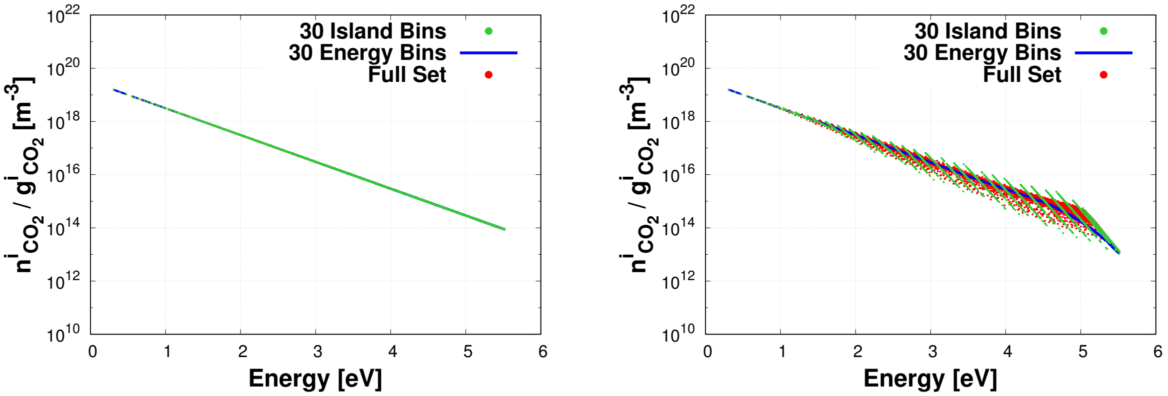

(a) $t = 0$ s

(b) $t = 10^{-8}$ s

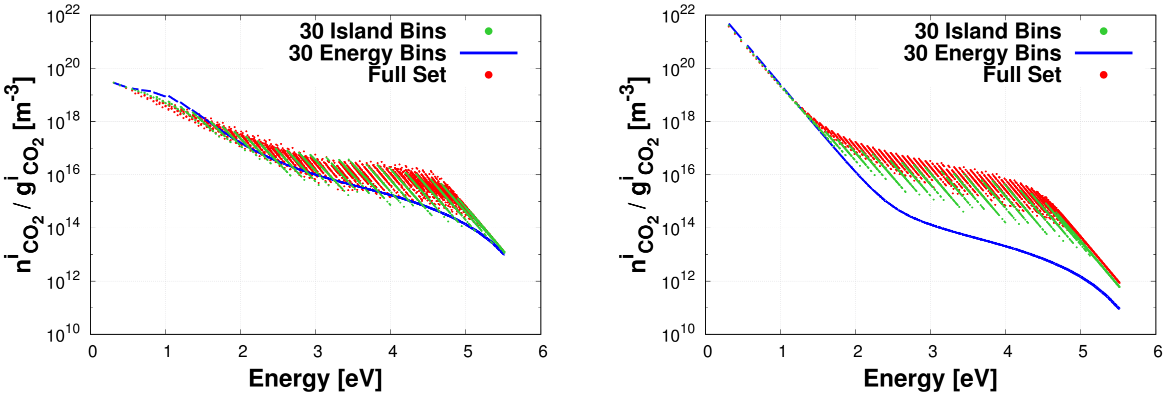

(c) $t = 10^{-6}$ s

(d) $t = 10^{-4}$ s

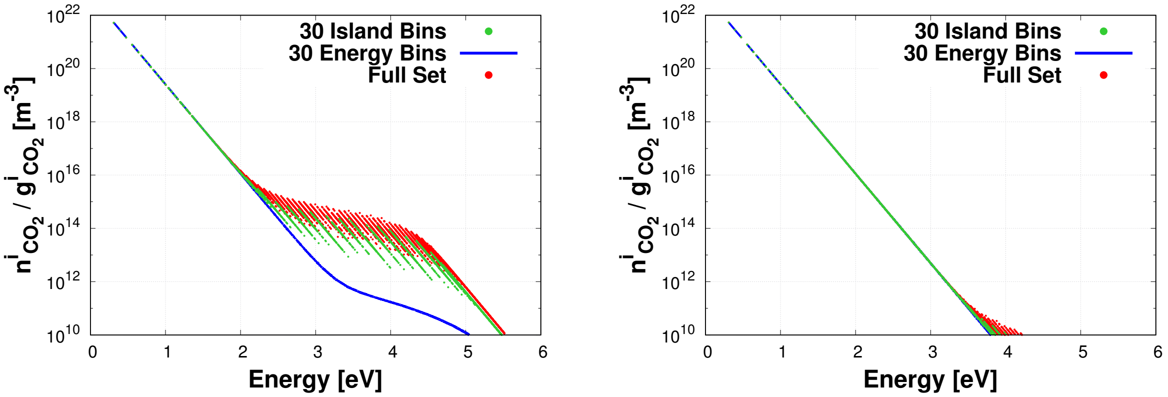

(e) $t = 10^{-3}$ s

(f) $t = 10^{-1}$ s

Figure 3.17: Comparison of time evolution of the CO_2 vibrational state distribution for $T_f = 1,500$ K, predicted using 30 linear bins based on the island algorithm, 30 linear bins based on energy binning, and the full state-to-state model

Bins") with the exact StS solution (*"Full Set"*). It should be noted that since fast/slow processes are defined on the basis of process type (V-V$_{m-k}$ / V-T$_2$), the definition for island bins remains invariant with respect to T_{bin}. Figure 3.15 compares the time-evolution of total mole-fraction of CO$_2$ computed using energy and island bins with the solution from StS master equations. A similar analysis is presented for the total vibrational energy of CO$_2$ molecules in Figure 3.16. Predictive capabilities with regards to these macroscopic quantities of MGME models based on the two binning strategies are starkly different. Energy bins converge slowly towards the exact value of CO$_2$ mole fraction and vibrational energy. This discrepancy is not rectified despite a significant increase in the total number of bins. On the other hand, macroscopic solutions obtained using only 10-30 island bins are in excellent agreement with the full-set simulation. Energy bins appear to start deviating from results obtained using StS modeling at 10^{-7} s. At this time instance, the population distribution breaks down into equilibrated low energy states, overpopulated upper levels, and a distinctive non-equilibrium region in the middle.

Figure 3.17 presents the CO$_2$ vibrational state populations at different time instances for 30 energy bins, 30 island bins and the full StS model. Energy bins, by disregarding StS kinetics, are unable to describe vibrational levels in a state of local equilibrium only when connected through fast transitions. This results in the reduced-order solution under-predicting the number density of upper energy states and over-predicting the lower levels. Consequently, the total vibrational energy of CO$_2$ appears to initially undershoot StS values (Figure 3.16a) while the contributions of higher levels is significant. The trend is reversed once recombination is initiated and the higher population of lower levels dominates total vibrational energy. These errors are minimized when switching to island bins because selective thermalization through efficient state-specific pathways can be reproduced even while using the MGME models [177]. The size and position of the transient non-equilibrium cloud are tracked using only 10-30 island bins. Equilibrium distribution is attained at a given energy value after the non-equilibirum region transits through it. This process of equilibration, beginning from the lower states, is also reflected in Figures 3.15b and 3.16b. The upper bins appear to reach equilibrium almost 10^{-2} s after the lower ones. Despite being a pronounced improvement over previous approaches, island bins predict slightly lower number densities for states in the transient non-equilibrium region and the thermalized over populated upper levels ($\epsilon^{v}_{\mathrm{CO}_2} > 1.5$ eV at $t = 10^{-4}$ s, $\epsilon^{v}_{\mathrm{CO_2}} > 2.5$ eV at $t = 10^{-3}$ s). This is a direct consequence of representing the numerous linear strands of the non-equilibrium comb structure with fewer bins. The concomitant error can be easily addressed by increasing the total number of bins in case a higher fidelity solution for that section of the vibrational energy spectrum is desired.

3.4 Summary

The efficacy of the MGME model reduction methodology with adaptive grouping has been investigated using a homogeneous isochoric chemical reactor with no spatial variation. Strong non-equilibrium conditions are induced by instantly changing reactor temperature. The ensuing time-varying evolution of the reaction mixture is studied using different reduced-order models and then compared to the exact StS solution. Two StS systems are considered in this chapter: $\mathrm{N_2}(^1\Sigma_\mathrm{g}^+) - \mathrm{N}(^4\mathrm{S_u})$ with rovibrational description of $\mathrm{N_2}$ and $\mathrm{CO_2}(\mathrm{X}^1\sum_\mathrm{g}^+) - \mathrm{M}$ with vibrational-specific description of $\mathrm{CO_2}$. The full StS solution for $\mathrm{N_2} - \mathrm{N}$ indicates that energy change between states with the same vibrational quantum number is favored, resulting in faster selective thermal equilibration. Consequently, the lower end of the state population distribution splits up into a fork-like structure, consisting of multiple linear strands that are in local equilibrium. Similarly, the unsteady $\mathrm{CO_2}$ vibrational state population distribution is a composite of disparate thermochemical dynamics: equilibrated lower levels, overpopulated upper levels, and a complex multi-strand structure in the middle. This multi-modal response under non-equilibrium is a consequence of localized thermalization through efficient V-V_{m-k} energy exchanges. MGME models derived using conventional energy-based binning cannot account for selective coupling between states due to highly probable transitions. Consequently, predictions made for the change in state population distribution and macroscopic properties do no match solutions of the StS master equations. Adaptive grouping overcomes these shortcomings by allowing the inherently different time-scales of state-specific kinetics to be reflected in choice of bins, *i.e.*, networks of states linked through faster processes constitute individual bins. This allows the dynamics of macroscopic quantities and internal state population distributions for both $\mathrm{N_2}$ and $\mathrm{CO_2}$ to be accurately reproduced using only 10-30 bins based on adaptive grouping.

Chapter 4

Solution Methods for Radiative Transfer Problems

Once thermochemical characteristics, *i.e.* chemical composition and internal state population distribution, shaped by collisional processes have been determined, the radiative environment around a spacecraft can be assessed. The computational methodology for resolving radiative transfer in participating media under non-equilibrium conditions is discussed in this chapter. A generalized three-dimensional radiative field is characterized by complex property variations in three separate domains: solid angle, physical space, and frequency. The complex domain of dependence renders solving such problems both theoretically challenging and computationally expensive. This chapter presents different numerical approaches based on discretizing angular, spatial, and spectral spaces while striking a balance between cost and accuracy. The solution procedure for radiation is built on two key components: a compound DOM-FV solver for the radiative transfer equations, and reduced-order wide-band spectral models for describing frequency-wise structures and their cumulative effects. The current chapter is organized as follows: a) Section 4.1 presents the governing equations for directed radiative transfer. b) Numerical methods for resolving angular and spatial components of three-dimensional radiation problems are discussed in Section 4.2. c) Different reduced-order wide-band approaches for lowering computational complexity in the frequency space are outlined in Section 4.3. d) Section 4.4 introduces a generalized grouping strategy for reduced-order spectral models that is applicable to non-equilibrium radiation problems. e) A brief summary of the current chapter is provided in Section 4.5.

4.1 Radiative Transfer Equation

The radiative field is assumed to instantaneously adjust to any changes in the flowfield in this analysis. This is a consequence of radiative transport occurring at time-scales (defined by the

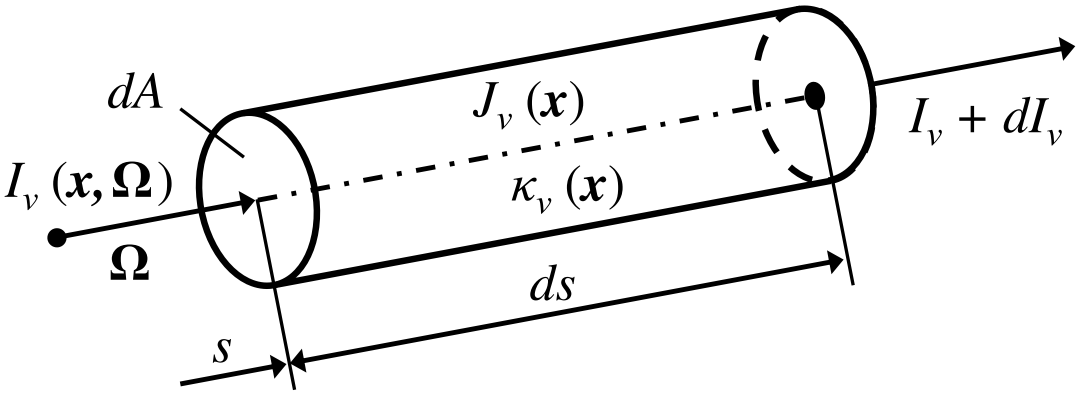

Figure 4.1: Radiative energy balance in a infinitesimal, emitting, absorbing cylinder along a single line-of-sight.

speed of light) which are much smaller than those for other hydrodynamic and chemical phenomena. The changes in steady radiative intensity are described by the radiative transfer equation (RTE) which is based on conservation of energy along a line-of-sight (LOS). Consider a beam of radiation defined by monochromatic intensity I_ν for frequency ν propagating in the direction $\mathbf{\Omega}$. Radiative energy through participating media is attenuated by absorption and scattering into other directions (out-scattering), and increases due to thermal emissions and incoming scattered energy from other directions (in-scattering). Scattering is an important consideration for particle-laden multi-phase flows [72] but can be ignored for the free-flight hypersonic applications discussed in the current work. Thus, energy balance on a differential volume element in the form of a cylinder with cross-section dA and length ds along direction $\mathbf{\Omega}$ results in:

$$\begin{aligned} \{I_\nu(\mathbf{x}+\mathbf{\Omega}\,ds,\mathbf{\Omega}) - I_\nu(\mathbf{x},\mathbf{\Omega})\}\,dA &= J_\nu(\mathbf{x})\,dA\,ds - \kappa_\nu(\mathbf{x})\,I_\nu(\mathbf{x},\mathbf{\Omega})\,dA\,ds \\ \Rightarrow \qquad dI_\nu \Big/ ds &= J_\nu(\mathbf{x}) - \kappa_\nu(\mathbf{x})\,I_\nu(\mathbf{x},\mathbf{\Omega}) \end{aligned} \tag{4.1}$$

where spectral opacity and emission values corresponding to ν are κ_ν and J_ν, respectively. The RTE can be viewed as a one-dimensional convection equation, with radiative intensity varying as a function of distance s along direction $\mathbf{\Omega}$. Equation 4.1 can be recast as a partial differential equation in the global cartesian reference frame which allows the computational grid for CFD simulations (and the same spatial discretization framework) to be reused for radiation calculations:

$$\boldsymbol{\Omega} \cdot \boldsymbol{\nabla}_{\boldsymbol{x}} \left\{ I_\nu(\mathbf{x}, \boldsymbol{\Omega}) \right\} \;=\; J_\nu(\mathbf{x}) \,-\, \kappa_\nu(\mathbf{x})\, I_\nu(\mathbf{x}, \boldsymbol{\Omega}) \tag{4.2}$$

A well-posed problem is obtained by prescribing the following boundary condition for domain-directed intensity at the walls of the spacecraft:

$$I_\nu \Big|_{\mathbf{S}_b} = J_\nu \,/\, \kappa_\nu \quad \text{if} \quad \Omega \cdot \mathbf{n}_b > 0 \tag{4.3}$$

where $\mathbf{n}_b$ is the unit vector normal to the boundary $\mathbf{S}_b$ and pointing into the domain. Similarly, the latent domain-directed radiative intensity at the cold farfield boundary is set to zero. The net heat flux at a given point in space is computed by integrating monochromatic intensity over the entire solid angle and frequency space:

$$\mathbf{q}_{\text{rad}} \;=\; \int_{\nu_i}^{\nu_f} \oint_{4\pi} I_\nu \, \boldsymbol{\Omega} \, d\Omega \, d\nu \tag{4.4}$$

The corresponding volumetric source term for energy addition due to net radiative flux through an infinitesimal element is obtained by applying the Green-Gauss theorem:

$$\Omega_{\text{rad}} \;:\; \qquad -\,\boldsymbol{\nabla}_{\boldsymbol{x}} \cdot \mathbf{q}_{\text{rad}} \;=\; -\,\boldsymbol{\nabla}_{\boldsymbol{x}} \cdot \int_{\nu_i}^{\nu_f} \oint_{4\pi} I_\nu \, \boldsymbol{\Omega} \, d\Omega \, d\nu \tag{4.5}$$

4.2 Angular and Spatial Solutions of RTE

The current section outlines the numerical approach for solving a system of RTEs (Eq. 4.2) to obtain angularly integrated, spatially resolved radiative heat flux corresponding to a given frequency ν. This aspect of radiation transport is completely detached from the way properties such as κ_ν and J_ν are modeled in the frequency space. The same solution procedure is used irrespective of the level of fidelity for spectral property models: LBL, narrow-band, wide-band, and grey-gas. The only differentiator is the number of complete angular-spatial evaluations required for computing spectrally integrated quantities $\mathbf{q}_{\text{rad}}$. This can range from a single complete calculation for grey-gas model to nearly $\mathcal{O}(10^6)$ calculations for the full LBL approach.

4.2.1 Angular Discretization

The integral over the complete solid angle in Eq. 4.4 transforms the LOS RTE into integro-differential equations. The discrete ordinate method (DOM) is an angular discretization procedure which circumvents this complication by solving the RTE only for a representative finite set of directions $\mathbf{\Omega}^m$. The underlying idea behind this is to approximate the original angular integral by a quadrature method based on a weighted sum of quantities computed for these discrete directions:

$$\mathbf{q}_{\text{rad}} = \int_{\nu_i}^{\nu_f} \oint_{4\pi} I_\nu \, \mathbf{\Omega} \, d\Omega = \int_{\nu_i}^{\nu_f} \sum_m w^m \, I_\nu^m \, \mathbf{\Omega}^m \, d\nu \tag{4.6}$$

The quadrature weight and radiative intensity associated with direction $\mathbf{\Omega}^m$ are denoted by w^m and I_λ^m. Quadrature schemes employed with DOM satisfy certain conditions pertaining to recovering the solid angle (or the area of a unit sphere) and symmetry:

$$\oint_{4\pi} d\Omega = \sum_m w^m = 4\pi \tag{4.7}$$

$$\oint_{4\pi} \mathbf{\Omega} \, d\Omega = \sum_m w^m \, \mathbf{\Omega}^m = 0 \tag{4.8}$$

A more exhaustive list of conditions for such schemes is presented in [178]. Efficient angular quadrature methods for radiative transfer have been the focus of extensive research [80]. Some notable developments in this regard are simple angular discretization based on constant latitude/longitude lines [179, 180], spherical rings arithmetic progression quadrature [181], piecewise quasilinear angular quadrature [182], and spherical symmetrical equal dividing quadrature [183]. Comparative studies [80, 178] suggest that Lebedev quadrature rules [184, 185] maximize accuracy for a fixed number of discrete directions while minimizing distortions due to ray effects and false scattering. These quadrature schemes have also been widely applied in fields as diverse as computational chemistry [186] and astrophysics [187]. Consequently, the current study uses Lebedev quadrature while defining the set of discrete directions for DOM. A detailed description for the process of calculating directions and corresponding weights by enforcing exact integration of polynomials upto a given order on a unit sphere can be found in [185].

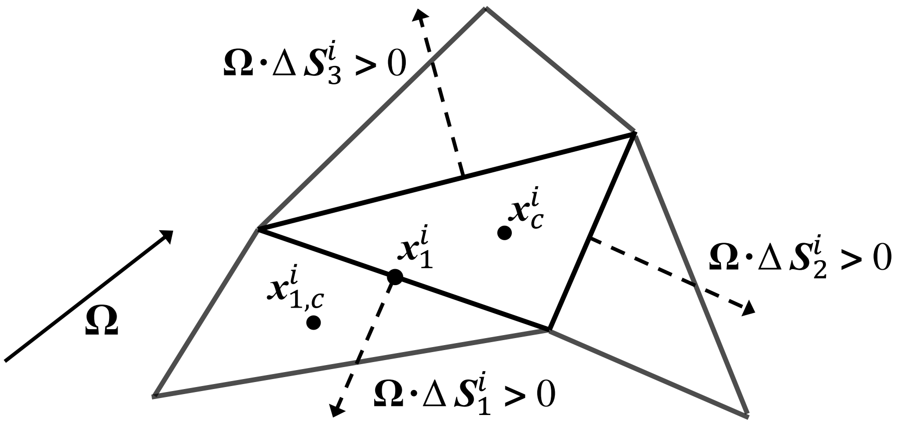

Figure 4.2: Computational cells for finite-volume discretization of RTE in $\mathbf{\Omega}$ direction.

4.2.2 Spatial Discretization

Angular discretization using DOM yields a system of RTEs for each of the discrete directions:

$$\mathbf{\Omega}^m \cdot \boldsymbol{\nabla}_{\boldsymbol{x}} \, \{I_\nu^m(\mathbf{x})\} \;=\; J_\nu(\mathbf{x}) - \kappa_\nu(\mathbf{x})\, I_\nu^m(\mathbf{x}) \,, \qquad I_\nu(\mathbf{x}, \mathbf{\Omega}^m) \,:\, I_\nu^m(\mathbf{x}) \tag{4.9}$$

Since, scattering is being ignored for hypersonic entry applications, radiative intensity in different directions remains decoupled and each of the m PDEs in Eq. 4.9 can be solved independently. As outlined in Section 1.2.2, spatial discretization of Eq. 4.9 can be done in a multitude of ways which includes finite difference techniques, finite element methods (FEM), and finite volume methods (FVM). The proposed unified non-equilibrium simulation methodology is aimed at interfacing with existing finite volume-based CFD solvers so that radiation and flowfield calculations can be performed in a loosely coupled manner. Therefore, in the interest of greater compatibility, a finite volume-based spatial discretization is adopted for resolving the RTE as well. It should be clarified that the current solution procedure [80, 188, 189] differs from some other approaches which disregard DOM and use finite volume discretization for both angular (solid angle element) and spatial (computational cell) domains [79, 190]. Equation 4.9 for direction $\mathbf{\Omega}^m$ and frequency ν is recast into the weak form by integration over the i^{th} computational cell (Fig. 4.2):

$$\int_{\mathbf{S}^\mathbf{i}} I_\nu^m \, \mathbf{\Omega}^m \cdot d\mathbf{S} \;=\; \int_{V^i} \left(J_\nu - \kappa_\nu I_\nu^m\right) dV \tag{4.10}$$

Standard finite volume simplifications are introduced by approximating volume integral as the product between the value at cell center ($\mathbf{x}_c^i$) and the cell volume (ΔV^i), and surface integral as the summation over faces of the product between the face-centered values (at $\mathbf{x}_k^i$) and the corresponding areas ($\Delta\mathbf{S}_k^i$):

$$\sum_k I_\nu(\mathbf{x}_k^i,\, \mathbf{\Omega}^m)\, \mathbf{\Omega}^m \cdot \Delta\mathbf{S}_k^i \;=\; \left\{ J_\nu(\mathbf{x}_c^i) - \kappa_\nu(\mathbf{x}_c^i)\, I_\nu(\mathbf{x}_c^i,\, \mathbf{\Omega}^m) \right\} \Delta V^i \tag{4.11}$$

The surface summation can be further split into incoming ($\mathbf{\Omega}^m \cdot \Delta\mathbf{S}_k^i < 0$) and outgoing ($\mathbf{\Omega}^m \cdot \Delta\mathbf{S}_k^i \geq 0$) components. A wide variety of flux reconstruction schemes (often with direct CFD analogues) have been used while solving the RTE using FVM. Some of the conventional approaches include step scheme (first-order upwinding), diamond scheme (central difference), and schemes based on exponential attenuation [189]. Several high-order schemes, originally developed for CFD, that have been applied to the problem of radiative transfer are reviewed in [191]. The more sophisticated schemes suffer from certain common drawbacks such as inability to guarantee bounded, positive radiative intensity solutions and degradation in accuracy for multi-dimensional problems. Consequently, the relatively simple step scheme which is positivity-preserving and ensures boundedness is used in the present work. First-order upwinding on the i^{th} computational cell results in outgoing radiative intensities at different face-centers being set equal to the appropriate cell-center value in the upstream direction:

$$I_\nu(\mathbf{x}_k^i,\, \mathbf{\Omega}^m) \;=\; \begin{cases} I_\nu(\mathbf{x}_{k,c}^i\,,\, \mathbf{\Omega}^m)\;, & \mathbf{\Omega}^m \cdot \Delta\mathbf{S}_k^i < 0 \\ I_\nu(\mathbf{x}_c^i,\, \mathbf{\Omega}^m)\;, & \text{otherwise} \end{cases} \tag{4.12}$$

where $I_\nu(\mathbf{x}_{k,c}^i,\, \mathbf{\Omega}^m)$ is the cell-center value for the neighboring computational cell across face k. Combining equations 4.11 and 4.12 allows $I_\nu(\mathbf{x}_c^i, \mathbf{\Omega}^m)$ to be expressed as:

$$I_\nu(\mathbf{x}_c^i,\, \mathbf{\Omega}^m) \;=\; \frac{\sum_{\forall k \,\ni\, \mathbf{\Omega}^m \cdot \Delta\mathbf{S}_k^i < 0} \; I_\nu(\mathbf{x}_{k,c}^i\,,\, \mathbf{\Omega}^m)\, |\mathbf{\Omega}^m \cdot \Delta\mathbf{S}_k^i| \,+\, J_\nu(\mathbf{x}_c^i)\, \Delta V^i}{\sum_{\forall k \,\ni\, \mathbf{\Omega}^m \cdot \Delta\mathbf{S}_k^i \geq 0} |\mathbf{\Omega}^m \cdot \Delta\mathbf{S}_k^i| \,+\, \kappa_\nu(\mathbf{x}_c^i)\, \Delta V^i} \tag{4.13}$$

where $|\,.\,|$ is the absolute value of a scalar. The incoming flux contribution in the numerator of Eq. 4.13 depends on intensity values in cells that are upstream with respect to direction $\mathbf{\Omega}^m$. The remaining terms constituting the right hand side can be evaluated using only the flowfield properties and the resultant emission/absorption behavior of the current cell centered at $\mathbf{x}_c^i$.

4.2.3 Mesh Reordering

Finite-volume discretization of the spatial domain based on Eq. 4.13 represents a sparse system of linear equations $\mathbf{A}^m \, \mathbf{I}_\nu^m = \mathbf{B}^m$ for radiative intensity corresponding to the m^{th} discrete direction. However, Eq. 4.13 can be evaluated explicitly at a given cell in case I_ν^m for all upstream neighboring cells have already been ascertained. In other words, the solution to RTE (a first-order convection equation) with upwinding is obtained by starting from a boundary surface and then marching along a discretized line-of-sight (or characteristic). This is akin to permuting the original system into a lower triangular system $\hat{\mathbf{A}}^m \, \hat{\mathbf{I}}_\nu^m = \hat{\mathbf{B}}^m$ (4.3) and then performing forward substitution. The sequence (referred to as the "advance-order list") in which computational cells are accessed while solving for radiative intensity in a given direction is determined using space-marching or mesh sweeping algorithms [192, 193]. Mesh sweep for direction $\boldsymbol{\Omega}^m$ starts from cells located at the edge of the computational domain. These cells have a boundary surface with an outward normal $\mathbf{n}_b \ni \boldsymbol{\Omega}^m \cdot \mathbf{n}_b < 0$. The remaining interior faces have an outward normal $\mathbf{n}_k^i \ni \boldsymbol{\Omega}^m \cdot \mathbf{n}_k^i > 0$, so that cell intensity can be uniquely determined only using the prescribed boundary conditions. The process continues along $\boldsymbol{\Omega}^m$, and interior cells are visited once all upstream cells, *i.e.*, cells adjacent to faces with $\boldsymbol{\Omega}^m \cdot \mathbf{n}_k^i < 0$, have been added to the advance-order list. Additional details on the algorithm can be found in Appendix B. This optimal marching order has to be computed and stored for all discrete directions being considered for DOM. A potential roadblock when performing sweeps on unstructured meshes is encountering regions of computational cells with circular dependencies.

$$\mathbf{A}^m = \begin{bmatrix} \blacksquare & & \blacksquare & & & \\ & \blacksquare & & & \blacksquare & \blacksquare \\ \blacksquare & & \blacksquare & & \blacksquare & \\ & \blacksquare & & \blacksquare & & \\ & \blacksquare & & & \blacksquare & \blacksquare \\ & & & \blacksquare & & \blacksquare \end{bmatrix} \qquad \hat{\mathbf{A}}^m = \begin{bmatrix} \blacksquare & & & & & \\ & \blacksquare & & & & \\ \blacksquare & \blacksquare & \blacksquare & & & \\ \blacksquare & & & \blacksquare & & \\ & \blacksquare & \blacksquare & & \blacksquare & \\ \blacksquare & & \blacksquare & \blacksquare & & \blacksquare \end{bmatrix}$$

(a) Original Mass Matrix **(b)** Permuted Mass Matrix

Figure 4.3: Permuting spatially discretized linear system using mesh sweeping algorithm.

This can result in an incomplete advance-order lists unless explicit measures are introduced for breaking out of such infinite loops. The current framework addresses the issue by first defining a threshold value ϵ^i for individual cells once a circular dependency is detected:

$$\epsilon^i \quad = \quad \alpha \min_k \left(\mathbf{\Omega}^m \cdot \Delta \mathbf{S}_k^i \right) \tag{4.14}$$

where α is a user-defined cut-off parameter. Subsequently, neighboring cells with $\mathbf{\Omega}^m \cdot \Delta \mathbf{S}_k^i > \epsilon^i$ are not considered to be in the upstream direction even if $\mathbf{\Omega}^m \cdot \Delta \mathbf{S}_k^i < 0$. The mesh sweep algorithm continues as before and the remainder of the advance-order list is assembled. The ϵ-based tie-breaker is only resorted to in case another infinite loop is discovered. An optimal marching sequence defined while adjusting for circular dependencies cannot accurately represent the spatial dependence of radiative intensity. This deficiency precludes a direct solution for I_ν^m and an iterative procedure is employed instead [194]. An artificially manipulated advance-order list can result in a computational cell being accessed before radiative intensity for all upstream cells have been updated in the current iteration. In such cases, solutions from the previous iteration for upstream neighbors are used when defining incoming fluxes. This process is comparable to the Gauss-Seidel method and allows converged, accurate values for I_ν^m to be computed even for complex meshes. A credible alternative to mesh sweeping could be the use of non-stationary iterative methods such as the generalized minimum residual (GMRES), generalized conjugate gradient (GCG), and generalized conjugate gradient least-squares (GCG-LS) methods, which are well-suited to solving large sparse linear systems [195]. These have been overlooked for the present work due to solver parameters for optimal convergence varying between problems [196] and high complexity of implementation [80].

The mesh sweeping process is demonstrated on a simple $5 \times 5 \times 5$ unstructured cube for different directions in Fig. 4.4. The sweep index is indicative of the relative dependence of radiative intensity for a given cell on other interior cell solutions. The sweep index value starts from one at the boundary cells, where intensity can be completely ascertained based on prescribed boundary conditions, and rises as one moves through the domain in the downstream direction. In order to ensure intensity can be explicitly evaluated (Eq. 4.13), computational cells are processed beginning with the lowest sweep index value to the highest.

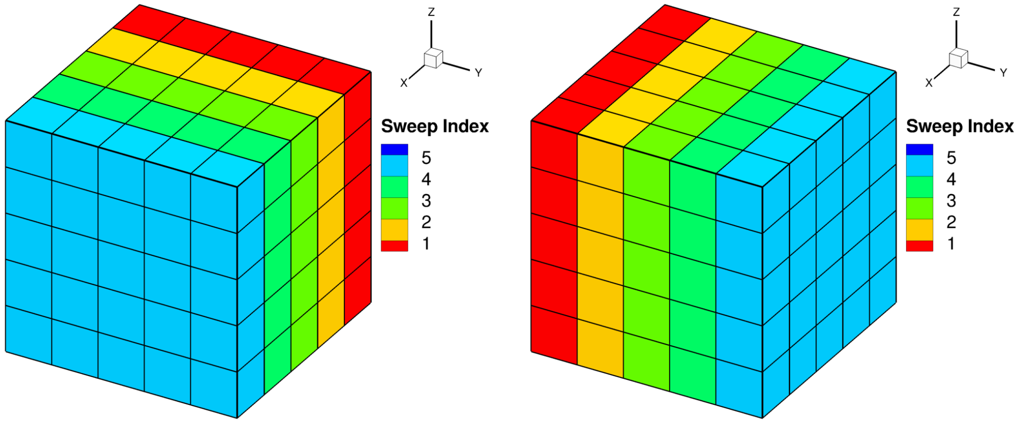

(a) Direction Cosines = $(1, 0, 0)$ **(b)** Direction Cosines = $(0, 1, 0)$

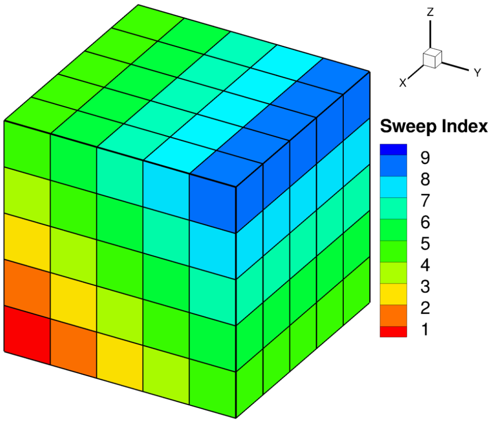

(c) Direction Cosines = $(0, 1/\sqrt{2}, 1/\sqrt{2})$

Figure 4.4: Mesh sweeping on a $5 \times 5 \times 5$ unstructured cube for different directions. A lower sweep index value implies less dependence on other interior cell solutions.

4.3 Reduced-order Spectral Models

The system of angularly-spatially resolved RTEs (equations 4.6 and 4.13) must be solved in its entirety for each discrete point included in a spectral property model. The fine spectral grid employed by LBL and narrow-band models results in nearly $10^4 - 10^6$ monochromatic transfer evaluations [104, 197]. Thus, despite offering high fidelity in the frequency space, their use for detailed flow-radiation coupled simulations of practical physical problems is unfeasible. The current section outlines three popular wide-band multi-group methodologies that attempt to reduce computational complexity (frequency-specific evaluations lowered to $\mathcal{O}(10^2)$) while offering good agreement with more detailed spectral databases. First, model reduction based on Planck-averaging [109, 198, 199] is presented along with an explanation based on the maximum entropy principle. Subsequently, statistics-based wide-band approaches, namely, the k-distribution method [11, 110] and theory of homogenization [111, 112] are summarized. The wide-band models outlined in the current work can be applied without modification to both LBL and narrow-band models. Spectral descriptions based on both LBL and narrow-band approaches are collectively referred to as *"full set models"* while only wide-band approaches are referred to as *"reduced-order models"*.

4.3.1 Planck-Averaging

A typical starting point for reduced-order methods involves defining larger groups that individual frequencies from a detailed spectral model can then be divided into. In order to better articulate the process of model reduction, groups are defined as simple non-overlapping intervals in frequency space [199]. The impact of more sophisticated grouping strategies is discussed later. The contributions of individual transitions constituting the i^{th} group ($\nu \in [\nu_i, \nu_{i+1}]$) can be integrated to obtain the governing equation for total group intensity $\hat{I}_i$ along direction $\mathbf{\Omega}$ (Eq. 4.2):

$$\begin{aligned} & \int_{\nu_i}^{\nu_{i+1}} \Big(\mathbf{\Omega} \cdot \nabla_{\boldsymbol{x}} I_\nu + \kappa_\nu I_\nu - J_\nu \Big)\, d\nu && = 0 \\ \Rightarrow \quad & \mathbf{\Omega} \cdot \nabla_{\boldsymbol{x}} \hat{I}_i + \hat{\kappa}_i \hat{I}_i - \hat{J}_i && = 0 \end{aligned} \tag{4.15}$$

where $\hat{\kappa}_i$ and $\hat{J}_i$ are the group-specific absorption coefficient and source term, respectively. The frequency-wise classification into groups remains invariant in physical space and therefore, the spectral integral in Eq. 4.15 has no angular/spatial dependence. The exact value of the group-wise source term is simply $\hat{J}_i = \int J_\nu \, d\nu$. However, the closure for group-wise absorption coefficient, $\hat{\kappa}_i = \int \kappa_\nu \, I_\nu \, d\nu \, / \int I_\nu \, d\nu$, requires the spectral solution I_ν. Setting I_ν equal to the Planck blackbody intensity yields reduced-order models based on Planck mean opacity. Turpault [89, 90] provides a reinterpretation of Planck-averaging based on a maximum entropy closure of the angularly-spectrally integrated RTE. The resultant M-1 reduced-order framework is built around piece-wise reconstruction of radiative intensity in the angular and spectral domains using polynomials that satisfy the maximum entropy principle. The governing equations for group-wise properties (and reconstruction coefficients) are derived based on moments of the RTE. The current work already utilizes the DOM method to capture angular dependence. Thus, the approach outlined in [89] can be simplified to account only for spectral variation in intensities. The starting point for reformulating Planck-averaging using the maximum entropy principle is the definition of entropy associated with a stream of photons [200, 201] at frequency ν and monochromatic intensity I_ν:

$$s\,(I_\nu, \nu) \;=\; \frac{2\,\mathrm{k_B}\,\nu^2}{\mathrm{c}^3}\left[(n_{I_\nu}+1)\log(n_{I_\nu}+1) \,-\, (n_{I_\nu})\log(n_{I_\nu})\right]\;, \quad n_{I_\nu} = \frac{\mathrm{c}^2}{2\,\mathrm{h_P}\,\nu^3}\,I_\nu \tag{4.16}$$

The total entropy of the i^{th} group is maximized while satisfying a single constraint based on group bin intensity $\hat{I}_i$:

$$\max_{I_\nu} S_i \;=\; \int\limits_{\nu_i}^{\nu_{i+1}} s\,(I_\nu,\nu)\,d\nu\;, \qquad \text{with} \int\limits_{\nu_i}^{\nu_{i+1}} I_\nu\,d\nu \;=\; \hat{I}_i \tag{4.17}$$

The modified objective function, $\hat{S}_i = S_i \,+\, \alpha_i\left(\int I_\nu\,d\nu \,-\, \hat{I}_i\right)$, is maximized using the method of Lagrange multipliers [202]:

$$\begin{aligned}
\left(\partial\hat{S}_i \Big/ \partial I_\nu\right)_\nu &= 0 \\
\Rightarrow\;\; \tfrac{2\,\mathrm{k_B}\,\nu^2}{\mathrm{c}^3}\left[\,n'_{I_\nu}\,\ln(n_{I_\nu}+1) \,-\, (n'_{I_\nu})\,\ln(n_{I_\nu})\,\right] \,+\, \alpha_i &= 0\,, \quad n'_{I_\nu} \;=\; \left(\partial n_{I_\nu} \Big/ \partial I_\nu\right)_\nu \\
\Rightarrow\;\; \tfrac{2\,\mathrm{k_B}\,\nu^2}{\mathrm{c}^3}\,n'_{I_\nu}\,\ln(1+1/n_{I_\nu}) \,+\, \alpha_i &= 0
\end{aligned} \tag{4.18}$$

Equation 4.18 can be further simplified by substituting $n'_{I_\nu} = \mathrm{c}^2/\left(2\,\mathrm{h_P}\,\nu^3\right)$:

$$\begin{aligned}
0 &= \frac{\mathrm{k_B}}{\mathrm{h_P}\,\nu\,\mathrm{c}}\,\ln(1+1/n_{I_\nu}) \,+\, \alpha_i \\
\Rightarrow\;\; (1+1/n_{I_\nu}) &= \exp\left(\frac{-\alpha_i\,\mathrm{h_P}\,\nu\,\mathrm{c}}{\mathrm{k_B}}\right) \\
\Rightarrow\;\; n_{I_\nu} &= \left\{\exp\left(\frac{-\alpha_i\,\mathrm{h_P}\,\nu\,\mathrm{c}}{\mathrm{k_B}}\right) \,-\, 1\right\}^{-1} \\
\Rightarrow\;\; I_\nu &= \frac{2\,\mathrm{h_P}\,\nu^3}{\mathrm{c}^2}\left\{\exp\left(\frac{-\alpha_i\,\mathrm{h_P}\,\nu\,c}{\mathrm{k_B}}\right) \,-\, 1\right\}^{-1}
\end{aligned} \tag{4.19}$$

Eq. 4.19 can be recast into the more familiar Planck intensity form by defining an equivalent blackbody temperature $T^{i}_{\mathrm{rad}} = -1/(\alpha_i\, \mathrm{c})$ [203]:

$$I_\nu \;=\; \frac{2\,\mathrm{h_P}\,\nu^3}{\mathrm{c}^2}\left[\exp\left(\frac{\mathrm{h_P}\,\nu\,\mathrm{c}}{\mathrm{k_B}\,T^{i}_{\mathrm{rad}}}\right)\;-\;1\right]^{-1} \;=\; I^{B}_{\nu}\,\left(T^{i}_{\mathrm{rad}}\right) \tag{4.20}$$

where $I^{B}_{\nu}\left(T^{i}_{\mathrm{rad}}\right)$ is simply the Planck blackbody intensity evaluated at T^{i}_{rad} for frequency ν. Group-wise T^{i}_{rad} can be obtained by inverting the non-linear relationship: $\int I^{B}_{\nu}\,\left(T^{i}_{\mathrm{rad}}\right) d\nu \;=\; \hat{I}_i$. The current work employs sub-iterations based on Picard's method to get converged radiative properties along a given line-of-sight. As a first approximation, T_{rad} can be set equal to the relevant flowfield temperature which simply yields the conventional Planck-averaging approach.

Multi-group Planck-averaging can now be viewed as group-wise (groups defined using frequency intervals or other strategies) reconstruction using a constrained maximum entropy distribution function. This interpretation follows the development of the MGME model for optimal reduced-order representation of unsteady thermochemical non-equilibrium presented in Section 2.3. Consequently, the reduced-order governing equation Eq. 4.15 is obtained by taking the zeroth-order moment of the original full set equations (Eq. 4.2) and integrating over the requisite frequency interval. Analogous to CFD methods and MGME modeling, the accuracy of the resultant reduced-order solutions can be improved either by increasing the number of groups (h-refinement) or by increasing the order of reconstruction (p-refinement). It should be noted that a single constraint of the form outlined in Eq. 4.17 suffices because only a zeroth-order reconstruction in frequency space is being sought. Raising the order of reconstruction would introduce additional group-wise coefficients and require supplementary constraints based on higher moments. Similarly, the possible inclusion of variation in the angular domain (as done in M-1 models) would necessitate integrating Eq. 4.17 over the complete solid angle, with moments (for deriving constraints or governing equations) computed with respect to the direction vector $\boldsymbol{\Omega}$.

4.3.2 Statistics-based Techniques

Reduced-order models developed using Planck-averaging prescribe a certain form for the spectral intensity while deriving group-wise closure relationships. Statistics-based wide-band reduced-order models attempt to eliminate this assumption and rely on capturing spectral variance through the use of probability distributions. Two such methods that are based on similar principles are considered: k-distribution and theory of homogenization. It should be noted that the current study is primarily focused on the use of Planck-averaging for reduced-order spectral modeling. The statistics-based techniques are employed only for comparative analysis. Thus, in the interest of completeness, only a brief review of these techniques is provided.

4.3.2.1 *k*-Distribution

The rapidly varying absorption coefficient is reordered into a monotonically increasing function over narrow-bands, frequency groups (part spectrum) or full spectrum in the k-distribution method [11, 204, 205]. It has been previously applied to model various non-equilibrium atomic and molecular radiation problems [110, 206]. Under non-equilibrium conditions, the Planck blackbody intensity appearing in the original LTE formulation is replaced by the non-equilibrium emission intensity $I_\nu^{\text{neq}} = J_\nu / \kappa_\nu$. Equation 4.1 is sorted into a k-distribution (in the opacity space) by multiplication with the Dirac-delta function $\delta(k - \kappa_\nu^{\text{ref}})$ and subsequent integration over the relevant frequency interval:

$$\boldsymbol{\Omega} \cdot \boldsymbol{\nabla}_{\boldsymbol{x}} I_k \;=\; \kappa_k \left[f_k \, I_k^{\text{neq}} - I_k \right] \;, \quad I_k \;=\; \int\limits_{\nu_i}^{\nu_{i+1}} I_\nu \, \delta(k - \kappa_\nu^{\text{ref}}) \, d\nu \tag{4.21}$$

It should be noted that κ_ν^{ref}, J_ν^{ref}, and $I_\nu^{\text{ref}} = \kappa_\nu^{\text{ref}} \,/\, J_\nu^{\text{ref}}$ are the absorption coefficient, source term, and emission intensity at a reference flowfield state. Therefore, $\kappa_k = (\, \kappa_\nu \,:\, \nu \ni \kappa_\nu^{\text{ref}} = k \,)$ and f_k is the emission-intensity weighted probability density for the k-distribution at reference values. The probability density function (PDF) f_k is computed as follows:

$$f_k \;=\; \int\limits_{\nu_i}^{\nu_{i+1}} I_\nu^{\text{neq}} \, \delta(k - \kappa_\nu^{\text{ref}}) \, d\nu \Bigg/ \int\limits_{\nu_i}^{\nu_{i+1}} I_\nu^{\text{neq}} \, d\nu \tag{4.22}$$

The k-distribution is ill-behaved around extrema values and so, a further transformation into the smoother g-space is effected:

$$g \;=\; \int\limits_{k}^{\infty} f_k \, dk \tag{4.23}$$

Additional commentary on the subsequent solution procedure and the general validity of the k-distribution method can be found in [204]. The total intensity emanating from a frequency group is obtained by integration in the g-space which spans the range $[0, 1]$. This has been performed numerically using Gaussian quadrature [207] in the present work. Thus, individual LOS evaluations for a frequency group are performed at spectral points ν_m that correspond to the requisite quadrature locations in g-space.

4.3.2.2 Theory of Homogenization

The method of homogenization developed by Haut et al. [111, 112] uses probability density functions and the correlated assumption, in a manner similar to k-distribution, to characterize the spectral variation in radiative properties. Non-equilibrium emission intensity I_ν^{neq} is employed in lieu of the Planck blackbody function from the original LTE formulation. The exact value of the spectral intensity I_ν can be expressed (analogous to Eq. 4.21):

$$I_\nu \;=\; \int_0^\infty I_\nu(k)\, p_\nu(k)\, dk \tag{4.24}$$

where the exact probability density function $p_\nu(k)$ is a Dirac-delta function peaking at $k = \kappa_\nu$. The probability density function is discretized using m opacity intervals for the i^{th} frequency group at reference conditions:

$$p_\nu \;\approx\; p_{ij} \quad \forall\, \nu \in [\nu_i, \nu_{i+1}] \;\ni\; \kappa_j \,\geq\, \kappa_\nu^{\mathrm{ref}} \,\geq\, \kappa_{j+1} \tag{4.25}$$

where p_{ij} is the probability of occupying the j^{th} opacity interval $[\kappa_j, \kappa_{j+1}]$ for the i^{th} frequency group $[\nu_i, \nu_{i+1}]$. This piece-wise probability density is computed as (equivalent to Eq. 4.22):

$$p_{ij} \;=\; \int_{\nu_i}^{\nu_{i+1}} I_\nu^{\mathrm{neq}}\, \mathcal{P}\, d\nu \Bigg/ \int_{\nu_i}^{\nu_{i+1}} I_\nu^{\mathrm{neq}}\, d\nu \;, \quad \mathcal{P} \;=\; \begin{cases} 1\,, & \text{if } \kappa_\nu^{\mathrm{ref}} \in [\kappa_j, \kappa_{j+1}] \\ 0\,, & \text{otherwise} \end{cases} \tag{4.26}$$

A weighted mean value of the absorption coefficient is also defined for the j^{th} opacity interval using $\mathcal{P}$:

$$\hat{\kappa}_{ij} \;=\; \int\limits_{\nu_i}^{\nu_{i+1}} \kappa_\nu \, I_\nu^{\text{neq}} \, \mathcal{P} \, d\nu \Bigg/ \int\limits_{\nu_i}^{\nu_{i+1}} I_\nu^{\text{neq}} \, \mathcal{P} \, d\nu \tag{4.27}$$

The discrete homogenized RTE corresponding to i^{th} frequency group and j^{th} opacity interval is:

$$\boldsymbol{\Omega} \cdot \boldsymbol{\nabla}_{\boldsymbol{x}} \hat{I}_{ij} \;=\; \hat{\kappa}_{ij} \left[\int\limits_{\nu_i}^{\nu_{i+1}} I_\nu^{\text{neq}} \, d\nu \,-\, \hat{I}_{ij} \right] \tag{4.28}$$

Finally, the total intensity I_i for the frequency group is obtained through a discretized approximation of Eq. 4.24 based on I_{ij} and p_{ij}:

$$\hat{I}_i \;=\; \sum_{j=0}^{m} p_{ij} \, \hat{I}_{ij} \tag{4.29}$$

It should be noted that p_ν and its discretized approximation p_{ij} play the same role as f_k from Eq. 4.21 in determining I_i. The homogenization approach and its multi-group form are discussed at length in [112].

4.4 Generalized Radiation Grouping Strategy

The present work attempts to establish a generalized criteria for grouping individual spectral points from a full set database while developing multi-group reduced-order models. This is crucial for improving predictions as it identifies sections of the spectra whose cumulative contribution can be replaced by group-wise properties $\hat{\kappa}_i$ and $\hat{J}_i$. Although the impact of the new grouping criteria is only studied for Planck-averaging, it can easily be applied to other reduced-order models based on a multi-group paradigm. The grouping procedure is performed using reference values for the absorption coefficient κ_ν^{ref} and the source term J_ν^{ref} for different frequencies ν. This ensures that group definitions – the full set to reduced-order group mapping – remain invariant in physical space. A range of schemes have been proposed for setting the reference state by different authors [110, 208, 209]. The current study employs an unweighted volumetric average in linear/logarithmic scale to define κ_ν^{ref} and J_ν^{ref}:

$$\kappa_\nu^{\text{ref}} = \int_V \kappa_\nu \, dV \Big/ V \qquad \text{or} \qquad \kappa_\nu^{\text{ref}} = \exp\left\{ \int_V \log\left(\kappa_\nu\right) dV \Big/ V \right\} \tag{4.30}$$

Choosing the appropriate averaging scheme for a given physical problem can appreciably improve accuracy for the same number of reduced-order groups. Additionally, numerical integration in frequency space is performed using the rectangle rule. This approximation on a frequency interval consisting of N spectral grid points results in:

$$\int_{\nu_i}^{\nu_{i+1}} I_\nu \approx \sum_{n=1}^{N-1} I_{\nu_n} \, \Delta\nu_n \tag{4.31}$$

A common approach for grouping individual frequencies while developing Planck-averaged reduced-order models is Multi-Band Opacity-Binning (MBOB) [208, 210]. The MBOB strategy can be broken down into two steps. The entire frequency range of the full set spectra is first divided into x equal logarithmic bands (logarithmic scaling has been found to capture spectral features more accurately). These bands are further sub-divided into opacity bins which are defined as contiguous ranges in the absorption coefficient space. This is also equivalent to a coarse-grain approximation of opacity distribution functions [211]. Following the recommendations of Scoggins et al. [209],

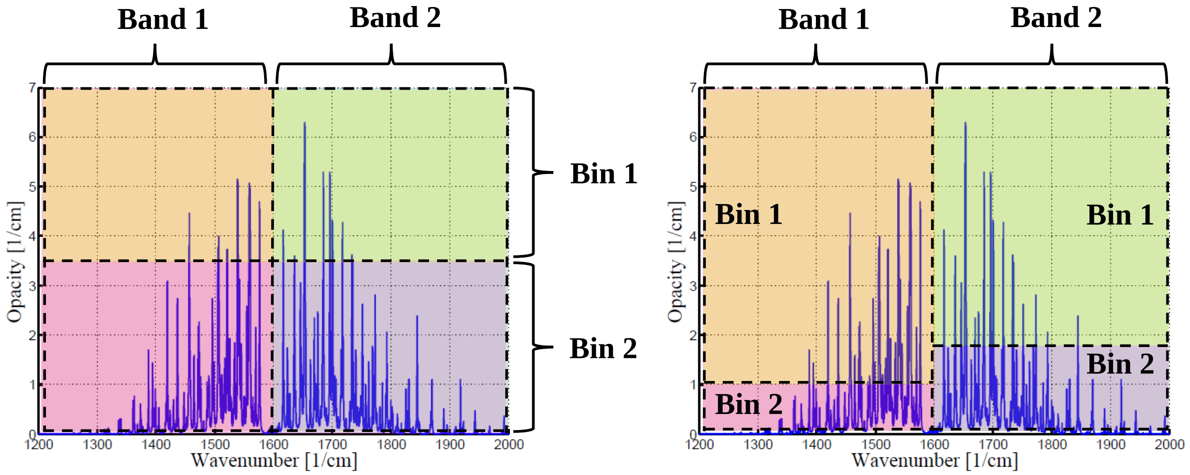

(a) Equal opacity intervals

(b) Equal number of frequencies per bin

Figure 4.5: Multi-Band Opacity-Binning (MBOB) on a representative spectra for a reduced-order system with two frequency bands and two opacity bins.

an equal number of spectral points are assigned to individual opacity bins. Previous approaches, with predefined opacity intervals (similar to the way frequency bands are created), would yield a large number of empty bins and consequently, suffer from poor resolution. In contrast, the MBOB paradigm used in the current work first reorders spectral points within a band in ascending order on the basis of $\kappa_\nu^{\mathrm{ref}}$. These sorted points are then equally divided into y opacity bins. The two techniques for defining opacity bins – intervals in opacity space and equally distributed spectral points – are illustrated in Fig. 4.5 for a representative spectrum.

The current work argues that the accuracy afforded by all three conventional wide-band models under study – Planck-averaging with MBOB and statistics-based k-distribution and theory of homogenization – is expected to be comparable. This is a consequence of all the aforementioned approaches effecting the same paradigm. A common frequency band is reordered in absorption coefficient space either explicitly (k-distribution, homogenization) or implicitly by collating full set spectral points on the basis of opacity intervals (Planck-averaged MBOB). This reordering process is the critical step in transforming rapidly varying spectral intensity into a more monotonic distribution which is more amenable to model-reduction [112]. The manner in which average properties are ascribed to individual reduced-order groups can then said to be secondary in terms of improving accuracy. This is analogous to different numerical integration schemes of the same order of accuracy (since the number of reduced-order groups or discrete evaluation points remain invariant) yielding similar results when applied to a smoothly varying distribution.

Furthermore, these conventional approaches share a common shortcoming – absorption coefficient κ_ν being used as the sole determinant when grouping or computing probability distributions – that stems from them being rigorously developed in the realm of Local Thermodynamic Equilibrium (LTE) radiation. Under LTE conditions, all terms except the absorption coefficient that appear in the RTE vary smoothly in frequency space. A breakdown of the LTE assumption results in the emission source term (no longer equal to the product of absorption coefficient and Planck blackbody intensity) exhibiting rapid oscillatory behavior independently of the absorption coefficient. Conventional approaches by disregarding the variance in emission source terms or other cross/higher-order terms can yield reduced-order models with diminished fidelity. Thus, a generalized grouping strategy accounting for both κ_ν and J_ν is the most straightforward approach to compensate for these limitations when describing Non Local Thermodynamic Equilibrium (NLTE) radiation. This development parallels the physically consistent adaptive grouping strategy described in Section 2.4 that is aimed at improving the applicability of MGME thermochemical models.

A non-intuitive binning strategy can be evolved by comparing LOS solutions for the detailed full set and reduced-order systems. The current analysis is simplified by assuming no incident radiation and a homogeneous medium with radiative properties set to their reference values (Eq. 4.30). The exact solution (from the original full set model) along direction $\mathbf{\Omega}$ for frequency point ν_n is:

$$\begin{aligned} I_{\nu_n}(s) &= \int_0^s J_{\nu_n}^{\mathrm{ref}} \exp\left(- \int_{s'}^{s} \kappa_{\nu_n}^{\mathrm{ref}}\, ds'' \right) ds' + \cancelto{0}{I_{\nu_n}(0) \exp\left(- \int_0^s \kappa_{\nu_n}^{\mathrm{ref}}\, ds' \right)} \\ &= \frac{J_{\nu_n}^{\mathrm{ref}}}{\kappa_{\nu_n}^{\mathrm{ref}}} \left\{ 1 - \exp(-\, \kappa_{\nu_n}^{\mathrm{ref}}\, s) \right\} \end{aligned} \tag{4.32}$$

Subsequently, a reduced-order solution for the g^{th} group ($\nu_n \in \mathcal{I}_g$, where $\mathcal{I}_g$ is the set of spectral points assigned to group g) is computed. The full set solution for I_{ν_n} can now be compared to group-intensity $\hat{I}_g$ that has been unpacked to obtain frequency-specific values:

$$\begin{aligned} I_{\nu_n}(s) &\approx \mathcal{F}_g(\nu_n)\, \hat{I}_g(s) \\ \Rightarrow \tfrac{J_{\nu_n}}{\kappa_{\nu_n}} \left\{ 1 - \exp(-\, \kappa_{\nu_n}\, s) \right\} &\approx \mathcal{F}_g(\nu_n)\, \frac{\hat{J}_g}{\hat{\kappa}_g} \left\{ 1 - \exp(-\, \hat{\kappa}_g\, s) \right\} \end{aligned} \tag{4.33}$$

where $\hat{I}_g$, $\hat{\kappa}_g$, and $\hat{J}_g$ are the total intensity, absorption coefficient, and source term for group g. The fraction of total group intensity emanating from frequency point ν_n is represented by $\mathcal{F}_g(\nu_n)$. The impact of different definitions for $\mathcal{F}_g$ is further outlined in Section 5.2.3. The superscript "ref" indicating the reference value for a given quantity has been dropped for notational convenience. It should be noted that since a homogeneous medium is being employed, both sides of Eq. 4.33 have the same dependence on the distance term s. Thus, a term-by-term comparison of the Taylor series expansion (with s canceled out) yields the following relationship:

$$J_{\nu_n} (\kappa_{\nu_n})^p = \mathcal{F}_g(\nu_n)\, \hat{J}_g (\hat{\kappa}_g)^p \,, \quad p = 0,\, 1,\, 2,\, \ldots \tag{4.34}$$

This can be further simplified to obtain the following relationship between full set and reduced-order radiation properties:

$$\frac{J_{\nu_n}}{\hat{J}_g} = \frac{J_{\nu_n}\,\kappa_{\nu_n}}{\hat{J}_g\,\hat{\kappa}_g} = \frac{J_{\nu_n}\,(\kappa_{\nu_n})^2}{\hat{J}_g\,(\hat{\kappa}_g)^2} = \ldots = \text{Const.} \tag{4.35}$$

A grouping strategy that satisfies Eq. 4.35 would allow an accurate representation of full set values using only the reduced-order solution. Although this relationship is exact only in the limit of a homogeneous medium at reference values, it serves as a powerful tool for guiding the development of better reduced-order models for more complex physical problems. The present work retains the MBOB paradigm while enforcing Eq. 4.35. The original frequency bands are replaced by equal logarithmic intervals in the J_ν space. These source-bands are further sub-divided into bins which are again defined as equal logarithmic intervals in the $(J_\nu\,\kappa_\nu)$ space. This simple procedure attempts to minimize variations in J_ν and $(J_\nu\,\kappa_\nu)$ within a band-bin pair and conform better with the new generalized criteria. Future work would entail incorporating higher-order terms and the use of more sophisticated techniques such as spectral clustering (Section 2.4.2) and optimal k-means unidimensional clustering [212] for imposing Eq. 4.35. It is interesting to note that opacity binning represents only a subset of all grouping permutations allowed by Eq. 4.35. An ideal opacity bin is composed of frequency points with the same reference values for the absorption coefficient. Such a bin with $(\kappa_{\nu_n} = \hat{\kappa}_g = \text{Const.})$ would trivially satisfy the generalized criteria. An invariant value of the absorption coefficient within a bin is highly improbable for a general radiative system. The new grouping methodology by incorporating J_ν and $(J_\nu\,\kappa_\nu)$ better enforces Eq. 4.35 and therefore, would produce more accurate reduced-order models.

4.5 Summary

This chapter presents the numerical framework for evaluating three-dimensional radiative transfer in participating media under non-equilibrium conditions. The domain of dependence for generalized radiation problems covers three disparate spaces: angular, spatial, and spectral. Solution procedures and the concomitant discretization for resolving variations in different physical spaces are aimed at balancing fidelity with computational tractability. The discrete ordinate method is used to reduce the dimensionality of angular-spatial integro-differential transfer equations. This is done by transforming the otherwise analytical integral over the complete solid angle into a weighted sum of quantities computed for a discrete set of directions. The resultant system of spatially-varying RTEs (each equation corresponds to a fixed direction) is solved using finite-volume discretization and first-order upwinding. Further efficiency gains are realized through the mesh sweeping algorithm which allows radiative intensity to be calculated explicitly by identifying the optimal sequence in which computational cells are analyzed. In similar vein, three reduced-order wide-band methods – Planck-averaging, k-distribution, theory of homogenization – which allow complex variations in the frequency domain to be accurately reproduced at significantly lowered costs are outlined. Reinterpreting Planck-averaging using the maximum entropy principle allows an equivalence to be drawn with the MGME method for non-equilibrium thermochemistry. Finally, a generalized grouping criteria for combining individual frequencies into larger groups during model reduction is evolved for non-equilibrium radiation. This analysis supersedes conventional viewpoints (which are largely based on LTE assumptions) by taking into account rapid oscillatory behavior of both the absorption coefficient and emission source term to devise reduced-order systems more reflective of NLTE dynamics. A comparative analysis of wide-band models and grouping methodologies based on LOS evaluations in different aerothermal environments is presented in the next chapter.

Chapter 5

Line-of-Sight Analysis of Reduced-order Spectral Models

A complete solution of three-dimensional radiative fields is obtained through a two-step process. First, frequency-wise variation in medium absorption/emission behavior is described on a discrete spectral grid. Next, angularly-integrated and spatially resolved transfer calculations are performed for each discrete spectral unit (frequency/reduced-order group). Thus, the number of independent evaluations in the frequency space required to correctly predict the effects of photochemical transitions can determine the viability of realizing detailed radiative solutions. The reduced-order wide-band spectral models outlined in Chapter 4 are critical for enabling cost-effective accurate calculations for radiative transfer problems especially when coupled with CFD simulations. The current chapter investigates the efficacy of these reduced-order spectral methods with regards to modeling radiative environments encountered by different planetary entry missions. Since the focus is on benchmarking spectral accuracy (and not the geometric spatial/angular aspects), the comparative analysis is performed along a single wall-normal line-of-sight. A simplified angular/spatial domain allows radiative intensity to be modeled precisely using detailed approaches such as LBL or narrow-band models which require a large number of frequency-wise evaluations ($\sim 10^4 - 10^6$). This reference solution is then used to assess different wide-band models (Section 4.3) and the impact of generalized radiation grouping (Section 4.4). This chapter is organized as follows: a) Section 5.1 details the discretized formulation for resolving radiative behavior along a single LOS. b) The accuracy of different conventional wide-band models is analyzed for Earth and Jovian planetary entry problems in Section 5.2. c) Next, improvements to reduced-order predictions due to the introduction of non-equilibrium radiation grouping and group-wise equivalent blackbody temperatures T^i_{rad} are presented in Section 5.3. d) Section 5.4 summarizes the key findings of the chapter.

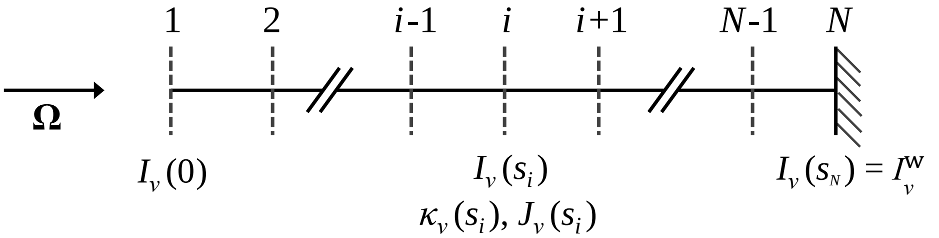

Figure 5.1: One-dimensional discretization of RTE in the wall-directed normal direction $\boldsymbol{\Omega}$.

5.1 Computational Methodology

The current chapter limits radiative transfer calculations to a single LOS along the wall-directed normal and concentrates on spectral characteristics. The numerical procedure outlined in Section 4.2 for angularly integrated heat flux in three-dimensional domains is excessively complicated. Instead, the one-dimensional RTE (Eq. 4.1) is integrated and then discretized to adequately describe the variation in radiative intensity along a given LOS. The exact radiative intensity [72] corresponding to frequency ν at distance s along the requisite LOS direction $\boldsymbol{\Omega}$ is:

$$I_\nu(s) \quad = \quad I_\nu(0)\exp\left\{-\int\limits_0^s \kappa_\nu(s')\,ds'\right\} + \int\limits_0^s J_\nu(s')\exp\left\{-\int\limits_{s'}^s \kappa_\nu(s'')\,ds''\right\}ds' \tag{5.1}$$

The incident radiation $I_\nu(0)$ from the cold farfield boundary is set to zero. Equation 5.1 is also further simplified by introducing the optical thickness τ_ν along a LOS:

$$I_\nu(s) \quad = \quad \int\limits_0^s J_\nu(s')\exp\left\{-\tau_\nu(s)\right\}\,\exp\left\{\tau_\nu(s')\right\}\,ds'\,, \qquad \tau_\nu(s) \;=\; \int\limits_0^s \kappa_\nu(s'')\,ds'' \tag{5.2}$$

Figure 5.1 presents the discretization of the one-dimensional space in s. The integral in Eq. 5.2 is replaced by a summation of contributions from individual one-dimensional cells:

$$I_\nu(s_n) \quad = \quad \sum_{i=1}^{n-1}\int\limits_{s_i}^{s_{i+1}} J_\nu(s')\exp\left\{-\tau_\nu(s_n)\right\}\,\exp\left\{\tau_\nu(s')\right\}\,ds' \tag{5.3}$$

The current work uses the approach developed by Hartung [105] for approximating properties within each cell defined by $s \in [s_{i-1}, s_i]$. The source term is set equal to the average between the end-point values:

$$J_\nu(s) \quad = \quad \frac{J_\nu(s_i) + J_\nu(s_{i-1})}{2} \quad \forall s \in [s_{i-1}, s_i] \tag{5.4}$$

However, a more detailed treatment for κ_ν is required for accurately solving Eq. 5.3. Hartung proposes a piecewise linear reconstruction of τ_ν within cells which minimizes errors while evaluating intensity for strongly absorbing spectral regions:

$$\tau_\nu(s) \quad = \quad \alpha_\nu^i + \beta_\nu^i s \quad \forall s \in [s_{i-1}, s_i] \tag{5.5}$$

$$\alpha_\nu^i \quad = \quad \frac{\tau_\nu(s_{i-1})\, s_i - \tau_\nu(s_i)\, s_{i-1}}{s_i - s_{i-1}} \tag{5.6}$$

$$\beta_\nu^i \quad = \quad \frac{\tau_\nu(s_i) - \tau_\nu(s_{i-1})}{s_i - s_{i-1}} \tag{5.7}$$

Applying Eq. 5.5 to Eq. 5.3 results in a definite integral of the form:

$$\begin{aligned}
\int_{s_{i-1}}^{s_i} \exp\left\{\tau_\nu(s')\right\} ds' &= \int_{s_{i-1}}^{s_i} \exp\left(\alpha_\nu^i + \beta_\nu^i s'\right) ds \\
&= \frac{1}{\beta_\nu^i} \left\{\exp\left(\alpha_\nu^i + \beta_\nu^i s_i\right) - \exp\left(\alpha_\nu^i + \beta_\nu^i s_{i-1}\right)\right\} \\
&= \frac{s_i - s_{i-1}}{\tau_\nu(s_i) - \tau_\nu(s_{i-1})} \left[\exp\left\{\tau_\nu(s_i)\right\} - \exp\left\{\tau_\nu(s_{i-1})\right\}\right] \qquad (5.8)
\end{aligned}$$

Equations 5.3, 5.4, and 5.8 are now combined to produce the final one-dimensional discretized formulation:

$$\begin{aligned}
I_\nu(s_n) \quad = \quad \sum_{i=1}^{n-1} \Bigg(& \frac{1}{2} \frac{J_\nu(s_i) + J_\nu(s_{i-1})}{\tau_\nu(s_i) - \tau_\nu(s_{i-1})} (s_i - s_{i-1}) \\
& \exp\left\{-\tau_\nu(s_n)\right\} \left[\exp\left\{\tau_\nu(s_i)\right\} - \exp\left\{\tau_\nu(s_{i-1})\right\}\right] \Bigg) \qquad (5.9)
\end{aligned}$$

The integral over frequency space $[\nu_0, \nu_f]$ is approximated using the rectangle rule (Section 4.4). Monochromatic intensity I_{ν_j} is evaluated at discrete points in the spectral grid for LBL/narrow-band models. Then, the total radiative intensity I is obtained as follows:

$$\int_{\nu_0}^{\nu_f} I_\nu \;\approx\; \sum_{j=1}^{V-1} I_{\nu_j}\,\Delta\nu_j \tag{5.10}$$

where the frequency space is discretized into V points for a given spectral model. Radiative transfer calculations for reduced-order wide-band models are also performed using Eq 5.9. The only difference is that individual LOS evaluations rather than being frequency specific, now attempt to predict the collective characteristics of reduced-order groups.

5.2 Comparison Between Conventional Reduced-order Methodologies

This section first compares the applicability of various reduced-order methodologies – maximum entropy enforcing Planck-averaging with conventional frequency bands and opacity binning (MBOB), homogenization, k-distribution – to a range of radiative systems. The conventional MBOB approach is realized by setting T_{rad} equal to the vibrational-electronic temperature from the flowfield. The impact of the proposed non-equilibrium grouping strategy on the accuracy of Planck-averaged reduced-order models is studied in the next section. Three hypersonic entry problems and the associated radiation field are considered: a) Earth entry of the Stardust probe, b) meteor entry that includes precursor radiation, c) and entry of Galileo probe into Jupiter.

Flow simulations for the current study have been performed using the LAURA non-equilibrium Navier-Stokes solver[213]. Radiative calculations have been conducted using the HARA radiation code [214]. A hybrid approach is adopted for describing frequency variance of radiative properties: SRB method is used for molecular bands with an LBL treatment of atomic radiation [7, 8, 215]. A spectral grid consisting of approximately $50,000$ points reproduces LBL characteristics with sufficient fidelity for hypersonic aerothermal applications. Since the objective of the current study is to contrast the aforementioned wide-band paradigms, no commentary is provided on the suitability of narrow-bands models. Additional discussion on the subject can be found in [216]. Results obtained using the hybrid-SRB method are considered exact and used as the reference solution for assessing different wide-band models. Spectral models based on the hybrid-SRB approach are referred to as *"full set models"* while only wide-band approaches are referred to as *"reduced-order models"*.

A two-step process is employed while analyzing each physical system. Firstly, a converged solution with flow-radiation coupling based on the full set model and tangent slab approximation is obtained using the LAURA-HARA framework [217]. Then, radiation along individual lines-of-sight (LOSs) is analyzed through the one-dimensional discretization procedure outlined in Section 5.1. These LOS calculations are repeated for both full set and reduced-order approaches, while keeping the flowfield fixed. It should be noted that the current work focuses on assessing the efficacy of spectral reduced-order modeling for different relevant entry problems. Thus, the underlying flowfield simulations, which have been reported at length in previous studies, are only briefly summarized. A more detailed discussion is presented for LOS variation in radiative response and the comparative characteristics of various reduced-order models.

Stardust entry is simulated using a two-temperature thermochemical non-equilibrium model comprising of 11 species air (N, N^+, O, O^+, NO, NO^+, N_2, ${N_2}^+$, O_2, ${O_2}^+$, and e^-) and kinetic rates presented by Johnston and Panesi [218] that also account for non-Boltzmann behavior in atomic nitrogen. The characteristic freestream velocities for meteoroids is higher and therefore, additional ionized species (N^{++} and O^{++}) are added to the air 11 gaseous mixture [219]. A comprehensive set of spectral data and non-Boltzmann models for diatomic molecules and atomic species relevant to high temperature air are considered in HARA while computing radiative properties [216, 220]. The impact of ablation is ignored for both Earth entry problems. The freestream gas during Jovian entry for the Galileo probe is modeled using seven species [221]: H_2, ${H_2}^+$, H, H^+, He, He^+, and e^-. The ablation product gas requires the inclusion of an additional 18 species: C, C^+, C_2, C_3, C_4, C_5, CH, C_2H, C_3H, C_4H, C_5H, CH_2, C_2H_2, O, O^+, O_2, CO, CO. Radiation transitions that involve H, H^+, C, C_2, C_3, O, O_2, and CO and can be classified as atomic lines, molecular bands, bound-free continuum, or free-free continuum have been accounted for in the present calculations [221].

The current work attempts to present a fair comparison between different methods by ensuring that grouping strategies and number of reduced-order groups are uniform. This can have different connotation for each technique. Thus, an $x \times y$ reduced-order system implies: a) x frequency bands with y opacity bins for conventional MBOB Planck averaging; b) identical x frequency bands and y opacity intervals as MBOB for the method of homogenization; c) the same x frequency bands as before with y quadrature points for integration within bands while using k-distribution.

5.2.1 Stardust Entry

The performance of the three reduced-order techniques is assessed for a LOS located in the wake region and originating from the backshell of the Stardust capsule. The flowfield properties and radiative environment have been analyzed at the 46 s trajectory point with freestream velocity $V_\infty = 11.69$ km/s and density $\rho_\infty = 1.05 \times 10^{-4}$ kg/m^3. Additional details on the computational setup, mesh configuration, and LOS properties can be found in [12]. The spectrally integrated wall-directed radiative intensity computed using the full set and differently sized reduced-order models is presented in Fig. 5.2. Linear averaging (Eq. 4.30) has been performed in order to define the reference value of absorption coefficients and source term for individual frequencies. The radiative field in the afterbody region is shaped by the overlap in the VUV region between molecular bands and atomic lines [110]. Emission from strong atomic nitrogen and oxygen lines (self-absorbing with significant non-Boltzmann effects) and molecular NO is absorbed by molecular species such as N_2 in the boundary layer. A comparison between the different 20×20 reduced-order systems indicates that Planck-averaging produces a larger overshoot while predicting the initial rise in radiative intensity through the far-wake and outlying shocked flow. Additionally, both Planck-averaging and homogenization (converse for k-distribution) over-predict the degree of absorption through the near-wall region. The use of a larger 25×50 reduced-order model improves some of these shortcomings resulting in smaller deviations from the the full set results. Fig. 5.2b clearly indicates that results for Planck-averaged MBOB are comparable to the more complex statistics-based methods. This outcome is interesting because the wake region is characterized by optically thick, spectrally overlapping atomic and molecular radiative processes and an inhomogeneous medium driving non-local absorption. According to the conventional rationale (Section 4.3.1), standard Planck-averaging should conspicuously fail under such conditions. However, it should be noted that both Planck-averaged MBOB and k-distribution continue to yield incorrect lower estimates at the wall. This highlights a common shortcoming of most reduced-order models while reproducing radiative intensities for Planck-limited sections of the spectra in optically thick regions.

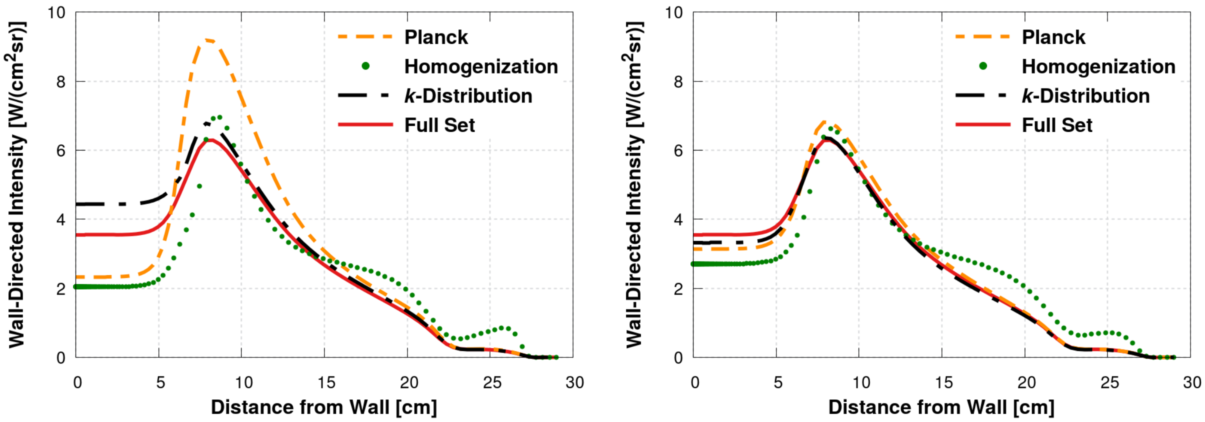

(a) 20 × 20 reduced-order models **(b)** 25 × 50 reduced-order models

Figure 5.2: Total wall-directed intensity along a backshell LOS during Stardust entry.

It is interesting to note that predictions based on homogenization are more error-prone at distances greater than 12 cm. The flowfield beyond that point is in a state of strong thermochemical non-equilibrium due to a combination of expanding flows and proximity to the oblique shock [217]. Thus, non-equilibrium emission intensity $I_\nu^{\text{neq}} = J_\nu/\kappa_\nu$, especially near atomic line centers, deviates strongly from the corresponding blackbody Planck intensity I_ν^B. The theory of homogenization has a rigorous mathematical framework for establishing accurate reduced-order models only for LTE radiation with the emission source term $J_\nu = \kappa_\nu\, I_\nu^B$. Under thermal non-equilibrium, both κ_ν and I_ν^{neq} exhibit rapid spectral variation. Model reduction based on homogenization cannot accurately account for this behavior, resulting in erroneous results for non-equilibrium radiation.

5.2.2 Meteor Precursor Radiation

The second physical problem considered is the Earth entry of a meteoroid. Coupled flow and radiative field calculations have been performed for a spherical meteoroid with radius equal to 1 m, freestream velocity $V_\infty = 20$ km/s, and altitude set to 50 km. Additionally, both precursor radiation and the impact of photochemical source terms on the species continuity equations are modeled in these simulations [219]. Meteoroids pose a unique challenge for reduced-order spectral approaches because of the higher entry speeds at lower altitudes as compared to reentry vehicles. This can result in the shock layer having a significantly larger optical thickness. Radiation coupling also yields thicker boundary layers and greater non-local absorption of wall-directed radiation [219, 222]. The total radiative intensity for current conditions is dominated by contributions from atomic nitrogen and oxygen lines and continuum emission. Predictions based on different reduced-order techniques and the full set for the stagnation LOS are compared in Fig. 5.3. These results have been obtained using the linear averaging scheme (Eq. 4.30) for defining κ_ν^{ref} and J_ν^{ref}. The smaller 10 × 10 Planck-averaged reduced-order model fails to accurately model emission through the hot shock layer. However, a switch to the larger 25 × 50 system remedies these issues. It is evident from Fig. 5.3b that the Planck-averaged MBOB offers more reliable results through the entire LOS. The two statistics-based methods over-predict (by differing degrees) the rise in radiative intensity through the thick post-shock region.

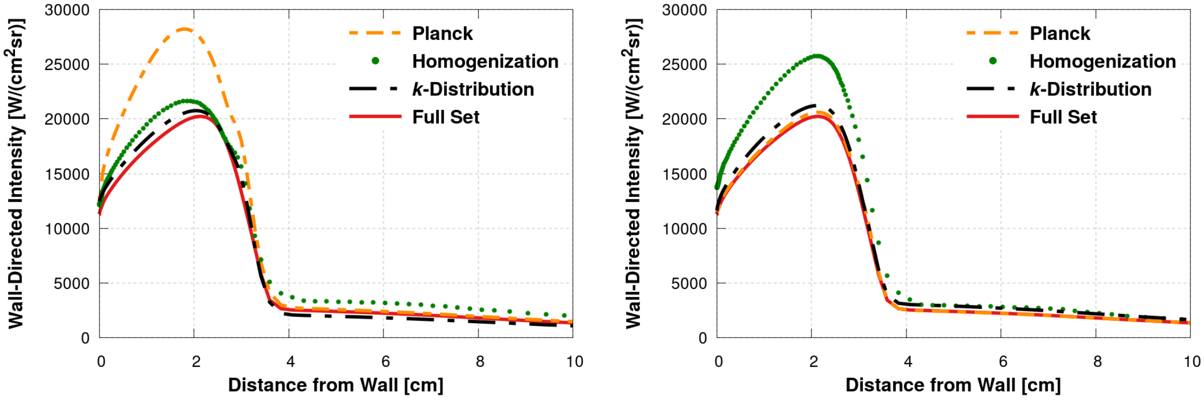

(a) 10 × 10 reduced-order models **(b)** 25 × 50 reduced-order models

Figure 5.3: Total wall-directed intensity along stagnation LOS during meteor entry.

A key challenge while characterizing this system is ensuring that precursor absorption in the freestream gas beyond the bow shock (∼ 4.5cm) is captured accurately. This is also crucial for correctly modeling photoionization and photodissociation which dominate over collisional processes that are impeded by low freestream densities [219, 223]. Thus, precursor influence can significantly alter flow composition and enthalpy as it approaches the shock front, besides increasing the total wall-directed radiative flux. Planck-averaging is able to resolve radiative features in the large precursor region with wall-directed intensity indistinguishable from the corresponding full set values. Predominance of non-equilibrium phenomena (high entry velocities and low freestream densities) also has an adverse impact on the accuracy of reduced-order models derived using homogenization.

Additionally, the error associated with reduced-order solutions based on homogenization does not monotonically decrease with increasing number of reduced-order groups. The discrepancy with the full set solution in Fig. 5.3 actually rises when going from the 10×10 to 25×50 systems before eventually decaying at higher number of band/bin combinations.

5.2.3 Galileo Entry

Flow calculations have been performed with radiative energy transfer and mass injection through ablation for the Galileo probe entry. A converged solution for the peak heating trajectory point (51.16 s) is obtained [221]. This corresponds to freestream velocity $V_\infty = 41.6$ km/s and density $\rho_\infty = 3.49 \times 10^{-4}$ kg/m^3. Previous studies [221, 224] indicate that ablation product gases are abundant in the near-wall region along the stagnation line. Furthermore, atomic species such as C can diffuse upstream to the high-temperature shock region and contribute further to wall-directed radiation. Thus, the total radiative intensity is defined by strong emissions from H and C lines in the shock layer and subsequent absorption through a complex interaction between overlapping molecular bands of C_2H and C_3. Results obtained using different reduced-order models and the original detailed spectral database for the stagnation LOS are presented in Fig. 5.4. Reference frequency-wise absorption coefficients and source terms are computed through logarithmic averaging (Eq. 4.30). Wall-directed intensity is over-predicted by k-distribution method for the smaller 15×15 reduced-order system. The values obtained using MBOB and homogenization are almost

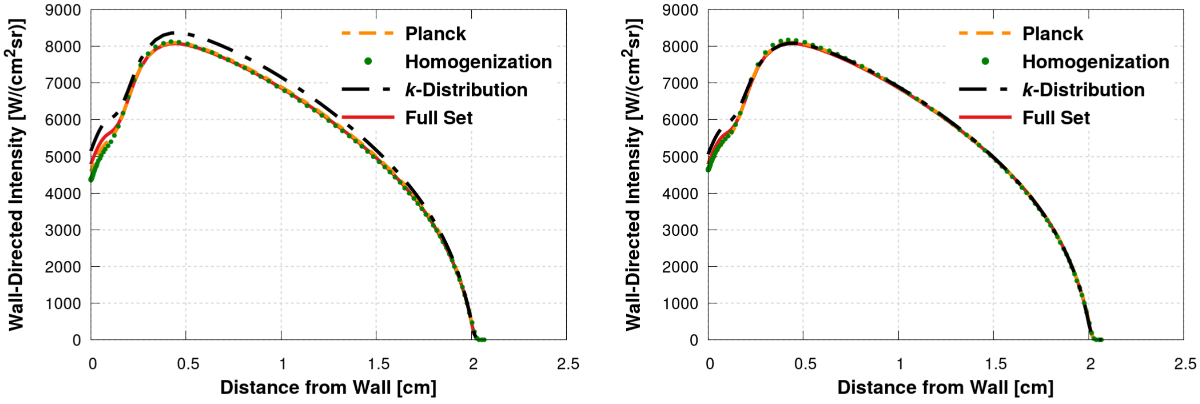

(a) 15 × 15 reduced-order models **(b)** 20 × 20 reduced-order models

Figure 5.4: Total wall-directed intensity along stagnation LOS during Galileo entry.

alike and reproduce the full set solution for the majority of the LOS. However, both methods under-predict intensity at the wall. This suggests that for current flow conditions $I_\nu^{\text{neq}} \approx I_\nu^B$, which renders both methods almost identical from a mathematical standpoint when using the same frequency bands and opacity intervals. The use of a larger 20×20 system improves agreement with the full set solution although k-distribution is slightly inaccurate while capturing radiation attenuation through the ablation dominated near-wall region.

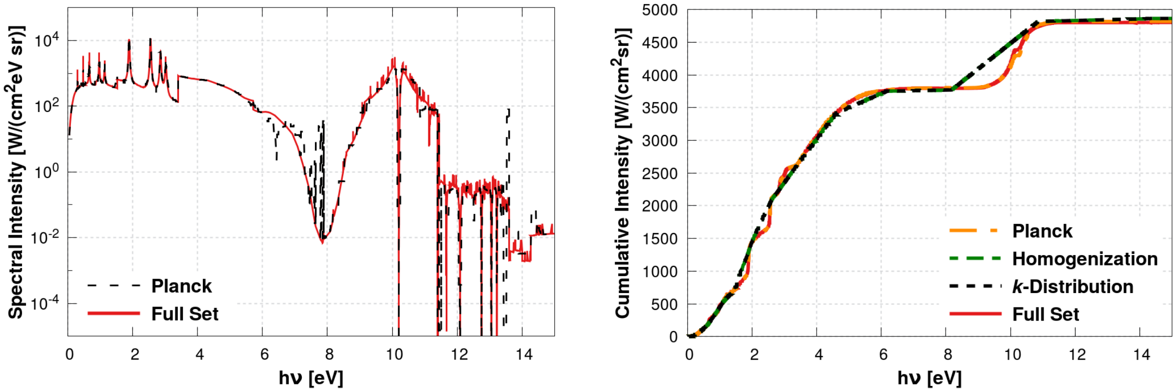

(a) Spectral Intensity **(b)** Cumulative Intensity

Figure 5.5: Spectral and cumulative wall-directed intensities at the wall computed using the full set and 25×25 reduced-order systems for Galileo entry.

Numerical experiments by the author indicate that the strategy employed by Johnston et al. [109] for unpacking reduced-order solutions to obtain a frequency-wise distribution offer the best agreement with the full LBL spectra. This involves defining the fraction $\mathcal{F}_{ij}(\nu_m)$ of total intensity (or other radiative quantity such as heat flux) from the i^{th} band and j^{th} bin pair that can be attributed to frequency point ν_n as:

$$\mathcal{F}_{ij}(\nu_n) = 1 \Bigg/ \sum_{\nu_n \in \{\nu\}_{ij}} \Delta\nu_n \tag{5.11}$$

A comparison between the full set spectra and unpacked reduced-order solution from a 25×25 sized system at the wall is presented in Fig. 5.5. It should be noted that the unpacking procedure requires simple post-processing of the reduced-order solution. Prominent spectral features are captured after only 25×25 evaluations along a LOS (corresponding to the number of reduced-order groups) rather than the original $\sim 50,000$ evaluations for the original detailed spectral approach. An analysis of

LOS radiative distributions indicates that conventional MBOB offers the most accurate estimates for both total and frequency-wise quantities amongst the different model reduction techniques studied here.

5.3 Impact of Generalized Grouping Strategy

The impact of the generalized grouping strategy on improving total and spectral predictions is analyzed in this section. It should be noted that T_{rad} (Eq. 4.20) is updated while applying the proposed grouping strategy to the convetional MBOB method. A maximum of four sub-iterations have been found to be sufficient while converging T_{rad} and other radiative properties for the current physical problems. Radiative properties for Galileo entry are well resolved using conventional MBOB. The new methodology yields no significant improvement in term of a smaller reduced-order model that can accurately reproduce the full set solution. Therefore, only the Stardust and meteor entry problems are discussed in the interest of brevity.

5.3.1 Stardust Entry

The same calculations outlined in Section 5.2.1 along the backshell LOS for Stardust entry are now repeated using the new generalized grouping strategy. These results, labeled *"Planck (New)"*, are presented in Fig. 5.6. A switch to the J_ν and $(J_\nu \, \kappa_\nu)$ informed grouping scheme not only mitigates shortcomings plaguing the original MBOB method (Fig. 5.2a) but also surpasses the more complex statistics-based schemes in terms of accuracy. The smaller 20×20 system is now sufficient for accurately resolving total intensity through non-uniform media with differing dominant radiative processes (atomic lines in shock layer versus molecular bands in near-wall region). Conventional reduced-order spectral models by disregarding the importance of grouping are not able to converge to full set results even with the significantly larger 25×50 system. Additional investigation indicates the use of an independent T_{rad} has minimal impact, with change in reduced-order solution between the first (T_{rad} equal to vibrational-electronic temperature) and final sub-iterations being less than 0.1%. Therefore, it can be concluded that accuracy gains in Planck-averaged predictions are mainly through the improved grouping strategy.

The unpacked spectral distribution from a 25×25 reduced-order system developed using the

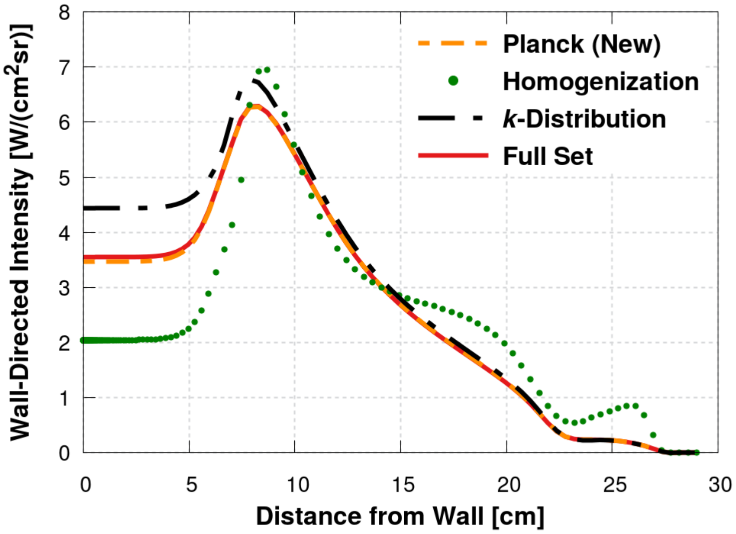

Figure 5.6: Total wall-directed intensity along a backshell LOS during Stardust entry. Reduced-order solutions based on 20 × 20 systems.

new grouping scheme is compared to the full set model in Fig. 5.7a. The behavior of key atomic lines that are impacted by non-Boltzmann effects, such as the 174 nm (7.1 eV) atomic nitrogen line, is accurately predicted by the reduced-order solution. Surprisingly, spectral decomposition based on a Planck blackbody $I_\nu^B(T_{\text{rad}})$ weighted fraction $\mathcal{F}_{ij}(\nu_m)$ (instead of the spectrally invariant $\mathcal{F}_{ij}(\nu_m)$ defined in Eq. 5.11) fails to match the actual full set spectra. Although the larger discrete peaks are accurately reproduced, the $I_\nu^B(T_{\text{rad}})$ weighted $\mathcal{F}_{ij}(\nu_m)$ under-predicts the lower continuum spectral intensity. Instead, a constant $\mathcal{F}_{ij}(\nu_m)$, which can also be viewed as a uniform spectral probability density, allows the frequency-wise variance from the full set solution to be captured as a simple post-processing step on an almost 2000 times smaller reduced-order system. Results obtained using only the more accurate constant fraction $\mathcal{F}_{ij}(\nu_m)$ approach (Eq. 5.11) are presented in Fig 5.7 and while analyzing spectral distributions in subsequent sections. High fidelity in the frequency space is particularly important while designing self-consistent coupled radiation reduced-order models for gaseous mixtures characterized by non-Boltzmann state population distributions [12, 225]. The same unpacking procedure is also applied to the conventional MBOB (labeled *"Planck (Old)"*) and statistics-based approaches. The cumulative intensity at the wall for both the full set and reduced-order models is presented in Fig. 5.7b. Results obtained using homogenization deviate notably from the reference full set predictions and have not been presented here. It is evident that the new generalized binning strategy ensures more reliable estimates for both spectral and total

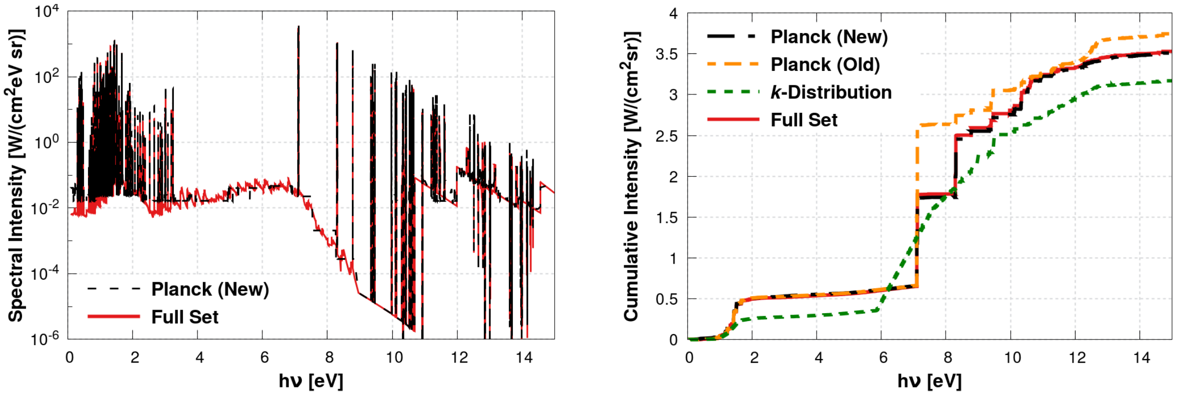

(a) Spectral Intensity **(b)** Cumulative Intensity

Figure 5.7: Spectral and cumulative wall-directed intensities at the wall computed using the full set and 25×25 reduced-order systems for Stardust entry.

radiative quantities of interest as compared to legacy methods.

5.3.2 Meteor Entry

The total wall-directed intensity along the stagnation LOS for the meteoroid problem is computed using the new grouping strategy. Results obtained for 10×10 reduced-order models are presented in Fig. 5.8. Despite the limited number of reduced-order groups employed, Planck-averaging in conjunction with generalized grouping successfully reproduces full set results across the entire length of the stagnation line. This case further highlights the suitability of the proposed approach in dealing with a complex set of interacting radiative systems for a large non-homogeneous physical domain. A comparison of spectral intensity at the wall between post-processed reduced-order solutions and direct full set values is presented in Fig. 5.9. Results obtained using only a 10×10 system based on the new grouping strategy are in excellent agreement with the original detailed spectra. Spectral intensity is slightly over-predicted for certain frequencies in the 12-14 eV region. However, the maximum error in the corresponding cumulative intensity remains bounded at approximately 3.5%. Fig. 5.9b also highlights the larger inconsistencies in spectral details while using conventional MBOB and k-distribution approaches. Frequency-wise unpacking for homogenization-based reduced-order models diverges from full set values by introducing large errors in the 0-4 eV region.

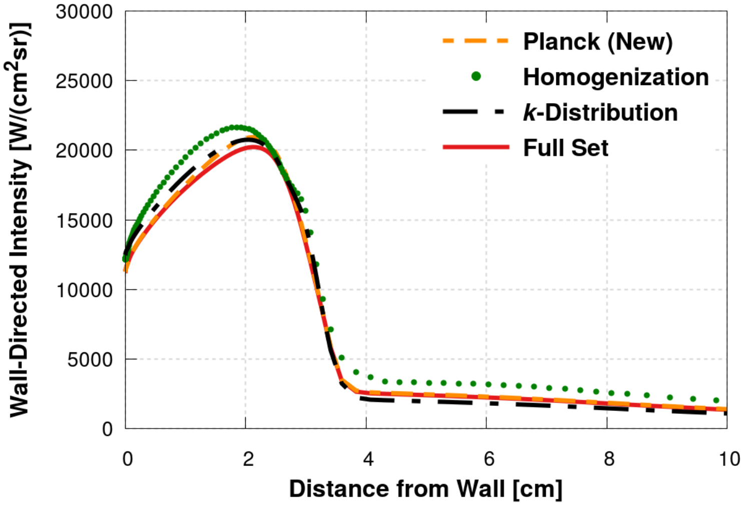

Figure 5.8: Total wall-directed intensity along stagnation LOS during meteor entry. Reduced-order solutions based on 10 × 10 systems.

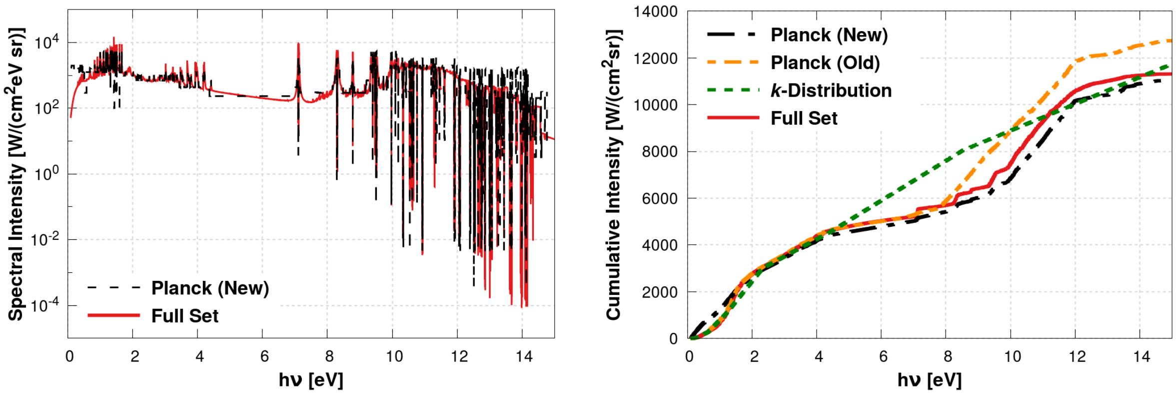

(a) Spectral Intensity

(b) Cumulative Intensity

Figure 5.9: Spectral and cumulative wall-directed intensities at the wall computed using the full set and 10 × 10 reduced-order systems for meteor entry.

5.4 Summary

This chapter examines the suitability of three reduced-order spectral modeling techniques – Planck-averaging, and statistics-based k-distribution and theory of homogenization – and the proposed non-equilibrium radiation grouping strategy. The geometric aspect of this study is simplified to solving the RTE along a single wall-directed normal direction. This allows reference solutions capturing minute spectral variations in the radiative environment to be computed using the hybrid SRB-LBL method. The same analysis is then repeated using reduced-order spectral models. The accuracy of different model reduction methods is assessed using both total radiative intensity and its distribution in frequency space. Radiative transfer calculations along stagnation line / wake flow LOSs are performed for different Earth and Jupiter entry problems. Planck-averaging and the two statistics-based approaches offer comparable levels of accuracy. However, convergence to the reference full set solution is slow and a large number of reduced-order groups are required to eliminate errors in total intensity predictions. A switch to Planck-averaging based on the new non-equilibrium grouping criteria allows not only total quantities of interest but also their detailed spectral variation to be predicted with a limited number of reduced-order groups. The model-reduction methodology outlined in the current work represents a two orders-of-magnitude speed-up with respect to narrow-band methods (and three to four orders with respect to original LBL approaches) and is ideal for coupled flow-radiation applications.

Chapter 6

Three-Dimensional Radiative-Hydrodynamics: Application to CO_2 Wake Flows

The current chapter combines different model-reduction techniques for resolving non-Boltzmann thermodynamics, chemical kinetics, and radiative transfer into a unified simulation procedure for solving complex three-dimensional flows. The MGME approach with adaptive binning allows for time-varying optimal reduced-order representation of the internal state population distribution while accounting for all collisional processes included in the state-to-state model. Similarly, radiative transfer calculations are performed efficiently by discretization in the spectral, angular, and spatial spaces. This reduction in computational overhead allows truly non-Boltzmann simulations with two-way coupling between the flow and radiation fields to be realized without simplifying approximations based on the tangent-slab method or local escape-factors.

Recent work on Martian atomspheric entry [226, 227, 228, 229] indicates that CO_2 infrared radiation (IR) dominates the total heat flux received by the backshell of spacecraft. These findings further underscore the impact of radiation on flowfield properties and flight characteristics at hypersonic entry speeds. However, simulations for CO_2 wake flows and associated IR radiation have largely been limited to the use of conventional MT models. Researchers have also modeled CO_2 vibrational non-equilibrium by defining independent temperatures for different modes (symmetric stretching, bending, asymmetric stretching) [230, 231]. Despite significant advances, these efforts still share a common shortcoming – internal vibrational states are forced into common mode-spanning Boltzmann distributions – which can lead to erroneous predictions under strong non-equilibrium. Additionally, existing research on the subject completely disregards the two-way coupling between thermochemistry and radiative transitions, with the radiative field computed simply as a post-processing step. Consequently, the proposed non-equilibrium methodology is applied in conjunction with the US3D flow solver to analyze the flowfield and radiative environment in the afterbody region of the Mars 2020 vehicle. This allows the present work to probe the possible influence of non-Boltzmann effects and non-local radiative emissions on CO_2 vibrational relaxation, bulk flow properties, and IR heating with unprecedented accuracy.

The current chapter is organized as follows: a) Section 6.1 presents the system of hydrodynamic equations while incorporating the MGME framework. b) The development of computationally efficient formulations for spectral properties and radiation-induced source terms from the CDSD-4000 database is delineated in Section 6.2. c) Results for non-equilibrium CO_2 wake flows and the resultant IR radiation around the Mars 2020 vehicle are discussed in Section 6.3. d) A summary for the chapter is provided in Section 6.4.

6.1 Hydrodynamic Governing Equations

The Maxwell transfer equations presented in Section 2.1 describe the evolution of bulk properties corresponding to individual internal states of chemical species and for the entire mixture under the combined effects of convection, diffusive or transport fluxes, and collision-induced volumetric changes. The familiar hydrodynamic equations of the Navier-Stokes form are derived using the Chapman-Enskog (CE) perturbation method [120, 121, 122]. This involves modeling the velocity distribution function f_{A_i} as a finite-order polynomial of the perturbation parameter ϵ [119]:

$$f_{\mathrm{A}_i} \;=\; f^0_{\mathrm{A}_i}\left(1 + \epsilon\,\phi^1_{\mathrm{A}_i} + \epsilon^2\,\phi^2_{\mathrm{A}_i}\right) + \mathcal{O}(\epsilon^3) \quad \forall\; i \in \mathcal{I}_{\mathrm{A}}\,,\; A \in \mathcal{S} \tag{6.1}$$

where $f^0_{\mathrm{A}_i}$ is the zeroth-order distribution function and $\phi^1_{\mathrm{A}_i}$ and $\phi^2_{\mathrm{A}_i}$ are its first and second-order perturbations, respectively. The perturbation parameter $\epsilon << 1$ in the hydrodynamic limit (similar to Knudsen number) where the gaseous mixture is collision dominated. The aforementioned form of f_{A_i} is substituted in the Boltzmann equation (Eq. 2.2). Comparing terms corresponding to the same order of ϵ yields the governing equations for $f^0_{\mathrm{A}_i}$, $\phi^1_{\mathrm{A}_i}$ and $\phi^2_{\mathrm{A}_i}$. A detailed description of the subsequent solution procedure and the requisite assumptions for ensuring uniqueness can be found in [119, 120]. Only the key observations from these detailed theses are highlighted here to better contextualize the flow governing equations used in the current study. The zeroth-order equations associated with ϵ^0 and defined using $f^0_{\mathrm{A}_i}$ and $\phi^1_{\mathrm{A}_i}$ constitute the system of Euler equations. The first-order equations, which introduce $\phi^2_{\mathrm{A}_i}$, translate into the more general Navier-Stokes system with transport/diffusive fluxes and volumetric source terms.

The different conservation equations are obtained based on the set of macroscopic collision invariants, *i.e.*, quantities that are conserved during collisions, assumed for a particular analysis. Thus, state-to-state CE method results in independent conservation equations for the density of individual internal states ρ_{A_i}, in addition to those for mixture momentum and total energy. Multi-temperature non-equilibrium models [4, 20] assume that different internal energy modes (vibration, rotation, electronic) equilibrate to Boltzmann distributions due to rapid intra-modal and selective inter-modal collisions (for equilibrium between disparate modes). This separation of time-scales between various types of collisional processes leads to the formulation of new collisional invariants. For instance, the two-temperature model assumes that the vibrational mode remains in equilibrium due to fast resonant vibrational (VV) transitions [19, 232]. The characteristic time for vibrational-translational (VT) interactions is much larger, engendering a state of non-equilibrium between the two modes. Thus, vibrational energy is defined as a collisional invariant because VT and other inelastic/reactive processes which transfer energy away from/to the vibrational modes cannot manifest themselves at such time-scales [121, 233]. This equilibration assumption replaces state-specific conservation equations with those for total species density $\rho_{\mathrm{A}} = \sum_{i \in \mathcal{I}_{\mathrm{A}}} \rho_{\mathrm{A}_i}$ and total vibrational energy.

Macdonald [130] provides a similar treatment for the MGME framework. The constitutive StS inelastic/reactive collisional processes are categorized as follows:

$$\tau_{\mathrm{react}} \simeq \tau_{\mathrm{inel}}^{bb'} >> \tau_{\mathrm{inel}}^{bb} \tag{6.2}$$

where τ_{react}, $\tau_{\mathrm{inel}}^{bb'}$, and $\tau_{\mathrm{inel}}^{bb}$ are the characteristic times associated with reactive processes (*e.g.*, dissociation, recombination, exchange), non-reactive transitions between bins (inter-bin), and non-reactive transitions within bins (intra-bin). The separation outlined in Eq. 6.2 is implicitly forced by the maximum entropy linear bin framework which assumes localized equilibrium within bins. Consequently, the mass and internal energy of groups are introduced as collisional invariants. In return, the hydrodynamic governing equations now include conservation equations for bin density and bin internal energy. The current study amalgamates these equations (for chemical species that are resolved using a multi-group reduced-order description) into the conventional two-temperature

(2-T) model [20]. It should be reiterated that the 2-T model assumes translational energy states to be in equilibrium at temperature T while vibrational and electronic modes are equilibrated at T_V. The hybrid system of conservation equations for mass, momentum, and energy are briefly summarized next. Readers are directed to [18, 20, 40] for a more comprehensive overview of flow equations, thermodynamics, chemical kinetics, transport properties, and energy coupling under the 2-T assumption.

6.1.1 Mixture Definition

The gaseous mixture comprising of atomic and molecular species is represented by $\mathcal{R}$. Chemical species for which a multi-group reduced-order StS description is obtained are included in set $\mathcal{S}$. The internal states for species $i \in \mathcal{S}$ are combined into $b(i)$ macroscopic bins. The remaining species modeled in the conventional manner as a unitary entity, with each internal mode described by only a single Boltzmann distribution, are included in $\mathcal{B}$. The present work focuses on low-speed Martian entry which translates into low predicted values ($\sim 0.5\%$) for the degree of ionization [234]. Thus, ionized species and free-electrons are neglected while developing the system of equations. The contributions of individual species (and bins) is summed to yield mixture mass density ρ and pressure P:

$$\rho = \sum \sum_{i \in \mathcal{S}} \sum_{b} \rho_i^b + \sum_{j \in \mathcal{S}} \rho_j \tag{6.3}$$

$$P = \sum_{i \in \mathcal{S}} \sum_{b} \rho_i^b \, \mathrm{R}_i \, T + \sum_{j \in \mathcal{S}} \rho_j \, \mathrm{R}_j \, T \tag{6.4}$$

The same process is repeated while defining internal energy e (including translational energy), enthalpy H, and total energy $\mathcal{E} = e + \frac{1}{2} \mathbf{u} \cdot \mathbf{u}$ per unit mass for the mixture. The Gordon-Mcbride thermodynamic database [235] (in its 9-coefficient polynomial form) is used to evaluate the enthalpy, entropy, and specific heat capacity for species $j \in \mathcal{B}$. Properties in this database are computed using the rigid-rotor harmonic-oscillator approximation with necessary modifications for anharmonicities, vibration-rotation interactions, rotational stretching, low-temperature quantum rotation, Fermi and Darling-Dennison resonance, and internal rotation [236]. The equilibrated translation and rotation modes are assumed to be fully excited with invariant heat capacities.

Thus, vibrational-electronic energy/entropy/heat capacity is easily computed by evaluating the total value of the required thermodynamic quantity at T_V and then subtracting the translational-rotational/formation components (rotational mode is modeled as a rigid rotor) [20, 237]. Section 2.3 provides a detailed description of bin-wise thermodynamics for the MGME framework. It should be noted that aggregate properties for species $i \in \mathcal{S}$ (to be used with conventional 2-T modeling) are obtained by forcing the constituent bins into a single Boltzmann distribution [238]. Both bin-wise and Boltzmann-aggregate thermodynamic properties have also been fitted using the NASA 9-coefficient polynomials (Appendix C). Furthermore, vibrational-electronic and translational-rotational components are split for $\mathcal{S}$ in the same manner as $\mathcal{B}$.

6.1.2 Mass Continuity Equations

The mass continuity equations comprise of independent conservation equations for bin-wise densities (species included in $\mathcal{S}$) and total species-wise densities (species included in $\mathcal{B}$):

$$\begin{aligned} \partial_t \rho_i^b + \boldsymbol{\nabla}_{\boldsymbol{x}} \cdot \left[\rho_i^b \left(\mathbf{u} + \boldsymbol{\mathcal{V}}_i^b\right)\right] &= \mathcal{M}_i^b \, \dot{\omega}_i^b \qquad b = 1, \ldots, b(i)\ , \quad \forall i \in \mathcal{S} && (6.5) \\ \partial_t \rho_j + \boldsymbol{\nabla}_{\boldsymbol{x}} \cdot \left[\rho_j \left(\mathbf{u} + \boldsymbol{\mathcal{V}}_j\right)\right] &= \mathcal{M}_j \, \dot{\omega}_j \qquad \forall j \in \mathcal{B} && (6.6) \end{aligned}$$

where symbol ∂_t is the partial time derivative $\partial/\partial t$. The mass production term due to chemical reactions for all species $j \in \mathcal{B}$ is formulated using the law of mass action:

$$\begin{aligned} \dot{\omega}_j &= \sum_{r=1}^{N_r^j} \left(\beta_{j,r} - \alpha_{j,r}\right) \left(R_{\mathrm{f},r} - R_{\mathrm{b},r}\right) && (6.7) \\ R_{\mathrm{f},r} &= K_r \prod_s \left(\rho_s \,/\, \mathcal{M}_s\right)^{\alpha_{s,r}} && (6.8) \\ R_{\mathrm{b},r} &= \bar{K}_r \prod_s \left(\rho_s \,/\, \mathcal{M}_s\right)^{\beta_{s,r}} && (6.9) \end{aligned}$$

where N_r^j is the total number of reactions included in the kinetics scheme for species j. The stoichiometric coefficients for reactants and products participating in the r^{th} reaction are represented by $\alpha_{s,r}$ and $\beta_{s,r}$. The forward and backward rates are determined in equations 6.8 and 6.9 using the rate coefficients K_r and $\bar{K}_r$. Forward rate coefficients are evaluated using Arrhenius fits from different kinetics databases [35, 36, 239, 240]. The corresponding coefficient for the backward direction is then calculated from the equilibrium constant and K_r through detailed balance. The net production rate for bins $\dot{\omega}_i^b$ is broken down into contributions from particle collisions and photochemical transitions. The collisional component stemming from state-specific energy exchange and chemical change is outlined in Appendix D. The impact of photochemistry during a two-way coupling between flow and radiation is discussed in Section 6.2.2. Although radiative transitions can induce chemical changes for all participating species (both in $\mathcal{S}$ and $\mathcal{B}$) [8, 49, 241], the present analysis is evolved strictly in the context of CO_2 IR radiation. However, the general form remains applicable while incorporating chemical effects generated by any radiative system into the MGME framework.

6.1.3 Mixture Momentum Equation

The mixture momentum equation requires no modifications and retains its original form from the 2-T model:

$$\partial_t (\rho \mathbf{u}) + \boldsymbol{\nabla}_{\boldsymbol{x}} \cdot (\rho \mathbf{u} \otimes \mathbf{u} + p \boldsymbol{\mathcal{I}}) = \boldsymbol{\nabla}_{\boldsymbol{x}} \cdot \boldsymbol{\tau} \tag{6.10}$$

6.1.4 Energy Equations

The 2-T assumption is derived on the basis of fast intra-modal and (selective) inter-modal processes resulting in translational-rotational equilibrium at T and vibrational-electronic equilibrium at T_V. Thus, the energy composition of the mixture is described using two independent equations associated with vibrational-electronic (e_V) and total ($\mathcal{E}$) energies:

$$\begin{aligned}\partial_t \rho e_V + \boldsymbol{\nabla}_{\boldsymbol{x}} \cdot (\rho\, e_V\, \mathbf{u}) + \boldsymbol{\nabla}_{\boldsymbol{x}} \cdot \sum_{i \in \mathcal{S}} \sum_{b} \rho_i^b\, \boldsymbol{\mathcal{V}}_i^b\, e_{V,i}^b + \boldsymbol{\nabla}_{\boldsymbol{x}} \cdot \sum_{j \in \mathcal{B}} \rho_j\, \boldsymbol{\mathcal{V}}_j\, e_{V,j} \\ = -\boldsymbol{\nabla}_{\boldsymbol{x}} \cdot \mathbf{q}_V + \Omega^{\mathrm{C}} + \Omega^{\mathrm{VT}} + \Omega_{\mathrm{rad}}\end{aligned} \tag{6.11}$$

$$\begin{aligned}\partial_t \rho \mathcal{E} + \boldsymbol{\nabla}_{\boldsymbol{x}} \cdot (\rho H \mathbf{u}) + \boldsymbol{\nabla}_{\boldsymbol{x}} \cdot \sum_{i \in \mathcal{S}} \sum_{b} \rho_i^b\, \boldsymbol{\mathcal{V}}_i^b\, h_i^b + \boldsymbol{\nabla}_{\boldsymbol{x}} \cdot \sum_{j \in \mathcal{B}} \rho_j\, \boldsymbol{\mathcal{V}}_j\, h_j \\ = \boldsymbol{\tau} : \boldsymbol{\nabla}_{\boldsymbol{x}} \mathbf{u} - \boldsymbol{\nabla}_{\boldsymbol{x}} \cdot \mathbf{q} + \Omega_{\mathrm{rad}}\end{aligned} \tag{6.12}$$

The heat flux vector resulting from vibrational-electronic and total energies is denoted by $\mathbf{q}_V$ and $\mathbf{q}$, respectively. The terms Ω^{C}, Ω^{VT}, and Ω_{rad} describe energy change due to vibrational-translational relaxation, chemistry vibrational-electronic coupling, and radiative heat transfer. Ideally, only the contributions of chemical species included in $\mathcal{B}$ should be included in defining e_V and the corresponding governing equation. A complete solution for MGME models with linear reconstruction requires independent equations for both bin-wise density ρ_i^b and internal energy $e^b_{\mathrm{int},i}$. Thus, the set of governing equations would be augmented by energy equations of the form [130]:

$$\begin{aligned} &\partial_t \rho_i^b \, e^b_{\mathrm{int},i} + \boldsymbol{\nabla}_{\boldsymbol{x}} \cdot \left(\rho_i^b \, e^b_{\mathrm{int},i} \, \mathbf{u} \right) + \boldsymbol{\nabla}_{\boldsymbol{x}} \cdot \boldsymbol{\mathcal{V}}_i^b \, e^b_{\mathrm{int},i} \\ &\quad = \; -\boldsymbol{\nabla}_{\boldsymbol{x}} \cdot \mathbf{q}^b_{\mathrm{int},i} + \Omega^b_{\mathrm{col},i} + \Omega^b_{\mathrm{rad},i} \qquad b = 1, \, \ldots, \, b(i) \; , \quad \forall i \in \mathcal{S} \end{aligned} \tag{6.13}$$

where $\Omega^b_{\mathrm{col},i}$ and $\Omega^b_{\mathrm{rad},i}$ represent changes in bin internal energy due to collisional and radiative processes, respectively. Equation 2.17 provides a general definition for $\Omega^b_{\mathrm{col},i}$. A closed-form expression for $\Omega^b_{\mathrm{rad},i}$ can be derived in a similar manner using the analysis in Section 6.2.2. However, as a first approximation, no independent bin energy equations are solved in the current calculations and the total internal energy of bins is divided between the mixture translational-rotational and vibrational-electronic energies (as evidenced by Eq. 6.11) [242]. In the MGME context, this implies that vibrational states within individual bins are in localized Boltzmann distributions at T_V. Efforts are currently underway to suitably modify the US3D flow solver and model bin-wise energies (and corresponding temperatures) through independent equations.

6.1.5 Non-equilibrium Closure Relationships

The Park model [20, 35] is used to account for thermal non-equilibrium ($T \neq T_V$) while computing rate-constants for non-StS species in $\mathcal{B}$. This involves defining a single rate-controlling temperature for both forward and backward directions based on geometric averaging: T^{1-q} and ${T_V}^q$. The parameter q is specific to a particular reaction and can vary between the forward/backward directions. Property fits for bin-averaged rate coefficients relevant to the current study (CO_2 is the only species included in $\mathcal{S}$) are presented in Section 2.3. The Blottner viscosity model is used to compute shear viscosity μ for the multi-species mixture [243]:

$$\boldsymbol{\tau} \;=\; \mu \left(\boldsymbol{\nabla}_{\boldsymbol{x}} \mathbf{u} + {\boldsymbol{\nabla}_{\boldsymbol{x}}}^{T} \mathbf{u} - \frac{2}{3} (\boldsymbol{\nabla}_{\boldsymbol{x}} \cdot \mathbf{u}) \boldsymbol{\mathcal{I}} \right) \tag{6.14}$$

The thermal conductivities corresponding to different energy modes are modeled using the Eucken approximation [244, 245] with the Wilke mixing rule [246, 247]:

$$\mathbf{q}_V = -\left(\lambda^{\text{vib}} + \lambda^{\text{el}}\right) \boldsymbol{\nabla}_{\boldsymbol{x}} T_V \,, \qquad \mathbf{q} = -\left(\lambda^{\text{tr}} + \lambda^{\text{rot}}\right) \boldsymbol{\nabla}_{\boldsymbol{x}} T + \mathbf{q}_V \tag{6.15}$$

where λ^{vib}, λ^{el}, λ^{tr}, and λ^{rot} are mixture thermal conductivities for the vibrational, electronic, translational, and rotational modes, respectively. The diffusion velocities $\boldsymbol{\mathcal{V}}$ obey Fick's law and are approximated using the self-consistent effective binary diffusion model [248, 249]. The vibrational-translational energy exchange is computed assuming a Landau-Teller type relaxation form for Ω^{VT} [33, 250]. The inter-species relaxation time for V-T exchange is based on the Millikan-White formula [34] and includes Parks high-temperature correction [4, 19]. The vibrational-electronic coupling term Ω^{C} is computed using a non-preferential dissociation model [20]. It should be noted that Chapman-Enskog analysis [251] can yield more rigorous descriptions for transport/diffusive fluxes and the coupling terms. However, these are overlooked in favor of semi-empirical approaches due to the present analysis focusing on low-speed planetary entry (lower peak temperatures and negligible ionization). Furthermore, in the interest of limiting complexity, the Blottner viscosity fits of all reduced-order bins for species $i \in \mathcal{S}$ are assigned a common value equal to the standard species model. Internal energy relaxation for bins is modeled using Landau-Teller relaxation with the same Millikan-White relaxation parameters as the complete species, as reported in the literature [35, 36]. These assumptions allow straightforward comparisons with traditional non-equilibrium modeling approaches. A first-order estimate of non-Boltzmann effects is obtained with bin-densities ρ_i^b no longer forced to adhere to a Boltzmann distribution. Conversely, a standard 2-T flowfield is recovered in case such non-Boltzmann deviations are absent.

6.2 Radiation Database for CO_2

The current section describes the reformulation of rovibrational IR radiative transitions for CO_2 in order to ensure consistency with an MGME-based reduced-order description for vibrational non-equilibrium. This entails extending the smeared band method [8, 105, 252] to compute spectral variation in absorption and emission behavior directly from non-Bolzmann bin properties. This modification is advantageous in two regards: a) Additional costs associated with unpacking bins into state-specific population distributions and then modeling state-to-state radiative transitions (traditionally done when introducing non-Boltzmann effects [49, 73, 253, 254]) are avoided. b) Absorption and emission coefficients due to photochemical processes between each bin-pair are separated. This allows radiative contributions to bin-specific mass change source terms $\dot{\omega}_i^b$ to be obtained in a straightforward manner.

6.2.1 Smeared Band Method

The starting point for the current analysis on CO_2 IR radiation is the CDSD-4000 database [97, 255]. The characteristics of radiative transitions in the CDSD database are determined from detailed quantum chemistry calculations involving effective Hamiltonian and dipole moment operators. The various operator parameters for these calculations are calibrated in order to obtain good agreement with experimentally determined line positions [256] and intensity values [257]. This database includes approximately 574 million unique transitions for the primary isotopologue of CO_2 divided into three distinct bands located at 1.5 μm, 2.7 μm, and 4.5 μm. Additionally, the maximum energy considered in CDSD-4000 corresponds to the dissociation limit of the ground electronic state of CO_2. This ensures better compatibility with the CO_2 chemistry StS model (Section 3.3) being used in the current study which also excludes electronic excitation. However, a key difference still remains: CDSD-4000 details radiative transitions between rovibrational states whereas the CO_2 chemistry model based on the work of Kustova *et al.* [140, 141] is vibrational state-specific. A rovibrational description (potentially involving $\mathcal{O}(10^6)$ individual states) of state-to-state CO_2 chemistry is computationally impractical in the current context. Thus, the more reasonable alternative based on reducing the fidelity of CDSD-4000 from rovibrational to vibrational specific is developed in this section. More rigorous formulations for effecting this transformation are under development [258, 259] but have not been considered here.

A line-by-line approach based on CDSD-4000 (574 million unique transitions) is ill-suited to three-dimensional flow-radiation coupled simulations. Instead, the database is reduced to a more convenient form using the smeared band method [8, 105]. The resultant spectral model is developed as a function of frequency, temperature, lower rovibrational level, and upper rovibrational level. First, the molecular band is divided into intervals $\Delta\nu$ to create a spectral grid consisting of discrete frequencies ν_m. Then, the absorption cross-sections within grid intervals are summed as follows:

$$\sigma_\nu^{i-j}(T_V) = \sum_{\substack{\forall k \\ \nu_k^{\mathrm{CL}} \in [\nu,\nu+\Delta\nu]}} \left[\frac{\mathcal{I}_k^{i-j}}{\Delta\nu} \frac{1}{1-\exp\{-\mathrm{h_P}\,\nu/(\mathrm{k_B} T_{ref})\}} \frac{Q_{\mathrm{CO_2}}(T_{ref})}{Q_{\mathrm{CO_2}}(T_V)} \frac{\exp\{-\epsilon^i_{\mathrm{CO_2}}/(\mathrm{k_B} T_V)\}}{\exp\{-\epsilon^i_{\mathrm{CO_2}}/(\mathrm{k_B} T_{ref})\}} \right] \tag{6.16}$$

where i and j represent the lower and upper rovibrational levels of the transition, respectively, and $Q_{\mathrm{CO_2}}$ is the total CO_2 rovibrational partition function. The transition strength of the k^{th} line from CDSD-4000 is denoted by $\mathcal{I}_k^{i-j}$ and has a centerline frequency ν_k^{CL}. Equation 6.16 is evaluated for each spectral grid point and the subscript in ν_m has been dropped for notational convenience. The smeared band method assumes a constant line shape of $(1/\Delta\nu)$ over the spectral interval – $\nu_k^{\mathrm{CL}} \in [\nu_m, \nu_{m+1} = \nu_m + \Delta\nu]$ – in which a particular transition k is located, instead of a complex function that varies with temperature, pressure, and $|\nu_k^{\mathrm{CL}} - \nu|$. This description of line broadening not only simplifies calculations but also ensures that centerline radiative properties are exactly recovered from a spectral integral. Additional details on the smeared band method and its application to non-equilibrium radiation problems can be found in [8, 105]. The smeared band method has been previously used to study CO_2 IR [109, 225, 227] and other molecular band [216, 260, 261] radiation tranfer in hypersonic flows. The normalized absorption cross-sections in Eq. 6.16 can simply be scaled by total CO_2 number density $N_{\mathrm{CO_2}}$ to obtain the absorption/emission terms for rovibrational levels in a Boltzmann distribution at temperature T_V. The breakdown of the Boltzmann equilibrium assumption requires the following non-equilibrium correction factor for rovibrational level number densities [4, 109]:

$$\phi^{i-j} \;=\; \frac{n^{j}_{\mathrm{CO_2}}}{n^{j,\mathrm{Bol}}_{\mathrm{CO_2}}}\,\frac{n^{i,\mathrm{Bol}}_{\mathrm{CO_2}}}{n^{i}_{\mathrm{CO_2}}} \;=\; \frac{n^{j}_{\mathrm{CO_2}}}{n^{i}_{\mathrm{CO_2}}}\,\frac{g^{i}_{\mathrm{CO_2}}}{g^{j}_{\mathrm{CO_2}}}\;\exp\left\{\frac{-(\epsilon^{i}_{\mathrm{CO_2}}-\epsilon^{j}_{\mathrm{CO_2}})}{\mathrm{k_B}T_V}\right] \tag{6.17}$$

where $n^{j}_{\mathrm{CO_2}}$ and $n^{j,\mathrm{Bol}}_{\mathrm{CO_2}}$ are the predicted (could be non-Boltzmann) and corresponding Boltzmann (at T_V) rovibrational number densities, respectively. Using ϕ, the absorption ($\kappa^{i,j}_{\nu}$) and emission ($j^{i,j}_{\nu}$) spectrum is defined in terms of $\sigma^{i,j}_{\nu}$ as follows [4, 109]:

$$\kappa^{i-j}_{\nu} \;=\; \frac{n^{i}_{\mathrm{CO_2}}}{n^{i,\mathrm{Bol}}_{\mathrm{CO_2}}}\,N_{\mathrm{CO_2}}\,\sigma^{i-j}_{\nu}\,\left[1\,-\,\phi^{i-j}\exp\left\{-\mathrm{h_P}\,\nu/(\mathrm{k_B}T_V)\right\}\right] \tag{6.18}$$

$$J^{j-i}_{\nu} \;=\; \kappa^{i-j}_{\nu}\,\frac{2\mathrm{h_P}\,\nu^3}{\mathrm{c}^2}\,\frac{\phi^{i-j}}{\left[\exp\left\{\mathrm{h_P}\,\nu/(\mathrm{k_B}T_V)\right\}\,-\,\phi^{i-j}\right]} \tag{6.19}$$

These relationships indicate that only σ^{i-j}_{ν} needs to be pre-computed as a function of frequency and T for each combination of i and j. This represents an excessive amount of data which is not even immediately congruous with the current vibrational-specific chemistry model. The first step in mitigating these shortcomings is splitting the total rovibrational energy into rotational and vibrational contributions [238]. The quantum state of internal state i is defined as $(v_i : (v_1, v_2, v_3), J_i)$, where v_i and J_i represent the vibrational (Section 3.3) and rotational configurations, respectively. The splitting operation on state i yields the following relationship:

$$\epsilon^{i}_{\mathrm{CO_2}}\,(v_i, J_i) \;=\; \epsilon^{i}_{(\mathrm{vib,CO_2})}\,(v_i) \,+\, \epsilon^{i}_{(\mathrm{rot,CO_2})}\,(J_i) \tag{6.20}$$

The vibrational and rotational components are considered to be uncorrelated. The energy of the rotational mode is computed using the rigid-rotor model [126]. These approximations also posit that the number of possible rotational configurations (and their corresponding energies/degeneracies) is the same for each vibrational state. Furthermore, since this study focuses on low-speed Martian entry which previous studies [227] indicate experience little thermal non-equilibrium, the rotational mode is assumed to be in equilibrium at T_V as well. The total internal partition function $Q_{\mathrm{CO_2}}$ is now expressed as a product of rotational $Q_{(\mathrm{rot,CO_2})}$ and vibrational $Q_{(\mathrm{vib,CO_2})}$ partition functions. The state-specific description for σ^{i-j}_{ν} is reduced further by introducing assumptions enshrined in the MGME framework. Thus, vibrational levels are assumed to be in a state of thermal equilibrium (at T_V) within their respective bins, whereas rotational modes continue remaining in equilibrium at T_V. The reconstructed number density is:

$$n^i_{\mathrm{CO_2}} = N^l_{\mathrm{CO_2}} \frac{g^i_{\mathrm{CO_2}} \; \exp\Big\{-\epsilon^i_{(\mathrm{rot,CO_2})}/(\mathrm{k_B}\, T_V)\Big\} \;\; \exp\Big\{-\epsilon^i_{(\mathrm{vib,CO_2})}/(\mathrm{k_B}\, T_V)\Big\}}{\hat{Q}^l_{\mathrm{CO_2}}} \tag{6.21}$$

where vibrational level v_i (corresponding to rovibrational state i) belongs to the l^{th} bin and $N^l_{\mathrm{CO_2}}$ is the requisite bin density. The bin partition function $\hat{Q}^l_{\mathrm{CO_2}}$ is defined as:

$$\hat{Q}^l_{\mathrm{CO_2}} \;\; = \;\; \hat{Q}^l_{(\mathrm{vib,CO_2})}(T_V)\, Q_{(\mathrm{rot,CO_2})}(T_V) \tag{6.22}$$

The rotational contribution is constant for all bins. On the other hand, vibrational component $\hat{Q}^l_{(\mathrm{vib,CO_2})}$ is obtained by summing over all individual vibrational levels included in the l^{th} bin. The bin-wise thermalization assumption allows an aggregate absorption cross-section to be defined, combining all radiative transitions from vibrational levels in bins l to u:

$$\hat{\sigma}^{l-u}_\nu \;=\; \sum_{\substack{\forall j \\ v_j \in \mathcal{I}_u}} \sum_{\substack{\forall i \\ v_i \in \mathcal{I}_l}} \sigma^{i-j}_\nu \frac{Q_{\mathrm{CO_2}}}{\hat{Q}^l_{\mathrm{CO_2}}} \;=\; \sum_{\substack{\forall j \\ v_j \in \mathcal{I}_u}} \sum_{\substack{\forall i \\ v_i \in \mathcal{I}_l}} \sigma^{i-j}_\nu \frac{Q_{(\mathrm{vib,CO_2})}(T_V)}{\hat{Q}^l_{(\mathrm{vib,CO_2})}(T_V)} \tag{6.23}$$

where $\mathcal{I}_u$ and $\mathcal{I}_l$ represent the set of vibrational levels included in bins u and l, respectively. The bin-invariant rotational partition function cancels out. Thus, the rotational component, with the assumption that it is uncorrelated with vibrational configuration, never needs to be separately evaluated while computing the aggregate cross-section and the resultant radiative properties. The bin-pair absorption and emission coefficients are obtained in a straightforward manner after scaling with the appropriate bin density (instead of total $\mathrm{CO_2}$ density):

$$\hat{\kappa}^{l-u}_\nu \;\; = \;\; N^l_{\mathrm{CO_2}}\, \hat{\sigma}^{l-u}_\nu \,\Big\{1 \,-\, \phi^{l-u} \exp\left[-\mathrm{h_P}\,\nu/(\mathrm{k_B} T_V)\right]\Big\} \tag{6.24}$$

$$\hat{j}^{u-l}_\nu \;\; = \;\; \hat{\kappa}^{l-u}_\nu \, \frac{2\mathrm{h_P}\,\nu^3}{\mathrm{c}^2} \, \frac{\phi^{l-u}}{\left\{\exp\left[\mathrm{h_P}\,\nu/(\mathrm{k_B} T_V)\right] \,-\, \phi^{l-u}\right\}} \tag{6.25}$$

The non-equilibrium correction factor ϕ^{l-u} is now computed using the predicted and corresponding Boltzmann bin number densities. Using these equations, emission coefficients for the $4.5\,\mu$m band originating from a Boltzmann distribution at 4,100 K for different bin-pairs and normalized for number density are presented in Fig. 6.1.

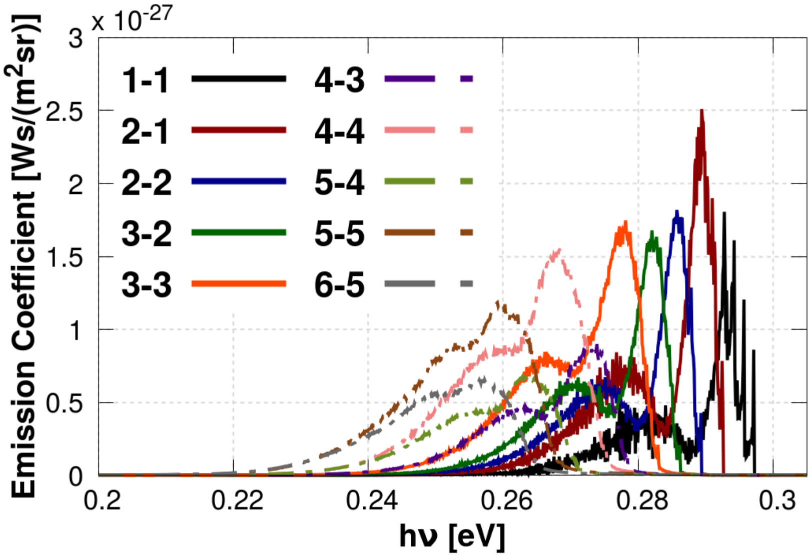

Figure 6.1: Normalized emission coefficients for the 4.5 μm band originating from a Boltzmann distribution at 4100 K.

Although the smeared band assumption can become inaccurate in optically-thick regions (error in total surface flux upto 20% in some cases), these discrepancies are significantly smaller in the afterbody region which is characterized by intermediate optical thickness. Moreover, any bias introduced through the smeared band method relative to line-by-line modeling is the same for both the reduced-order StS and conventional flow simulations. Therefore, the spectral modeling approach presented here represents a computationally efficient means of enabling consistent comparisons between the two flowfield models and isolating the impact of non-Boltzmann population distributions. The CO_2 IR bands encompass narrow regions in frequency space (~ 0.1 eV) as compared to the much wider spectral distributions (> 15 ev) encountered in Earth/Jovian entry problems discussed in Chapter 5. A relatively fine grid resolution $\Delta\nu = 1$ cm^{-1} yields a discretized spectral space consisting of only about 1000 points. Spectral models based on the application of the smeared band method to such spectral grids offer excellent agreement with the exact line-by-line approach. The reduced-order wide-band models presented in Section 4.3 would only provide limited gains in terms of computational efficiency but introduce additional sources of uncertainty. Therefore, they have not been incorporated into the current study on CO_2 IR radiation. However, it should be noted that implementing any alternative spectral models such as the line-by-line approach or the wide-bands models would only require modifications to Eq. 6.16.

6.2.2 Self-consistent Radiation-Flowfield Coupling

The development of bin-wise absorption and emission coefficients allows changes in bin densities due to photochemical processes to be determined in a straightforward manner. Spontaneous emission based on the radiative transitions from vibrational levels included in CO_2 bin u (upper) to vibrational levels in CO_2 bin l (lower) are a result of the following kinetic process:

$$\text{Spontaneous Emission: } \mathrm{CO}_2(v_j) \quad \longrightarrow \quad \mathrm{CO}_2(v_i) + \mathrm{h_P}\,\nu \qquad i \in \mathcal{I}_l\ , \quad j \in \mathcal{I}_u \tag{6.26}$$

where $\mathrm{h_P}\nu$ is the emitted photon. Thus, the angularly-spectrally integrated emission term corresponds to the rate at which radiative transitions that result in de-excitation from bins u to l. A bin-averaged rate coefficient that is consistent with the law of mass action form for chemical change can be defined as follows:

$$\bar{K}^{\mathrm{em}}_{u-l} \quad = \quad \frac{\mathcal{M}_u}{\rho_u\,\mathrm{N_A}} \int_{\nu_i}^{\nu_f} \frac{\hat{J}^{u-l}_{\nu}}{\mathrm{h_P}\,\nu}\, 4\pi\, d\nu \tag{6.27}$$

where $\hat{J}^{u-l}_{\nu}$ is the emission coefficient for transitions between vibrational bins u and l for frequency ν, and ρ_u and $\mathcal{M}_u$ $(= \mathcal{M}_{\mathrm{CO}_2})$ are the partial density and molar mass of the u^{th} CO_2 vibrational bin. Similarly, kinetic processes that are initiated by an interaction with a photon can result in stimulated emission and absorption:

$$\text{Stimulated Emission:} \quad \mathrm{CO}_2(v_j) + \mathrm{h_P}\,\nu \ \longrightarrow\ \mathrm{CO}_2(v_i) + 2\,\mathrm{h_P}\nu \qquad i \in \mathcal{I}_l\ , \quad j \in \mathcal{I}_u \tag{6.28}$$

$$\text{Absorption:} \quad \mathrm{CO}_2(v_i) + \mathrm{h_P}\,\nu \ \longrightarrow\ \mathrm{CO}_2(v_j) \qquad i \in \mathcal{I}_l\ , \quad j \in \mathcal{I}_u \tag{6.29}$$

The effective rate of absorption is obtained by subtracting out the rate of stimulated emission which reverses the effect of the kinetic process in Eq. 6.29. This is done while defining the operative value of the absorption coefficient in the line-by-line spectral model itself. Thus, the resultant absorption rate represents excitation of vibrational levels from bins l to u through energy gained from the incoming photon. The rate coefficient for this process depends on both $\hat{\kappa}^{l-u}_{\nu}$ and the angularly/spectrally integrated radiative intensity at a given spatial location:

$$K^{\mathrm{ab}}_{l-u} \;=\; \frac{\mathcal{M}_l}{\rho_l\,\mathrm{N_A}} \int_{\nu_i}^{\nu_f} \left(\frac{\hat{\kappa}^{l-u}_{\nu}}{\mathrm{h_P}\,\nu} \oint_{4\pi} I_\nu d\boldsymbol{\Omega} \right) d\nu \tag{6.30}$$

where $\hat{\kappa}^{l-u}_{\nu}$ is the absorption coefficient for transitions between vibrational bins l and u for frequency ν. The evaluation of K^{ab}_{l-u} for the LBL approach is computationally challenging because of the dependence on non-local radiative intensity and the need to recompute absorption coefficients for individual transitions for all relevant frequency ranges. The current framework overcomes this problem through a combination of reduced-order models for thermochemistry and radiative properties, and an efficient RTE solver based on finite volume and discrete ordinate methods. The following chemical change source terms arising from radiative transitions are added to the species continuity equation for the l^{th} $\mathrm{CO_2}$ vibrational bin:

$$\dot{\omega}^{l}_{\mathrm{rad,CO_2}} \;=\; \sum_{\forall u | u \neq l} \left(-K^{\mathrm{ab}}_{l-u}\,\frac{\rho_l}{\mathcal{M}_l} \,+\, \bar{K}^{\mathrm{em}}_{u-l}\,\frac{\rho_u}{\mathcal{M}_u} \right) \tag{6.31}$$

Similarly, volumetric energy addition due to net radiative heat flux is defined as [262]:

$$\Omega_{\mathrm{rad}} \;=\; -\boldsymbol{\nabla}_{\boldsymbol{x}} \cdot \mathbf{q}_{\mathrm{rad}} \;=\; -\boldsymbol{\nabla}_{\boldsymbol{x}} \cdot \int_{\nu_i}^{\nu_f} \oint_{4\pi} I_\nu\,\boldsymbol{\Omega}\,d\Omega\,d\nu \tag{6.32}$$

This source term is included in both the mixture total energy and vibrational-electronic energy hydrodynamic equations. The IR radiation transitions being studied here occur between the different vibrational levels (or the reduced-order bins). The resultant radiative heat flux represents a spatial redistribution of vibrational energy in the domain. Thus, the energy change term Ω_{rad} has been added to the vibrational-electronic energy conservation equation as well. Although the rate coefficients stemming from photochemical processes are developed for $\mathrm{CO_2}$, a similar approach can be applied when describing radiation-induced chemical change within the MGME framework. A more general overview of the radiation-chemistry coupling, including state-to-state analysis, can be found in [8, 9, 263]. It should be noted that equations 6.26 and 6.30 can be reformulated using the fundamental Einstein coefficients A_{ji}, B_{ij}, and B_{ji} [8, 12, 218]. However, it is the author's view that the functional definitions for $\bar{K}^{\mathrm{em}}_{u-l}$ and K^{ab}_{l-u} presented here provide a more physically intuitive link between bin-wise chemical changes and the underlying radiative processes (which have A_{ji}, B_{ij}, B_{ji} embedded in them).

6.3 Results

The new reduced-order state-specific non-equilibrium framework has been used to improve predictive capabalities of the US3D flow solver [113, 114, 115]. The US3D code solves the chemically reacting non-equilibrium Navier-Stokes equations on unstructured grids using implicit data-parallel line-relaxation based on upwind numerical flux functions. This entails computing inviscid fluxes using the modified Steger-Warming flux splitting method [264, 265] with second-order accurate MUSCL extrapolation and a Min-Mod limiter [266]. Viscous fluxes are computed using gradients based on the weighted least-squares fit method. The US3D solver has been used extensively to study a wide variety of hypersonic flow problems including afterbody wakes [115, 267, 268, 269, 270]. The standard Mars gaseous mixture comprising of five species – CO_2, CO, O_2, C and O – is considered in the present analysis [240]. Reduced-order StS calculations replace CO_2 with 10 vibrational bins (Section 3.3), which provides an optimal trade-off between accuracy and computational speed. All other species in the mixture are treated conventionally.

Absorption/emission spectra and subsequent radiative transfer calculations are performed using the non-equilibrium radiation (NERO) library [225]. This library is being developed by the author to analyze complex three-dimensional radiative fields at reduced computational outlays by incorporating efficient numerical discretization techniques for RTEs and reduced-order modeling in frequency space. The three main bands for CO_2 IR radiation – $1.5\,\mu$m, $2.7\,\mu$m and $4.5\,\mu$m – are considered in the present work. The smeared band technique is used to formulate band-wise spectral models, each comprising of 1000 frequency points. A total of 170 discrete quadrature directions and 10 sub-iterations (to correct for circular dependencies during mesh-sweeps) are found to be sufficient for accurately modeling the radiation field around typical afterbody geometries. The finite-volume based RTE solver has been verified using canonical test cases such as radiative transfer inside a sphere with prescribed temperature profiles [11]. Additionally, afterbody surface radiative heat flux estimates obtained using NERO for the conventional 2-T flowfield are in excellent agreement with previous studies based on detailed line-by-line models and ray-tracing calculations [13, 227]. Verification test problems are discussed in greater detail in Appendix E. The flowfield solution is accessed by NERO after a pre-defined number of iterations (set to $5,000$ for this study). This information is used to update the spectral properties and re-compute spatially resolved, angularly integrated radiative intensity. Furthermore, in coupled mode, the volumetric radiative source terms for both species (Eq. 6.31) and energy (Eq. 6.32) equations are determined and then passed on to the flow solver.

6.3.1 Simulation Methodology

The present work is aimed at characterizing the interactions between flow structures, thermochemistry, and radiation for the Mars 2020 vehicle [116, 117]. The upstream flow conditions are: $\mathrm{V}_\infty = 3.9\,\mathrm{km/s}$, $\rho_\infty = 1.84 \times 10^{-3}\,\mathrm{kg/m^3}$, and angle-of-attack in the $x-z$ plane $\alpha = 15.8\,\mathrm{deg}$. These conditions correspond to the trajectory point at $t = 91.5\,\mathrm{s}$ and result in high backshell radiative heat flux as identified by previous studies [13, 227]. Supersonic inflow and outflow conditions are imposed on the outer periphery of the flow-domain. The surface of the spacecraft is assumed to be a no-slip, isothermal ($T_{\mathrm{wall}} = 523$ K), super-catalytic wall. The super-catalytic boundary condition, as outlined in [271], is a conservative limiting case for design purposes when not modeling exact finite-rate surface reactions. It assumes that the gaseous mixture is forced back to its freestream composition and the available mixture chemical enthalpy is entirely reclaimed at the wall. This approximation has been widely used in aerothermal analysis of previous Martian missions such as the Mars Exploration Rover (MER), Phoenix, and Mars Science Laboratory (MSL). The flowfield is assumed to be laminar and no special turbulence models are employed for the present work.

The computational mesh for the current study is illustrated in Fig. 6.2. Certain features, such as a sharp step between the heatshield-backshell juncture, which were present in the original outer mold line of the Mars 2020 capsule have been simplified in the interest of reducing simulation complexity. The resultant point-matched, multiblock structured mesh comprises of $1,740,800$ volumetric elements and $13,600$ elements on the vehicle surface. The original mesh has also been tailored at the outer grid boundary while clustering off-wall normal cells to allow sufficient resolution of the bow shock and boundary layer. Additional details on grid generation, element distribution, and mesh convergence for the Mars 2020 afterbody envrioment can be found in [13, 272, 273].

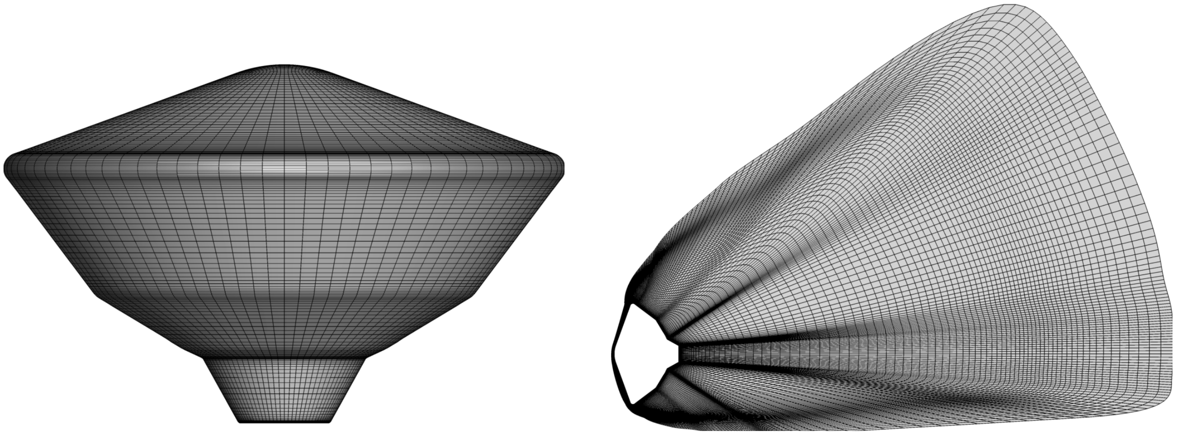

(a) Surface grid **(b)** Along the $y = 0\,\mathrm{m}$ plane

Figure 6.2: Computational mesh for modeling the Mars 2020 wake flow.

Aerothermodynamic simulation best practices favored by previous work on afterbody heating for the Mars 2020 and Mars Science Laboratory missions [13, 274] have been adopted to obtain statistically converged flowfield and surface results. This involves first converging the forebody flowfield and then performing unsteady calculations with global time-stepping while computing running means of afterbody surface heat flux. The flowfield is considered to be converged once the change in the running means is below a certain threshold. All subsequent analysis is then performed on the mean flowfield and the resultant radiation transfer phenomenon. Three sets of simulations are compared – first using the conventional 2-T Boltzmann approach (decoupled from radiation), next based on the reduced-order state-specific thermochemistry model (decoupled from radiation), and lastly with coupled reduced-order thermochemistry and radiation.

6.3.2 Decoupled Radiation

6.3.2.1 Flow Phenomenology

This section compares the difference in flowfield characteristics for the conventional 2-T and the ten bin-based StS approaches [275]. Figure 6.3 presents the distribution of the translational-rotational temperature T, vibrational-electronic temperature T_V, and total CO_2 mass-fraction Y_{CO_2} along the $y = 0\,\mathrm{m}$ plane. Individual streamlines and lines-of-sight (LOSs) for analyzing the evolution of flowfield and radiative intensity are also outlined. The typical dynamics of wake flows are clearly

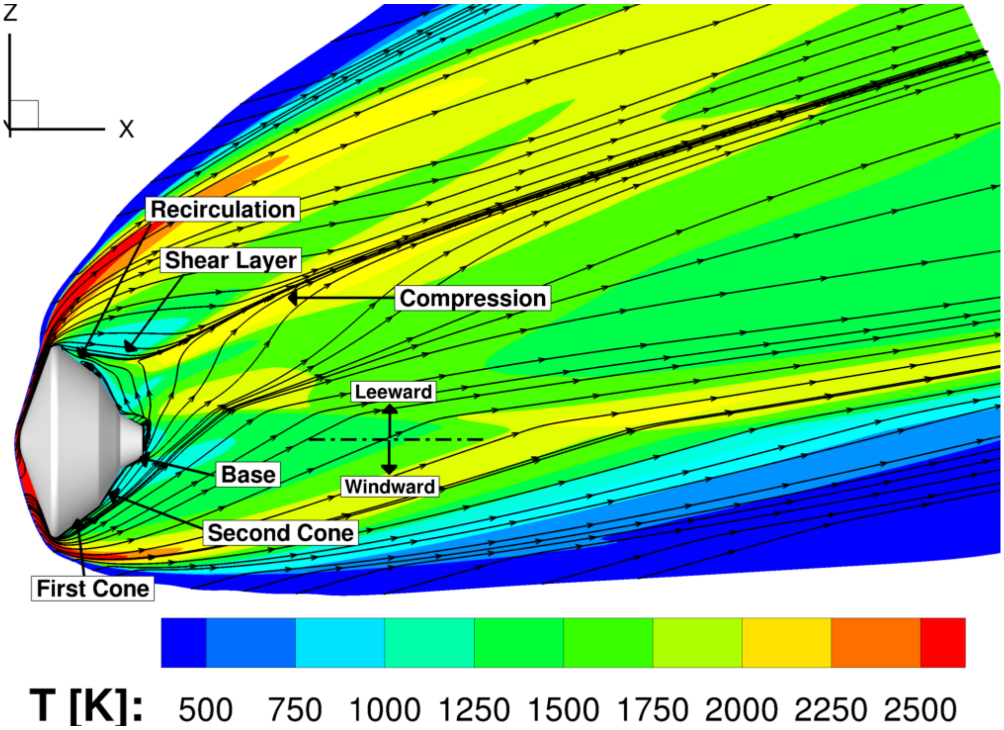

(a) Translational-rotational temperature T

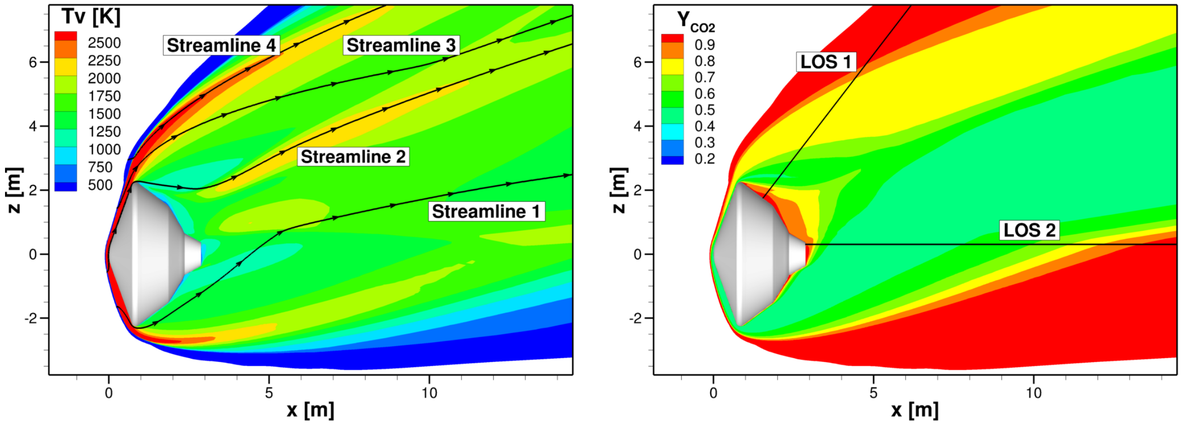

(b) Vibrational-electronic temperature T_V **(c)** Total CO_2 density

Figure 6.3: Distribution for T, T_V, and ρ_{CO_2} along the $y = 0\,\mathrm{m}$ plane for the 10 bin-based StS model. Individual streamlines and LOSs for analyzing flowfield and radiative intensity, respectively, are also defined.

captured through the flow streamlines in Fig. 6.3a. A detached bow shock is formed ahead of the spacecraft which rapidly converts kinetic energy into internal energy resulting in a sharp increase in temperature and the onset of thermochemical non-equilibrium. The strength of the shock, characterized by the sudden change in properties across it, diminishes as it stretches downstream of the vehicle. The flow undergoes rapid expansion as it travels around the shoulder. The rate at which this temperature/pressure change occurs and the likelihood that the flow would be "frozen" in a state of non-equilibrium decreases as distance from the spacecraft surface increases. Despite this drop in temperature, the flowfield continues to be dominated by CO, O, and O_2 due to the large characteristic time-scales for CO_2 recombination [276]. Viscous and pressure forces (which dominate inertial forces in the near-wake region) together result in the boundary layer originating from the vehicle surface separating and forming a free shear layer. A combination of viscous effects and an adverse pressure gradient in the immediate vicinity of the vehicle results in the flow past the shoulder eventually separating and forming a recirculation region. Since, the current simulation has been performed for $\alpha = 15.8\,\text{deg}$, the system of rotating vortices typifying this region are no longer symmetric. Instead, the delay in separation on the windward side results in the recirculation region being skewed towards the leeward side with large vortices on the leeward first cone and the base and smaller vortices near the windside second cone. Further downstream the flow turns into itself and undergoes compression upon reaching the outer wake. The asymmetry due to a non-zero angle of attack also induces higher angles of deflection for streamlines moving from the windward side to the leeward side and results in stronger compression shocks and higher temperatures on the leeward side.

6.3.2.2 Non-Boltzmann Thermochemistry

The trajectory profile for Mars entry is characterized by relatively low freestream velocities. Consequently, the conventional 2-T model, barring narrow isolated zones around the bow shock and the shoulder, yields similar predictions for both T and T_V. This behavior has also been observed in previous studies focusing on wake flows during Mars entry [227, 277]. Minimal differences in T and T_V values further underpins the fact that conventional multi-temperature models fail to sufficiently resolve non-equilibrium effects stemming from complex thermal relaxation mech-

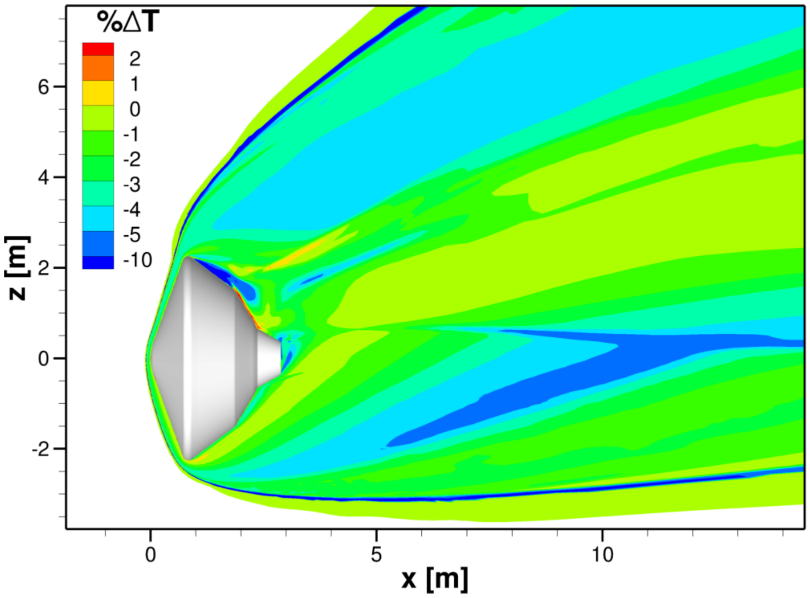

Figure 6.4: Percentage difference in predicted translational-rotational temperature T between bin-based StS and 2-T models: $(T^{\text{StS}} - T^{\text{2-T}})\,/\,T^{\text{2-T}} \times 100\%$.

anisms and non-Boltzmann state population distributions. Figure 6.4 compares predictions for the translational-rotational temperature T obtained using the bin-based StS and 2-T models. The percentage difference between quantities of interest from the two approaches is computed as: $(Q^{\text{StS}} - Q^{\text{2-T}})\,/\,|Q^{\text{2-T}}| \times 100\%$. Similarly, the difference in partial densities of CO_2 vibrational bins 1, 2, 5, and 8 are presented in Fig. 6.5. The corresponding bin-wise properties for the conventional 2-T model are obtained as a post-processing step by assuming that CO_2 vibrational states lie on a Boltzmann distribution at T_V. StS modeling in an ideal chemical reactor (summarized in Section 3.3) allows a rough interpretation of non-equilibrium dynamics for wake flows. The first three bins already reach a Boltzmann distribution at $t = 10^{-4}$ s ($\sim$ average flow transit time) once the reactor is suddenly cooled. The high energy states ($> 1.5\,\text{eV}$) on other hand are overpopulated and form a complex non-Boltzmann comb-like structure which is equilibrated only at $t \sim 10^1$ s. This disparity in equilibration time scales is also observed Fig.6.5, with partial density estimates varying by multiple orders of magnitude between the StS and 2-T approaches for the upper bins. The difference for the first three bins, which represent about 99% of all CO_2 molecules, is significantly lower. Thus, the sparsely populated upper bins have minimal impact on the bulk T (which also includes contributions from other mixture species) and despite their strongly non-Boltzmann

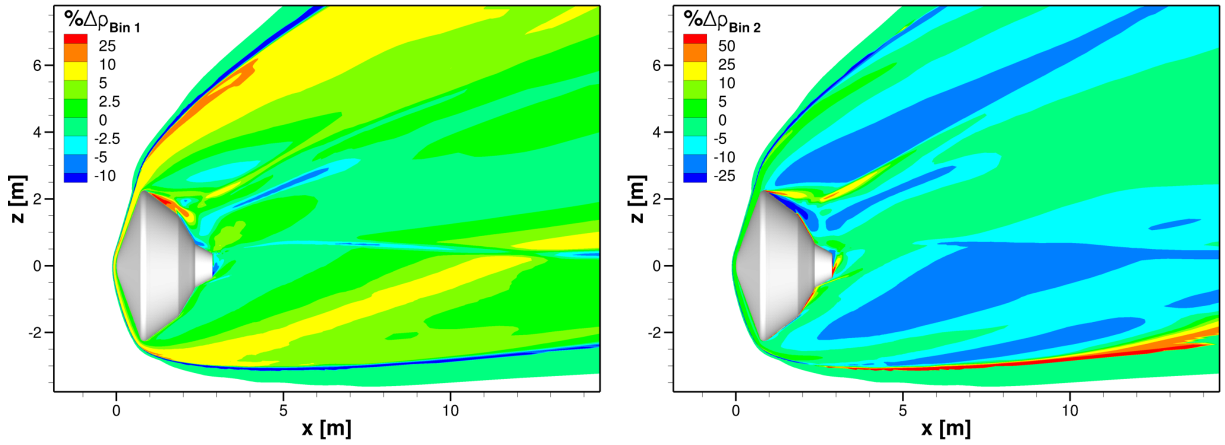

(a) Bin 1 **(b)** Bin 2

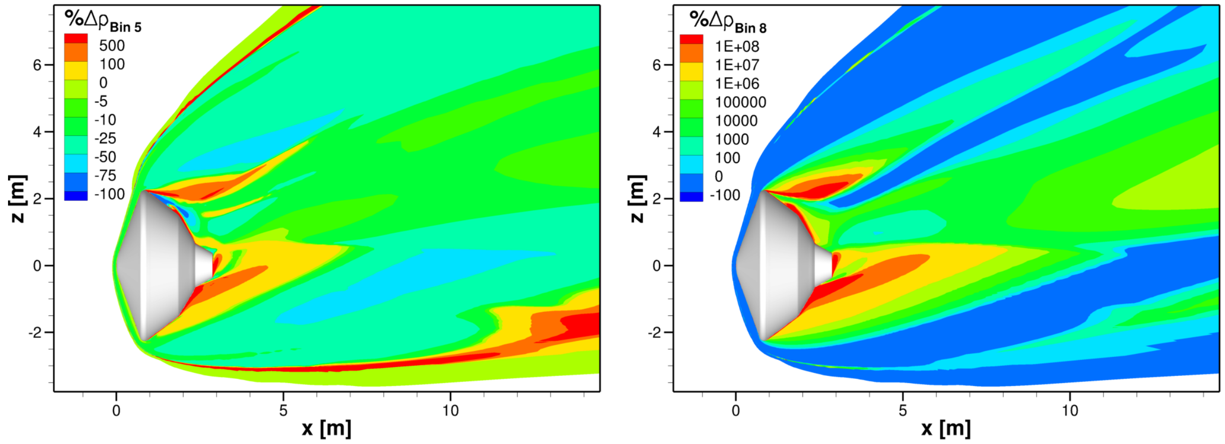

(c) Bin 5 **(d)** Bin 8

Figure 6.5: Percentage difference in predicted partial densities of CO_2 vibrational bins 1, 2, 5, and 8 between bin-based StS and 2-T models: $(\rho_{bin}^{\text{StS}} - \rho_{bin}^{\text{2-T}}) \,/\, \rho_{bin}^{\text{2-T}} \times 100\%$.

behavior, $|\%\Delta T| < 4\%$ for most of the afterbody.

The streamlines defined in Fig. 6.3b are characterized by different rates at which the flow expands while traveling around the shoulder to the afterbody region. Thus, while streamlines 1 and 2 experience “freezing” in the near-wake region, streamline 4 completely skips the core viscous wake and experiences no concomitant expansion after the oblique shock. Figure 6.6 highlights the variation in rate of expansion and the subsequent recovery due to compression along streamlines 2 and 3. It is clear that both T (black) and T_V (red) match each other except for a narrow region around the shoulder. Additionally, T and T_V values computed using the bin-based StS (solid) model are slightly lower than those for the conventional 2-T (dashed) model. Bin densities for both

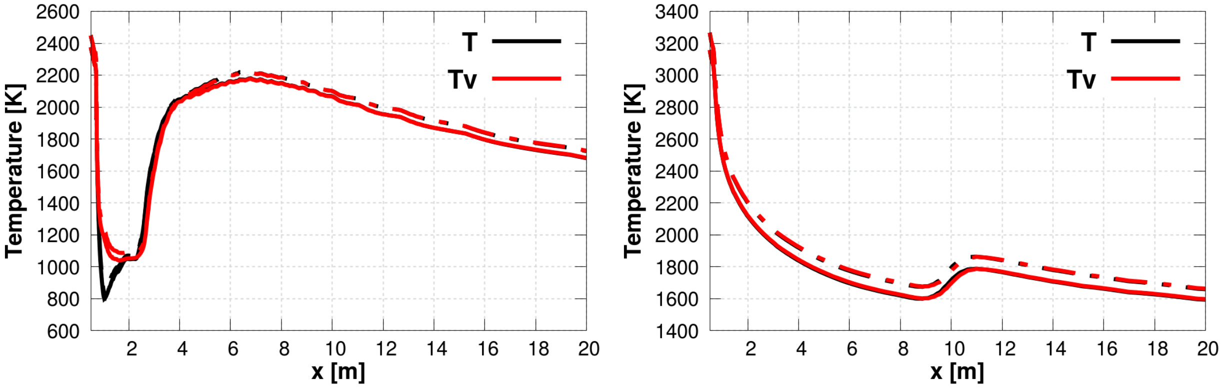

(a) Streamline 2 **(b)** Streamline 3

Figure 6.6: Distribution of T (black) and T_V (red) along streamlines 2 and 3. Solid and dashed lines represent bin-based StS and conventional 2-T models, respectively.

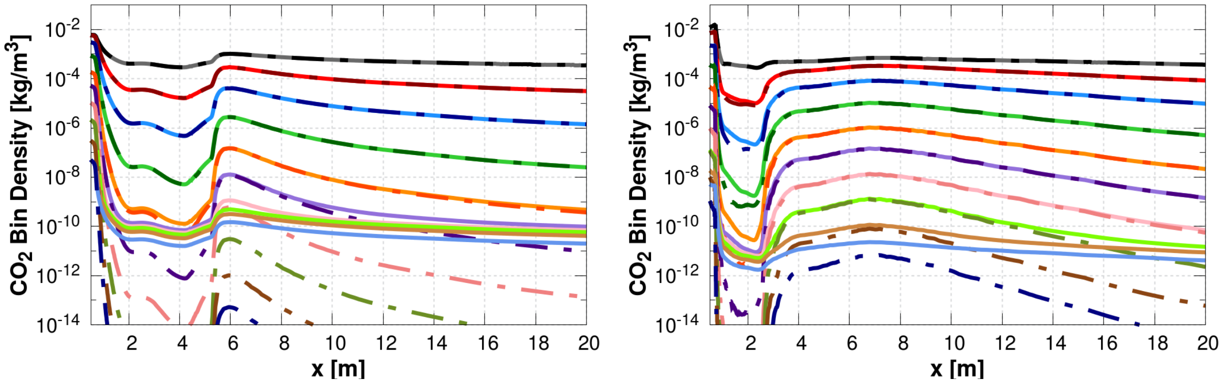

(a) Streamline 1 **(b)** Streamline 2

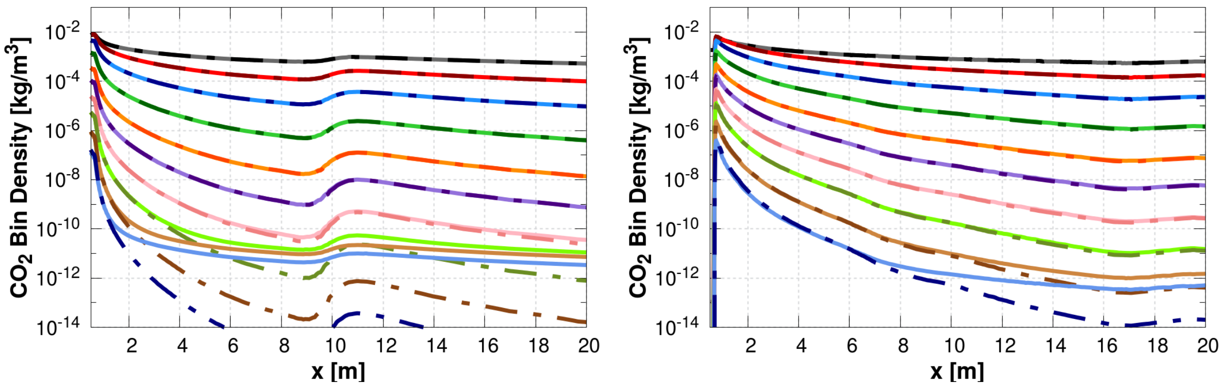

(c) Streamline 3 **(d)** Streamline 4

Figure 6.7: Partial densities of CO_2 vibrational bins along different streamlines. Solid and dashed lines represent bin-based StS and conventional 2-T models, respectively. Bin indices increase from top to bottom of each figure.

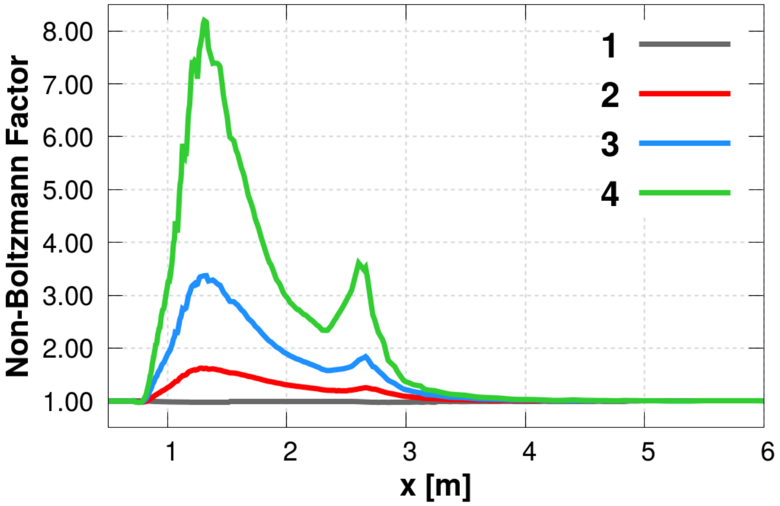

Figure 6.8: Non-Boltzmann factor (Eq. 6.33) for CO_2 vibrational bins 1 to 4 along streamline 2.

bin-based StS (solid) and 2-T (dashed) models along the four streamlines are plotted in Fig. 6.7. A simple rule of thumb for the reduced-order model is that a higher density value corresponds to a lower bin index. A common theme for all four streamlines is the limited dissimilarity between results for the first four bins which constitute the lower end of the state population distribution. On the contrary, partial densities for the last four bins differ by almost nine orders of magnitude. Low number densities and temperatures during expansion severely restricts thermal relaxation and renders the state population distribution unable to respond to changes in flow conditions. This behavior is particularly pronounced for the upper bins with high characteristic relaxation times, resulting in the conventional 2-T model under-predicting bin populations due to the assumption of instantaneous equilibration at T_V . It is interesting to note that relaxation time-scales for the last two bins are so large that non-equilibrium behavior is induced even in streamline 4 once the flow has moved sufficiently away from the high temperature region around the bow shock. A non-Boltzmann factor to quantify deviation from a Boltzmann state population distribution for the i^{th} bin can be defined as:

$$NB_i \quad = \quad \rho_i \,/\, \rho_i^{\mathrm{Bol}} \tag{6.33}$$

where ρ_i is the bin density obtained directly from the reduced-order StS simulation and ρ_i^{Bol} is the

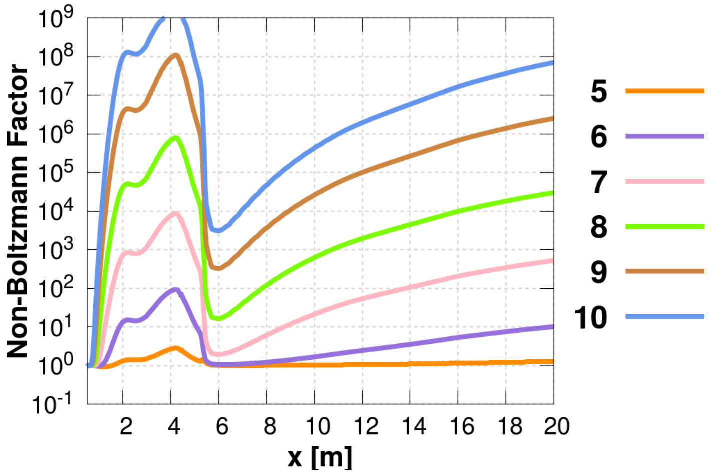

(a) Streamline 1

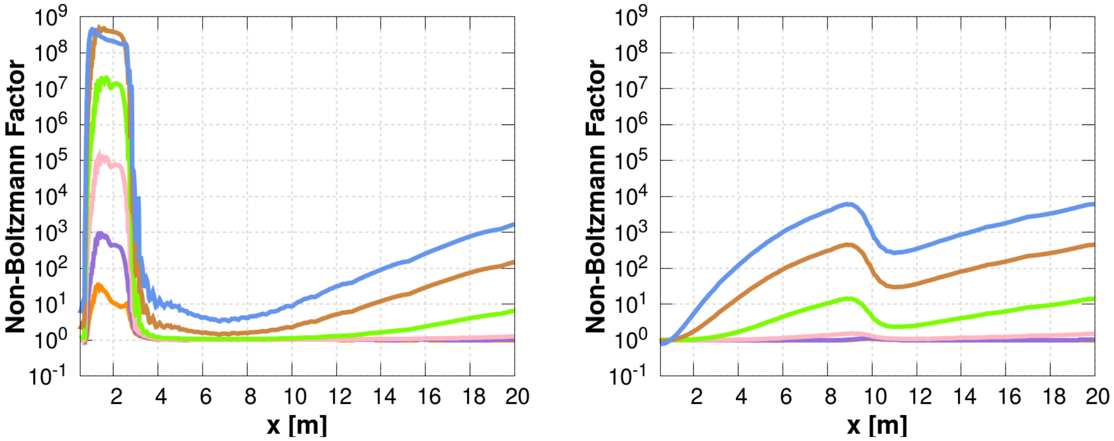

(b) Streamline 2 **(c)** Streamline 3

Figure 6.9: Non-Boltzmann factor (Eq. 6.33) for CO_2 vibrational bins 5 to 10 along different streamlines.

corresponding bin density based on a Boltzmann distribution at T_V and total CO_2 density ρ_{CO_2} from the same simulation. The non-Boltzmann factor for the first four bins remains close to 1 except for the strong expansion region near the shoulder of the spacecraft (Fig 6.8). The strong non-equilibrium experienced by the upper bins is illustrated in Fig. 6.9 with NB_i for different bins ranging between 10^1 and 10^9. The increasing distance from the vehicle surface and easing rate of expansion between streamlines 1 and 3 allows thermalization to proceed further and reduces the peak value of NB_i from 10^9 to 10^4. Non-Boltzmann effects persist longer along streamline 1 on the windward side as compared to streamline 2 on the leeward side (as evidenced by figures 6.7 and 6.9) despite more rapid expansion and a larger re-circulation zone on the leeward side. This is a direct consequence of weaker recompression and lower temperature recovery on the windward side which reduces the collision rates and retards equilibration.

6.3.2.3 Radiative Transfer

Although the current framework computes the three-dimensional angularly integrated radiation field, it is still instructive to compare flowfield properties and the resultant radiative intensity along individual LOSs for the two approaches [278]. The two LOSs outlined in Fig. 6.3c are normal to the first cone and the base of the afterbody on the leeward side. A parameter called flow factor F_{i-j} is defined which attempts to condense the impact of bin densities, T_V, and degree of non-Boltzmann behavior on radiative transitions between the i^{th} and j^{th} bins into one convenient term:

$$F_{i-j} \;=\; \rho_i \, \frac{NB_j}{NB_i} \, \exp\!\left(\frac{-\mathrm{h_P}\,\nu}{\mathrm{k_B} T_V}\right) \tag{6.34}$$

where $\mathrm{h_P}$ is the Planck's constant, $\mathrm{k_B}$ is the Boltzmann constant, and ρ_i is bin density either obtained directly from the reduced-order StS simulation or post-processed in the case of conventional 2-T modeling. The flow factor term appears in the expression for absorption κ_ν^{i-j} and J_ν^{i-j} emission coefficients for a given bin pair (equations 6.24 and 6.25):

$$\hat{\kappa}_\nu^{i-j} \;=\; \frac{\sigma_\nu^{i-j}}{\mathrm{N_A}} \left(\rho_i \,-\, F_{i-j}\right) \tag{6.35}$$

$$\hat{J}_\nu^{j-i} \;=\; \frac{\sigma_\nu^{i-j}}{\mathrm{N_A}} \, \frac{2\mathrm{h_P}\,\nu^3}{\mathrm{c}^2} \, F_{i-j} \tag{6.36}$$

where σ_ν^{i-j} is the absorption cross-section at ν, $\mathrm{N_A}$ is Avogadro's number, and c is the speed of light. A larger value of F_{i-j} implies more emission and less absorption emanating from radiative transitions between bin pair $i-j$ and would increase radiative intensity along a LOS. In order to simplify the flow factor analysis, ν is set equal to the frequency at the middle of the dominant $4.5\,\mu$m band. Figure 6.1 indicates that emission coefficients per unit bin density for radiative transitions between bin pairs $1-1$, $2-1$, $2-2$, $3-2$, $3-3$, $4-3$, and $4-4$ are comparable. However, the partial densities of the first two bins are much larger compared to the remaining bins. Flow factors and resulting radiative emissions from transitions involving these two bins are significantly higher

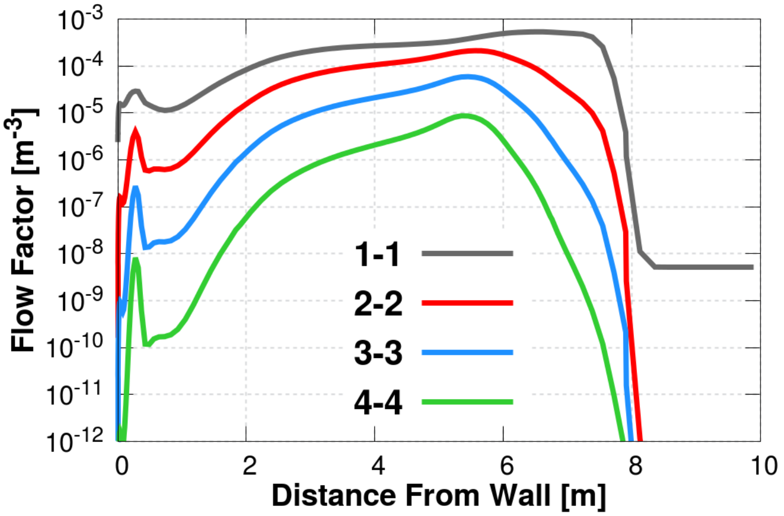

Figure 6.10: Flow factors (Eq. 6.36) for the first four CO_2 vibrational bins along LOS 1.

as well. Thus, IR radiation for the afterbody region is shaped entirely by the characteristics of bin 1 and to a lesser extent bin 2.

Figure 6.11 presents the variation in temperatures (both T and T_V with solid and dashed lines corresponding to bin-based StS and conventional 2-T models, respectively), percentage difference in flow factors, and total radiative intensity along the two LOSs. The total radiative intensity for the first LOS reaches $\sim 90\%$ of its peak value approximately 5 m from the wall surface. This location is marked as a white dot in Fig. 6.12 which also presents the percentage different in total CO_2 density between bin-based StS and 2-T models. Figure 6.12 indicates the rise in radiative intensity occurs almost exclusively in a region bounded by the bow shock and streamline 4 which comprises of dissociating flow that undergoes no expansion. Kustova *et al.* [279] have previously shown that conventional 2-T modeling overpredicts the rate of dissociation when compared to the current StS model. Thus, $\%\Delta\rho_{\mathrm{CO}_2} > 0$, and T/T_V are lower for the bin-based StS model. One possible explanation for this could be that a higher CO_2 mass-fraction results in larger mixture heat capacity. This trend is reversed in the case of the second bin, with partial density (Figure 6.5) being smaller for the bin-based StS model due to lower T_V. The two competing effects of higher density and lower temperature characterizing the first bin appear to cancel each other out with $\%\Delta F_{1-1}$ being only slightly negative. Conversely, $\%\Delta F_{2-2}$ has a more pronounced negative value due to

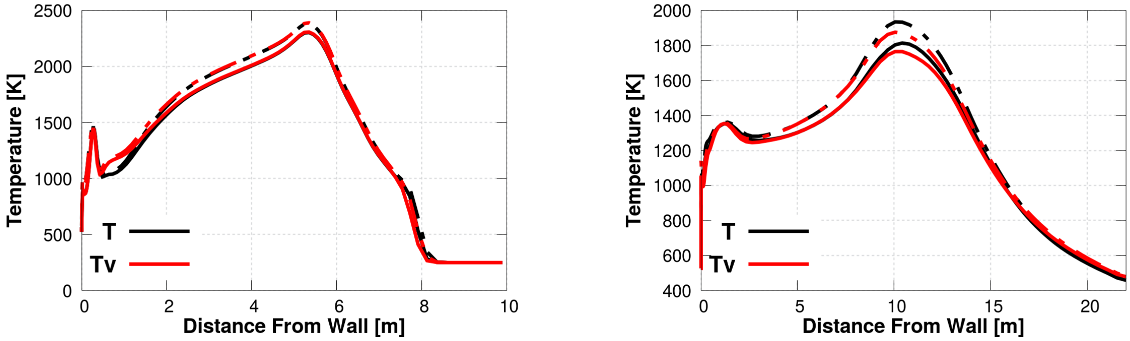

(a) LOS 1 **(b)** LOS 2

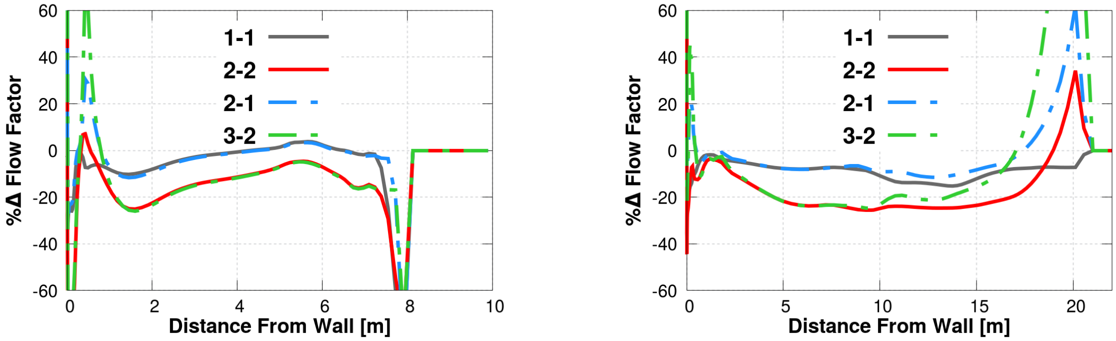

(c) LOS 1 **(d)** LOS 2

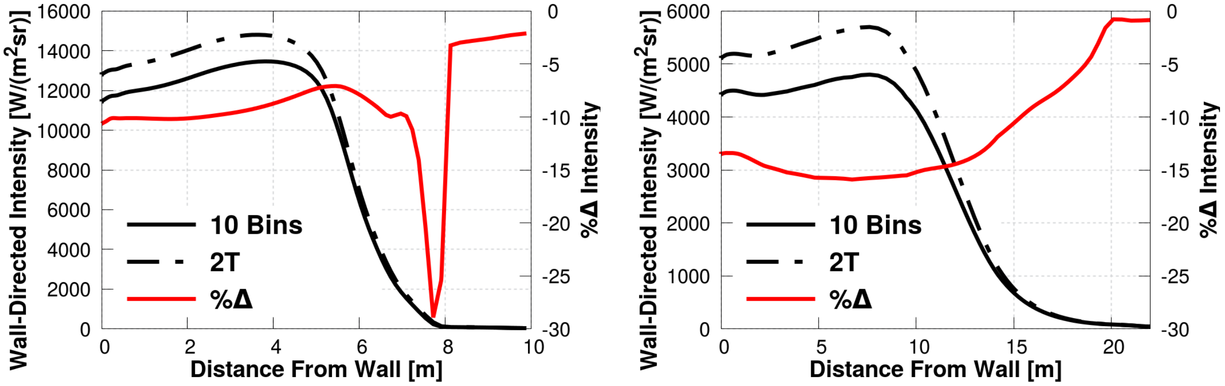

(e) LOS 1 **(f)** LOS 2

Figure 6.11: Temperatures - T and T_V (solid and dashed lines correspond to bin-based StS and conventional 2-T models, respectively), $\%\Delta F_{i-j}$, and total radiative intensity along different LOSs. Percentage difference is computed as: $\left(Q^{\text{StS}} - Q^{\text{2-T}}\right) / \left|Q^{\text{2-T}}\right| \times 100\%$.

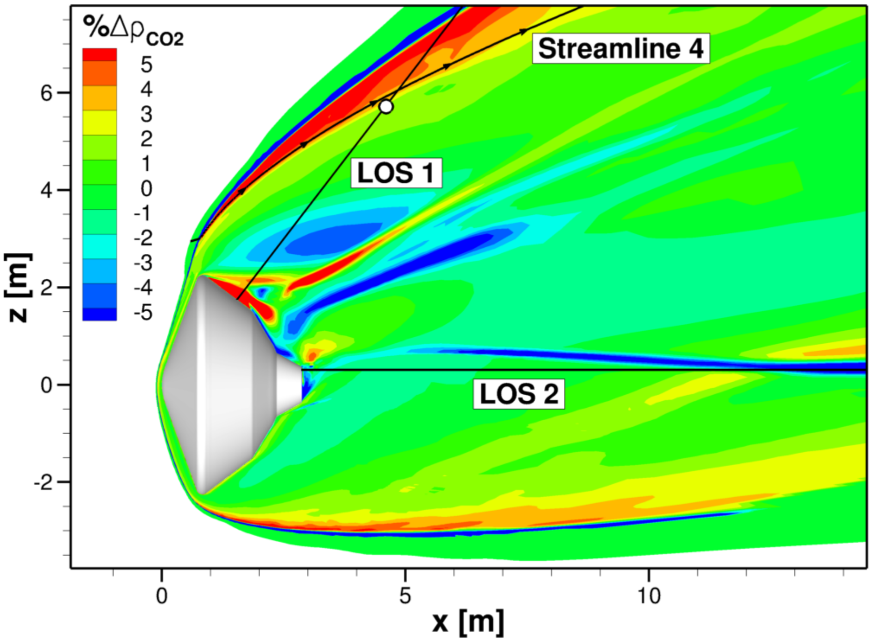

Figure 6.12: Percentage difference in total CO_2 density between bin-based StS and 2-T models: $(\rho^{\text{StS}}_{\text{CO}_2} - \rho^{\text{2-T}}_{\text{CO}_2})\,/\,\rho^{\text{2-T}}_{\text{CO}_2} \times 100\%$.

both density and temperature effects reinforcing each other. It should be noted that $\%\Delta F_{2-1}$ and $\%\Delta F_{3-2}$ follow $\%\Delta F_{1-1}$ and $\%\Delta F_{2-2}$, respectively, except for the recirculation region where non-equilibrium effects dominate. The utility of analyzing local radiative behavior using flow factors is evident in Fig. 6.11, with changes in $\%\Delta I$ mirroring the behavior of $\%\Delta F_{i-j}$. The percentage difference in radiative intensity at the wall is approximately the weighted mean value along the LOS of $\%\Delta F_{i-j}$ for the dominant bin-pairs. The same behavior borne out of slower dissociation for the StS approach is seen along the middle-section of LOS 2. Crucially, non-Boltzmann effects are more pronounced further into the viscous wake ($\sim 12\,\text{m}$ onwards) which results in F_{i-j} being higher for the StS model. An important conclusion that can be drawn from this analysis is that radiative energy emanating from the bow shock is much higher compared to the rest of the wake.

Figure 6.13 presents divergence of the total radiative heat flux $\boldsymbol{\nabla}_{\boldsymbol{x}} \cdot \mathbf{q}_{\text{rad}}$ along the $y = 0\,\text{m}$ plane for the bin-based StS simulation and the percentage difference between the two models. A positive (negative) value for $\boldsymbol{\nabla}_{\boldsymbol{x}} \cdot \mathbf{q}_{\text{rad}}$ indicates that the flow at a particular location is a net emitter (absorber) of radiative energy and adds to the radiative heat flux received by the vehicle. The consistently high magnitude of the $\boldsymbol{\nabla}_{\boldsymbol{x}} \cdot \mathbf{q}_{\text{rad}}$ term associated with the hot dissociating flow after

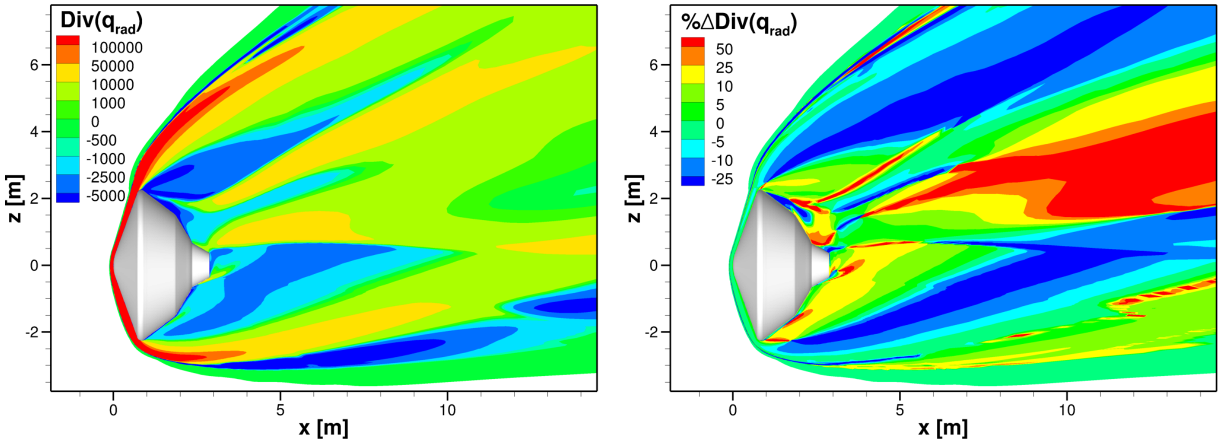

(a) Bin-based StS **(b)** Percentage difference

Figure 6.13: Negative value of volumetric radiative heating term. Percentage difference computed as: $(\boldsymbol{\nabla}_{\boldsymbol{x}} \cdot \mathbf{q}^{\text{StS}}_{\text{rad}} - \boldsymbol{\nabla}_{\boldsymbol{x}} \cdot \mathbf{q}^{\text{2-T}}_{\text{rad}}) \,/\, |\boldsymbol{\nabla}_{\boldsymbol{x}} \cdot \mathbf{q}^{\text{2-T}}_{\text{rad}}| \times 100\%$ (right).

the oblique shock further confirms that radiative surface heat flux is dominated by the properties of this small section of the flowfield. Figure 6.14 compares the total radiative heat flux received by the afterbody and the difference between the two approaches along the $y = 0\,\text{m}$ edge. The conventional 2-T model clearly overpredicts surface heat flux which is in line with the previous LOS analysis. It is interesting to note that the percentage difference in estimates for incident radiative flux continues to hover around the same value as $\%\Delta I$ at the wall for LOS 1 and $\%\Delta\,(\boldsymbol{\nabla}_{\boldsymbol{x}} \cdot \mathbf{q}_{\text{rad}})$ near the bow shock region. The enclosed expanding wake despite experiencing significant non-Boltzmann behavior (resulting in higher $\%\Delta\,(\boldsymbol{\nabla}_{\boldsymbol{x}} \cdot \mathbf{q}_{\text{rad}})$ and $\%\Delta I$ for LOS 2) is rendered radiatively non-participating due to a significant drop in CO_2 density. Thus, its role in determining vehicle radiation characteristics is largely limited even for the base ($z \in [-0.37, 0.37]\,\text{m}$) which has a comparatively smaller view factor with respect to the bow shock. Furthermore, unlike atomic radiation [12] the impact of non-Boltzmann effects on total CO_2 IR heating is further minimized due to the preponderance of radiative transitions within the ground vibrational bin which has a short thermal relaxation time period. This also leads the author to conclude that increasing the total number of vibrational bins would not appreciably change estimates for surface radiative flux. The dominant lower bins (although now more in number) would continue to remain in an equilibrium Boltzmann distribution, matching the behavior implicitly obtained through the 2-T model.

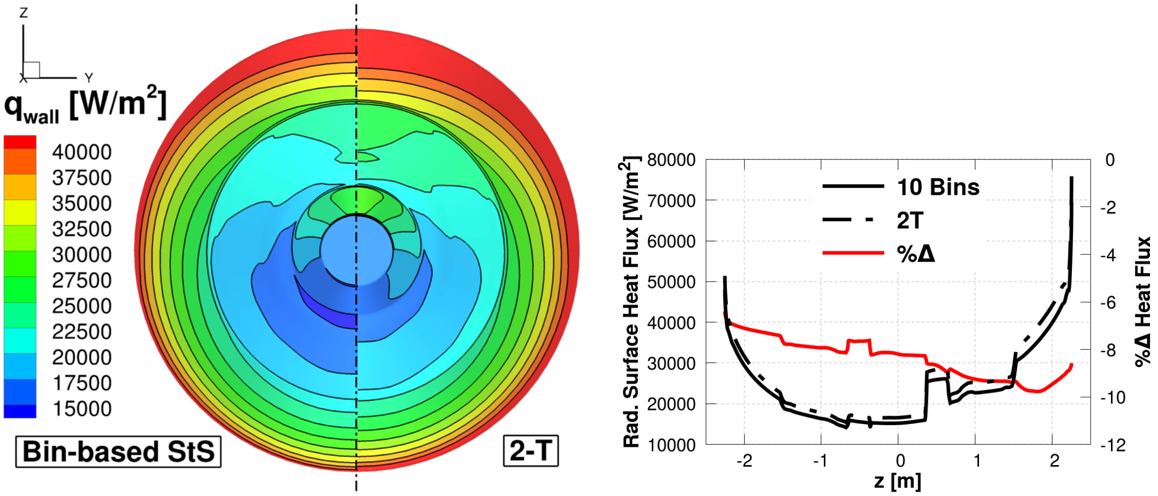

(a) Afterbody surface

(b) Along $y = 0\,\mathrm{m}$ edge

Figure 6.14: Total radiative surface heat flux q_{wall} from StS and 2-T models. Percentage difference computed as: $(q^{\mathrm{StS}}_{\mathrm{wall}} - q^{\mathrm{2\text{-}T}}_{\mathrm{wall}})\,/\,q^{\mathrm{2\text{-}T}}_{\mathrm{wall}} \times 100\%$.

6.3.3 Coupled Radiation

Previous studies on earth entry flows with low density wakes [12] have indicated that radiative transitions outlined in Section 6.2.2 can have a significant on the population of higher energy levels. Conventional techniques for coupling radiation to flow chemistry / thermal relaxation rely on the escape factor approximation [98] for computing reaction rate coefficients due to absorption K^{ab}_{l-u}. An escape factor parameter EF_{l-u} with a value between 0 (optically thick transitions) and 1 (optically thin transitions) is used to express K^{ab}_{l-u} as a fraction of the total spontaneous emission from a given location:

$$K^{\mathrm{ab}}_{l-u} = (1 \,-\, EF_{l-u})\,\bar{K}^{\mathrm{em}}_{u-l}\,\frac{\rho_u}{\rho_l} \tag{6.37}$$

The escape factor EF_{l-u} is either prescribed a constant value [280] or computed solely on the basis of local properties at a given location [98]. Additionally, this approach is unable to model strong absorption of non-local emission because EF_{l-u} cannot be assigned negative values. The current framework eschews these simplifications in order to accurately assess the possible effects of absorption of non-local IR radiation emanating from surrounding flows. This is computationally prohibitive without the use of model-reduction techniques, and apart from a few exceptions involving atomic species [12, 241], has typically been avoided while studying complex three-dimensional flow problems. An exact value for EF_{l-u} is later computed as a post-processing step using the detailed values of $\bar{K}^{\mathrm{em}}_{u-l}$ and K^{ab}_{l-u} in order to gain useful insights into the coupling between local thermochemistry and the global radiative field:

$$EF_{l-u} \quad = \quad 1 - \frac{K^{\mathrm{ab}}_{l-u}\,\rho_l}{\bar{K}^{\mathrm{em}}_{u-l}\,\rho_u} \tag{6.38}$$

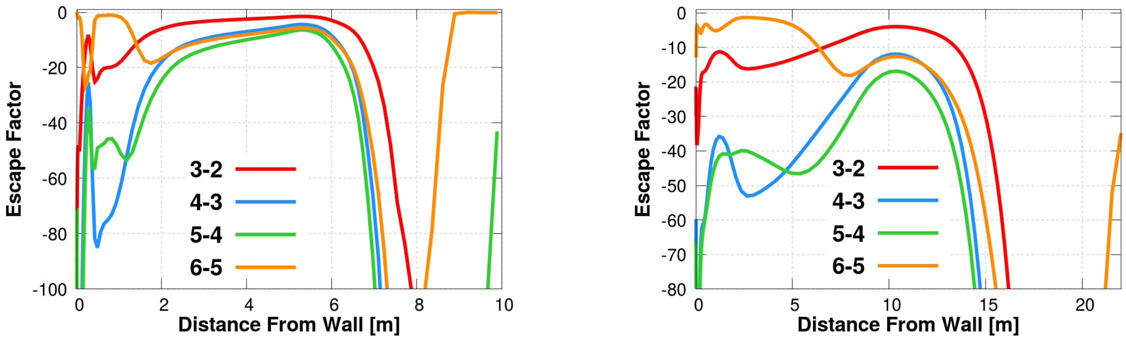

(a) LOS 1 **(b)** LOS 2

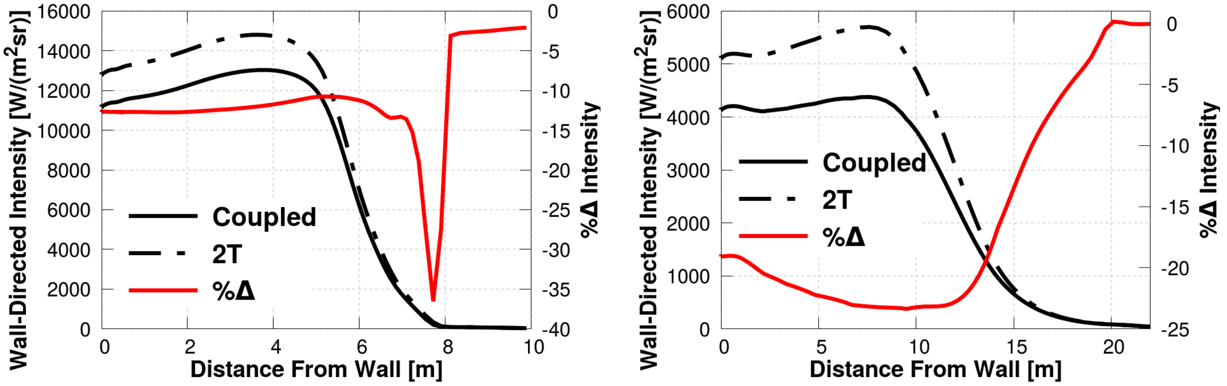

(c) LOS 1 **(d)** LOS 2

Figure 6.15: Escape factor and total radiative intensity along different LOSs. Percentage difference is computed as: $(Q^{\mathrm{StS}} - Q^{2\text{-T}})\,/\,|Q^{2\text{-T}}| \times 100\%$.

The escape factors for transitions involving the upper vibrational bins such as 3-2, 4-3, 5-4, and 6-5 along the two LOSs for 10 bins-based StS simulations with self-consistent non-local radiation coupling are outlined in Fig. 6.15. It should be noted that unlike approximate escape factor methods, the lower limit for escape factors is not set to zero in the current study. Large negative values in Fig. 6.15 indicate that owing to the global radiation field (represented by the scalar integral $\oint_{4\pi} I_\nu d\mathbf{\Omega}$ in Eq. 6.30), transition rates due to absorption are significantly higher than those due to emission. This is a direct consequence of photochemical transitions involving different CO_2 vibrational levels (or bins for the current reduced-order StS description) overlapping in frequency space as outlined in Fig 6.1. Thus, emission by the dominant first bin becomes available for absorption by the upper bins. This radiative environment is fundamentally different from those for atomic species [220] where the underlying spectra largely consists of separated lines. However, Fig. 6.10 and the subsequent analysis indicate that absorption/emission coefficients for the upper bins are smaller than those of the first bin by multiple orders of magnitude. Additionally, the characteristic radiative intensity for Martian missions is lower than that for Earth-return profiles due to the large difference in entry speeds. Consequently, there is no significant repopulation of the upper bins and their contribution to total radiative emission remains minimal even for the coupled simulation. Moreover, lower radiative intensity also results in internal dynamics of the first two bins being dominated by collisional processes in the strongly emitting regions with radiative processes having a discernible impact only in the radiatively insignificant near-wake zone.

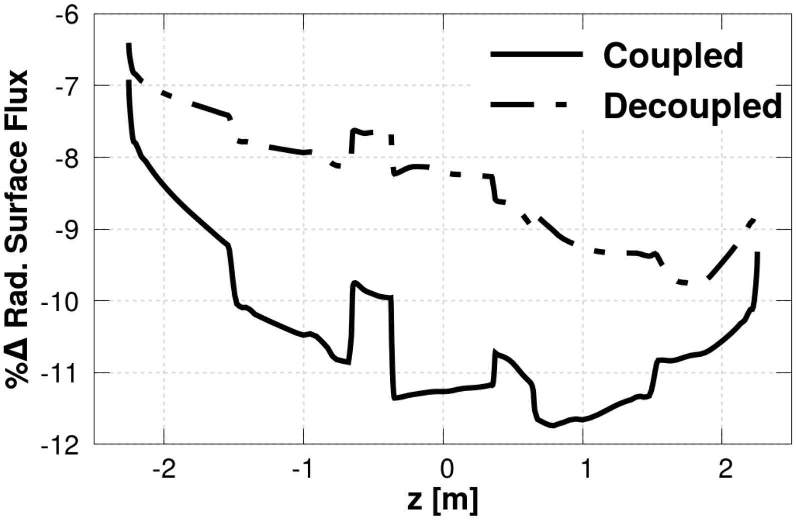

Figure 6.16: Percentage difference in total radiative surface heat flux coupled/uncoupled bin-based StS and 2-T models along the $y = 0\,\mathrm{m}$ edge: $(q_{\mathrm{wall}}^{\mathrm{StS}} - q_{\mathrm{wall}}^{\mathrm{2\text{-}T}}) \,/\, q_{\mathrm{wall}}^{\mathrm{2\text{-}T}} \times 100\%$

The energy source term from Eq. 6.32 has a more pronounced impact on total radiative heat flux. The majority of the flowfield barring the recirculation zone are net emitters of radiative energy (Fig. 6.13). This loss of energy results in a drop in temperature and subsequently, lowered spontaneous emissions. Thus, radiative intensities for StS simulations with radiative coupling are lower than those for the uncoupled StS and 2-T cases. A comparison between the total radiative surface heat flux along the $y = 0\,\text{m}$ edge obtained using the 2-T, uncoupled StS, and coupled StS simulations is presented in Fig. 6.16.

6.4 Summary

Reduced-order approaches outlined in previous chapters are combined into a unified methodology for modeling non-equilibrium thermochemistry and radiative transfer in complex three-dimensional flows. The resultant non-equilibrium toolset is employed with the US3D flow solver for characterizing CO_2 wake flows during planetary entry of the Mars 2020 vehicle. Thermochemical response stemming from non-Boltzmann vibrational state population distributions is resolved using the MGME framework. Similarly, the expansive CDSD-4000 rovibrational CO_2 radiation database is reduced to a more computationally tractable spectral model that is also compatible with the multi-bin paradigm. Further efficiency gains are realized through DOM and finite-volume based solutions of the radiative transfer problem.

Statistically converged solutions for hypersonic flows around the Mars 2020 vehicle are obtained using the conventional 2-T model and a 10 bin-based StS model for CO_2 vibrational non-equilibrium. This includes both decoupled radiative calculations (by post-processing the final flowfield) and flow-radiation two-way coupled simulations. The translational-rotational temperature is found equal to the vibrational-electronic temperature for most of the flowfield. This strongly suggests that non-Boltzmann deviations in vibrational state population distributions cannot be fundamentally accounted for through conventional multi-temperature approaches. Streamlines that pass through the near-wake region undergo rapid expansion resulting in the population of mid-lying and upper CO_2 vibrational levels being frozen. The bin-based StS approach captures this non-equilibrium behavior whereas the 2-T model by forcing thermal equilibration underpredicts the population distribution by multiple orders of magnitude. However, both ideal chemical reactor and flowfield simulations suggest that the lowest vibrational levels (bins 1 and 2) reach their final equilibrium state fairly rapidly. Hence, bulk properties such as temperature, density, and total CO_2 mass-fraction do not differ significantly between the bin-based StS and 2-T approaches.

An analysis of the resultant radiative transfer indicates that its dynamics are completely dominated by the ground vibrational levels (bin 1) owing to their considerably higher number densities. Furthermore, radiative intensities along LOSs crossing the bow shock reach their final values exclusively in a narrow high density/temperature region around the shock that undergoes no discernible expansion. Thus, the impact of non-Boltzmann effects induced in near-wake flows on the total afterbody radiative heat flux are largely minimized. Nevertheless, surface heat flux predicted by the 2-T model is almost 10% greater due to higher post-shock temperatures. Coupled flow-radiation simulations accentuate the difference in surface flux estimates between the two approaches to a slightly higher 12%. Non-local absorption (negative escape factors) of radiative energy emitted by the shock result in re-population of the higher levels in the wake. But, lower Martian entry speeds (less total radiative intensity) and the dynamics of ground vibrational levels still being informed by collisional processes restricts the overall influence of flow-radiation coupling.

Chapter 7

Conclusions and Future Work

7.1 Conclusions

The current work develops a unified methodology comprising of self-consistent reduced-order models for describing thermochemical changes and radiative transfer under strong non-equilibrium conditions. An optimal trade-off between fidelity and computational efficiency ensures that this simulation procedure can be applied to practical CFD problems involving complex geometries. Thus, a definitive pathway originating from detailed chemistry and radiation databases to realizable large-scale three-dimensional radiation hydrodynamics calculations is forged.

The MGME method provides a robust reduced-order framework for predicting non-Boltzmann internal state population distributions. Individual internal states included in the larger macroscopic bins are assumed to equilibrate instantly and their population is reconstructed using piece-wise linear polynomials that maximize entropy. The governing equations and concomitant phenomenological coefficients describing bin properties are developed through moment closure while retaining key details from the original StS model. The introduction of adaptive grouping allows clusters of rapidly thermalizing states to be identified *a priori* based on state-specific kinetics and energies. This allows the multi-fidelity description adopted by the MGME method to be better aligned with the exact state population dynamics. The chemical reactor analysis presented in Chapter 3 highlights the level of accuracy offered by the combination of the MGME method and adoptive grouping even under unrealistically severe non-equilibrium conditions. Reduced-order models, by being informed by STS kinetics through the modified island algorithm and spectral clustering, are able to reproduce complex multi-modal behavior of the evolving state population distribution function. This includes the low energy fork-like splitting in N_2 (due to rotational parity preserving transitions between same vibrational quantum numbers) or the mid-energy multi-strand structure (selective

V-V relaxation) for CO_2. The improvements in computational tractability are outstanding as well – a full StS simulation takes approximately two hours on a single core while the same procedure with 10-30 bins (sufficiently accurate predictions for both macroscopic properties and state-specific distributions) is completed under three minutes. In addition to their utility in developing MGME-based models, both the island algorithm and spectral clustering can also be used as exploratory tools to automatically map out key mechanisms for internal energy transfer and chemical change from voluminous state-specific databases.

Owing to the multi-variate domain of dependence, radiative response in participating media can be more expediently solved if segmented into geometric transfer and spectral modeling problems. The current study employs the discrete-ordinate method coupled with finite-volume discretization based on first-order upwinding to obtain angularly-spatially resolved solutions of the RTE. Additionally, this geometric evaluation is transformed into an explicit problem through the use of a mesh sweeping algorithm. The hybrid DOM-FVM solver is ideally suited for flow-radiation coupled calculations since it limits any redundancies in the number of LOSs that are solved to completely characterize the radiative field. Similarly, cost-savings are targeted in the spectral domain through the use of wide-band models. A multi-group paradigm based on Planck-averaging (which can also be viewed as the maximum entropy closure in frequency space) is an uncomplicated yet reliable choice for reduced-order spectral modeling of radiative properties. It can also be argued that with the requisite grouping strategy (MBOB), Planck-averaging is comparable to the more complex statistics-based approaches. This is also reflected in the LOS analysis presented in Chapter 5 focusing on various Earth and Jovian entry problems. Furthermore, the underlying assumptions guiding the development of these wide-band models are strictly applicable in an LTE setting. This serves as the motivation for evolving a generalized grouping strategy that is more appropriate for non-equilibrium radiation by accounting for the rapid frequency variation in both absorption and emission (ignored in previous LTE-inspired approaches) coefficients. The application of this generalized grouping allows both total quantities-of-interest and detailed spectral features to be reliably predicted while enabling a two orders-of-magnitude speed-up with respect to narrow-band methods (and three to four orders with respect to full LBL modeling).

Finally, this combined non-equilibrium methodology in conjunction with the US3D flow solver is used to investigate the impact of non-Boltzmann deviations in shaping flow physics and the resultant IR field in the afterbody region of the Mars 2020 vehicle. These calculations entail solving composite MGME-MT hydrodynamics equations coupled to the system of RTEs. Spectral-reduced order models that are compatible with the MGME multi-bin description of CO_2 vibrational non-equilibrium are developed from the detailed CDSD-4000 database. This congruity also allows volumetric mass source terms corresponding to absorption and emission to be developed in a straightforward manner. The DOM-FVM RTE solver together with reduced-order spectral modeling ensures that the cost of each radiation update is commensurate to approximately 5000 flow iterations. Thus, while the cost of techniques such as ray-tracing for determining surface radiative heat flux could be lower, the current approach is the more efficient alternative when computing directionally resolved radiative intensity in the entire computational domain. Statistically converged solutions for the combined radiation-hydrodynamics problem, with radiation updates at every 5000 iterations, are obtained at only a two-fold increase in computing time as compared to purely flowfield simulations. Results obtained using MGME-based bins capture non-Boltzmann deviations in the vibrational population distribution induced by the rapid expansion in the near-wake region. This effect is particularly pronounced in the upper bins that have a low collisional frequency, resulting in bin densities becoming frozen and unable to respond to changes in flowfield conditions. The conventional 2-T model, by forcing exact conformity to a Boltzmann distribution, *i.e.*, instantaneous thermal equlibration, underpredicts state population in the mid to high energy region by multiple orders of magnitude. In similar vein, radiation coupling enables absorption of photons emitted from spatially distant regions which repopulates upper levels. However, the overall impact of non-Boltzmann effects and flow-radiation coupling on the total surface radiative heat flux is tempered by various factors that are detailed in Chapter 6.

7.2 Future Work

The current work provides a cost-effective modular framework that can be applied to the study of non-equilibrium dominated problems ranging from hypersonic planetary entry to low-temperature plasmas in material processing and manufacturing. However, further improvements can still be made to the constituent reduced-order models. The current implementation of adaptive grouping is still reliant on a complete knowledge of state-specific kinetics for optimizing the division of internal states in macroscopic bins. This can become a major impediment when computing rate-coefficients for all possible StS transitions (as in the case of $N_2 - N_2$ collisions) is computationally unfeasible. Recently, Macdonald et al. [129, 172] have integrated the MGME method with QCT calculations which circumvents formulating state-specific databases and allows bin-averaged rate coefficients to be directly calculated. Nevertheless, bin indices for internal states still have to be assigned *a priori* either through energy binning or incorporating the kinetics of a simpler chemical system such as $N_2 - N$. A more optimal strategy can be evolved by leveraging QCT data (on-the-fly binning) and salient features of the diatomic potential/PES for a given chemical system [281]. Another important facet of the MGME paradigm that needs to explored pertains to developing closed-form expressions for bin-wise transport properties. Reference [130] develops the MGME governing equation starting from the Boltzmann equation and could serve as the ideal starting point for this endeavor. The further application of the Chapman-Enskog method would allow Navier-Stokes type hydrodynamics equations and constitutive relations for coefficients such as viscosity and thermal conductivity to be derived.

The geometric component of resolving radiative transfer can potentially be made more efficient through the use of M-1 models [89, 90]. This would also enable greater symmetry in the non-equilibrium methodology with constrained maximum entropy distributions describing intensity variation in solid angle space, in addition to intensity in frequency space (Planck-averaging) and the state population distribution (MGME method). A more obvious avenue for future research is an investigation into other hypersonic entry problems (Earth-return, Titan entry). Higher entry speeds and a preponderance of atomic species could see two-way flow-radiation coupling with correct treatment for non-Boltzmann behavior having a more pronounced impact on vehicle parameters [12]. Under such conditions, the current simulation framework can provide more refined predictions as compared to state-of-the-art approaches.

The validity of the original StS databases have a strong bearing on the accuracy of the resultant reduced-order thermochemistry models. The current work relies on a vibrational-specific description of CO_2 that is derived using modified-SSH theory and legacy experimental data. Conventional multi-temperature models for thermochemical non-equilibrium also attempt to reproduce these experimental results. This common reliance could explain the limited contrast between the current 2-T and bin-based StS predictions. Research is being currently performed to develop CO_2 StS model from first-principles quantum chemistry calculations [276] that can introduce two key improvements: a) eliminate selective vibrational transitions that are an artifact of extrapolating low energy rates through SSH theory, and b) correctly replicate CO_2 recombination which involves a transient electronically-excited triplet state being formed from ground CO and O and then decaying to the ground singlet state $\mathrm{CO_2(X^1 \sum_g^+)}$. The results from Chapter 6 will be reexamined in future once these ab-initio rates for CO_2 become available.

Appendix A

Additional Analysis for Ideal Chemical Reactor Simulations of $N_2(^1\Sigma_g^+) - N(^4S_u)$ System

This appendix provides supplementary details for the reduced-order dynamics of the $N_2(^1\Sigma_g^+) - N(^4S_u)$ system that was studied using an ideal chemical reactor in Section 3.2.2. Two additional aspects of the original analysis are outlined: the impact of spectral binning parameters (β_K, β_E) on overall error and unsteady thermochemical response for final reactor temperature $T_f = 30,000$ K.

A.1 Impact of Model Parameters on Spectral Clustering

Model parameters β_E and β_K that define the strength of connection (Eq. 2.31) between individual states during spectral clustering have been adjusted to obtain the best possible agreement between predictions from reduced-order and StS modeling for non-equilibrium relaxation. The current study achieves this by computing errors associated with the state distribution function (Fig. 3.10), and total mole fraction (Fig. 3.5a) and internal energy (Fig. 3.5b) profiles for different values of β_E and β_K. The optimal values (Section 3.2.2) which minimize the different errors have been subsequently used to characterize adaptive binning and assess its efficacy. The variation in relative errors corresponding to global quantities and the state population distribution with respect to β_K for a fixed value of β_E (0.85) at $T_f = T_{bin} = 10,000\ K$ is presented in Fig. A.1. The same analysis is repeated in Fig. A.2 for different values of β_E with $\beta_K = 2.35$. The ability of the reduced-order model to correctly predict both global quantities and the state distribution is degraded when β_K and β_E deviate from their optimal values of 2.35 and 0.85, respectively. Future work will focus on the use of different optimization techniques that can simplify this analysis and reliably determine the model parameters.

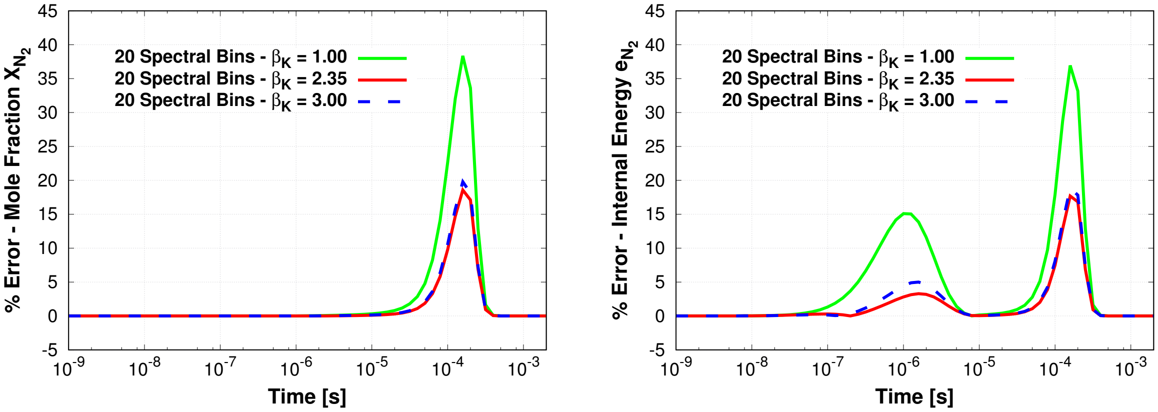

(a) Total Mole Fraction **(b)** Total Internal Energy

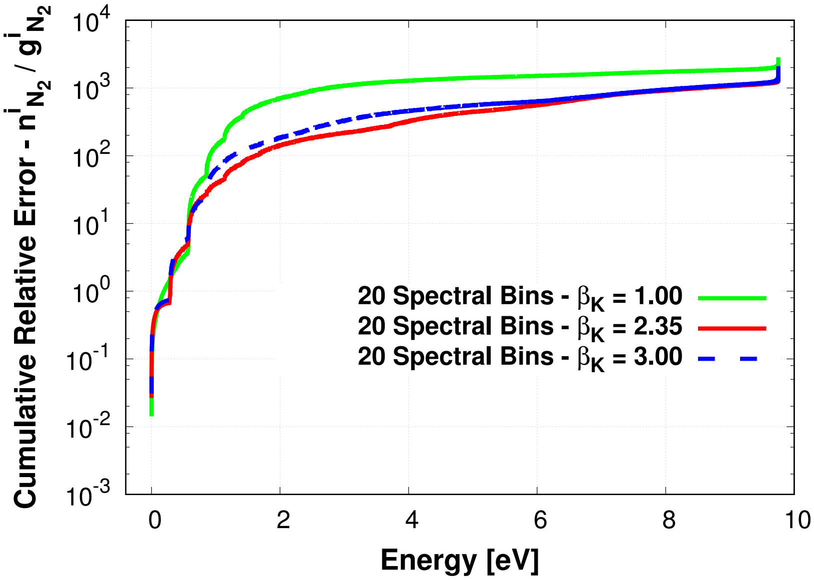

(c) State distribution at at $t = 1.2 \times 10^{-7}\ s$

Figure A.1: Comparison of relative errors in predictions for global quantities and state population distribution, with $T_f = 10,000\ K$ and $\beta_{\mathrm{E}} = 0.85$, obtained using 20 linear bins based on different β_{K} values.

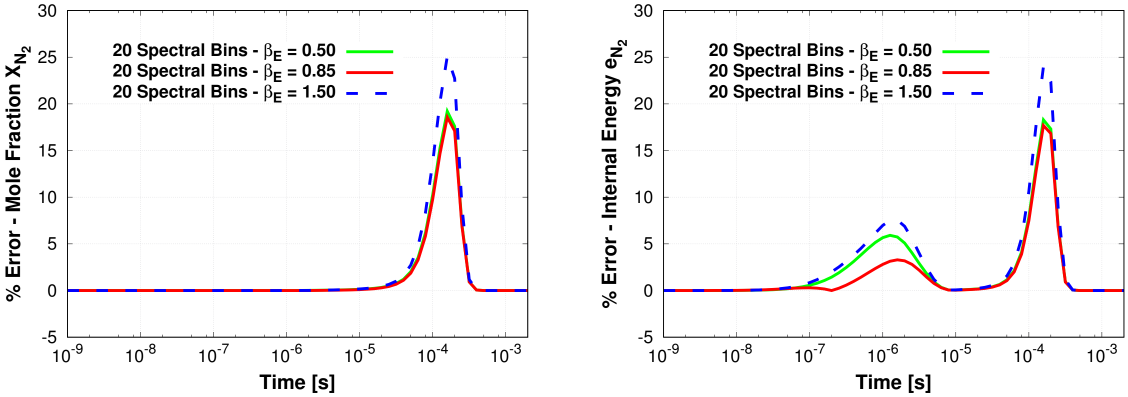

(a) Total Mole Fraction

(b) Total Internal Energy

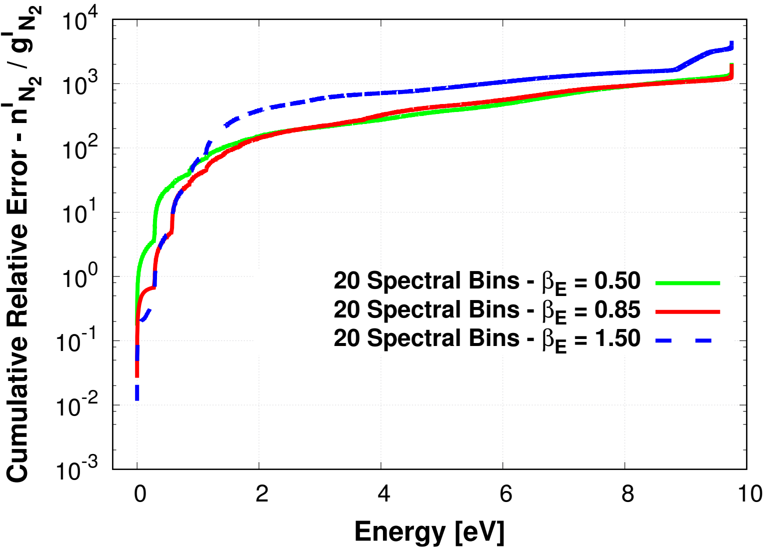

(c) State distribution at at $t = 1.2 \times 10^{-7}\ s$

Figure A.2: Comparison of relative errors in predictions for global quantities and state population distribution, with $T_f = 10,000\ K$ and $\beta_{\mathrm{K}} = 2.35$, obtained using 20 linear bins based on different β_{E} values.

A.2 Maximum Entropy Linear Bins with $T_f = 30,000$ K

Numerical investigations for $T_f = 30,000\ K$ indicate that energy relaxation and dissociation do not occur as disparate processes, and there is significant overlap between them. This results in the low energy fork-like structure becoming less pronounced due to the limited time for localized thermalization before the onset of dissociation. Consequently, the accuracy of energy-based binning improves due to energy equilibration occurring with a distinctively weaker quantum bias ($\Delta v = 0$ and odd/even J). However, the errors associated with predictions for macroscopic properties such as N_2 mole-fraction and rovibrational energy indicate that spectral clustering continues to outperform both the island algorithm and the conventional energy approach. Reduced-order solutions based on spectral clustering also better resolve individual linear strands corresponding to similar values of v and the parity of rotational levels J. The general trends previously observed for the quantum composition of individual bins using different grouping strategies remain unchanged when $T_{bin} = 30,000\ K$.

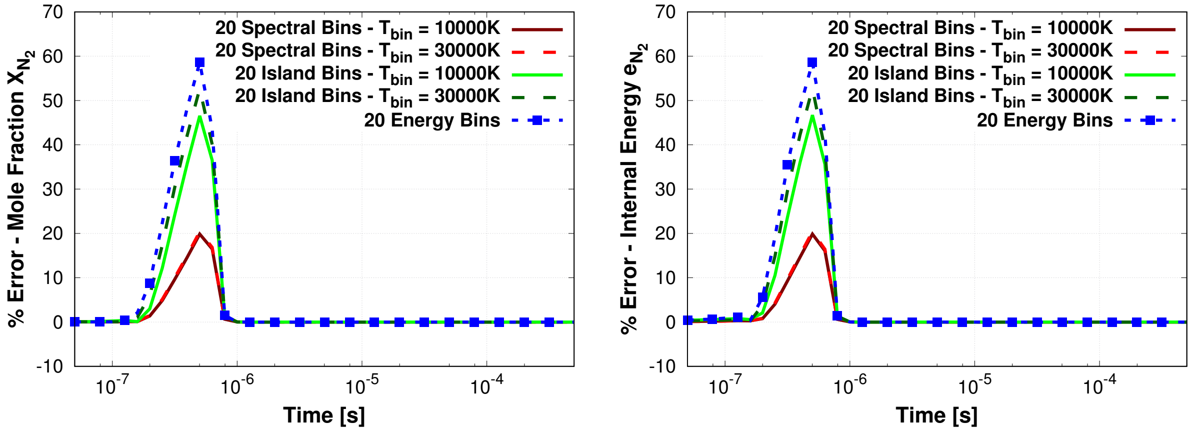

(a) Total Mole Fraction **(b)** Total Internal Energy

Figure A.3: Comparison of relative errors in predictions for global quantities, with $T_f = 30,000\ K$, obtained using 20 linear bins based on different binning strategies and T_{bin} values.

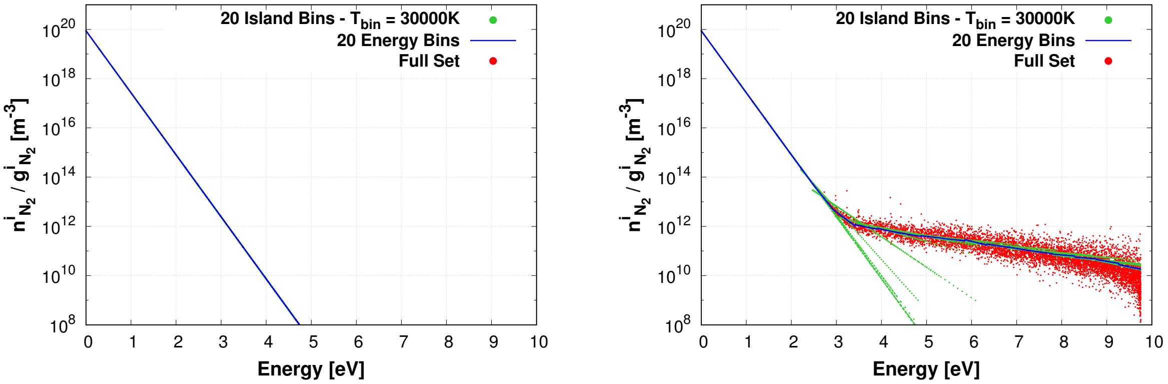

(a) $t = 0\ s$ **(b)** $t = 10^{-12}\ s$

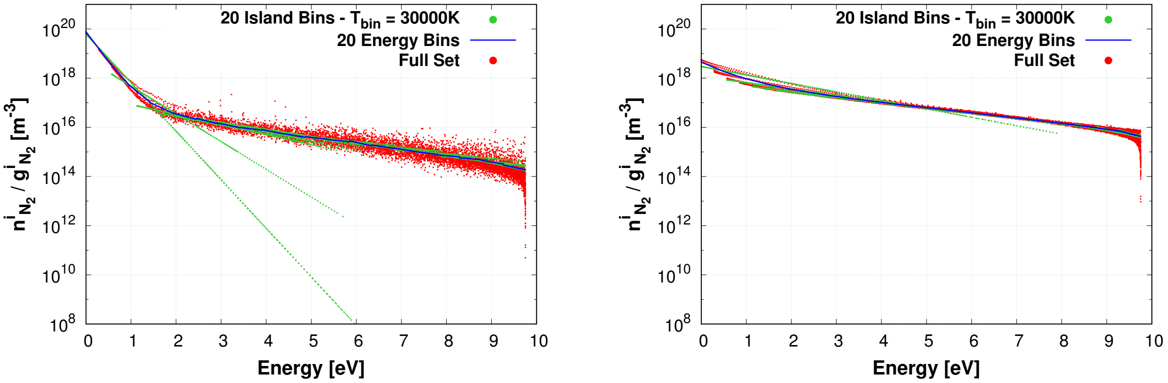

(c) $t = 10^{-8}\ s$ **(d)** $t = 1.2 \times 10^{-7}\ s$

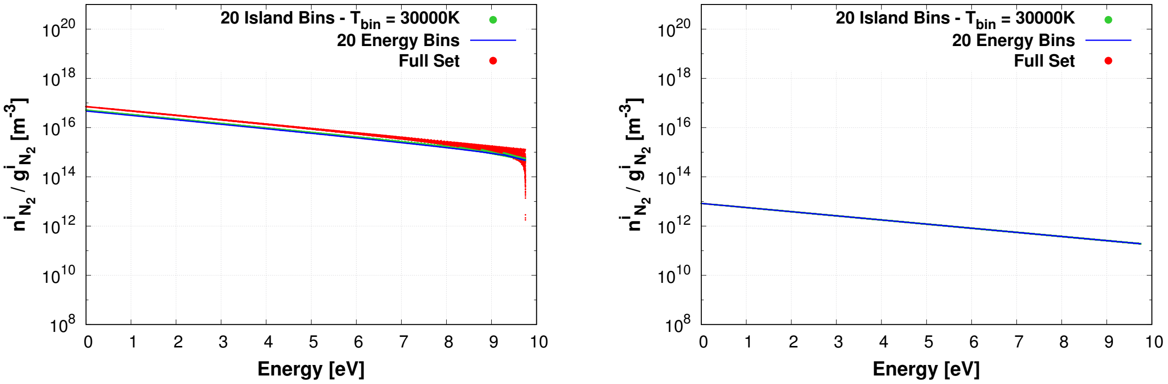

(e) $t = 3 \times 10^{-7}\ s$ **(f)** $t = 10^{-5}\ s$

Figure A.4: Comparison of time evolution of the N_2 rovibrational state distribution for $T_f = T_{bin} = 30,000\ K$, predicted using 20 linear bins based on the modified island algorithm, 20 linear bins based on energy binning, and the full state-to-state model.

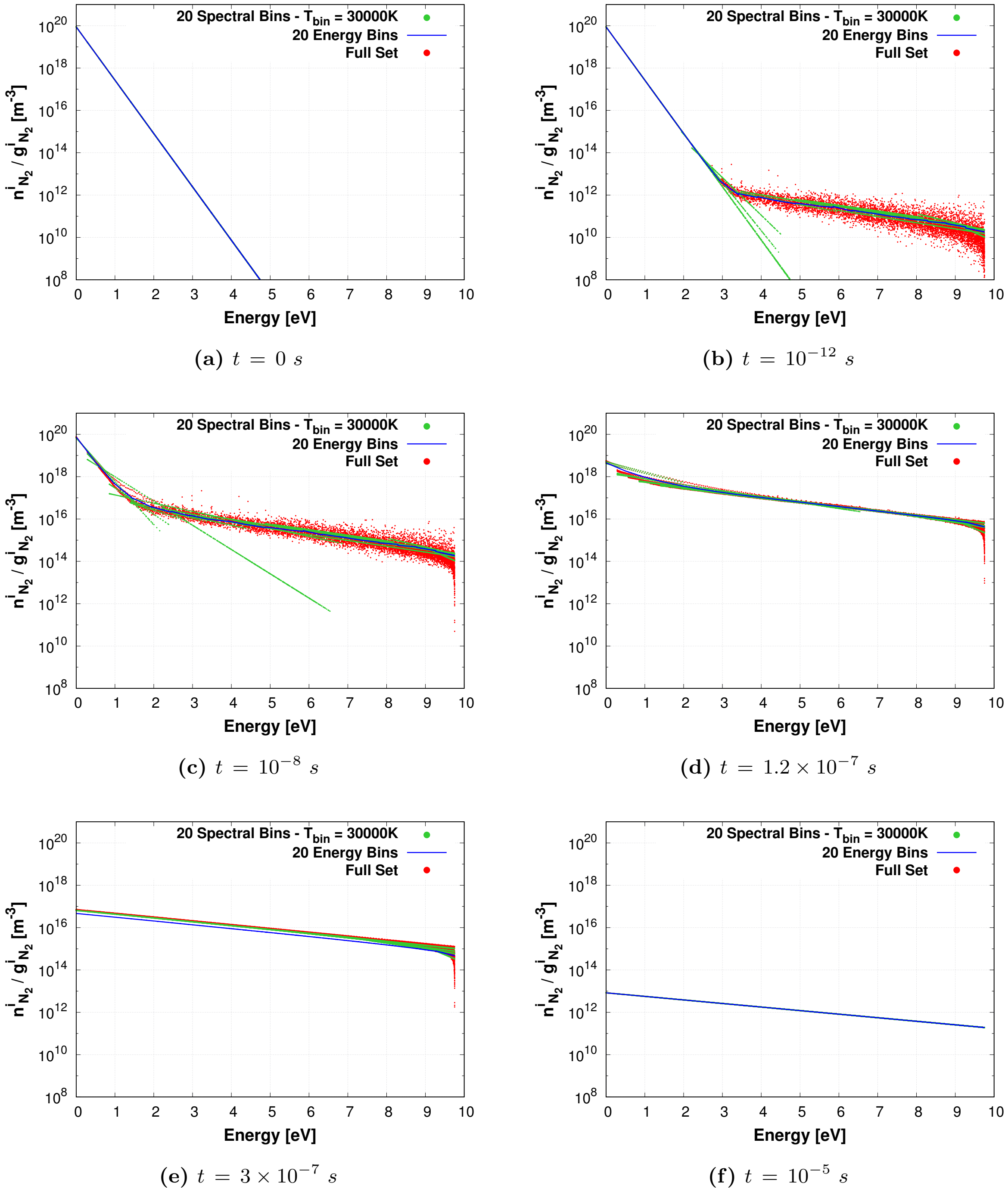

(a) $t = 0\ s$

(b) $t = 10^{-12}\ s$

(c) $t = 10^{-8}\ s$

(d) $t = 1.2 \times 10^{-7}\ s$

(e) $t = 3 \times 10^{-7}\ s$

(f) $t = 10^{-5}\ s$

Figure A.5: Comparison of time evolution of the N_2 rovibrational state distribution for $T_f = T_{bin} = 30,000\ K$, predicted using 20 linear bins based on spectral clustering, 20 linear bins based on energy binning, and the full state-to-state model.

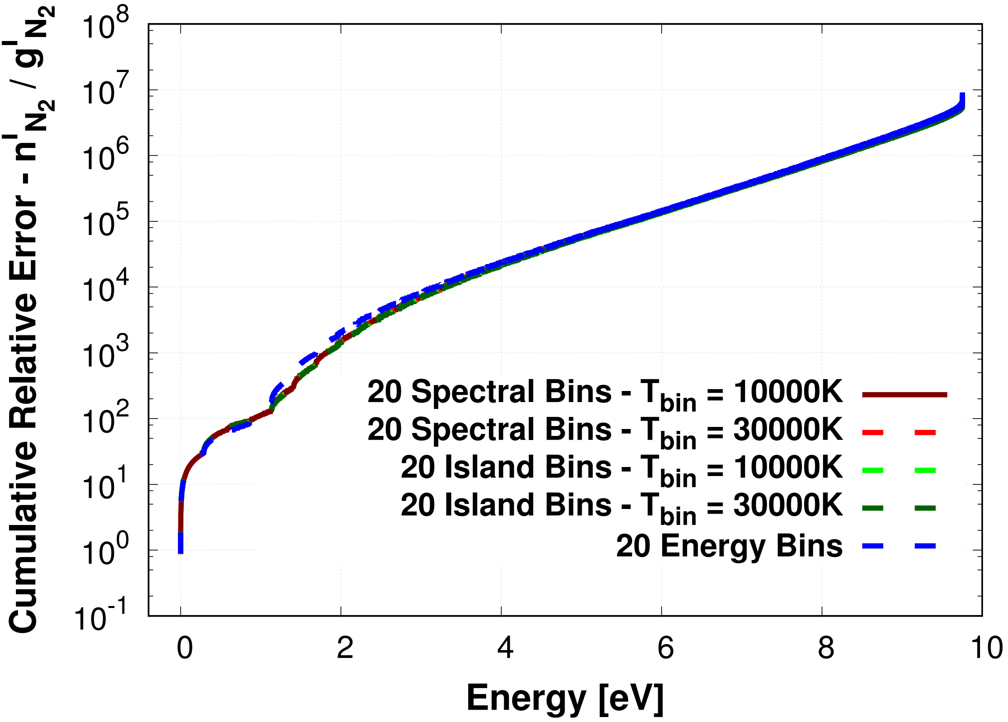

Figure A.6: Comparison of cumulative relative error in predictions for N_2 rovibrational state population for $T_f = 30,000\ K$, obtained using 20 linear bins based on different binning strategies and T_{bin} values at $t = 1.2 \times 10^{-7}\ s$.

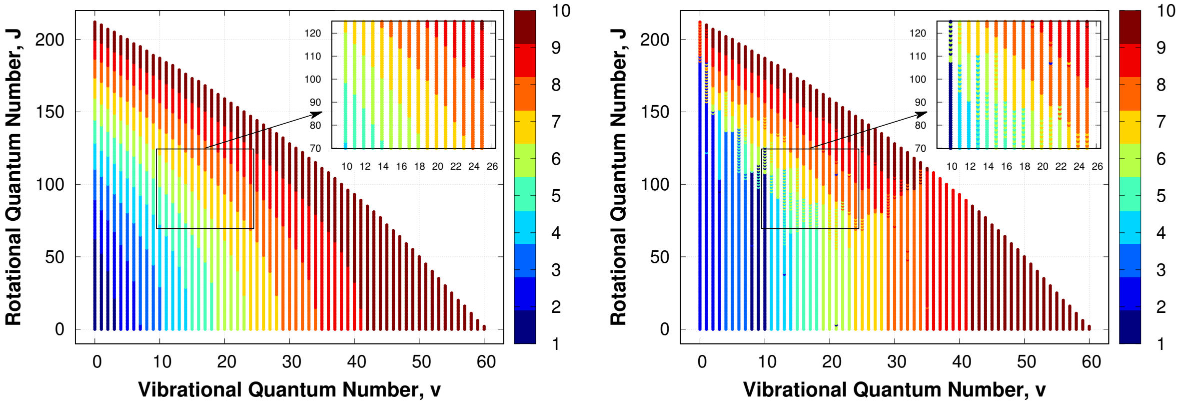

(a) Energy-based binning

(b) Adaptive binning using island algorithm

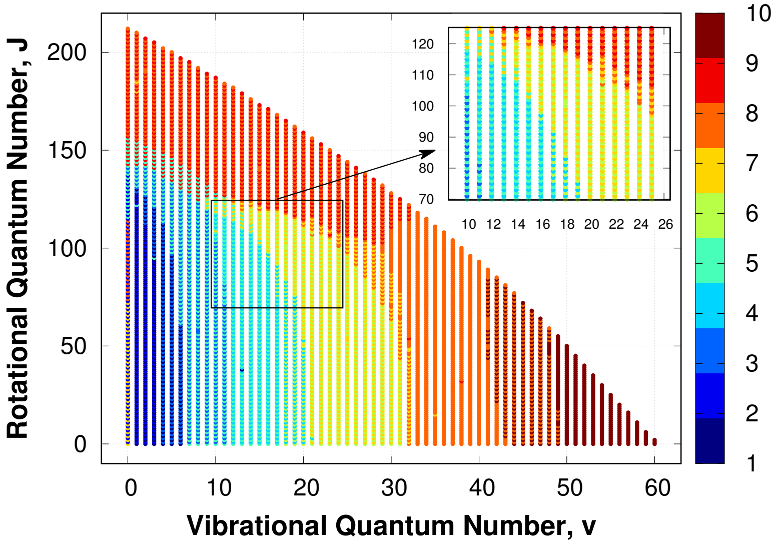

(c) Adaptive binning using spectral clustering

Figure A.7: Quantum configuration of individual states clustered into different bins. The color map on the right represents the bin index for a reduced-order model comprising of 10 linear bins. Adaptive binning is performed at $T_{bin} = 30,000\ K$

Appendix B

Mesh Sweeping Algorithm

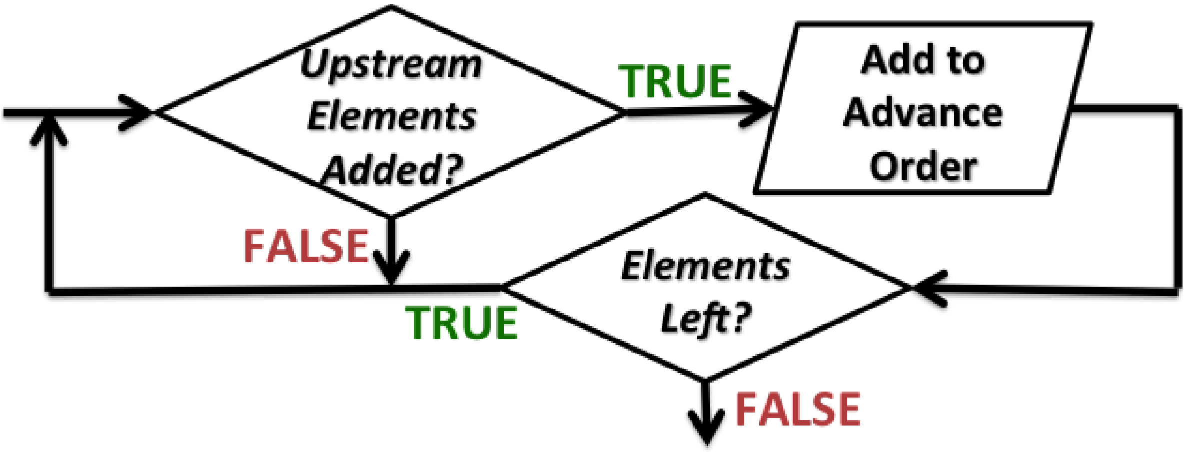

Figure B.1: Mesh sweep workflow while looping over all computational cells.

The mesh sweeping algorithm introduced in Section 4.2 allows radiative intensity along a given direction to be solved explicitly. This is done by identifying the optimal sequence (the "advance-order list") in which computational cells are accessed and the associated intensity values updated. Individual cells are positioned subsequent to all upstream neighbors in the advance-order list for direction $\mathbf{\Omega}^m$. Combining mesh sweeping with first-order upwinding while defining incoming fluxes ensures that cell-centered intensities are obtained through a simple closed-form expression (Eq. 4.13). The typical workflow while adding computational cells to the advance-order list is outlined in Fig. B.1. Mesh sweeping starts at boundary cells with no dependence on the domain interior, *i.e.* all interior faces have outward normals $\mathbf{n}_b \ni \mathbf{\Omega}^m \cdot \mathbf{n}_b < 0$. Consequently, radiative intensity is computed using only the stipulated boundary conditions for these cells. The algorithm then marches through the rest of the domain, adding cells only after their upstream neighbors in direction $\mathbf{\Omega}^m$ have been included in the advance-order list.

Appendix C

Polynomial Fits for Thermodynamic Properties

The current work employs the NASA 9-coefficient parameterization [235] for storing both bin-averaged and the equivalent Boltzmann-aggregate species thermodynamic properties. These fits can be evaluated during CFD calculations to obtain reference state specific heat capacity, enthalpy, and entropy in the following manner:

$$\frac{C_p^\circ(T)}{R} = \frac{a_1}{T^2} + \frac{a_2}{T} + a_3 + a_4\,T + a_5\,T^2 + a_6\,T^3 + a_7\,T^4 \tag{C.1}$$

$$\frac{h^\circ(T)}{R\,T} = -\frac{a_1}{T^2} + a_2\,\frac{\ln T}{T} + a_3 + a_4\,\frac{T}{2} + a_5\,\frac{T^2}{3} + a_6\,\frac{T^3}{4} + a_7\,\frac{T^4}{5} + \frac{b_1}{T} \tag{C.2}$$

$$\frac{s^\circ(T)}{R} = -\frac{a_1}{2\,T^2} - \frac{a_2}{T} + a_3\ln T + a_4\,T + a_5\,\frac{T^2}{2} + a_6\,\frac{T^3}{3} + a_7\,\frac{T^4}{4} + b_2 \tag{C.3}$$

The thermodynamic coefficients for the 10 CO_2 vibrational bins (Chapter 6) in the standard FORTRAN format are:

```
CO2(1)            Lopez-2018
 3 g 7/88     1.00    2.00    0.00    0.00    0.00 0   44.0095000    -393492.770
    200.000   1000.0007 -2.0 -1.0  0.0  1.0  2.0  3.0  4.0  0.0         9382.699
  0.99468936D+05 -0.14980760D+04  0.11333191D+02 -0.18470760D-01  0.38304057D-04
 -0.35146526D-07  0.11169238D-10                 -0.41289507D+05 -0.39235789D+02
   1000.000   6000.0007 -2.0 -1.0  0.0  1.0  2.0  3.0  4.0  0.0         9382.699
 -0.72928174D+07  0.19288645D+05 -0.10420361D+02  0.51536616D-02 -0.10434884D-05
  0.10962035D-09 -0.46679256D-14                 -0.17579344D+06  0.11521378D+03
   6000.000  20000.0007 -2.0 -1.0  0.0  1.0  2.0  3.0  4.0  0.0         9382.699
  0.10978903D+08 -0.37224683D+04  0.41600422D+01 -0.59009145D-04  0.27355714D-08
 -0.60321372D-13  0.45462189D-18                 -0.13268833D+05  0.36183845D+01

CO2(2)            Lopez-2018
 3 g 7/88     1.00    2.00    0.00    0.00    0.00 0   44.0095000    -338058.094
    200.000   1000.0007 -2.0 -1.0  0.0  1.0  2.0  3.0  4.0  0.0        64817.375
  0.55673195D+05 -0.86572396D+03  0.83154769D+01 -0.95564158D-02  0.16543340D-04
 -0.13999977D-07  0.43073904D-11                 -0.37714804D+05 -0.18916145D+02
   1000.000   6000.0007 -2.0 -1.0  0.0  1.0  2.0  3.0  4.0  0.0        64817.375
 -0.24230496D+07  0.57456743D+04  0.10293232D+01  0.47992601D-03 -0.29954276D-07
```

```
 -0.24530551D-11  0.29736478D-15                 -0.80708996D+05  0.31448096D+02
   6000.000  20000.0007 -2.0 -1.0  0.0  1.0  2.0  3.0  4.0  0.0        64817.375
  0.17646002D+07  0.19802601D+03  0.35431842D+01 -0.15535154D-04  0.16278834D-08
 -0.73239392D-13  0.12170311D-17                 -0.40498478D+05  0.11041172D+02

CO2(3)            Lopez-2018
 3 g 7/88     1.00    2.00    0.00    0.00    0.00 0   44.0095000    -290696.101
    200.000   1000.0007 -2.0 -1.0  0.0  1.0  2.0  3.0  4.0  0.0       112179.368
  0.65887218D+05 -0.90484641D+03  0.86451877D+01 -0.98071407D-02  0.14643499D-04
 -0.10950287D-07  0.31004606D-11                 -0.31837134D+05 -0.19530836D+02
   1000.000   6000.0007 -2.0 -1.0  0.0  1.0  2.0  3.0  4.0  0.0       112179.368
 -0.12497220D+07  0.20015694D+04  0.50247920D+01 -0.13184923D-02  0.38174599D-06
 -0.49567083D-10  0.24344047D-14                 -0.51205138D+05  0.35097442D+01
   6000.000  20000.0007 -2.0 -1.0  0.0  1.0  2.0  3.0  4.0  0.0       112179.368
 -0.42327945D+05  0.11168887D+04  0.34817015D+01 -0.24325500D-04  0.31276462D-08
 -0.15096491D-12  0.25963898D-17                 -0.42312426D+05  0.13083280D+02

CO2(4)            Lopez-2018
 3 g 7/88     1.00    2.00    0.00    0.00    0.00 0   44.0095000    -236158.053
    200.000   1000.0007 -2.0 -1.0  0.0  1.0  2.0  3.0  4.0  0.0       166717.416
  0.25627475D+05 -0.17126189D+03  0.53421085D+01 -0.19727956D-02  0.42220849D-05
 -0.39522947D-08  0.12428405D-11                 -0.28876694D+05  0.47198413D+00
   1000.000   6000.0007 -2.0 -1.0  0.0  1.0  2.0  3.0  4.0  0.0       166717.416
 -0.97226880D+06  0.15685159D+04  0.50780715D+01 -0.12464247D-02  0.35117091D-06
 -0.44942866D-10  0.21871248D-14                 -0.41430101D+05  0.37535156D+01
   6000.000  20000.0007 -2.0 -1.0  0.0  1.0  2.0  3.0  4.0  0.0       166717.416
  0.13311042D+07  0.34266150D+03  0.36466917D+01 -0.41926252D-04  0.41374584D-08
 -0.18079896D-12  0.29532469D-17                 -0.29594237D+05  0.12537922D+02

CO2(5)            Lopez-2018
 3 g 7/88     1.00    2.00    0.00    0.00    0.00 0   44.0095000    -182699.186
    200.000   1000.0007 -2.0 -1.0  0.0  1.0  2.0  3.0  4.0  0.0       220176.283
 -0.10156851D+06  0.12197148D+04  0.79211298D+00  0.57143422D-02 -0.27504975D-05
 -0.11243866D-08  0.88877589D-12                 -0.29727818D+05  0.28881045D+02
   1000.000   6000.0007 -2.0 -1.0  0.0  1.0  2.0  3.0  4.0  0.0       220176.283
 -0.13085793D+07  0.32871782D+04  0.26531970D+01 -0.44884040D-04  0.61729882D-07
 -0.10751315D-10  0.60270702D-15                 -0.45236015D+05  0.21693034D+02
   6000.000  20000.0007 -2.0 -1.0  0.0  1.0  2.0  3.0  4.0  0.0       220176.283
 -0.13045841D+07  0.19419045D+04  0.31340476D+01  0.34990931D-04 -0.17828800D-08
  0.45734023D-13 -0.45832603D-18                 -0.35842256D+05  0.17367728D+02

CO2(6)            Lopez-2018
 3 g 7/88     1.00    2.00    0.00    0.00    0.00 0   44.0095000    -137922.486
    200.000   1000.0007 -2.0 -1.0  0.0  1.0  2.0  3.0  4.0  0.0       264952.983
 -0.78381625D+04 -0.69097002D+03  0.13135647D+02 -0.27595017D-01  0.42036816D-04
 -0.30810687D-07  0.86793424D-11                 -0.15682167D+05 -0.38860660D+02
   1000.000   6000.0007 -2.0 -1.0  0.0  1.0  2.0  3.0  4.0  0.0       264952.983
```

```
 -0.93148237D+06  0.19676921D+04  0.43169298D+01 -0.81484488D-03  0.23836217D-06
 -0.30874822D-10  0.15105222D-14                 -0.31569137D+05  0.10282293D+02
   6000.000  20000.0007 -2.0 -1.0  0.0  1.0  2.0  3.0  4.0  0.0       264952.983
 -0.84595983D+07  0.64179313D+04  0.21199356D+01  0.15413460D-03 -0.94360590D-08
  0.30097476D-12 -0.39150310D-17                 -0.65702643D+05  0.26924737D+02

CO2(7)            Lopez-2018
 3 g 7/88     1.00    2.00    0.00    0.00    0.00 0   44.0095000      -86887.691
    200.000   1000.0007 -2.0 -1.0  0.0  1.0  2.0  3.0  4.0  0.0       315987.778
  0.26234246D+06 -0.42942207D+04  0.29876115D+02 -0.62596632D-01  0.80031001D-04
 -0.51832162D-07  0.13373166D-10                  0.81601591D+04 -0.13565394D+03
   1000.000   6000.0007 -2.0 -1.0  0.0  1.0  2.0  3.0  4.0  0.0       315987.778
 -0.85600450D+06  0.21624540D+04  0.39766313D+01 -0.63107200D-03  0.19143205D-06
 -0.25060236D-10  0.12293067D-14                 -0.26306811D+05  0.13179037D+02
   6000.000  20000.0007 -2.0 -1.0  0.0  1.0  2.0  3.0  4.0  0.0       315987.778
  0.15521322D+07  0.50320633D+03  0.35192379D+01 -0.16268769D-04  0.18461849D-08
 -0.85011834D-13  0.14250803D-17                 -0.12325091D+05  0.15238387D+02

CO2(8)            Lopez-2018
 3 g 7/88     1.00    2.00    0.00    0.00    0.00 0   44.0095000      -37101.008
    200.000   1000.0007 -2.0 -1.0  0.0  1.0  2.0  3.0  4.0  0.0       365774.461
  0.23739092D+06 -0.34405313D+04  0.21490057D+02 -0.31560947D-01  0.29490262D-04
 -0.13583706D-07  0.23620190D-11                  0.10697456D+05 -0.92258327D+02
   1000.000   6000.0007 -2.0 -1.0  0.0  1.0  2.0  3.0  4.0  0.0       365774.461
 -0.11890340D+06  0.27364072D+03  0.60277143D+01 -0.15375039D-02  0.39543221D-06
 -0.48098142D-10  0.22632788D-14                 -0.80784825D+04 -0.13101823D+01
   6000.000  20000.0007 -2.0 -1.0  0.0  1.0  2.0  3.0  4.0  0.0       365774.461
  0.96580823D+07 -0.42571212D+04  0.47584819D+01 -0.17874225D-03  0.13248423D-07
 -0.49355767D-12  0.72855543D-17                  0.31725999D+05  0.51423387D+01

CO2(9)            Lopez-2018
 3 g 7/88     1.00    2.00    0.00    0.00    0.00 0   44.0095000       17874.679
    200.000   1000.0007 -2.0 -1.0  0.0  1.0  2.0  3.0  4.0  0.0       420750.148
  0.61183110D+05 -0.68876666D+03  0.56052195D+01  0.10519508D-01 -0.24784530D-04
  0.20442901D-07 -0.60390301D-11                  0.43220200D+04 -0.37436839D+01
   1000.000   6000.0007 -2.0 -1.0  0.0  1.0  2.0  3.0  4.0  0.0       420750.148
 -0.10028968D+07  0.32644081D+04  0.29781568D+01 -0.20765331D-03  0.98488714D-07
 -0.14796745D-10  0.77793419D-15                 -0.20446857D+05  0.21419489D+02
   6000.000  20000.0007 -2.0 -1.0  0.0  1.0  2.0  3.0  4.0  0.0       420750.148
  0.62428701D+07 -0.21210994D+04  0.41426866D+01 -0.92204771D-04  0.68701043D-08
 -0.25673635D-12  0.37986470D-17                  0.21636332D+05  0.10652079D+02

CO2(10)           Lopez-2018
 3 g 7/88     1.00    2.00    0.00    0.00    0.00 0   44.0095000       63983.025
    200.000   1000.0007 -2.0 -1.0  0.0  1.0  2.0  3.0  4.0  0.0       466858.494
 -0.55832869D+05  0.86296109D+03 -0.17509587D+01  0.26245779D-01 -0.39690694D-04
  0.25730495D-07 -0.62897919D-11                  0.22496120D+04  0.38726879D+02
```

```
   1000.000   6000.0007 -2.0 -1.0  0.0  1.0  2.0  3.0  4.0  0.0       466858.494
 -0.20601034D+07  0.72842207D+04 -0.18200516D+01  0.20283331D-02 -0.42443338D-06
  0.46005749D-10 -0.20144186D-14                 -0.39858520D+05  0.56197147D+02
   6000.000  20000.0007 -2.0 -1.0  0.0  1.0  2.0  3.0  4.0  0.0       466858.494
  0.25343141D+07  0.26269925D+03  0.33088614D+01  0.36562915D-04 -0.31713624D-08
  0.13018645D-12 -0.20512744D-17                  0.84726156D+04  0.17490589D+02
```

Combined properties for the entire species can be defined by constraining the constituent reduced-order bins into a single Boltzmann distribution. The fit coefficients for Boltzmann-aggregate properties of CO_2 are:

```
CO2               Lopez-2018
 3 g 7/88     1.00    2.00    0.00    0.00    0.00 0   44.0095000    -393492.770
    200.000   1000.0007 -2.0 -1.0  0.0  1.0  2.0  3.0  4.0  0.0         9382.699
  0.28921359D+05 -0.32914874D+03  0.36107385D+01  0.74241524D-02 -0.77103798D-05
  0.50154596D-08 -0.14889774D-11                 -0.46701555D+05  0.22822403D+01
   1000.000   6000.0007 -2.0 -1.0  0.0  1.0  2.0  3.0  4.0  0.0         9382.699
  0.21424733D+07 -0.78102971D+04  0.15194992D+02 -0.39197053D-02  0.10768108D-05
 -0.13993445D-09  0.64261166D-14                 -0.76168213D+03 -0.75868447D+02
   6000.000  20000.0007 -2.0 -1.0  0.0  1.0  2.0  3.0  4.0  0.0         9382.699
 -0.34147621D+09  0.13415783D+06 -0.58143271D+01 -0.18435983D-03  0.48795708D-07
 -0.20587385D-11  0.28157023D-16                 -0.11949701D+07  0.11402940D+03
```

Appendix D

Fitting Procedure for CO_2 Bin-averaged Rate Coefficients

The present study is primarily aimed at characterizing flowfield properties and radiative response during low-speed Martian atmospheric entry. The low freestream velocity encountered during such missions allows ample time for the gaseous mixture to thermalize completely [227]. Figures 6.6 and 6.11 add further credence to this claim, with translational-rotational temperature T and vibrational-electronic temperature T_V remaining equal almost in the entire domain. In the context of MGME reduced-order modeling, bin internal and translational temperatures being alike simplifies the process of computing bin-averaged rate coefficients (Section 2.3). The single temperature dependence then allows rate-coefficients to be fitted using the Arrhenius form:

$$K \quad = \quad A\,T^n \exp\left(\frac{-E_a}{T}\right) \tag{D.1}$$

Additionally, the micro-reversibility principle can be applied to bin-wise reactions under thermal equilibrium conditions. Thus, the backward rate-coefficient $\bar{K}_r$ is computed using the equilibrium constant and K_r. Although not required in the current analysis, a simple first-order approximation of thermal non-equilibrium ($T \neq T_V$) effects can be obtained by using Park geometric-averaged temperatures [20, 35] in Eq. D.1.

Arrhenius fit coefficients due to bin-wise collisional processes for the 10 CO_2 vibrational bins used in Chapter 6 are presented next. It should be noted that only rate coefficients for bin-specific mass change stemming from StS reactions are discussed here. The first process considered is bin-wise dissociation. The global CO_2 dissociation rate-coefficient that is then unpacked into state-specific values can be found in [36].

$$\mathrm{CO_2}(i) + \mathrm{M} \quad \longleftrightarrow \quad \mathrm{CO} + \mathrm{O} + \mathrm{M} \tag{D.2}$$

	A [m^3/(kmol s)]			
Bin (i)	M $=$ CO_2, CO, O_2	M $=$ C, O	n	E_a
1	3.598E+09	7.1960E+09	-3.66E-02	6.5832E+04
2	6.038E+08	1.2076E+09	1.97E-01	5.9297E+04
3	1.837E+09	3.6740E+09	1.46E-01	5.3623E+04
4	2.972E+09	5.9440E+09	1.59E-01	4.7045E+04
5	2.773E+09	5.5460E+09	2.19E-01	4.0558E+04
6	1.045E+10	2.0900E+10	1.44E-01	3.5148E+04
7	2.378E+10	4.7560E+10	1.20E-01	2.8962E+04
8	1.039E+11	2.0780E+11	3.55E-02	2.2967E+04
9	1.770E+11	3.5400E+11	4.07E-02	1.6322E+04
10	9.691E+10	1.9382E+11	1.40E-01	1.0722E+04

Table D.1: Bin-specific dissociation for 10 bin CO_2 model.

Next, excitation/de-excitation between vibrational bins for different collisional partners is detailed:

$$CO_2(i) + M \longleftrightarrow CO_2(j) + M \tag{D.3}$$

		Collisional Partner M $=$ CO_2		
Initial Bin (i)	Final Bin (j)	A [m^3/(kmol s)]	n	E_a
2	1	3.423E+03	1.78E+00	1.5534E+03
3	2	8.763E+03	1.75E+00	1.5854E+03
4	3	1.128E+04	1.78E+00	1.5763E+03
5	4	8.683E+03	1.86E+00	1.5410E+03
6	5	1.528E+04	1.81E+00	1.5526E+03
7	6	1.741E+04	1.82E+00	1.5504E+03
8	7	2.790E+04	1.77E+00	1.5701E+03
9	8	2.072E+04	1.83E+00	1.5556E+03
10	9	7.407E+03	2.00E+00	1.5132E+03

Table D.2: Bin-specific excitation/de-excitation with M $=$ CO_2 for 10 bin CO_2 model.

Collisional Partner M = CO				
Initial Bin (i)	Final Bin (j)	A [m^3/(kmol s)]	n	E_a
2	1	5.594E+03	1.69E+00	1.7143E+03
3	2	1.432E+04	1.65E+00	1.7463E+03
4	3	1.843E+04	1.68E+00	1.7372E+03
5	4	1.419E+04	1.76E+00	1.7019E+03
6	5	2.498E+04	1.71E+00	1.7135E+03
7	6	2.846E+04	1.72E+00	1.7113E+03
8	7	4.561E+04	1.68E+00	1.7310E+03
9	8	3.387E+04	1.74E+00	1.7165E+03
10	9	1.211E+04	1.90E+00	1.6741E+03

Table D.3: Bin-specific excitation/de-excitation with M = CO for 10 bin CO_2 model.

Collisional Partner M = O_2				
Initial Bin (i)	Final Bin (j)	A [m^3/(kmol s)]	n	E_a
2	1	9.485E+03	1.76E+00	2.0246E+03
3	2	2.428E+04	1.73E+00	2.0566E+03
4	3	3.125E+04	1.76E+00	2.0475E+03
5	4	2.406E+04	1.84E+00	2.0122E+03
6	5	4.235E+04	1.79E+00	2.0238E+03
7	6	4.825E+04	1.80E+00	2.0216E+03
8	7	7.732E+04	1.75E+00	2.0413E+03
9	8	5.742E+04	1.82E+00	2.0268E+03
10	9	2.053E+04	1.98E+00	1.9844E+03

Table D.4: Bin-specific excitation/de-excitation with M = O_2 for 10 bin CO_2 model.

Collisional Partner M = C, O				
Initial Bin (i)	Final Bin (j)	A [m^3/(kmol s)]	n	E_a
2	1	6.646E+04	1.69E+00	2.3092E+03
3	2	1.702E+05	1.65E+00	2.3412E+03
4	3	2.190E+05	1.68E+00	2.3321E+03
5	4	1.686E+05	1.77E+00	2.2968E+03
6	5	2.968E+05	1.71E+00	2.3084E+03
7	6	3.381E+05	1.72E+00	2.3062E+03
8	7	5.419E+05	1.68E+00	2.3259E+03
9	8	4.023E+05	1.74E+00	2.3114E+03
10	9	1.438E+05	1.90E+00	2.2690E+03

Table D.5: Bin-specific excitation/de-excitation with M = C, O for 10 bin CO_2 model.

Atomic oxygen exchange reactions do not presently have a state-specific description. Therefore, the same Arrhenius coefficients are prescribed for every CO_2 vibrational bin. The other reactions that make up the rest of the kinetic scheme for the five species Mars gaseous mixture are:

Reaction	A [$m^3/(kmol\,s)$]	n	E_a
$CO_2(i) + O \longleftrightarrow O_2 + CO$	2.710274E+11	0.00E+00	3.3797E+04
$CO + M \longleftrightarrow C + O + M$ $M = CO_2, CO, O_2$	1.2E+18	-1.00E+00	1.2900E+05
$CO + M \longleftrightarrow C + O + M$ $M = C, O$	1.8E+18	-1.00E+00	1.2900E+05
$O_2 + M \longleftrightarrow O + O + M$ $M = CO_2, CO, O_2$	2.0E+18	-1.50E+00	5.9360E+04
$O_2 + M \longleftrightarrow O + O + M$ $M = C, O$	1.0E+19	-1.50E+00	5.9360E+04

Table D.6: Remaining reactions for five species Mars gaseous mixture.

Appendix E

Verification Studies for NERO Radiative Transfer Solver

The NERO solver (Chapter 6) for computing angularly-spectrally resolved radiative fields on three-dimensional unstructured computational grids has been verified using two different problems.

E.1 Sphere with Radially Variant Temperature

The first verification case considered is radiative transfer through a sphere occupied by an 11-species air mixture [245] at local thermodynamic equilibrium (LTE). The following Gaussian temperature profile is imposed in the radial direction:

$$T(r) \;=\; T_{\text{max}} - (T_{\text{max}} - T_{\text{min}}) \, \frac{1 - \exp\left\{(0.01\, r \,/\, \Delta T)^2\right\}}{1 - \exp\left\{(0.01\, r_{\text{max}} \,/\, \Delta T)^2\right\}} \tag{E.1}$$

where $T_{\text{max}} = 12,000$ K, $T_{\text{min}} = 1,000$ K, $r_{\text{max}} = 1.5 \times 10^{-2}$ m, and $\Delta T = 7.1 \times 10^{-5}$ m are profile parameters. A constant value of pressure $P = 1$ atm is used throughout the domain. Spectral properties of the LTE mixture are modeled using a Planck-averaged wide-band model derived using 100 frequency bands. Additional details on spectral modeling for 11-species air can be found in [209]. Two sets of calculations are performed: a) Numerical solution computed using the NERO solver, and b) reference solution based on the semi-analytical tangent-sphere method for one-dimensional spherical medium [11].

The computational mesh used for numerically solving the current spherical radiative transfer problem is presented in Figure E.1. Although the mesh is stored in an unstructured format, it has been constructed using a multi-block structured approach to ensure greater control over grid point distribution. The final mesh consists of 578, 125 cells split into seven blocks: six identical truncated spherical segments and one central cube. The cubic block is necessary for avoiding singularities

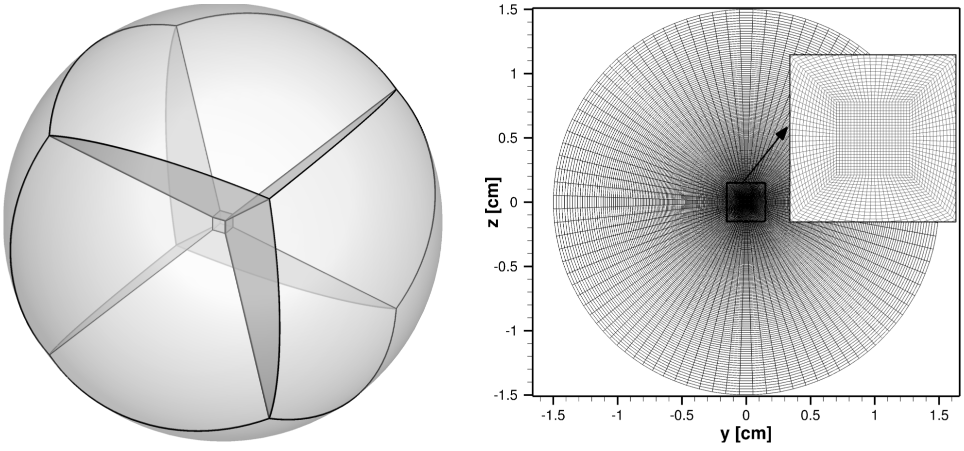

(a) Multi-block Structure **(b)** Along $y = 0$ m plane

Figure E.1: Computational mesh for modeling spherical radiative transfer.

at the center. The total number of discrete quadrature directions and sub-iterations (required to compensate for circular dependencies during mesh-sweeps) are set equal to 170 and 10, respectively. The radial distribution of divergence of total radiative heat flux (negative of volumetric radiative heating) is presented in Fig E.2. Numerical predictions converge to the reference solution obtained using the semi-analytical tangent-sphere method. However, there is a slight discrepancy (error $\sim 1\%$) between the two approaches for radial distances less than 0.05 cm. The deviation from reference values in close proximity to the center occurs while transiting from the spherical segments to the cubic core. This abrupt change introduces misalignment in the mesh and aggravates cell skewness. Consequently, there is a marginal dip in accuracy.

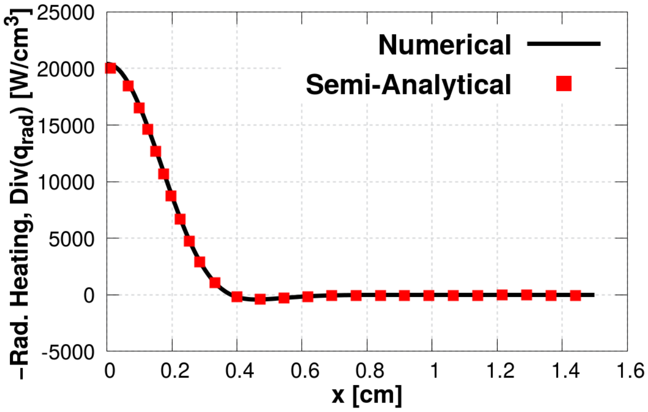

Figure E.2: Numerical and semi-analytical reference solutions for divergence of radiative heat flux along radial direction.

E.2 Comparison with HARA-LAURA Framework

Next, the afterbody radiative surface heat flux computed in the current study (Fig. 6.14) is compared to results using the HARA-LAURA combined framework [227, 229]. The Langley Aerothermodynamic Upwind Relaxation Algorithm (LAURA) [213] is a structured grid hypersonic CFD solver that has been widely used for performing non-equilibrium Navier-Stokes calculations. The High-temperature Aerothermodynamic Radiation (HARA) radiation solver [216, 220] is capable of accurately modeling both spectral variation in absorption/emission behavior and the geometric aspect of radiative transfer in a three-dimensional domain. The flowfield is first computed using LAURA. Then, HARA provides radiative surface heat flux values using a full angular integration methodology based on ray-tracing [83]. The same models for species thermodynamics, chemical kinetics, and absorption/emission spectra have been employed while computing radiative and aerothermal behavior with the NERO-US3D and HARA-LAURA frameworks. Figure 6.14 presents the total radiative heat flux received by the Mars 2020 afterbody along the $y = 0\,\mathrm{m}$ edge for the standard 2-T model and $t = 91.5\,\mathrm{s}$ trajectory point. It should be noted that radiation-flow calculations are not coupled during these comparisons.

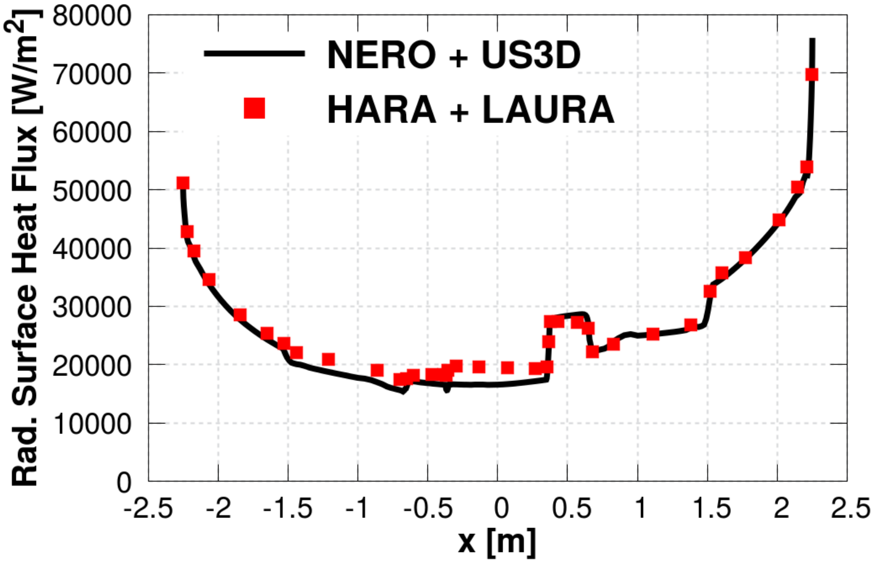

Figure E.3: Surface radiative heat flux along $y = 0$ m edge on the Mars 2020 afterbody at the $t = 91.5\,\mathrm{s}$ trajectory point for the standard 2-T model. Flowfield and radiative behavior is computed using the US3D-NERO (*present work*) and LAURA-HARA frameworks.

Good agreement between results obtained using the two disparate flow-radiation solvers is observed. The slight discrepancies in predicted values arise due to marginally dissimilar computational meshes and inherent differences in the numerical schemes and treatment of boundary conditions employed by US3D and LAURA flow solvers [227]. These verification tests, both canonical radiation problems and comparisons with LAURA-HARA, lend confidence to the numerical results reported in the current work.

References

[1] P. A. Gnoffo. Planetary-entry gas dynamics. *Annual Review of Fluid Mechanics*, 31(1): 459–494, 1999.

[2] J. D. Anderson Jr. *Hypersonic and high-temperature gas dynamics*. American Institute of Aeronautics and Astronautics, 2006.

[3] G. V. Candler. Rate effects in hypersonic flows. *Annual Review of Fluid Mechanics*, 51: 379–402, 2019.

[4] C. Park. *Nonequilibrium hypersonic aerothermodynamics*. Wiley, New York, 1990.

[5] A. Q. Eschenroeder. Ionization nonequilibrium in expanding flows. *ARS Journal*, 32(2): 196–203, 1962.

[6] S. M. Scala and D. H. Sampson. Heat transfer in hypersonic flow with radiation and chemical reaction. Technical Report, General Electric Company, 1963.

[7] C. O. Johnston, P. A. Gnoffo, and A. Mazaheri. Influence of coupled radiation and ablation on the aerothermodynamic environment of planetary entry vehicles. *Radiation and Gas-Surface Interaction Phenomena in High Speed Re-Entry*, 2013.

[8] C. O. Johnston. *Nonequilibrium shock-layer radiative heating for Earth and Titan entry*. Phd Thesis, Virginia Polytechnic Institute and State University, 2006.

[9] M. Panesi. *Physical models for nonequilibrium plasma flow simulations at high speed re-entry conditions*. Phd Thesis, Università di Pisa, 2009.

[10] H. K. Cheng and G. Emanuel. Perspective on hypersonic nonequilibrium flow. *AIAA Journal*, 33(3):385–400, 1995.

[11] M. F. Modest. *Radiative heat transfer*. Academic Press, 2013.

[12] C. O. Johnston and M. Panesi. Impact of state-specific flowfield modeling on atomic nitrogen radiation. *Physical Review Fluids*, 3(1):013402, 2018.

[13] A. Wise, D. K. Prabhu, C. O. Johnston, D. A. Saunders, and K. T. Edquist. Computational aerothermodynamic environments for the Mars 2020 entry capsule. *2018 Joint Thermophysics and Heat Transfer Conference*, AIAA Paper 2018-3116, 2018.

[14] M. J. Wright, F. S. Milos, and P. Tran. Afterbody aeroheating flight data for planetary probe thermal protection system design. *Journal of Spacecraft and Rockets*, 43(5):929–943, 2006.

[15] J. P. Appleton and K. N. C. Bray. The conservation equations for a non-equilibrium plasma. *Journal of Fluid Mechanics*, 20(4):659–672, 1964.

[16] J. H. Lee. Basic governing equations for the flight regimes of aeroassisted orbital transfer vehicles. *Thermal Design of Aeroassisted Orbital Transfer Vehicles*, 96:3–53, 1985.

[17] C. Park. Two-temperature interpretation of dissociation rate data for N_2 and O_2. *26th Aerospace Sciences Meeting*, AIAA Paper 88-0458, 1988.

[18] C. Park. Assessment of a two-temperature kinetic model for dissociating and weakly ionizing nitrogen. *Journal of Thermophysics and Heat Transfer*, 2(1):8–16, 1988.

[19] C. Park. Assessment of two-temperature kinetic model for ionizing air. *Journal of Thermophysics and Heat Transfer*, 3(3):233–244, 1989.

[20] P. A. Gnoffo, R. N. Gupta, and J. L. Shinn. Conservation equations and physical models for hypersonic air flows in thermal and chemical non-equilibrium. Technical Report, NASA Langley Research Center, 1989.

[21] D. Rapp and T. E. Sharp. Vibrational energy transfer in molecular collisions involving large transition probabilities. *The Journal of Chemical Physics*, 38(11):2641–2648, 1963.

[22] R. N. Schwartz, Z. I. Slawsky, and K. F. Herzfeld. Calculation of vibrational relaxation times in gases. *The Journal of Chemical Physics*, 20(10):1591–1599, 1952.

[23] C. E. Treanor, J. W. Rich, and R. G. Rehm. Vibrational relaxation of anharmonic oscillators with exchange-dominated collisions. *The Journal of Chemical Physics*, 48(4):1798–1807, 1968.

[24] M. Capitelli. *Nonequilibrium vibrational kinetics*, Vol. 39. Springer Science & Business Media, 2012.

[25] C. E. Treanor and P. V. Marrone. Effect of dissociation on the rate of vibrational relaxation. *The Physics of Fluids*, 5(9):1022–1026, 1962.

[26] P. V. Marrone and C. E. Treanor. Chemical relaxation with preferential dissociation from excited vibrational levels. *The Physics of Fluids*, 6(9):1215–1221, 1963.

[27] J. S. Ogden. *Introduction to molecular symmetry.* Oxford University Press, 2001.

[28] E. V. Kustova and E. A. Nagnibeda. State-to-state theory of vibrational kinetics and dissociation in three-atomic gases. *Proceedings of the 22nd International Symposium on Rarefied Gas Dynamics*, Vol. 585, Pages 620–627. AIP, 2001.

[29] R. R. Jacobs, K. J. Pettipiece, and S. J. Thomas. Rate constants for the CO_2 $02^00 - 10^00$ relaxation. *Physical Review A*, 11(1):54, 1975.

[30] R. L. Jaffe. Vibrational and rotational excitation and dissociation of CO_2 reexamined. *9th AIAA Aerospace Sciences Meeting*, AIAA Paper 2011-447, 2011.

[31] M. Fertig and G. Herdrich. The advanced URANUS Navier-Stokes code for the simulation of nonequilibrium re-entry flows. *Transactions of the Japan Society for Aeronautical and Space Sciences, Space Technology Japan*, 7(ists26):Pe_15–Pe_24, 2009.

[32] S. Doraiswamy. *Computational study of nonequilibrium chemistry in high temperature flows.* Phd Thesis, University of Minnesota, 2010.

[33] L. Landau and E. Teller. Contribution to the theory of sound dispersion. *Physikalische Zeitschrift der Sowjeturtion*, 10:34, 1936.

[34] R. C. Millikan and D. R. White. Systematics of vibrational relaxation. *The Journal of Chemical Physics*, 39(12):3209–3213, 1963.

[35] C. Park. Review of chemical-kinetic problems of future NASA missions. I-Earth entries. *Journal of Thermophysics and Heat transfer*, 7(3):385–398, 1993.

[36] C. Park, J. T. Howe, R. L. Jaffe, and G. V. Candler. Review of chemical-kinetic problems of future NASA missions. II-Mars entries. *Journal of Thermophysics and Heat transfer*, 8(1): 9–23, 1994.

[37] C. Park. Problems of rate chemistry in the flight regimes of aeroassisted orbital transfer vehicles. *Progress in Astronautics and Aeronautics*, 96:511–537, 1985.

[38] M. Capitelli, C. M. Ferreira, B. F. Gordiets, and A. I. Osipov. *Plasma kinetics in atmospheric gases*, Vol. 31. Springer Science & Business Media, 2013.

[39] P. Hammerling, J. D. Teare, and B. Kivel. Theory of radiation from luminous shock waves in nitrogen. *The Physics of Fluids*, 2(4):422–426, 1959.

[40] S. Losev. Two temperature chemical kinetics in gas dynamics. *Fluid Dynamics Conference*, AIAA Paper 96-2026, 1996.

[41] S. O. Macheret and J. W. Rich. Theory of nonequilibrium dissociation rates behind strong shock waves. *28th Thermophysics Conference*, 1993.

[42] S. O. Macheret, A. A. Fridman, I. V. Adamovich, J. W. Rich, and C. E. Treanor. Mechanisms of nonequilibrium dissociation of diatomic molecules. *6th AIAA/ASME Joint Thermophysics and Heat Transfer Conference*, 1994.

[43] M. Panesi, T. E. Magin, A. Bourdon, A. Bultel, and O. Chazot. Fire II flight experiment analysis by means of a collisional-radiative model. *Journal of Thermophysics and Heat Transfer*, 23(2):236–248, 2009.

[44] M. Panesi, T. E. Magin, A. Bourdon, A. Bultel, and O. Chazot. Study of electronically excited state populations of atoms and molecules predicted by means of a collisional-radiative model for the Fire II flight experiment. *Journal of Thermophysics and Heat Transfer*, 25:361–374, 2011.

[45] M. G. Kapper and J. L. Cambier. Ionizing shocks in argon. Part I: Collisional-radiative model and steady-state structure. *Journal of Applied Physics*, 109(11):113308, 2011.

[46] A. Bultel and J. Annaloro. Elaboration of collisional-radiative models for flows related to planetary entries into the Earth and Mars atmospheres. *Plasma Sources Science and Technology*, 22(2):025008, 2013.

[47] D. A. Gonzales and P. L. Varghese. Vibrational relaxation models for dilute shock heated gases. *Chemical Physics*, 195(1-3):83–91, 1995.

[48] G. Colonna, I. Armenise, D. Bruno, and M. Capitelli. Reduction of state-to-state kinetics to macroscopic models in hypersonic flows. *Journal of Thermophysics and Heat Transfer*, 20 (3):477–486, 2006.

[49] A. Aliat, P. Vedula, and E. Josyula. State-to-state modeling of radiation coupled to vibration-translation relaxation and dissociation in nonequilibrium gas flows. *Physical Review E*, 83 (6):067302, 2011.

[50] D. A. Andrienko and I. D. Boyd. Kinetic models of oxygen thermochemistry based on quasi-classical trajectory analysis. *Journal of Thermophysics and Heat Transfer*, 32(4):904–916, 2016.

[51] M. Panesi, R. L. Jaffe, D. W. Schwenke, and T. E. Magin. Rovibrational internal energy transfer and dissociation of $N_2(^1\sum_g^+) - N(^4S_u)$ system in hypersonic flows. *The Journal of Chemical Physics*, 138(4):044312, 2013.

[52] J. G. Kim and I. D. Boyd. State-resolved master equation analysis of thermochemical nonequilibrium of nitrogen. *Chemical Physics*, 415:237–246, 2013.

[53] M. Panesi, A. Munafò, T. E. Magin, and R. L. Jaffe. Nonequilibrium shock-heated nitrogen flows using a rovibrational state-to-state method. *Physical Review E*, 90(1):013009, 2014.

[54] I. S. Ulusoy, D. A. Andrienko, I. D. Boyd, and R. Hernandez. Quantum and quasi-classical collisional dynamics of $O_2 - Ar$ at high temperatures. *The Journal of Chemical Physics*, 144 (23):234311, 2016.

[55] S. O. Macheret and I. V. Adamovich. Semiclassical modeling of state-specific dissociation rates in diatomic gases. *The Journal of Chemical Physics*, 113(17):7351–7361, 2000.

[56] I. Armenise and E. V. Kustova. State-to-state models for CO_2 molecules: From the theory to an application to hypersonic boundary layers. *Chemical Physics*, 415:269–281, 2013.

[57] D. G. Truhlar. *Potential Energy Surfaces and Dynamics Calculations: For Chemical Reactions and Molecular Energy Transfer.* Springer Science & Business Media, 2013.

[58] D. G. Truhlar and J. T. Muckerman. Reactive scattering cross sections III: Quasiclassical and semiclassical methods. *Atom-Molecule Collision Theory*, Pages 505–566. Springer, 1979.

[59] G. M. Chaban, R. L. Jaffe, D. W. Schwenke, and W. Huo. Dissociation cross sections and rate coefficients for nitrogen from accurate theoretical calculations. *46th AIAA Aerospace Sciences Meeting and Exhibit*, AIAA Paper 2008-1209, 2008.

[60] D. W. Schwenke. Dissociation cross sections and rates for nitrogen. Technical report, DTIC Document, 2009.

[61] J. D. Bender, P. Valentini, I. Nompelis, Y. Paukku, Z. Varga, D. G. Truhlar, T. E. Schwartzentruber, and G. V. Candler. An improved potential energy surface and multi-temperature quasiclassical trajectory calculations of $N_2 + N_2$ dissociation reactions. *The Journal of Chemical Physics*, 143(5):054304, 2015.

[62] R. S. Chaudhry, J. D. Bender, T. E. Schwartzentruber, and G. V. Candler. Quasiclassical trajectory analysis of nitrogen for high-temperature chemical kinetics. *Journal of Thermophysics and Heat Transfer*, 32(4):833–845, 2018.

[63] N. Singh and T. E. Schwartzentruber. Nonequilibrium internal energy distributions during dissociation. *Proceedings of the National Academy of Sciences*, 115(1):47–52, 2018.

[64] A. Bellemans, G. Aversano, A. Coussement, and A. Parente. Feature extraction and reduced-order modelling of nitrogen plasma models using principal component analysis. *Computers & Chemical Engineering*, 115:504–514, 2018.

[65] K. Haug, D. G. Truhlar, and N. C. Blais. Monte Carlo trajectory and master equation simulation of the nonequilibrium dissociation rate coefficient for $\mathrm{Ar} + \mathrm{H_2} \rightarrow \mathrm{Ar} + 2\mathrm{H}$ at 4500 K. *The Journal of Chemical Physics*, 86(5):2697–2716, 1987.

[66] T. E. Magin, M. Panesi, A. Bourdon, R. L. Jaffe, and D. W. Schwenke. Coarse-grain model for internal energy excitation and dissociation of molecular nitrogen. *Chemical Physics*, 398: 90–95, 2012.

[67] M. Panesi and A. Lani. Collisional radiative coarse-grain model for ionization in air. *Physics of Fluids*, 25(5):057101, 2013.

[68] Y. Liu, M. Panesi, A. Sahai, and M. Vinokur. General multi-group macroscopic modeling for thermo-chemical non-equilibrium gas mixtures. *The Journal of Chemical Physics*, 142(13): 134109, 2015.

[69] Y. Liu, M. Vinokur, M. Panesi, and T. E. Magin. A multi-group maximum entropy model for thermo-chemical nonequilibrium. *10th AIAA/ASME Joint Thermophysics and Heat Transfer Conference*, AIAA Paper 2010-4332, 2010.

[70] Y. Liu, M. Panesi, M. Vinokur, and P. Clarke. Microscopic simulation and macroscopic modeling of thermal and chemical non-equilibrium gases. *44th AIAA Thermophysics Conference*, AIAA Paper 2013-3146, 2013.

[71] A. Munafò, Y. Liu, and M. Panesi. Modeling of dissociation and energy transfer in shock-heated nitrogen flows. *Physics of Fluids*, 27(12):127101, 2015.

[72] M. Q. Brewster. *Thermal radiative transfer and properties.* John Wiley & Sons, 1992.

[73] A. Munafò, A. Lani, A. Bultel, and M. Panesi. Modeling of non-equilibrium phenomena in expanding flows by means of a collisional-radiative model. *Physics of Plasmas*, 20(7):073501, 2013.

[74] T. Sakai, T. Tsuru, and K. Sawada. Computation of hypersonic radiating flowfield over a blunt body. *Journal of Thermophysics and Heat Transfer*, 15(1):91–98, 2001.

[75] S. I. Pai. *Radiation gas dynamics.* Springer, 1966.

[76] S. Chandrasekhar. *Radiative transfer.* Courier Corporation, 1960.

[77] D. J. Hyde and J. S. Truelove. The discrete ordinates approximation for multidimensional radiant heat transfer in furnaces. Technical Report, AERE Harwell, UK, 1977.

[78] J. S. Truelove. Three-dimensional radiation in absorbing-emitting-scattering media using the discrete-ordinates approximation. *Journal of Quantitative Spectroscopy and Radiative Transfer*, 39(1):27–31, 1988.

[79] J. C. Chai, H. S. Lee, and S. V. Patankar. Finite volume method for radiation heat transfer. *Journal of Thermophysics and Heat Transfer*, 8(3):419–425, 1994.

[80] P. J. Coelho. Advances in the discrete ordinates and finite volume methods for the solution of radiative heat transfer problems in participating media. *Journal of Quantitative Spectroscopy and Radiative transfer*, 145:121–146, 2014.

[81] S. Richling, E. Meinköhn, N. Kryzhevoi, and G. Kanschat. Radiative transfer with finite elements-I. Basic method and tests. *Astronomy & Astrophysics*, 380(2):776–788, 2001.

[82] G. Kanschat. Solution of radiative transfer problems with finite elements. *Numerical methods in multidimensional radiative transfer*, Pages 49–98. Springer, 2009.

[83] A. Mazaheri, C. O. Johnston, and S. Sefidbakht. Three-dimensional radiation ray-tracing for shock-layer radiative heating simulations. *Journal of Spacecraft and Rockets*, 50(3):485–493, 2013.

[84] W. A. Fiveland. Discrete-ordinates solutions of the radiative transport equation for rectangular enclosures. *Journal of Heat Transfer*, 106(4):699–706, 1984.

[85] E. Boman, J. Tervo, and M. Vauhkonen. Modelling the transport of ionizing radiation using the finite element method. *Physics in Medicine & Biology*, 50(2):265, 2004.

[86] V. Kourganoff. *Basic Methods in Transfer Problems.* Dover Publications, 1963.

[87] C. E. Siewert. A spherical-harmonics method for multi-group or non-gray radiation transport. *Journal of Quantitative Spectroscopy and Radiative Transfer*, 49(2):95–106, 1993.

[88] A. S. Eddington. *The internal constitution of the stars.* Dover Publications, 1959.

[89] R. Turpault. A consistent multigroup model for radiative transfer and its underlying mean opacities. *Journal of Quantitative Spectroscopy and Radiative Transfer*, 94(3-4):357–371, 2005.

[90] R. Turpault. Properties and frequential hybridisation of the multigroup M1 model for radiative transfer. *Nonlinear Analysis: Real World Applications*, 11(4):2514–2528, 2010.

[91] T. Christen and F. Kassubek. Minimum entropy production closure of the photo-hydrodynamic equations for radiative heat transfer. *Journal of Quantitative Spectroscopy and Radiative Transfer*, 110(8):452–463, 2009.

[92] T. Christen and F. Kassubek. Entropy production moment closures and effective transport coefficients. *Journal of Physics D: Applied Physics*, 47(36):363001, 2014.

[93] J. R. Howell. The Monte Carlo method in radiative heat transfer. *Journal of Heat Transfer*, 120(3):547–560, 1998.

[94] J. R. Howell, M. P. Menguc, and R. Siegel. *Thermal radiation heat transfer.* CRC press, 2015.

[95] L. S. Rothman, I. E. Gordon, Y. Babikov, A. Barbe, D. C. Benner, P. F. Bernath, M. Birk, L. Bizzocchi, V. Boudon, L. R. Brown, et al. The HITRAN2012 molecular spectroscopic database. *Journal of Quantitative Spectroscopy and Radiative Transfer*, 130:4–50, 2013.

[96] L. S. Rothman, I. E. Gordon, R. J. Barber, H. Dothe, R. R. Gamache, A. Goldman, V. I. Perevalov, S. A. Tashkun, and J. Tennyson. HITEMP, the high-temperature molecular spectroscopic database. *Journal of Quantitative Spectroscopy and Radiative Transfer*, 111(15): 2139–2150, 2010.

[97] S. A. Tashkun and V. I. Perevalov. CDSD-4000: High-resolution, high-temperature carbon dioxide spectroscopic databank. *Journal of Quantitative Spectroscopy and Radiative Transfer*, 112(9):1403–1410, 2011.

[98] E. E. Whiting, C. Park, Y. Liu, J. O. Arnold, and J. A. Paterson. NEQAIR96, nonequilibrium and equilibrium radiative transport and spectra program: User's manual. Technical Report, NASA Ames Research Center, 1996.

[99] Y. Ralchenko, A. E. Kramida, J. Reader, et al. NIST atomic spectra database. *National Institute of Standards and Technology*, 2008.

[100] C. L. Tien. Thermal radiation properties of gases. *Advances in Heat Transfer*, Vol. 5, Pages 253–324. Elsevier, 1969.

[101] R. M. Goody. A statistical model for water-vapour absorption. *Quarterly Journal of the Royal Meteorological Society*, 78(338):638–640, 1952.

[102] W. Malkmus. Random lorentz band model with exponential-tailed S^{-1} line-intensity distribution function. *Journal of the Optical Society of America*, 57(3):323–329, 1967.

[103] A. Soufiani and J. Taine. High temperature gas radiative property parameters of statistical narrow-band model for H_2O, CO_2 and CO, and correlated-k model for H_2O and CO_2. *International Journal of of Heat and Mass Transfer*, 40(4):987–991, 1997.

[104] J. M. Lamet, P. Rivière, M. Y. Perrin, and A. Soufiani. Narrow-band model for nonequilibrium air plasma radiation. *Journal of Quantitative Spectroscopy and Radiative Transfer*, 111 (1):87–104, 2010.

[105] L. C. Hartung. Predicting radiative heat transfer in thermochemical non-equilibrium flowfields. Theory and user's manual for the LORAN code. Technical Report, NASA Langley Research Center, 1994.

[106] S. S. Yang and T. H. Song. An improved WSGGM-based narrow band model for the CO_2 4.3 μm band. *International Journal of Thermal Sciences*, 38(3):228–238, 1999.

[107] C. D. Levermore. Moment closure hierarchies for kinetic theories. *Journal of Statistical Physics*, 83(5-6):1021–1065, 1996.

[108] S. Karl, D. Potter, M. Lambert, and K. Hannemann. Computational analysis of radiative heat loading on hypervelocity reentry vehicles. *Journal of Spacecraft and Rockets*, 52(1): 63–75, 2014.

[109] C. O. Johnston, A. Sahai, and M. Panesi. Extension of multiband opacity-binning to molecular, non-Boltzmann shock layer radiation. *Journal of Thermophysics and Heat Transfer*, Pages 1–6, 2017.

[110] A. Bansal, M. F. Modest, and D. A. Levin. Multi-scale k-distribution model for gas mixtures in hypersonic nonequilibrium flows. *Journal of Quantitative Spectroscopy and Radiative Transfer*, 112(7):1213–1221, 2011.

[111] T. S. Haut, C. D. Ahrens, A. Jonko, A. T. Till, and R. B. Lowrie. Resolving rapid variation in energy for particle transport. Technical Report, Los Alamos National Laboratory, 2016.

[112] T. S. Haut, C. Ahrens, A. Jonko, R. Lowrie, and A. Till. A new multigroup method for cross-sections that vary rapidly in energy. *Journal of Quantitative Spectroscopy and Radiative Transfer*, 187:461–471, 2017.

[113] I. Nompelis, T. W. Drayna, and G. V. Candler. Development of a hybrid unstructured implicit solver for the simulation of reacting flows over complex geometries. *34th AIAA Fluid Dynamics Conference and Exhibit*, AIAA Paper 2004-2227, 2004.

[114] I. Nompelis, T. W. Drayna, and G. V. Candler. A parallel unstructured implicit solver for hypersonic reacting flow simulation. *Parallel Computational Fluid Dynamics 2005*, Pages 389–395. Elsevier, 2006.

[115] G. V. Candler, H. B. Johnson, I. Nompelis, V. M. Gidzak, P. K. Subbareddy, and M. Barnhardt. Development of the US3D code for advanced compressible and reacting flow simulations. *53rd AIAA Aerospace Sciences Meeting*, AIAA Paper 2015-1893, 2015.

[116] NASA. Mars 2020 mission, 2016. URL `https://mars.nasa.gov/mars2020/`.

[117] F. Abilleira, S. Aaron, C. Baker, D. Burkhart, G. Kruizinga, J. Kangas, M. Jesick, R. Lange, S. E. McCandless, M. Ryne, et al. Mars 2020 mission design and navigation overview. *29th AAS/AIAA Astrodynamics Specialist Conference*, AAS 19-203, 2019.

[118] H. G. Kaper and J. H. Ferziger. *Mathematical theory of transport processes in gases*. North-Holland Publishing, 1972.

[119] V. Giovangigli. Multicomponent flow modeling. *Science China Mathematics*, 55(2):285–308, 2012.

[120] A. Munafò. *Multi-Scale models and computational methods for aerothermodynamics*. Phd Thesis, Ecole Centrale Paris, 2014.

[121] E. A. Nagnibeda and E. V. Kustova. *Non-equilibrium reacting gas flows: Kinetic theory of transport and relaxation processes*. Springer Science & Business Media, 2009.

[122] S. Chapman, T. G. Cowling, and D. Burnett. *The mathematical theory of non-uniform gases: An account of the kinetic theory of viscosity, thermal conduction and diffusion in gases*. Cambridge University Press, 1990.

[123] D. Bruno, F. Esposito, and V. Giovangigli. Relaxation of rotational-vibrational energy and volume viscosity in $\mathrm{H}-\mathrm{H}_2$ mixtures. *The Journal of Chemical Physics*, 138(8):084302, 2013.

[124] A. Ern and V. Giovangigli. *Multicomponent transport algorithms*, Vol. 24. Springer Science & Business Media, 1994.

[125] M. Sharma, Y. Liu, and M. Panesi. Advanced modeling of non-equilibrium flows using a maximum entropy quadratic formulation. *55th AIAA Aerospace Sciences Meeting*, AIAA Paper 2017-1612, 2017.

[126] N. M. Laurendeau. *Statistical thermodynamics: Fundamentals and applications.* Cambridge University Press, 2005.

[127] P. Diaconis. Application of the method of moments in probability and statistics. *Moments in Mathematics*, 37:125–142, 1987.

[128] D. A. McQuarrie. Statistical thermodynamics. 1973.

[129] R. L. Macdonald, R. L. Jaffe, D. W. Schwenke, and M. Panesi. Construction of a coarse-grain quasi-classical trajectory method. I. Theory and application to $N_2 - N_2$ system. *The Journal of Chemical Physics*, 148(5):054309, 2018.

[130] R. L. Macdonald. *Reduced-order model framework for thermochemical non-equilibrium hypersonic flows.* Phd Thesis, University of Illinois at Urbana-Champaign, 2019.

[131] A. Sahai, B. Lopez, C. O. Johnston, and M. Panesi. Adaptive coarse graining method for energy transfer and dissociation kinetics of polyatomic species. *The Journal of Chemical Physics*, 147(5):054107, 2017.

[132] R. Tarjan. Depth-first search and linear graph algorithms. *SIAM Journal on Computing*, 1 (2):146–160, 1972.

[133] J. Hopcroft and R. Tarjan. Algorithm 447: Efficient algorithms for graph manipulation. *Communications of the ACM*, 16(6):372–378, 1973.

[134] J. Shi and J. Malik. Normalized cuts and image segmentation. *IEEE Transactions on Pattern Analysis and Machine Intelligence*, 22(8):888–905, 2000.

[135] A. Y. Ng, M. I. Jordan, Y. Weiss, et al. On spectral clustering: Analysis and an algorithm. *Advances in Neural Information Processing Systems*, 2:849–856, 2002.

[136] U. Von Luxburg. A tutorial on spectral clustering. *Statistics and Computing*, 17(4):395–416, 2007.

[137] N. Grira, M. Crucianu, and N. Boujemaa. Unsupervised and semi-supervised clustering: A brief survey. *A Review of Machine Learning Techniques for Processing Multimedia Content*, 1:9–16, 2004.

[138] E. W. Dijkstra. *A discipline of programming*, Vol. 1. Prentice-Hall Englewood Cliffs, 1976.

[139] T. H. Cormen, C. E. Leiserson, R. L. Rivest, and C. Stein. *Introduction to algorithms*, Vol. 6. MIT Press Cambridge, 2001.

[140] E. V. Kustova and E. A. Nagnibeda. On a correct description of a multi-temperature dissociating CO_2 flow. *Chemical Physics*, 321(3):293–310, 2006.

[141] E. V. Kustova and E. A. Nagnibeda. Kinetic model for multi-temperature flows of reacting carbon dioxide mixture. *Chemical Physics*, 398:111–117, 2012.

[142] L. Zelnik-Manor and P. Perona. Self-tuning spectral clustering. Pages 1601–1608, 2005.

[143] X. Ji and W. Xu. Document clustering with prior knowledge. *Proceedings of the 29th Annual International ACM SIGIR Conference on Research and Development in Information Retrieval*, Pages 405–412. ACM, 2006.

[144] F. R. K. Chung. *Spectral graph theory.* Number 92. American Mathematical Society, 1997.

[145] D. Wagner and F. Wagner. Between min cut and graph bisection. *International Symposium on Mathematical Foundations of Computer Science*, Pages 744–750. Springer, 1993.

[146] M. L. Overton and R. S. Womersley. Optimality conditions and duality theory for minimizing sums of the largest eigenvalues of symmetric matrices. *Mathematical Programming*, 62(1-3): 321–357, 1993.

[147] H. Zha, X. He, C. Ding, M. Gu, and H. D. Simon. Spectral relaxation for k-means clustering. *Advances in Neural Information Processing Systems*, Pages 1057–1064, 2002.

[148] H. Lütkepohl. *Handbook of matrices*, Vol. 1. John Wiley & Sons, 1996.

[149] A. Pothen, H. D. Simon, and K. P. Liou. Partitioning sparse matrices with eigenvectors of graphs. *SIAM Journal on Matrix Analysis and Applications*, 11(3):430–452, 1990.

[150] R. Bhatia. *Matrix analysis*, Vol. 169. Springer Science & Business Media, 2013.

[151] M. Meila and J. Shi. A random walks view of spectral segmentation. 2001.

[152] M. Meila and J. Shi. Learning segmentation by random walks. *Advances in Neural Information Processing Systems*, Pages 873–879, 2001.

[153] L. Kaufman and P. J. Rousseeuw. *Finding groups in data: An introduction to cluster analysis*, Vol. 344. John Wiley & Sons, 2009.

[154] J. A. Hartigan and M. A. Wong. Algorithm AS 136: A k-means clustering algorithm. *Journal of the Royal Statistical Society. Series C (Applied Statistics)*, 28(1):100–108, 1979.

[155] S. Lloyd. Least squares quantization in PCM. *IEEE Transactions on Information Theory*, 28(2):129–137, 1982.

[156] P. R. Mahaffy, C. R. Webster, S. K. Atreya, H. Franz, M. Wong, P. G. Conrad, D. Harpold, J. J. Jones, L. A. Leshin, H. Manning, et al. Abundance and isotopic composition of gases in the martian atmosphere from the Curiosity rover. *Science*, 341(6143):263–266, 2013.

[157] A. Coustenis and F. W. Taylor. *Titan: Exploring an Earthlike world*, Vol. 4. World Scientific, 2008.

[158] A. T. Basilevsky and J. W. Head. The surface of Venus. *Reports on Progress in Physics*, 66 (10):1699, 2003.

[159] J. M. Wallace and P. V. Hobbs. *Atmospheric science: An introductory survey*, Vol. 92. Elsevier, 2006.

[160] S. D. Cohen and A. C. Hindmarsh. CVODE, a stiff/nonstiff ODE solver in C. *Computers in Physics*, 10(2):138–143, 1996.

[161] A. C. Hindmarsh, P. N. Brown, K. E. Grant, S. L. Lee, R. Serban, D. E. Shumaker, and C. S. Woodward. SUNDIALS: Suite of nonlinear and differential/algebraic equation solvers. *ACM Transactions on Mathematical Software*, 31(3):363–396, 2005.

[162] Z. Xianyi, W. Qian, and Z. Yunquan. Model-driven level 3 BLAS performance optimization on Loongson 3A processor. *2012 IEEE 18th International Conference on Parallel and Distributed Systems*, Pages 684–691. IEEE, 2012.

[163] Q. Wang, X. Zhang, Y. Zhang, and Q. Yi. AUGEM: Automatically generate high performance dense linear algebra kernels on x86 CPUs. *Proceedings of the International Conference on High Performance Computing, Networking, Storage and Analysis*, Pages 1–12. IEEE, 2013.

[164] L. Dagum and R. Menon. OpenMP: An industry standard API for shared-memory programming. *Computational Science & Engineering, IEEE*, 5(1):46–55, 1998.

[165] C. Vuik. Krylov subspace solvers and preconditioners. *ESAIM: Proceedings and Surveys*, 63: 1–43, 2018.

[166] V. Hernandez, J. E. Roman, and V. Vidal. SLEPc: A scalable and flexible toolkit for the solution of eigenvalue problems. *ACM Transactions on Mathematical Software*, 31(3):351–362, 2005.

[167] V. Hernandez, J. E. Roman, and V. Vidal. SLEPc: Scalable Library for Eigenvalue Problem Computations. *International Conference on High Performance Computing for Computational Science*, 2565:377–391, 2003.

[168] G. W. Stewart. A Krylov–Schur algorithm for large eigenproblems. *SIAM Journal on Matrix Analysis and Applications*, 23(3):601–614, 2002.

[169] R. Jaffe, D. Schwenke, and G. M. Chaban. Theoretical analysis of N_2 collisional dissociation and rotation-vibration energy transfer. *47th AIAA Aerospace Sciences Meeting*, AIAA Paper 2009-1569, 2009.

[170] R. Jaffe, D. Schwenke, and G. M. Chaban. Vibrational and rotational excitation and dissociation in $N_2 - N_2$ collisions from accurate theoretical calculations. *10th AIAA/ASME Joint Thermophysics and Heat Transfer Conference*, AIAA Paper 2010-4517, 2010.

[171] R. L. Macdonald, A. Munafò, and M. Panesi. Rovibrational grouping for $N_2(^1\sum_g^+) - N_2(^1\sum_g^+)$ energy transfer using state-to-state model. *46th AIAA Thermophysics Conference*, AIAA Paper 2016-4315, 2016.

[172] R. L. Macdonald, M. S. Grover, T. E. Schwartzentruber, and M. Panesi. Construction of a coarse-grain quasi-classical trajectory method. II. Comparison against the direct molecular simulation method. *The Journal of Chemical Physics*, 148(5):054310, 2018.

[173] A. Munafò, M. Panesi, and T. E. Magin. Boltzmann rovibrational collisional coarse-grained model for internal energy excitation and dissociation in hypersonic flows. *Physical Review E*, 89(2):023001, 2014.

[174] K. P. Huber, G. Herzberg, and J. W. Gallagher. NIST chemistry webbook. *NIST Standard Reference Database*, 69, 2011.

[175] O. V. Achasov and D. S. Ragosin. Rate constants of V–V exchange for CO_2 – GDL,. *Preprint 16, Institute of Heat and Mass Transfer*, 16:242, 1986.

[176] Y. D. Shevelev, N. G. Syzranova, E. V. Kustova, and E. A. Nagnibeda. Numerical simulation of hypersonic flows around space vehicles descending in the Martian atmosphere. *Mathematical Models and Computer Simulations*, 3(2):205–224, 2011.

[177] A. Sahai, B. Lopez, C. O. Johnston, and M. Panesi. A reduced order maximum entropy model for chemical and thermal non-equilibrium in high temperature CO_2 gas. *46th AIAA Thermophysics Conference*, AIAA Paper 2016-3695, 2016.

[178] R. Koch and R. Becker. Evaluation of quadrature schemes for the discrete ordinates method. *Journal of Quantitative Spectroscopy and Radiative Transfer*, 84(4):423–435, 2004.

[179] A. F. Woodrow. The selection of discrete ordinate quadrature sets for anisotropic scattering. *Fundamentals of Radiation Heat Transfer*, 160:89–96, 1991.

[180] C. P. Thurgood, A. Pollard, and H. A. Becker. The TN quadrature set for the discrete ordinates method. *Journal of Heat Transfer*, 117(4):1068–1070, 1995.

[181] B. W. Li, Q. Yao, X. Y. Cao, and K. F. Cen. A new discrete ordinates quadrature scheme for three-dimensional radiative heat transfer. *Journal of Heat Transfer*, 120(2):514–518, 1998.

[182] S. A. Rukolaine and V. S. Yuferev. Discrete ordinates quadrature schemes based on the angular interpolation of radiation intensity. *Journal of Quantitative Spectroscopy and Radiative Transfer*, 69(3):257–275, 2001.

[183] B. W. Li, H. G. Chen, J. H. Zhou, X. Y. Cao, and K. F. Cen. The spherical surface symmetrical equal dividing angular quadrature scheme for discrete ordinates method. *Journal of Heat Transfer*, 124(3):482–490, 2002.

[184] V. I. Lebedev. Values of the nodes and weights of ninth to seventeenth order Gauss-Markov quadrature formulae invariant under the octahedron group with inversion. *USSR Computational Mathematics and Mathematical Physics*, 15(1):44–51, 1975.

[185] V. I. Lebedev. Quadratures on a sphere. *USSR Computational Mathematics and Mathematical Physics*, 16(2):10–24, 1976.

[186] B. D. Shizgal, N. Ho, and X. Yang. The computation of radial integrals with nonclassical quadratures for quantum chemistry and other applications. *Journal of Mathematical Chemistry*, 55(2):413–422, 2017.

[187] X. P. Lu, X. J. Huang, W. H. Ip, and C. H. Hsia. Lebedev acceleration and comparison of different photometric models in the inversion of lightcurves for asteroids. *Planetary and Space Science*, 153:1–10, 2018.

[188] F. Liu, H. A. Becker, and A. Pollard. Spatial differencing schemes of the discrete-ordinates method. *Numerical Heat Transfer*, 30(1):23–43, 1996.

[189] A. Wray. Improved finite-volume method for radiative hydrodynamics. *7th International Conference on Computational Fluid Dynamics*, 2012.

[190] E. H. Chui, G. D. Raithby, and P. M. J. Hughes. Prediction of radiative transfer in cylindrical enclosures with the finite volume method. *Journal of Thermophysics and Heat transfer*, 6(4): 605–611, 1992.

[191] P. J. Coelho. A comparison of spatial discretization schemes for differential solution methods of the radiative transfer equation. *Journal of Quantitative Spectroscopy and Radiative Transfer*, 109(2):189–200, 2008.

[192] D. Joseph, M. El Hafi, R. Fournier, and B. Cuenot. Comparison of three spatial differencing schemes in discrete ordinates method using three-dimensional unstructured meshes. *International Journal of Thermal Sciences*, 44(9):851–864, 2005.

[193] M. P. Adams, M. L. Adams, W. D. Hawkins, T. Smith, L. Rauchwerger, N. M. Amato, T. S. Bailey, and R. D. Falgout. Provably optimal parallel transport sweeps on regular grids. Technical report, Lawrence Livermore National Laboratory, 2013.

[194] F. C. Miranda, F. di Mare, A. Sadiki, and J. Janicka. Performance analysis of different solvers for computing the radiative transfer equation in complex geometries using finite volume method and block structured grids. *Computational Thermal Sciences: An International Journal*, 9(3), 2017.

[195] O. Axelsson. *Iterative solution methods.* Cambridge University Press, 1996.

[196] K. Krishnaprakas, K. B. Narayana, and C. Pradip Dutta. Use of GCG methods for the efficient solution of matrix problems arising from the FVM formulation of radiative transfer. *Numerical Heat Transfer, Part B: Fundamentals*, 40(6):515–533, 2001.

[197] J. M. Lamet, Y. Babou, P. Riviere, M. Y. Perrin, and A. Soufiani. Radiative transfer in gases under thermal and chemical nonequilibrium conditions: Application to Earth atmospheric re-entry. *Journal of Quantitative Spectroscopy and Radiative Transfer*, 109(2):235–244, 2008.

[198] J. Taine and A. Soufiani. Gas IR radiative properties: From spectroscopic data to approximate models. *Advances in Heat Transfer*, Vol. 33, Pages 295–414. Elsevier, 1999.

[199] T. Sakai, K. Sawada, and M. Mitsuda. Application of Planck-Rosseland-Gray model for high-enthalpy arc heaters. *Journal of Thermophysics and Heat Transfer*, 15(2):176–183, 2001.

[200] C. Kittel and H. Kroemer. *Thermal physics.* W. H. Freeman, 1998.

[201] B. Dubroca and J. L. Feugeas. Moment closure hierarchy for the radiative transfer equation. *Inertial Fusion Sciences and Applications 99.* 2000.

[202] I. S. Liu. Method of Lagrange multipliers for exploitation of the entropy principle. *Archive for Rational Mechanics and Analysis*, 46(2):131–148, 1972.

[203] T. Goudon and C. Lin. Analysis of the M1 model: Well-posedness and diffusion asymptotics. *Journal of Mathematical Analysis and Applications*, 402(2):579–593, 2013.

[204] M. F. Modest and H. Zhang. The full-spectrum correlated-k distribution for thermal radiation from molecular gas-particulate mixtures. *Journal of Heat Transfer*, 124(1):30–38, 2002.

[205] H. Chu, F. Liu, and H. Zhou. Calculations of gas radiation heat transfer in a two-dimensional rectangular enclosure using the line-by-line approach and the statistical narrow-band correlated-k model. *International Journal of Thermal Sciences*, 59:66–74, 2012.

[206] A. Bansal and M. F. Modest. Modeling of radiative heat transfer in carbonaceous atmospheres using k-distribution models. *Journal of Thermophysics and Heat Transfer*, 27(2):217–225, 2013.

[207] A. H. Stroud and D. Secrest. Gaussian quadrature formulas. *Prentice-Hall Series in Automatic Computation*, 1966.

[208] A. A. Wray, J. F. Ripoll, and D. K. Prabhu. Computation of radiation in the Apollo AS-501 reentry using opacity distribution functions. *AIAA Journal*, 45(9):2359–2363, 2007.

[209] J. B. Scoggins, T. E. Magin, A. A. Wray, and N. N. Mansour. Multi-group reductions of LTE air plasma radiative transfer in cylindrical geometries. *44th AIAA Thermophysics Conference*, AIAA Paper 2013-3142, 2013.

[210] A. A. Wray, D. K. Prabhu, and J. F. Ripoll. Opacity distribution functions applied to the CEV reentry. *39th AIAA Thermophysics Conference*, AIAA Paper 2007-4542, 2007.

[211] D. Mihalas and B. W. Mihalas. *Foundations of radiation hydrodynamics.* Courier Corporation, 2013.

[212] H. Wang and M. Song. Ckmeans.1d.dp: Optimal k-means clustering in one dimension by dynamic programming. *The R Journal*, 3(2):29–33, 2011.

[213] A. Mazaheri, P. A. Gnoffo, C. O. Johnston, and B. Kleb. LAURA users manual: 5.5-65135. Technical Report, NASA Langley Research Center, 2013.

[214] C. O. Johnston, D. Bose, A. Mazaheri, D. K. Prabhu, P. A. Gnoffo, K. Sutton, W. L. Kleb, and A. M. Brandis. Assessment of radiative heating uncertainty for hyperbolic earth entry. *42nd AIAA Thermophysics Conference*, AIAA Paper 2011-3145, 2011.

[215] C. O. Johnston, B. R. Hollis, and K. Sutton. Radiative heating methodology for the Huygens probe. *Journal of Spacecraft and Rockets*, 44(5):993–1002, 2007.

[216] C. O. Johnston, B. R. Hollis, and K. Sutton. Spectrum modeling for air shock-layer radiation at lunar-return conditions. *Journal of Spacecraft and Rockets*, 45(5):865–878, 2008.

[217] C. O. Johnston and A. Mazaheri. Impact of non-tangent-slab radiative transport on flowfield-radiation coupling. *Journal of Spacecraft and Rockets*, 55(4):899–913, 2018.

[218] C. Johnston and M. Panesi. Advancements in afterbody radiative heating simulations for Earth entry. *46th AIAA Thermophysics Conference*, AIAA Paper 2016-3693, 2016.

[219] C. O. Johnston, E. C. Stern, and L. F. Wheeler. Radiative heating of large meteoroids during atmospheric entry. *Icarus*, 309:25–44, 2018.

[220] C. O. Johnston, B. R. Hollis, and K. Sutton. Non-boltzmann modeling for air shock-layer radiation at lunar-return conditions. *Journal of Spacecraft and Rockets*, 45(5):879–890, 2008.

[221] S. Matsuyama, N. Ohnishi, A. Sasoh, and K. Sawada. Numerical simulation of Galileo probe entry flowfield with radiation and ablation. *Journal of Thermophysics and Heat Transfer*, 19 (1):28–35, 2005.

[222] C. O. Johnston. Influence of coupled radiation and ablation on meteor entries. *47th AIAA Thermophysics Conference*, AIAA Paper 2017-4533, 2017.

[223] C. O. Johnston and A. M. Brandis. Aerothermodynamic characteristics of 16-22 km/s Earth entry. *45th AIAA Thermophysics Conference*, AIAA Paper 2015-3110, 2015.

[224] C. Park. Stagnation-region heating environment of the Galileo probe. *Journal of Thermophysics and Heat Transfer*, 23(3):417–424, 2009.

[225] A. Sahai, B. Lopez, C. O. Johnston, and M. Panesi. Novel approach for modeling CO_2 nonequilibrium radiation: Application to wake flows. *AIAA Scitech 2019 Forum*, AIAA Paper 2019-1051, 2019.

[226] S. T. Surzhikov. Comparative analysis of radiative aerothermodynamics of Martian entry probes. *43rd AIAA Thermophysics Conference*, AIAA Paper 2012-2867, 2012.

[227] A. M. Brandis, D. A. Saunders, C. O. Johnston, B. A. Cruden, and T. R. White. Radiative heating on the after-body of Martian entry vehicles. *45th AIAA Thermophysics Conference*, AIAA Paper 2015-3111, 2015.

[228] H. Takayanagi, A. Lemal, S. Nomura, and K. Fujita. Measurement of carbon dioxide infrared radiation in the afterbody of a Mars entry capsule. *55th AIAA Aerospace Sciences Meeting*, AIAA Paper 2017-1369, 2017.

[229] T. K. West, J. Theisinger, A. J. Brune, and C. O. Johnston. Backshell radiative heating on human-scale Mars entry vehicles. *47th AIAA Thermophysics Conference*, AIAA Paper 2017-4532, 2017.

[230] S. Doraiswamy, J. D. Kelley, and G. V. Candler. Vibrational modeling of CO_2 in high-enthalpy nozzle flows. *Journal of Thermophysics and Heat Transfer*, 24(1):9–17, 2010.

[231] D. Yatsukhno, S. T. Surzhikov, D. A. Andrienko, J. Annaloro, and P. Omaly. Different estimations of the convective and radiative heating for the Martian entry probes. *AIAA Scitech 2019 Forum*, AIAA Paper 2019-0793, 2019.

[232] R. Matsuzaki and N. Hirabayashi. Prediction of temperatures and velocity in a nonequilibrium nozzle flow of air. *22nd Thermophysics Conference*, AIAA Paper 87-1477, 1987.

[233] S. Pascal and R. Brun. Transport properties of nonequilibrium gas mixtures. *Physical Review E*, 47(5):3251, 1993.

[234] R. L. Jaffe, D. W. Schwenke, G. M. Chaban, D. K. Prabhu, C. O. Johnston, and M. Panesi. On the development of a new nonequilibrium chemistry model for Mars entry. *55th AIAA Aerospace Sciences Meeting*, AIAA Paper 2017-1372, 2017.

[235] B. J. McBride, M. J. Zehe, and S. Gordon. NASA Glenn coefficients for calculating thermodynamic properties of individual species. Technical Report, NASA Glenn Research Center, 2002.

[236] L. V. Gurvich. Reference books and data banks on the thermodynamic properties of individual substances. *Pure and Applied Chemistry*, 61(6):1027–1031, 1989.

[237] G. V. Candler and R. W. MacCormack. Computation of weakly ionized hypersonic flows in thermochemical nonequilibrium. *Journal of Thermophysics and Heat Transfer*, 5(3):266–273, 1991.

[238] A. Sahai, B. Lopez, C. O. Johnston, and M. Panesi. Novel approach for CO_2 state-to-state modeling and application to multidimensional entry flows. *55th AIAA Aerospace Sciences Meeting*, AIAA Paper 2017-0213, 2017.

[239] R. A. Mitcheltree and P. A. Gnoffo. Wake flow about a MESUR mars entry vehicle. *6th Joint Thermophysics and Heat Transfer Conference*, AIAA Paper 94-1958, 1994.

[240] A. M. Brandis, C. O. Johnston, M. Panesi, B. A. Cruden, D. K. Prabhu, and D. Bose. Investigation of nonequilibrium radiation for Mars entry. *51st AIAA Aerospace Sciences Meeting*, AIAA Paper 2013-1055, 2013.

[241] I. Sohn, Z. Li, D. A. Levin, and M. F. Modest. Coupled DSMC-PMC radiation simulations of a hypersonic reentry. *Journal of Thermophysics and Heat Transfer*, 26(1):22–35, 2012.

[242] W. M. Huo, M. Panesi, and T. E. Magin. Ionization phenomena behind shock waves. *High Temperature Phenomena in Shock Waves*, Pages 149–192. Springer, 2012.

[243] F. G. Blottner, M. Johnson, and M. Ellis. Chemically reacting viscous flow program for multi-component gas mixtures. Technical Report, Sandia National Laboratories, 1971.

[244] J. O. Hirschfelder. Heat conductivity in polyatomic or electronically excited gases. II. *The Journal of Chemical Physics*, 26(2):282–285, 1957.

[245] R. N. Gupta, J. M. Yos, R. A. Thompson, and K. P. Lee. A review of reaction rates and thermodynamic and transport properties for an 11-species air model for chemical and thermal non-equilibrium calculations to 30,000 K. Technical Report, NASA Langley Research Center, 1990.

[246] J. W. Buddenberg and C. R. Wilke. Calculation of gas mixture viscosities. *Industrial & Engineering Chemistry*, 41(7):1345–1347, 1949.

[247] C. R. Wilke. A viscosity equation for gas mixtures. *The Journal of Chemical Physics*, 18(4): 517–519, 1950.

[248] J. D. Ramshaw and C. H. Chang. Ambipolar diffusion in multicomponent plasmas. *Plasma Chemistry and Plasma Processing*, 11(3):395–402, 1991.

[249] J. D. Ramshaw and C. H. Chang. Ambipolar diffusion in two-temperature multicomponent plasmas. *Plasma Chemistry and Plasma Processing*, 13(3):489–498, 1993.

[250] L. D. Landau and E. M. Lifshitz. *Statistical Physics, Volume 5 of Course of Theoretical Physics*. Pergamon Press, 1980.

[251] L. Monchick, K. S. Yun, and E. A. Mason. Formal kinetic theory of transport phenomena in polyatomic gas mixtures. *The Journal of Chemical Physics*, 39(3):654–669, 1963.

[252] L. C. Hartung. Development of a nonequilibrium radiative heating prediction method for coupled flowfield solutions. *Journal of Thermophysics and Heat Transfer*, 6(4):618–625, 1992.

[253] M. Capitelli, G. Colonna, L. D. Pietanza, and G. D'Ammando. Coupling of radiation, excited states and electron energy distribution function in non equilibrium hydrogen plasmas. *Spectrochimica Acta Part B: Atomic Spectroscopy*, 83:1–13, 2013.

[254] A. M. Brandis and B. A. Cruden. NEQAIRv14.0 release notes: Nonequilibrium and equilibrium radiative transport spectra program. Technical Report, NASA Ames Research Center, 2014.

[255] S. A. Tashkun and V. I. Perevalov. CDSD-4000: High-temperature spectroscopic CO_2 databank. *11th Biennial HITRAN Conference*, 2010.

[256] S. A. Tashkun, V. I. Perevalov, J. L. Teffo, L. S. Rothman, and V. l. G. Tyuterev. Global fitting of $^{12}C^{16}O_2$ vibrational–rotational line positions using the effective hamiltonian approach. *Journal of Quantitative Spectroscopy and Radiative Transfer*, 60(5):785–801, 1998.

[257] S. A. Tashkun, V. I. Perevalov, J. L. Teffo, and V. I. G. Tyuterev. Global fit of $^{12}C^{16}O_2$ vibrational–rotational line intensities using the effective operator approach. *Journal of Quantitative Spectroscopy and Radiative Transfer*, 62(5):571–598, 1999.

[258] J. F. Vargas, B. Lopez, M. Panesi, and M. Lino Da Silva. Refitting of detailed CO_2 IR databases to vibrationally specific databases tailored for aerothermodynamic flows. *2018 Joint Thermophysics and Heat Transfer Conference*, AIAA Paper 2018-4177, 2018.

[259] J. F. Vargas, B. Lopez, M. Panesi, and M. Lino Da Silva. Refitting of ro-vibrational specific CO_2 radiation database to vibrationally specific. *AIAA Scitech 2019 Forum*, AIAA Paper 2019-1779, 2019.

[260] C. O. Johnston, P. A. Gnoffo, and K. Sutton. Influence of ablation on radiative heating for earth entry. *Journal of Spacecraft and Rockets*, 46(3):481–491, 2009.

[261] C. O. Johnston, A. Mazaheri, P. A. Gnoffo, B. Kleb, and D. Bose. Radiative heating uncertainty for hyperbolic Earth entry, Part 1: Flight simulation modeling and uncertainty. *Journal of Spacecraft and Rockets*, 50(1):19–38, 2013.

[262] A. Sahai, N. N. Mansour, B. Lopez, and M. Panesi. Modeling of high pressure arc-discharge with a fully-implicit Navier–Stokes stabilized finite element flow solver. *Plasma Sources Science and Technology*, 26(5):055012, 2017.

[263] Y. Ralchenko. *Modern methods in collisional-radiative modeling of plasmas*, Vol. 90. Springer, 2016.

[264] J. L. Steger and R. F. Warming. Flux vector splitting of the inviscid gasdynamic equations with application to finite-difference methods. *Journal of Computational Physics*, 40(2):263–293, 1981.

[265] R. W. MacCormack and G. V. Candler. The solution of the Navier-Stokes equations using Gauss-Seidel line relaxation. *Computers & Fluids*, 17(1):135–150, 1989.

[266] M. J. Wright, G. V. Candler, and M. Prampolini. Data-parallel lower-upper relaxation method for the Navier-Stokes equations. *AIAA Journal*, 34(7):1371–1377, 1996.

[267] J. M. Brock, P. K. Subbareddy, and G. V. Candler. Detached-eddy simulations of hypersonic capsule wake flow. *AIAA Journal*, 53(1):70–80, 2014.

[268] G. V. Candler, P. K. Subbareddy, and J. M. Brock. Advances in computational fluid dynamics methods for hypersonic flows. *AIAA Journal*, 52(1):17–28, 2014.

[269] G. V. Candler, C. R. Alba, and R. B. Greendyke. Characterization of carbon ablation models including effects of gas-phase chemical kinetics. *AIAA Journal*, 31(3):512–526, 2017.

[270] J. M. Brock, E. C. Stern, and M. C. Wilder. Computational fluid dynamics simulations of supersonic inflatable aerodynamic decelerator ballistic range tests. *Journal of Spacecraft and Rockets*, 56(2):526–535, 2018.

[271] M. J. Wright, C. Y. Tang, K. T. Edquist, B. R. Hollis, P. Krasa, and C. A. Campbell. A review of aerothermal modeling for Mars entry missions. *48th AIAA Aerospace Sciences Meeting*, AIAA Paper 2010-443, 2010.

[272] K. T. Edquist, A. A. Dyakonov, M. J. Wright, and C. Y. Tang. Mars science laboratory entry capsule aerothermodynamics environments: Revision B. Technical Report, Jet Propulsion Laboratory, California Institute of Technology, 2010.

[273] K. T. Edquist, B. R. Hollis, C. O. Johnston, D. Bose, T. R. White, and M. Mahzari. Mars science laboratory heat shield aerothermodynamics: Design and reconstruction. *Journal of Spacecraft and Rockets*, 51(4):1106–1124, 2014.

[274] K. T. Edquist. Afterbody heating predictions for a Mars science laboratory entry vehicle. *38th AIAA Thermophysics Conference*, AIAA Paper 2005-4817, 2005.

[275] A. Sahai, B. Lopez, C. O. Johnston, and M. Panesi. Flow-radiation coupling in CO_2 hypersonic wakes using reduced-order non-Boltzmann models. *Physical Review Fluids*, 2019. Accepted.

[276] L. T. Xu, R. L. Jaffe, D. W. Schwenke, and M. Panesi. The effect of the spin-forbidden $\mathrm{CO}(^1\sum^+) + \mathrm{O}(^3\mathrm{p}) \longrightarrow \mathrm{CO2}(^1\sum_g^+)$ recombination reaction on afterbody heating of Mars entry vehicles. *47th AIAA Thermophysics Conference*, AIAA Paper 2017-3486, 2017.

[277] A. Kosareva and G. Shoev. Numerical simulation of a CO_2, CO, O_2, O, C mixture: Validation through comparisons with results obtained in a ground-based facility and thermochemical effects. *Acta Astronautica*, 160:461–478, 2019.

[278] A. Sahai, B. Lopez, C. O. Johnston, and M. Panesi. Reduced-order modeling of non-equilibrium kinetics and radiation for CO_2 axisymmetric wake flows. *Proceedings of the 31st International Symposium on Rarefied Gas Dynamics*, 2132(1):130002, 2019.

[279] E. V. Kustova, E. A. Nagnibeda, T. Y. Alexandrova, and A. Chikhaoui. Non-equilibrium dissociation rates in expanding flows. *Chemical Physics Letters*, 377(5):663–671, 2003.

[280] A. Alberti, A. Munafò, C. Pantano, J. Freund, and M. Panesi. Modeling of air breakdown by single-mode and multi-mode lasers. *AIAA Scitech 2019 Forum*, AIAA Paper 2019-1250, 2019.

[281] S. Venturi, M. Sharma Priyadarshini, A. Racca, and M. Panesi. Effects of ab-initio potential energy surfaces on O_2 – O non-equilibrium kinetics. *AIAA Aviation 2019 Forum*, AIAA Paper 2019-3358, 2019.